PRINTED ISSN: 1308-9080 / OLINE ISSN: 1308-9099

Volume: 19 / Number: 2 / Year: 2024

TURKISH JOURNAL OF SCIENCE & TECHNOLOGY

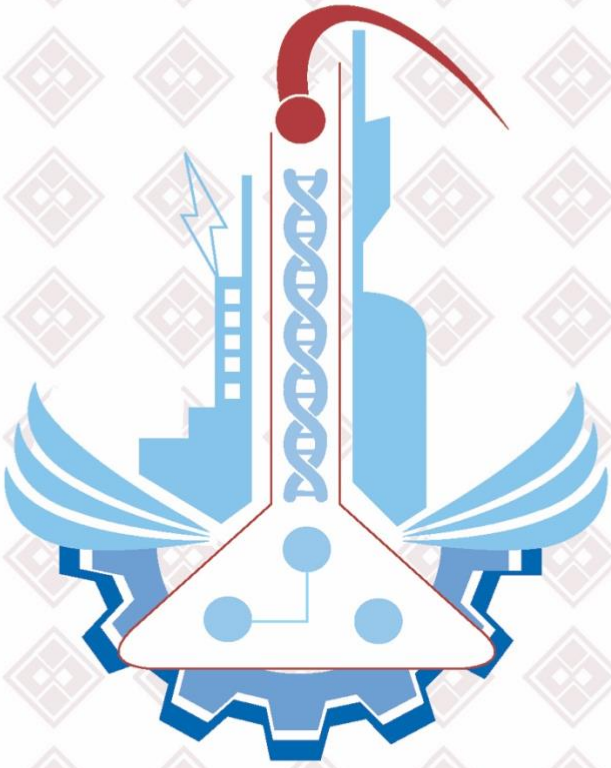

TURKISH JOURNAL OF SCIENCE AND TECHNOLOGY (TJST)

Year: 2024 Vol: 19 Number: 2

Address:
Fırat Universitesi
Fen Bilimleri Enstitüsü
23119, Elazig - TURKEY

Tel: 0 424 212 27 07
Fax: 0 424 236 99 55
e-mail: fenbilim@firat.edu.tr

New ISSN
Online: 1308-9099
Printed: 1308-9080

Old ISSN
Online: 1306 – 8555
Printed: 1306 – 8547

Refereed journal. Published twice a year

https://dergipark.org.tr/tr/pub/tjst

TURKISH JOURNAL OF SCIENCE & TECHNOLOGY (TJST)
Published by Firat University

Fırat University Turkish Journal of Science & Technology (TJST)
19-2, 2024

CONTENTS / İÇİNDEKİLER

Turkish Journal of Science & Technology
19(2), 305-313, 2024

Research Paper
https://doi.org/10.55525/tjst.1381587

Enhancing Blurred Facial Images Using Generative Adversarial Networks

Kenan BAKIR[1*], Yaman AKBULUT[2]
[1,2] Department of Software Engineering, Faculty of Technology, Firat University, Elazig, Turkey
[*1] kenanbakir4@gmail.com, [2] yamanakbulut@firat.edu.tr

(Geliş/Received: 26/10/2023; Kabul/Accepted: 09/11/2023)

Abstract: This research examines the improvement of facial images using generative adversarial networks (GANs). The significance of this topic lies in its potential for enhancing image processing and facial recognition systems. The primary objective of this study is to evaluate the effectiveness of GANs in enhancing the quality of facial images. The hypotheses put forth in this thesis suggest that GAN-based methods can succeed in increasing the resolution and realism of facial images. The sample consists of 70.000 different facial images, representing the primary data source for this study. The method primarily involves the creation and training of a GAN model. A GAN consists of a generator that attempts to mimic real images during the learning process and a discriminator network that evaluates the realism of these images. The findings of the study demonstrate the effectiveness of GANs in making facial images higher in resolution and more realistic. This has the potential to improve the performance of facial recognition systems and enable more precise diagnoses in medical imaging applications. This information underscores the importance of GAN-based methods in enhancing facial images.

Key words: GAN, facial images, image processing, resolution enhancement, face recognition.

Üretici Çekişmeli Ağlar ile Bulanık Yüz Görüntülerinin Geliştirilmesi

Öz: Bu araştırma, üretici çekişmeli ağlar (ÜÇA) kullanarak yüz görüntülerinin geliştirilmesini incelemektedir. Bu konunun önemi, görüntü işleme ve yüz tanıma sistemlerinin gelişmesine yönelik potansiyeli içermektedir. Bu çalışmanın ana hedefi, ÜÇA'ların yüz görüntülerinin kalitesini artırma yeteneğini değerlendirmektir. Bu tezin önerdiği hipotezler, ÜÇA temelli tekniklerin yüz görüntülerinin çözünürlüğünü artırma ve daha gerçekçi hale getirme konularında başarılı olabileceğini iddia etmektedir. Örnekleme, 70,000 farklı yüz görüntüsünden oluşmaktadır ve bu örneklem boyutu, bu çalışmanın temel veri kaynağını temsil etmektedir. Yöntem öncelikle ÜÇA modelinin oluşturulmasını ve eğitilmesini içermektedir. ÜÇA, öğrenme süreci sırasında gerçek görüntülerin taklit edilmesine çalışan bir üretici ve bu görüntülerin gerçekçilik derecesini değerlendiren bir ayrımcı ağdan oluşur. Araştırma sonuçları, ÜÇA'ların yüz görüntülerini daha yüksek çözünürlükte ve daha gerçekçi hale getirme yeteneğini göstermektedir. Bu, yüz tanıma sistemlerinin performansını artırabilir ve tıbbi görüntüleme uygulamalarında daha hassas teşhisler koyma potansiyelini sunar. Bu bilgi, ÜÇA temelli yöntemlerin yüz görüntülerinin geliştirilmesindeki önemini vurgulamaktadır.

Anahtar kelimeler: ÜÇA, yüz görüntüleri, görüntü işleme, çözünürlük arttırma, yüz tanıma.

1. Introduction

Image enhancement focuses on a scientific problem critical to many aspects of modern technology, particularly the challenge of improving the quality of low-resolution images. The significance of this problem arises from the frequent loss of information associated with low-resolution images, which can often prove inadequate for tasks such as object recognition, detail identification, and other analyses. Therefore, image enhancement holds great importance in various fields, ranging from medical imaging systems to security cameras and digital art platforms. In today's world, it is a highly prominent and sought-after research area, central to both computer vision and artificial intelligence. Fundamentally, one of the primary goals in this field is to enhance the quality of low-resolution (LR) images and convert them into high-resolution (HR) results. This objective is critically important in numerous applications, from object recognition systems to medical imaging. While traditional approaches typically rely on simple filtering methods for LR image enhancement, recent years have witnessed the expansion of the boundaries of image enhancement, primarily through deep learning techniques, especially Generative Adversarial Networks (GANs). Deep learning, along with techniques like GANs, offers significant potential in transforming LR images into HR ones, yielding more realistic results. GANs represent a transformation in this field, with their ability to capture visual content more effectively and produce more convincing outcomes. Image enhancement is a pivotal research area, garnering substantial attention within the computer vision and artificial intelligence communities. Specifically, improving the inadequate quality of LR images and generating HR results holds substantial promise in numerous application domains, such as medical imaging, video compression, image restoration, and more. Traditional image enhancement methods typically rely

[*] Corresponding author: kenanbakir4@gmail.com ORCID Number of authors: [1] 0000-0003-3885-5189, [2] 0000-0002-4760-4843

on filtering or interpolation techniques to convert LR images into HR ones, whereas deep learning methods, particularly GANs, have brought about significant changes in this field, effectively capturing visual information and enhancing LR images in a more realistic manner [1]. The assimilation of uniquely human capabilities, such as visual, auditory, and cognitive faculties, by machines, represents a significant research area with a rich historical background. Artificial neural networks (ANNs) have been devised to emulate complex tasks akin to the human brain. However, tasks aimed at being accomplished using ANNs often demand substantial computational power and resources. In this context, progress in this field remained sluggish until advancements in hardware technologies came into play. In recent years, especially with the harnessing of the high computational capabilities of Graphics Processing Units (GPUs), these obstacles have begun to be overcome. Moreover, the development of diverse ANN architectures and algorithms has spurred noteworthy advancements in this domain. The ascent of deep learning models has facilitated the deployment of ANNs across various domains, offering highly accurate analyses. Consequently, deep learning has rapidly gained prominence as an approach. Notably, image enhancement has undergone a substantial transformation, driven by novel methods rooted in deep learning algorithms like GANs. GANs have emerged as potent tools employed to more effectively capture visual content, yielding improved outcomes in the realm of image enhancement. Image super-resolution (SR) using GANs has been a significant area of research, primarily focusing on the transformation of low-resolution images into high-resolution results. These studies have highlighted the potential of GAN-based approaches in image enhancement and underscored the importance of deep learning methods in this field. Therefore, image enhancement with GANs has been attracting increasing attention in both academic and industrial domains. As examples of recent summaries on image SR, articles such as Nasrollahi et al. [2] (Nasrollahi & Moeslund, 2014) or Yang et al. [3] (Yang et al., 2014) can be provided. In this context, these summaries primarily concentrate on single-image super-resolution (SISR) and methods for obtaining HR images from multiple LR images [4, 5]. Prediction-based methods were among the earliest approaches used to address the SISR problem. For instance, filtering approaches like linear, bicubic, or Lanczos [6] can be computationally efficient, but they often oversimplify the SISR problem, resulting in excessively smooth textures. Methods emphasizing edge preservation have also been suggested [1, 7].

More robust approaches aim to create a complex mapping between LR and HR image information and are typically based on training data. Many methods based on example pairs rely on LR training patches for which corresponding HR counterparts are known. Early works in this domain were presented by Freeman et al. [8, 9]. Similar approaches for the SR problem have roots in compressive sensing [10-12]. In the study by Glasner et al. [13], the concept of reusing patches at different scales within an image was introduced, and this notion of similarity has also been utilized in the work by Huang et al. [14], where similarity dictionaries permit smaller transformations and deformations. An approach proposed by Gu et al. [15], involving convolutional sparse coding, enhances consistency across adaptation while realistically reconstructing edge details, thereby avoiding edge artifacts. Tai et al. [16] combine learning-based detail synthesis with an edge-guided SR algorithm based on gradient profile priorities. Zhang et al. [17] suggest a multi-scale dictionary to capture repetitions of similar LR patches at different scales. To super-resolve landmark images, Yue et al. [18] extract HR images with similar content from the web and propose a structure-sensitive matching criterion for alignment. Neighborhood embedding approaches locate similar LR training patches within a low-dimensional manifold to reconstruct corresponding HR patches [19, 20]. Kim et al. [21] emphasize overfitting tendencies in neighborhood approaches and create a more general example pair map. Regression problems can be solved using Gaussian process regression [22], trees [23], or Random Forests. Dai et al. [24] learn multiple patch-specific regressors and select the most appropriate regressors during testing. Recently, convolutional neural network (CNN)-based SR algorithms have demonstrated exceptional performance. Perception-based approaches have been suggested to enhance the visual quality of SR results. Guided by the idea of being closer to perceptual similarity, perceptual loss [25] is proposed to minimize the error in feature space rather than pixel space, improving visual quality. Contextual loss [26] is developed to generate images with natural image statistics by focusing on a target that utilizes feature distribution. Ledig et al. [27] propose the SRGAN model, which uses perceptual loss and adversarial loss to prefer outputs found within the manifold of natural images. Sajjadi et al. [28] develop a similar approach and explore local texture matching loss further. Building upon these works, Wang et al. [29] suggest spatial feature transformation to effectively incorporate semantic priors in an image and enhance recovered textures. Most SR algorithms [30-37] typically focus on super-resolution of grayscale or single-channel images. For color images, the above-mentioned methods first transform the problem into a different color space (YCbCr or YUV), and SR is applied only to the luminance channel. Additionally, there are studies that attempt to super-resolve all channels simultaneously.

2. Super-Resolution

Super-resolution (SR) is a highly significant concept in image processing and computer science. SR involves the process of converting a LR input image into a HR output. Its primary goal is to enhance the details contained

in LR images, creating a sharper and more detailed HR image. SR has diverse applications, particularly in fields such as medical imaging, video analysis, facial recognition, security systems, art restoration, and high-resolution video production. SR algorithms can be based on various methods, including single-image SR, multi-image SR, and deep learning-based SR techniques. Single-image SR attempts to obtain HR output using only a single LR input, while multi-image SR generates HR images by utilizing multiple LR inputs. Deep learning-based SR, especially with CNNs, has gained popularity for processing large datasets to achieve high-resolution results. One challenging aspect of SR is the need for paired LR and HR data, meaning that corresponding high and low-resolution versions of training data must be available, which can be challenging to obtain depending on the application. In summary, Super-Resolution is a widely used technique in enhancing low-resolution images' quality and detail, continually evolving and being subject to innovative research in the field of image processing. Generative adversarial networks play a crucial role in achieving realistic and detailed high-resolution image outputs, reducing data requirements and increasing adaptability in various applications.

The terms high-resolution (HR) and low-resolution (LR) images hold critical importance in the fields of image processing and computer graphics. HR represents the details and clarity of an image and is characterized by a high pixel density. HR images, often having larger file sizes, excel at capturing fine details and are particularly essential in fields such as photography, medical imaging, and high-quality visualization. Conversely, LR images exhibit lower pixel density, typically featuring smaller file sizes and representing images with reduced detail. While LR images offer advantages in data storage and transmission, they come with limitations in terms of image quality. SR is a process that aims to bridge the gap between these two contrasting concepts, as it strives to convert LR images into high-quality and detailed HR images. This holds critical importance in various applications, including medical image analysis, video enhancement, and many others. Therefore, HR and LR terminologies are fundamental concepts in the fields of image processing and image analysis, significantly influencing image quality and usability.

HR and LR images play a vital role in the field of facial recognition. Facial recognition systems are critical for identifying individuals or faces, performing identity verification, enhancing security, automation, and a wide range of applications. Here are some reasons explaining the importance of HR and LR images in the field of facial recognition:

- **Detail and Recognition Capability:** High-resolution images capture facial details and characteristic features more effectively. This results in more reliable and precise outcomes for recognition systems. HR images allow facial recognition algorithms to distinguish individuals more accurately.

- **Reliability and Accuracy:** Low-resolution images can adversely affect the performance of facial recognition systems. The low pixel density in LR images may reduce the accuracy of facial recognition algorithms, leading to false positives or false negatives. HR images minimize these issues.

- **Application Diversity**: Facial recognition is used in various application areas, such as security systems, mobile phones, automation, banking, and more. HR images offer a broader range of applications, accommodating the requirements of these diverse fields.

- **Facial Databases and Training:** Training and verifying facial recognition algorithms require extensive databases. HR images, with their higher level of detail, enhance the quality of these databases. Databases created with LR images may compromise recognition performance.

- **Privacy and Security:** Using facial recognition with LR images can raise privacy concerns. HR image usage provides higher security and privacy levels, as it is more challenging for misuse or unauthorized recognition.

In conclusion, HR and LR images are of great importance in the field of facial recognition. High-resolution images provide the foundation for building more reliable and precise recognition systems, contributing to enhanced security, identity verification, and the development of more effective facial recognition solutions for various applications.

SISR has greatly benefited from the significance of GANs. GANs are particularly useful in addressing the SISR problem because it involves numerous challenges in transforming LR input images into HR results.

Here are detailed explanations of why GANs are essential for SISR:

- **Image Generation and Restoration:** GANs are utilized to transform LR inputs into HR results, forming the basis of the SISR problem. During the training process, GANs learn the relationships between LR and HR images and use these relationships to add missing details or enhance blurry regions, generating HR images.

- **Adding Details:** GANs add or enhance missing details and structures in HR images, making the results look more natural and realistic. This is crucial, especially in applications where details are critical, such as facial recognition or medical imaging.

- **Data Generation:** Acquiring a sufficient number of paired LR and HR training data for SISR is challenging. GANs provide the capability to generate missing data. Starting with LR images, GANs can augment training data, resulting in improved SISR models.

- **Realism and Richness:** GANs help HR images generated to be more realistic and detailed, leading to higher quality and natural-looking results.

- **Flexibility and Adaptability:** GANs can be applied to SISR problems at different resolutions and in various applications. GAN-based SISR methods can work at various scales and formats, making them adaptable to a wide range of application requirements.

In conclusion, GANs play a crucial role in solving the SISR problem by enhancing the process of transforming LR images into high-resolution results. This significantly improves SISR results in image enhancement, medical image analysis, art restoration, and many other application areas. GANs are also instrumental in addressing the challenge of missing data, as they can regenerate limited or incomplete training data, leading to the creation of superior SISR models.

Peak signal-to-noise ratio (PSNR) quantifies the similarity between two images, although in reality, it measures differences rather than similarity. PSNR gauges the relationship between the signal and noise in the comparison between an original image and a reference image. A high PSNR value indicates that the two images are similar, meaning there is low data loss. Higher PSNR values indicate greater similarity between the two images and less data loss. It is particularly used to assess data loss resulting from compression or processing. Below is a reference frame:

- Below 20 dB: Low quality, noticeable data loss.
- 20-25 dB: Average quality, acceptable but still significant data loss.
- 25-30 dB: Good quality, largely acceptable, noticeable data loss is rare.
- 30 dB and above: Very good quality, nearly indistinguishable from the original image, minimal data loss.

A high structural similarity index (SSIM) value indicates that two images have a high level of similarity. This signifies that the two images are close to each other, details are preserved, and there is a high-quality restoration. Therefore, high SSIM values indicate that a restored image is closer to the original, which is generally considered a positive outcome. Here's a reference frame:

- 0.00 - 0.20: Low similarity and quality level.
- 0.20 - 0.40: Moderate similarity and quality, acceptable but noticeable differences may exist.
- 0.40 - 0.60: Good similarity and quality, often considered acceptable.
- 0.60 - 0.80: High similarity and quality, a high quality level.
- 0.80 - 1.00: Very high similarity and quality, nearly identical to the original image.

Table 1. Image quality assessment metrics.

Metrics	Description	Value Range	Applications	Disadvantages
Peak Signal-to-Noise Ratio (PSNR)	PSNR measures the similarity of pixel values between the original and enhanced images. It calculates differences between two images.	Typically falls between 20-50 dB.	Compression, comparison of similar images.	Does not measure perceptual differences.
Structural Similarity Index (SSIM)	SSIM is a metric used to evaluate the similarity and quality between two images. This measure quantifies the similarities between two images with the aim of obtaining results closer to human visual perception.	Has a value between -1 to 1.	Image enhancement, compression, image processing tasks.	May perform poorly in some cases with high-resolution images.

3. Material and Method

For enhancing facial images, StyleGAN, a foundational GAN structure, has been developed and customized, especially designed for generating creative images and portraits. The success of StyleGAN is attributed to being a large and complex model that demands a significant amount of training data and computational power. It features numerous layers and parameters and initiates with pre-trained weights, which are then customized for a specific task or application. In the initial step of this process used in image processing and facial restoration, a degraded image is taken as input. This distorted image is processed through a series of preprocessing steps. In particular, the image is read in RGB format and resized as needed, which encompasses the necessary steps for data processing and analysis. Subsequently, one of the key components of facial restoration, the facial region, is extracted from the image. This step is of vital importance as it involves isolating the face and enhancing specific facial features. The StyleGAN2 Generator Model Architecture plays a central role in this stage. StyleGAN2 is a model that constitutes the foundation of the facial restoration process and enables the attainment of high-quality results. This model encompasses the design of the basic structure that will be used during the restoration process. Then, new trainable layers are added to further customize and enhance the process. Specifically, the G_synthesis/noise layers are updated. These layers form a part of the generator portion of StyleGAN2 and are used to control and adjust the visual characteristics produced by the model. Latent encoding comes into play at this stage, expressing the model's internal representation. This representation includes essential information like visual styles, features, and details. The trained Generator Model represents the model available at this stage of the process. This model has been pre-trained and optimized for the facial restoration process. Lastly, the Server Model Repository signifies a database where the trained model is stored and made accessible. The request-response process entails starting from a degraded input image and culminating in the creation and presentation of a high-quality facial image to the user.

3.1. Dataset

The FFHQ (Flickr-Faces-HQ) dataset was utilized for this thesis study. FFHQ is a large and diverse dataset containing high-resolution facial photographs. This dataset encompasses over 70.000 unique facial images, representing individuals from various races, age groups, and genders. The FFHQ dataset serves as a significant resource for deep learning models, facial recognition algorithms, and other artificial intelligence applications. With its wide variety of high-resolution photographs, this dataset contributes to the development of advanced image processing and analysis techniques and offers researchers an extensive range of data. Creating and using a test dataset is an essential step in artificial intelligence and data analysis projects. Hence, while working with the FFHQ dataset, approximately 500 images were collected and used to assess the project's accuracy and test the model's performance. This test dataset was used to evaluate how well the model performed at the end of the learning process. Each image was chosen to represent different resolutions and various positions, races, age groups, and genders of faces. This was crucial to test the model's generalization and its performance against various variations. The evaluations conducted on the test dataset were used to assess the model's sensitivity, specificity, and other

performance metrics. In conclusion, this test dataset consisting of approximately 500 images was employed to evaluate the accuracy and performance of artificial intelligence models working on the FFHQ dataset, contributing significantly to assessing the project's success.

4. Experimental Results and Discussion

This study utilized the StyleGAN model to investigate the potential of GAN technology in facial enhancement applications. Firstly, when examining the results using the PSNR metric, PSNR is a metric that measures the similarity between original and enhanced facial images. High PSNR values indicate increased similarity between two images. In this study, the PSNR values of enhanced facial images generated using StyleGAN were significantly higher compared to the original facial images. This can be considered a significant finding that validates StyleGAN's ability in facial enhancement. Similarly, the SSIM metric was also used in our evaluations. SSIM is another important metric that measures the degree of similarity between two images. The enhanced facial images produced with StyleGAN had high SSIM values compared to the original facial images, indicating positive results in terms of structural similarity. One of the underlying reasons for the success of StyleGAN in facial enhancement applications is its deep learning capabilities and training with a large dataset. This allows StyleGAN to better understand facial features and make detailed improvements. Examples from the face enhancement test dataset are shown in Table 2.

In the field of image processing and restoration, metrics like PSNR and SSIM are commonly used to assess the quality of restoration processes. These metrics aim to measure the similarity and quality difference between an original image and its restored version. In the context of evaluating a series of images using PSNR and SSIM metrics, the results obtained are as follows:

- In the first row, a PSNR value of 29.26 and an SSIM value of 0.92 were measured. These results indicate that the image restoration process has a very high quality. A high PSNR value suggests that the restored image closely resembles the original. A high SSIM value highlights the structural similarity between the two images. These results show that the restoration process is highly successful.

- In the second row, a PSNR value of 28.25 and an SSIM value of 0.77 were determined. Although PSNR is still quite high, the SSIM value is lower. These results may indicate that some structural features in the image have been lost or altered. While a high PSNR value suggests that some details are preserved, the low SSIM value signifies the loss of structural similarity. This indicates partial success in restoration but shortcomings in preserving certain structures.

- In the third row, a PSNR value of 27.94 and an SSIM value of 0.77 were measured. These results show that the quality of restoration is similar to the previous result, but the PSNR value is slightly lower. This may suggest the loss of some details and variations in colors.

- In the fourth row, again, a PSNR value of 28.25 and an SSIM value of 0.77 were determined. These results are consistent with the previous ones and provide a similar evaluation.

- In the fifth row, a PSNR value of 27.91 and an SSIM value of 0.80 were measured. While the PSNR value is slightly lower, the SSIM value is higher. These results indicate that the restoration process better preserves some structural similarities, resulting in higher similarity between the two images.

In conclusion, PSNR and SSIM values are essential tools for evaluating the quality of image restoration. However, a high PSNR value alone may not always indicate high quality. Therefore, using the SSIM metric, which also measures structural similarity, provides a more comprehensive evaluation. Restoration processes can yield different results depending on the application context and specific requirements. Therefore, evaluating PSNR and SSIM values together helps us better understand the quality of the process.

Table 2. Examples from the face enhancement test dataset.

Input	PSNR	SSIM	Output
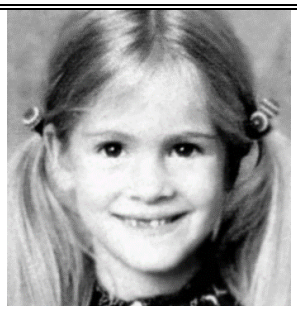	29.26	0.92	
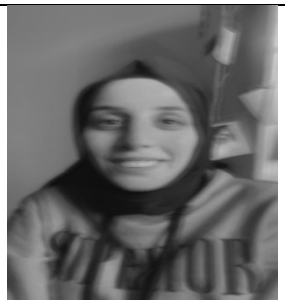	28.25	0.77	
	27.94	0.77	
	28.25	0.77	
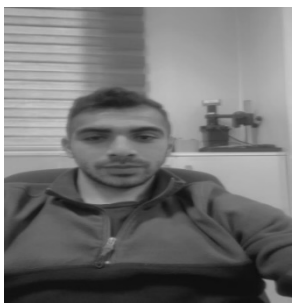	27.91	0.80	

5. Conclusion

This study demonstrates the impressive potential of the StyleGAN model in facial enhancement applications. When examining the results obtained using evaluation metrics like PSNR and SSIM, they are found to be highly positive and satisfactory. These results underline the importance of image enhancement and suggest a significant potential for achieving more aesthetically appealing results, with higher resolution, better contrast, and reduced noise in enhanced facial images. Additionally, this study emphasizes the significance of deep learning. The StyleGAN model successfully enhances facial images through deep learning techniques, offering a more effective approach compared to traditional methods. This highlights the considerable potential of deep learning in the fields of facial enhancement and image quality improvement. Furthermore, this study indicates that deep learning models continue to evolve and improve. These advancements underscore the importance of using larger and more diverse datasets and adopting more complex architectural structures. In the future, these developments could enable the generation of higher-resolution images and more controlled manipulations. This study, along with the success of the StyleGAN model, highlights the importance of deep learning and image enhancement while also emphasizing their future potential. Moreover, this work suggests that these techniques have creative applications and potential use in various industries. Therefore, supporting and advancing research and developments in this field holds great significance. The development and improvement of facial recognition systems play a crucial role in many areas such as security, identity verification, personalized services, and public safety. The results of this study emphasize the need for the strong development of facial recognition technology. In the realm of security, facial recognition systems can be critical in recognizing individuals and detecting threats. This can support crime prevention and resolution efforts, contributing to public safety. In terms of identity verification and security, facial recognition systems can limit access to personal information and provide stronger protection against cyberattacks. This is particularly important for financial institutions and digital service providers. In personalized services, facial recognition technology can enhance user experiences. In conclusion, this study demonstrates the potential of facial recognition systems to enhance security, identity verification, and personalized services, among other crucial applications. The development and improvement of this technology allow society to benefit from enhanced security and personalized services. Therefore, the development of facial recognition systems holds great importance for both technology and society.

References

[1] Allebach J, Wong PW. Edge-directed interpolation. Proceedings of International Conference on Image Processing. 1996; 707–710.
[2] Nasrollahi K, Moeslund TB. Super-resolution: A comprehensive survey. Machine Vision and Applications 2014; 25: 1423–1468.
[3] Yang C-Y, Ma C, Yang M-H. Single-image super-resolution: A benchmark. European Conference on Computer Vision (ECCV), Springer, 2014; 372–386.
[4] Borman S, Stevenson RL. Super-Resolution from Image Sequences - A Review. Midwest Symposium on Circuits and Systems, 1998; 374–378.
[5] Farsiu S, Robinson MD, Elad M, Milanfar P. Fast and robust multiframe super resolution. IEEE Transactions on Image Processing 2004; 13(10): 1327–1344.
[6] Duchon CE. Lanczos Filtering in One and Two Dimensions. Journal of Applied Meteorology 1979; 18: 1016–1022.
[7] Li X, Orchard MT. New edge-directed interpolation. IEEE Transactions on Image Processing 2001; 10(10): 1521–1527.
[8] Freeman WT, Jones TR, Pasztor EC. Example-based superresolution. IEEE Computer Graphics and Applications 2002; 22(2): 56–65.
[9] Freeman WT, Pasztor EC, Carmichael OT. Learning low-level vision. International Journal of Computer Vision 2000; 40(1): 25–47.
[10] Yang J, Wright J, Huang T, Ma Y. Image super-resolution as sparse representation of raw image patches. IEEE Conference on Computer Vision and Pattern Recognition (CVPR) 2008; 1–8.
[11] Dong W, Zhang L, Shi G, Wu X. Image deblurring and super-resolution by adaptive sparse domain selection and adaptive regularization. IEEE Transactions on Image Processing 2011; 20(7): 1838–1857.
[12] Do N-T, Na I-S, Kim S-H. Forensics face detection from GANs using convolutional neural network. ISITC, 2018.
[13] Glasner D, Bagon S, Irani M. Super-resolution from a single image. IEEE International Conference on Computer Vision (ICCV) 2009; 349–356.
[14] Huang JB, Singh A, Ahuja N. Single image super-resolution from transformed self-exemplars. IEEE Conference on Computer Vision and Pattern Recognition (CVPR) 2015; 5197–5206.
[15] Gu S, Zuo W, Xie Q, Meng D, Feng X, Zhang L. Convolutional sparse coding for image super-resolution. IEEE International Conference on Computer Vision (ICCV) 2015; 1823–1831.
[16] Tai Y-W, Liu S, Brown MS, Lin S. Super Resolution using Edge Prior and Single Image Detail Synthesis. IEEE Conference on Computer Vision and Pattern Recognition (CVPR) 2010; 2400–2407.

[17] Zhang K, Gao X, Tao D, Li X. Multi-scale dictionary for single image super-resolution. IEEE Conference on Computer Vision and Pattern Recognition (CVPR) 2012; 1114–1121.
[18] Yue H, Sun X, Yang J, Wu F. Landmark image superresolution by retrieving web images. IEEE Transactions on Image Processing 2013; 22(12) 4865–4878.
[19] Timofte R, De Smet V, Van Gool L. Anchored neighborhood regression for fast example-based super-resolution. IEEE International Conference on Computer Vision (ICCV) 2013; 1920–1927.
[20] Timofte R, De Smet V, Van Gool L. A+: Adjusted anchored neighborhood regression for fast super-resolution. Asian Conference on Computer Vision (ACCV) 2014; 111–126.
[21] Kim KI, Kwon Y. Single-image super-resolution using sparse regression and natural image prior. IEEE Transactions on Pattern Analysis and Machine Intelligence 2010; 32(6): 1127–1133.
[22] He H, Siu WC. Single image super-resolution using gaussian process regression. IEEE Conference on Computer Vision and Pattern Recognition (CVPR) 2011; 449–456.
[23] Salvador J, Perez-Pellitero E. Naive bayes super-resolution forest. IEEE International Conference on Computer Vision (ICCV) 2015; 325–333.
[24] Dai D, Timofte R, Van Gool L. Jointly optimized regressors for image super-resolution. Computer Graphics Forum 2015; 34: 95–104.
[25] Johnson J, Alahi A, Fei-Fei L. Perceptual losses for real-time style transfer and super-resolution. European Conference on Computer Vision (ECCV) 2016.
[26] Mechrez R, Talmi I, Shama F, Zelnik-Manor L. Maintaining natural image statistics with the contextual loss 2018.
[27] Ledig C, Theis L, Huszár F, Caballero J, Cunningham A, Acosta A, Aitken A, Tejani A, Totz J, Wang Z, et al. Photo-realistic single image super-resolution using a generative adversarial network. IEEE Conference on Computer Vision and Pattern Recognition (CVPR) 2017.
[28] Sajjadi MS, Schölkopf B, Hirsch M. Enhancenet: Single image super-resolution through automated texture synthesis. IEEE International Conference on Computer Vision (ICCV) 2017.
[29] Wang X, Yu K, Dong C, Loy CC. Recovering realistic texture in image superresolution by deep spatial feature transform. IEEE Conference on Computer Vision and Pattern Recognition (CVPR) 2018.
[30] Bevilacqua M, Roumy A, Guillemot C, Morel MLA. Low-complexity single-image super-resolution based on nonnegative neighbor embedding. Proceedings of the British Machine Vision Conference (BMVC) 2012; 1–10.
[31] Chang H, Yeung DY, Xiong Y. Super-resolution through neighbor embedding. IEEE Conference on Computer Vision and Pattern Recognition (CVPR), Washington, DC, USA, 2004.
[32] Freeman WT, Pasztor EC, Carmichael OT. Learning low-level vision. International Journal of Computer Vision 2000; 40(11): 25–47.
[33] Mo H, Chen B, Luo W. Fake faces identification via convolutional neural network. ACM IH&MMSEC, 2018.
[34] Yang J, Wang Z, Lin Z, Cohen S, Huang T. "Coupled dictionary training for image super-resolution." IEEE Transactions on Image Processing 2012; 21(11): 3467–3478.
[35] Lago F, Pasquini C, Böhme R, et al. More real than real: A study on human visual perception of synthetic faces. 2021.
[36] Yang J, Wright J, Huang TS, Ma Y. Image super-resolution via sparse representation. IEEE Transactions on Image Processing 2010; 19(11): 2861–2873.
[37] Zeyde R, Elad M, Protter M. On single image scale-up using sparse-representations. Proceedings of the 7th International Conference on Curves and Surfaces 2012; 711–730.

Turkish Journal of Science & Technology
19(2), 315-324, 2024

Research Paper
https://doi.org/10.55525/tjst.1386253

A YOLOV3-Based Method for Detecting Deepfake Manipulated Facial Images

Mehmet KARAKÖSE[1], Hasan YETİŞ[2*], Mert ÇEÇEN[3]
[1,2,3] Department of Computer Engineering, Engineering Faculty, Fırat University, Elazığ, Türkiye
[1] mkarakose@firat.edu.tr, [*2] h.yetis@firat.edu.tr, [3] mert.cecen23@gmail.com

(Geliş/Received: 07/11/2023; Kabul/Accepted: 26/02/2024)

Abstract: With the advancement of technology and the development of applications that make it easier to transfer images, sounds and videos to the virtual environment, it has become much easier to access people's personal information, videos and images. Deepfake technology produces fakes of authentic images or sounds using deep learning and artificial intelligence techniques. Today, in addition to being used in the entertainment and film industries, it is also used in situations such as creating fake news and discrediting people. Different studies have been conducted in the literature to detect deepfake images and videos to prevent these situations. In this study, a comprehensive literature review was conducted. Real and fake images were collected and labelled from different datasets or videos, and a dataset was created by applying the necessary pre-processing steps. With the created dataset, training was carried out with YOLOv3 technology, which calculates class probabilities differently from traditional methods using Convolutional Neural Networks (CNN) and handles all operations in a single regression problem, which can make fast and high-accurate detection, and the modelling process is explained. With the tests performed in the study, the model that can detect fake images produced with deepfake technology with 95% accuracy was obtained.

Keywords: Convolutional neural networks, deepfake image detection, deep learning, YOLOv3.

Derin Sahte ile Manipüle Edilmiş Yüz Görüntülerin Tespiti için YOLOV3 Tabanlı Bir Yöntem

Öz: Teknolojinin ilerlemesi ve görüntü, ses ve videoların sanal ortama aktarılmasını kolaylaştıran uygulamaların gelişmesiyle birlikte insanların kişisel bilgi, video ve görsellerine ulaşmak çok daha kolay hale gelmiştir. Derin sahte teknolojisi, derin öğrenme ve yapay zekâ tekniklerini kullanarak gerçek görüntü veya seslerin sahtelerini üretmek için kullanılmaktadır. Günümüzde eğlence ve film endüstrilerinde kullanılmasının yanı sıra, sahte haber oluşturma ve insanları itibarsızlaştırma gibi durumlarda da kullanılmaktadır. Bu durumların önüne geçmek için literatürde derin sahte görsel ve videoların tespitine yönelik farklı çalışmalar yapılmıştır. Bu çalışmada kapsamlı bir literatür taraması yapılmış ve farklı veri setlerinden veya videolardan gerçek ve sahte görseller toplanmış, etiketlenmiş ve gerekli ön işleme adımları uygulanarak bir veri seti oluşturulmuştur. Oluşturulan veri seti ile Evrişimli Sinir Ağlarını kullanarak geleneksel yöntemlerden farklı bir şekilde sınıf olasılıklarını hesaplayan ve tüm işlemleri tek bir regresyon probleminde ele alan hızlı ve yüksek doğrulukla tespit yapabilen YOLOv3 teknolojisi ile eğitim gerçekleştirilmiş ve modelleme süreci anlatılmıştır. Çalışmada yapılan testlerle derin sahte teknolojisiyle üretilmiş sahte görüntüleri %95 doğrulukla tespit edebilen bir model elde edilmiştir.

Anahtar kelimeler: Evrişimli sinir ağları, deepfake görüntü algılama, derin öğrenme, YOLOv3.

1. Introduction

In today's society, most people use advanced lenses and cameras. In addition, with the applications developed for the digital environment, it has become very easy for users to share and upload images to the internet. It has become easier to access users'personal information, videos and images in these environments developed for people to share [1]. As a result, access to the personal images of government officials, business people, celebrities and many others has become much easier, and the opportunity to use these images has also become much easier. Deepfakes is a widely used technology to generate fake content from real images and sounds using deep learning techniques [2, 3]. The most frequently used deepfake production method uses face replacement with deep neural networks and automatic encoders [4]. In this method, the target video and several images of the face desired to be used in this video are generally used to create a deepfake [5]. Deepfakes are fake media content created using artificial intelligence to create fake news agendas, fake political agendas or personal attacks. When used for malicious purposes, deepfakes can harm individuals' reputations by sabotaging personal data security. Since there is no law prohibiting deepfakes today, detecting deepfakes is an important element in separating real images and fake image data and ensuring their security. The use of Generative Adversarial Networks (GANs) in the production of deepfake images is quite common [6]. Karras and colleagues proposed a controversial generative network model called StyleGAN to generate images of faces that have never existed before [7]. In another study, Zhu et al.

* Corresponding author: h.yetis@firat.edu.tr. ORCID Number of authors: [1] 0000-0002-3276-3788, [2] 0000-0001-7608-3293, [3] 0009-0008-3658-047X

introduced a face replacement method based on a generative adversarial network called CycleGAN [8]. Choi et al. introduced a technique called StarGAN, which can alter facial features like hair or skin colour, gender, age, and the presence of eyeglasses [9]. Thies et al. employed the Face2Face technique, which is based on a generative adversarial network, to manipulate the facial expressions of individuals in images [10]. As creating such fake images has become widespread and deepfake technology has developed dramatically, methods used to detect images created using this technology have also begun to be developed. Models were trained using data sets to detect deepfake images, and some signs and anomalies were tried to be detected to distinguish fake images from real images with the models created. Deepfake Detection technology detects fake images or videos [11-14]. Deepfake Detection is the process of detecting deepfake content. It was developed to detect fake or modified media content using deep learning techniques and artificial intelligence. There are different studies in the literature on detecting deepfake images. Deepfake detection studies, where the images used in these studies and the methods used to detect these images are explained in Table 1.

Table 1. Deepfake detection studies.

Reference	Images used in Deepfake Detection	Methods used in Deepfake Detection
[15]	Any video images that met the requirement of not exceeding a 50 Mb file size was used.	MesoInception4, FWA, VA-MLP, Xception-c23, ClassNSeg, Capsule, DSP-FWA, CNNDetection, Upconv, WM, Selim methods.
[16]	A new dataset containing high-quality Deepfake images with different models from DeepFakes was used.	The authors developed a method to identify high-quality Deepfakes by designing DMA-STA, a simple and effective Deepfakes model no-hold method based on spatial and temporal attention.
[17]	Images showing head posture and all features of the face were used using central areas from the images in the DARPA MediFor GAN Image/Video Challenge dataset and the images obtained from real and fake video frames in the UADFV dataset.	To determine whether the existing images in the datasets they used were fake or real, the authors performed training using Support Vector Machine (SVM), which is based on detecting differences between head poses estimated using facial landmarks and those in central facial regions.

An open-source online platform that can integrate Deepfake detection methods, called DeepFake-o-meter, was created by Yuezun Li et al. [15]. Users using this platform choose one of the methods that can upload any video that meets the condition of not exceeding 50 Mb file size and use it based on the advanced Inception modules, one of the deepfake detection methods offered by the system. These methods are MesoInception4, FWA, VA-MLP, Xception-c23, ClassNSeg, Capsule, DSP-FWA, CNNDetection, Upconv, WM, Selim methods [18]. After the uploaded video passes through the Docker containers, the faces in the video are extracted. After the captured images go through various pre-processing steps, it is determined whether the face is fake or not. Shan Jia et al. created a new data set by collecting different deepfake images. In this set, they used FaceSwap software and Autoencoder models to create five valid categories for Deepfake videos with examples in encoder, decoder, middleware, and input data. By designing a simple and effective Deepfakes model no-hold method, DMA-STA, based on spatial and temporal attention, achieved and evaluated over 70% accuracy in identifying high-quality Deepfakes on the DFDM dataset [16]. Yang and his colleagues compared head posture poses using facial features with central areas of the face in photographs and videos. To detect fake and real images or videos, they used the images contained in the DARPA MediFor GAN Image/Video Challenge dataset and the images in frames from the videos in the UADFV dataset. They used the differences in head poses as a feature vector to train the support vector machine (SVM). As a result of the studies, they revealed that the SVM classifier achieved 0.890 AUROC in the UADFV dataset and 0.843 AUROC in the DARPA MediFor GAN Image/Video Challenge dataset by using separate frames as the unit of analysis with the Area Under ROC (AUROC) as the performance measurement. [17].

Within the scope of these studies in the literature, different deep learning methods have been used to detect deepfake images and videos. Deep learning is a subset of machine learning that uses classification processes and learning methods to represent data in a specific format [19]. Deep learning is based on using the data set as an input and creating a model that can predict the outputs with the help of artificial intelligence. When classifying with deep learning, pre-processing steps significantly amplify the inputs and irrelevant variations are significantly suppressed [20]. Convolutional Neural Network (CNN), Recurrent Neural Network (RNN), Deep Belief Network, Deep Boltzmann Machine and Deep Autoencoder techniques are used in deep learning. Convolutional Neural

Networks have achieved great success in areas such as image processing, object detection, face recognition and video analysis [20, 21]. A convolutional Neural Network is a neural network that contains one or more convolutional layers, subsampling layers, and standard multiple layers. Although neural networks are not new, they are based on Alexnet [21] and Imagenet [22] technologies used to classify large-scale data. The working principle of Convolutional Neural Networks includes layers that can automatically extract and represent complex data features. YOLO technology takes the entire image simultaneously and estimates bounding box coordinates and class probabilities [23]. The training process of YOLO technology ensures that it has better generalisation ability overall as it is created using a large data set. In addition, better results can be achieved as it allows users to use various data augmentation techniques.

In this study, it is aimed to detect fake medical images created by deepfake methods. Chapter 2 provides information about YOLOv3 architecture and how to use it in practice. In Chapter 3, the application results are given experimentally and comparisons are made with current literature studies with similar purposes. In the Chapter 4, last section, the findings obtained as a result of the study are given and discussed.

1.1. Motivation

Deepfake is used to produce a different image by transferring the face of a source individual to the target person's body. Internet users first encountered the images produced by this technology in 2017 [24,25]. The first studies on producing deepfakes were carried out in 2014 by training Generative Adversarial Networks (GANs) with very large data sets. Deepfake, a type of artificial media that uses artificial intelligence to transform a person's image into a manipulated photo or video, can make people appear to say or do things they actually do not. Research reports state that images, sounds or videos produced with this technology may be used to facilitate crime in the coming years. In order to prevent these incidents from occurring, a study was carried out to detect the images produced by deepfake. In this study, a data set created with images taken from different data sets and videos and a model training was carried out using YOLOv3 technology to determine whether the images produced with deepfake are real or fake.

2. Proposed Method

In this study, it is aimed to detect an image if it is real or created by deepfake techniques. The proposed method contains of dataset collection, data regulation, detection (training-validation-testing the model) steps. In data collection step, the original images of the people and the fake images produced from these original images with deepfake technology were collected manually and turned into a data set. Orientation, image resizing, rotation, and brightness correction is applied on collected images. Because 416x416 YOLOv3 version is used, the images are resized according to the YOLO structure for faster training process. After applying the image pre-processing steps, the data set obtained. The obtained data set is divided into training, validation and testing data. 70% of all data is used for training, 10% of all data used for validation, and 20% of all data is used for test. Then training, validation, and test of the model actualized. After images are labelled as fake or real, the training process begins. Validation data was issued to measure the model's accuracy, while testing data was used to test the model after it was built. The general block diagram of the proposed method is given in Figure 1. In Figure 1, the last block refers to deep learning model. In the model, n is 1,2,4 and 8 respectively. When n is 2 then the 52x52 feature map is used for obtaining detailed (small) objects. When n is 4 medium-scale objects are detected from 26x26 feature map. And when n is 8, 13x13 feature map is used for less detailed (big) objects. The last block, model block, is shortening form of YOLOv3, given in Figure 2. At last, YOLO inferences from small, medium, and big objects, and determine the bounding box. Beside the bounding box, a class label (real or fake for our problem) is produced by YOLO.

Real and fake images produced with deepfake technology are collected to obtain the data set step. The bounding box labelling method was applied to the collected images. Automatic orientation was applied to the existing images to enrich the collected images before adding them to the data set. All image data was resized to 416 × 416 to be trained effectively and quickly in YOLOv3 technology. Then, a 10° rotation and a 25% brightness adjustment were made on the images for better recognition of each image. After the operations, the number of images in the dataset was obtained as 44,100. The clustered datasets are divided into 70% training, 10% validation, and 20% testing data.

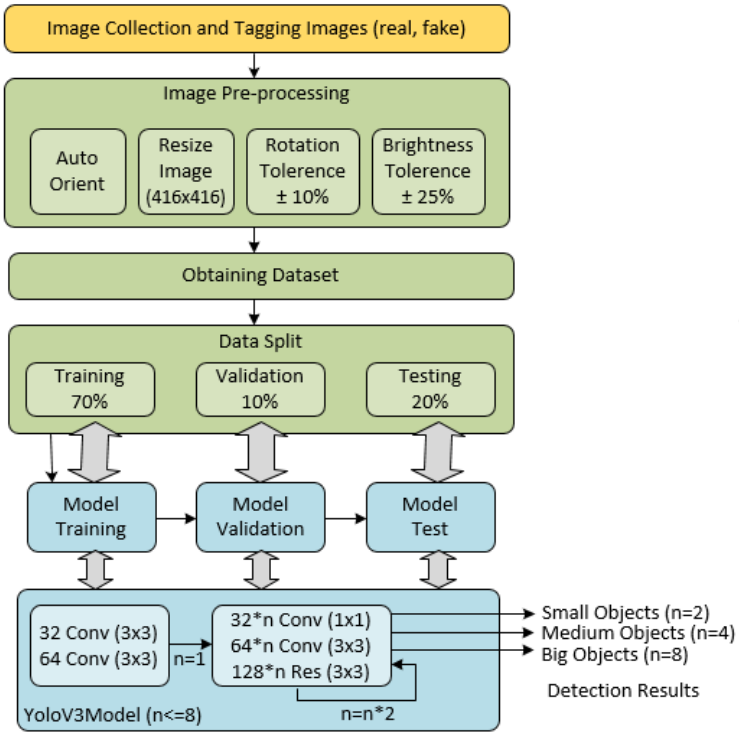

Figure 1. The block diagram of the proposed method.

In model stage, YOLOv3 technology using Convolutional Neural Networks was used. YOLOv3 technology was chosen among YOLO versions in order to train the model quickly and with high accuracy. Depending on different YOLO architectures, variable input sizes can be used: 320 × 320, 416 × 416 and 608 × 608. In this study, 416x416 sized inputs were used in order not to reduce image quality and increase processing speed. YOLOv3 uses Darknet-53 model for feature extraction. Figure 2 shows the main stages of the YOLOv3 algorithm with 416x416 image input. Convolution and residual layers are applied according to Darknet-53 model as shown in Figure 2. After reducing the image size to 52x52, 26x26 and 13x13, some other convolution layers are applied for detection of the interest area and the label. In YOLOv3, three different estimation scales are employed during the estimation process. The detection layer is employed to identify feature maps with three distinct dimensions, characterised by strides of 32, 16, and 8. The hyper parameters of the proposed method are given in Table 2.

Table 2. Hyper parameters of proposed method.

Parameter	Value
Input size	416x416
Classes	2
Threshold	0.3
Batch	64
Subdivisions	16
Channels	3
Momentum	0.9
Decay	0.0005
Learning rate	0.001
Max batches	4000

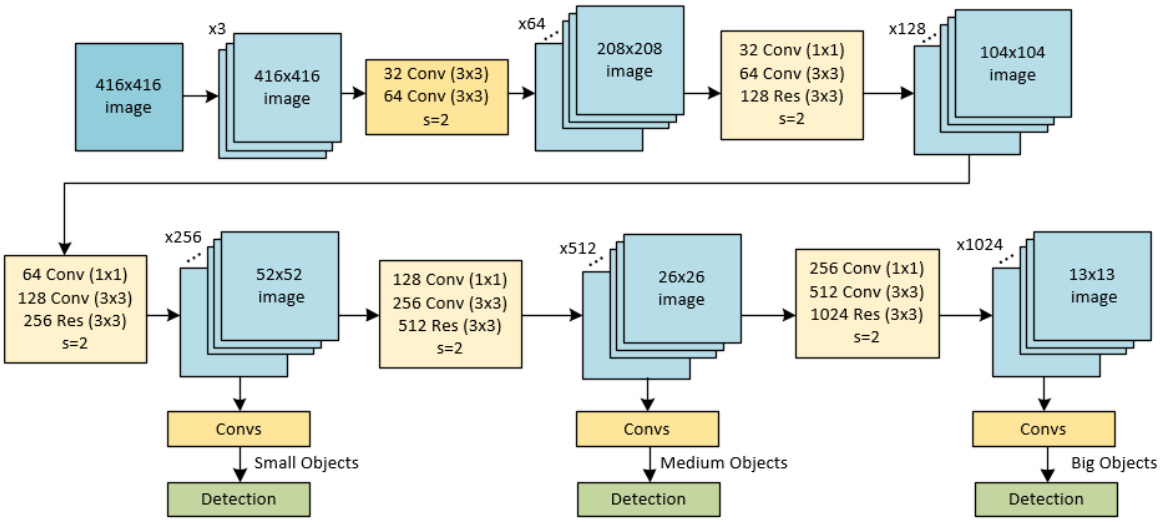

Figure 2. Architecture of YOLOv3 [26].

3. Experimental results

In order to achieve high success in the studies, the Graphics Processing Unit (GPU), which enables the creation of clear graphics, and the Google Collaboratory technology, which provides storage support by accessing the cloud environment, were used. Before the training was carried out, CUDA (Compute Unified Device Architecture) technology produced by NVIDIA was installed on the Jupyter Notebook created in the Colab environment. While creating the data set, labeling operations were performed with the bounding box method and Roboflow technology was used for these operations. Jupyter Notebook was created in the Colaboratory cloud environment created by Google and the necessary code blocks and parameter values were added. While making predictions with the created data set, YOLOv3 technology, which can detect objects by treating object detection as a single regression problem using Convolutional Neural Networks (CNN), was used. Thanks to the Darknet-53 network structure used by YOLOv3 in feature extraction, the evaluation is made more efficient and faster. The training process started by transferring the technologies and files to the cloud environment.

The training graphics of the created data set and the graphics showing the accuracy of the trained model as a result of the studies performed are explained in this section. The studies were carried out in the Google Colaboratory environment, which belongs to Google and provides users with GPU and cloud storage. After the images in the data set to be used for model training were collected, they were transferred to the Roboflow environment. Then, they were labeled with the bounding box method in this environment. Finally, the graphs obtained after applying the necessary pre-processing steps to the created data set are shown in Figure 3.

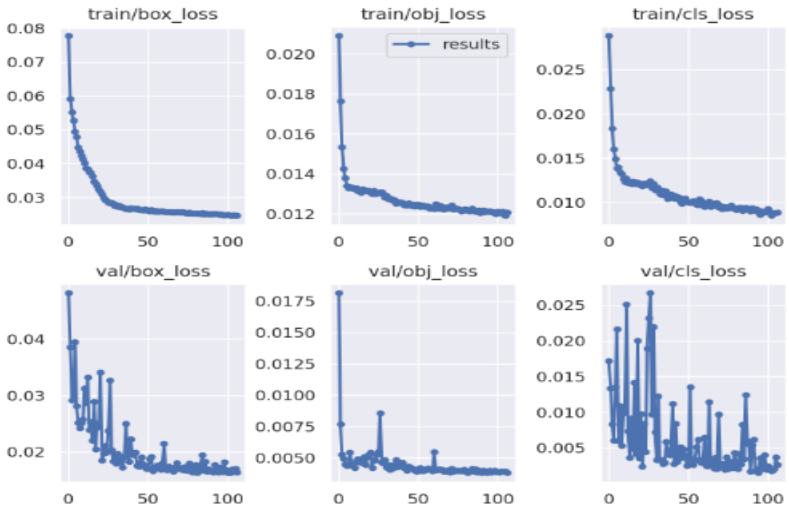

Figure 3. Training graphs loss values.

The train values in the graph in Figure 3 represent the measurements of the values of the training set, while the val values represent the measurements of the values of the validation set. The box_loss value focuses on the measure of the loss rate that will occur after the application of the bounding box technique used in labeling operations. Low values in the graph indicate that the model has improved to generalize and the data set is better labeled. The cls_los value shows the measure of the loss rate resulting from the classification. The decrease in the value in the graph indicates that a better classification is done.

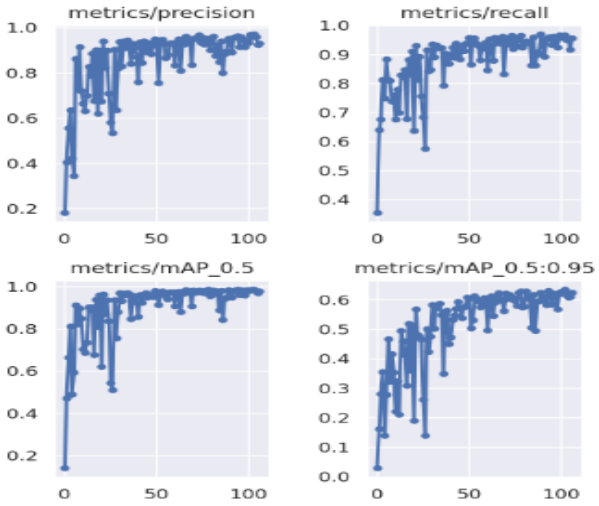

Figure 4. Training graphs metrics values.

The precision value in Figure 4 shows the precision values in the given prediction of the model, while the recall value shows the current performance of the system. The value of mAP_0.5 in the other graph indicates the average sensibility value, and the value of mAP_0.5:0.95 indicates the average precision. From the results in the graph, it is seen that the modeling process was successful and a good data set was created.

During the model training process, a Jupyter Notebook was created, and then the necessary codes were written in the code blocks in the created file to download the technologies and libraries to be used in deepfake detection. First of all, Darknet technology was installed on the cloud environment under study. Darknet technology is used to determine the detection rate of images entered into the model to be used in detecting deepfake images. After the darknet technology

was cloned, the CUDA technology offered by NVIDIA, which we will use to carry out the training, was uploaded to the cloud environment by adding the necessary codes.

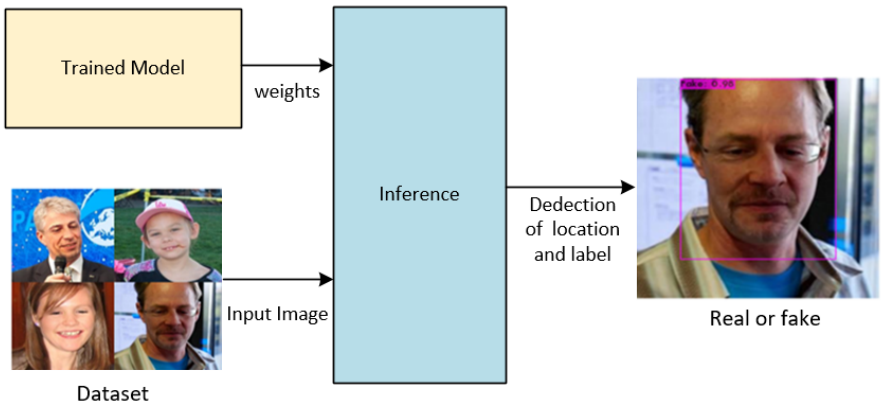

Figure 5. Model architecture.

As seen in Figure 5, first real and fake images were collected manually and turned into a data set. Data, names and cfg model files were created for the created dataset. Information on how many classes will be trained, the file paths of the test and training data, the file path containing the tag name of the class to be trained, and the file path where the backup file will be located when the training is completed have been entered into the data file. Then, the training process was started on the Google Colab platform by specifying the data, cfg network file and weight file that we stored under the Darknet main folder. The training process was terminated when the average loss value among the results obtained during training became very low as 0.1552. After the training was carried out with YOLOv3 technology, the weight values obtained as a result of the training were added to the Backup file of the Google Drive account. Different images were given to the created model, which was determined using the OpenCV library of the Python programming language. It was observed that the probability of the images being deepfake was over 95% due to the predictions.

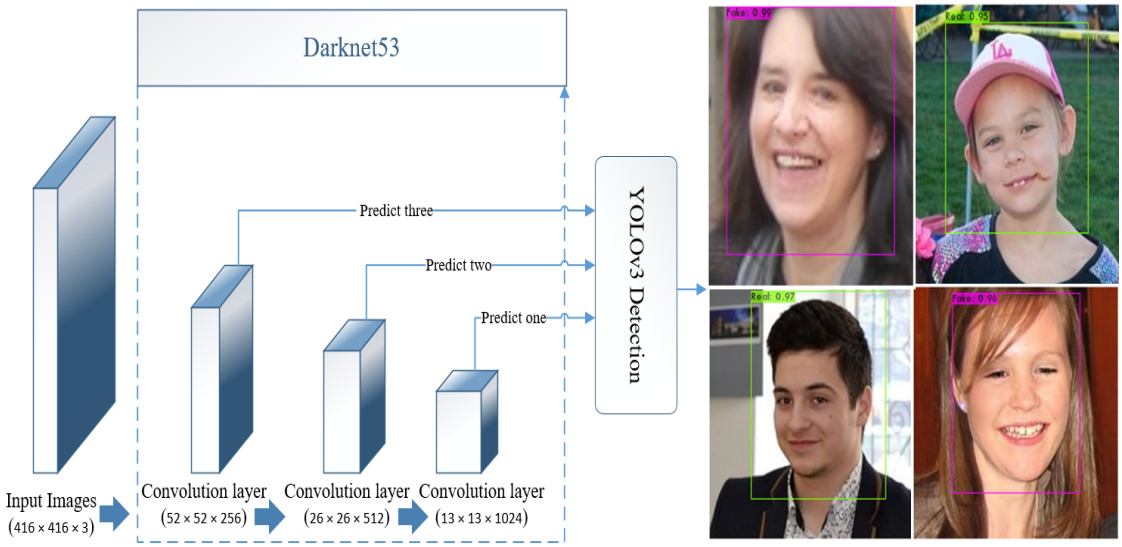

Figure 6. Rates of detecting whether some of the images are fake or real as a result of the YOLOv3 detection method.

Figure 6 shows the accuracy percentages obtained as a result of determining the fakeness and reality status of the visual by transferring the images into the model after creating and training the images in the data set, which includes fake images created with deepfake technology and real human images. The images entered into the model with a size of 416 × 416 were detected more efficiently by feature extraction processes of the Darknet-53 network used by YOLOv3, and then the probability of being a deepfake was estimated. After estimation was made with

the obtained weight values, these ratios were printed using the OpenCV library of the Python programming language. The results obtained by testing the study show that the model can detect images with high accuracy.

Different studies have been conducted in the literature using different data sets and Convolutional Neural Networks to detect deepfake images and videos. In this article, a table has been created showing the accuracy rates obtained from studies using deep learning techniques and Convolutional Neural Networks, the data sets used by other studies in the literature, and the accuracy rates obtained from these data sets. Comparison results with studies in the literature are shown below.

Table 3. Comparison results with studies in the literature.

Reference	Method	Advantages	Disadvantages	Dataset	Accuracy Rates
[27]	The images were compressed by dividing into 8x8 blocks and training was carried out.	- High Accuracy - Works with Scaled and Compressed Images	They filtered the images preserving only those with the smaller side equal or greater than 30 pixels	OpenForensics	99.20%
[28]	Model training was performed using low-resolution video image data.	Works on low-resolution and short-time clips	-Need face detection before giving the model -It is done on video clips which has many variants of one pose	Kaggle Deepfake Detection Challenge (DFDC)	94.93%
				Face Forensics++	93.20%
[29]	Fake face detection was performed in images using two-stream face classification and patch trio.	- Ability to detect videos forged with traditional and deepfake methods.	- Weak against to low resolutions -It is done on video clips which has many variant of one pose	A dataset created by the authors using the Deepfake tools.	91.70%
This Study	Model training was carried out with real and fake image data by performing resizing and automatic orientation.	- High Accuracy -Detection and training on single images -No need extra step	Since it works on a single image basis, clip frame transition features cannot be used.	A mixed dataset created by the authors	95.00%

In the first study in Table 3, the authors aimed to design a deepfake detector that is robust to background and image size variability by accurately detecting resized and compressed images. While performing this process, they first took the images in the OpenForensics dataset as input data and divided them into 8x8 blocks. The resulting outputs were processed with Discrete Cosine Transform. When they tested the CNN architecture they designed, they achieved 99.2% accuracy. While performing different transformations in the study increases the processing load, filtering the data set causes the success rate to be high. In the second study in the table, the authors trained a CNN to detect deepfakes from low-resolution and short-duration videos in the Kaggle Deepfake Detection Challenge (DFDC) and Face Forensics++ datasets. As a result of their training, they reached an accuracy value of 94.93% for the DFDC dataset and 93.2% for the FaceForensics++ dataset in detecting fake videos. In the fourth study in the table, the authors proposed a two-stream network model for fake face detection, including two-stream face classification and patch triplets. They trained a CNN model by performing two different classifications of facial images as real and fake on a dataset collected for the first time using the FaceSwap and SwapMe tools. An accuracy of 92.70% was achieved in the data sets they created. Finally, in this study, a data set was created by combining real images of people taken from different videos and data sets on the internet and fake images obtained

from these images using deepfake technology. Using the created data set and YOLOv3 technology working with CNN, a model that can detect whether the images are fake or real was created. As a result of the studies, it was seen that this model was 95% successful and when compared to other studies in the literature, an effective model was developed among the models trained using CNN.

4. Conclusion

The development of applications and devices that make it easier to share personal images on the internet and the increase in digitalization have greatly increased the opportunities for individuals to access their personal data and images. With the increase in images in the virtual environment, deepfake technology is used maliciously to manipulate photos or videos of famous people, to create and spread fake news content, and to defame or blackmail politicians or government officials. In this respect, it has the potential to cause serious social, political and economic problems. Studies show that the use of deepfake technology in illegal events will increase. For these reasons, deepfake images have become an increasing concern and pose a major threat to people's personal spaces. To prevent these situations, techniques developed for detecting and identifying deepfake images are gaining importance day by day. Although deepfake technology has potential risks, it may be possible to reduce them by developing detection and prevention methods.

In this study, detailed research was conducted on detecting deepfake videos and images, and then a method was developed to detect these fake images. First, a data set was created, and images created with different deepfake techniques were added to this data set. Then, using CNN, one of the deep learning methods, model training was carried out to detect deepfake images with YOLOv3 technology, which calculates class probabilities differently than traditional methods and handles all processes in a single regression. problem that can be detected quickly and with high accuracy. The model obtained from the training was tested to evaluate the possibility of deepfake in new images. As a result of the tests, model training, and evaluation, over 95% of the results were successful. This situation shows that an effective method has been developed for detecting deepfake images compared to literature studies. The continuous development of deepfake applications requires the model to be updated accordingly to detect the images produced by these applications.

Future studies aim to expand the data set and obtain better results by integrating new technologies into our model. In this context, different deepfake images will be collected manually and added to the data set to enlarge the data set. Then, as a result of training the expanded data set in different versions of YOLO technology, the rates obtained in these versions will be compared. As a result of the studies, the YOLO version that gives the best results will be selected to help researchers working in this field. Also potential improvements or adaptations of the YOLOV3 method for deepfake detection will be investigated.

Acknowledgements

This study was supported by the TUBİTAK (The Scientific and Technological Research Council of Turkey) under Grant No: 122E676.

References

[1] Çeçen M, Karaköse M. A Deepfake Image Detection Approach Based on YOLOv3. In: 2th International Conference on Advances and Innovations in Engineering; 21-23 September 2023. pp. 10-18.

[2] Franklin RJ, Mohona. Traffic Signal Violation Detection using Artificial Intelligence and Deep Learning. In: International Conference on Communication and Electronics Systems; 10-12 June 2020. pp. 839 - 844.

[3] İlhan İ., Balı E., Karaköse M. An Improved DeepFake Detection Approach with NASNetLarge CNN. In: IEEE International Conference on Data Analytics for Business and Industry; 25-26 October 2022. pp. 598-602.

[4] Seow JW, Lim MK, Phan R, Liu J. A comprehensive overview of Deepfake: Generation, detection, datasets, and opportunities. Elsevier Neurocomputing 2022; 513: 351–371.

[5] İlhan İ, Karaköse M. Derin Sahte Videoların Tespiti ve Uygulamaları için Bir Karşılaştırma Çalışması. Adıyaman Üniversitesi Mühendislik Bilimleri Dergisi 2021; 8(14): 47-60.

[6] John J, Sherif B. Comparative Analysis on Different DeepFakeDetection Methods and Semi Supervised GAN Architecture for DeepFake Detection. In: Proceedings of the Sixth International Conference on I-SMAC (IoT in Social, Mobile, Analytics and Cloud); 10-12 November 2022.

[7] Karras T, Laine S, Alia T. A Style-Based Generator Architecture for Generative Adversarial Networks. IEEE Transactions on Pattern Analysis and Machine Intelligence 2021; 43: 4217-4228.

[8] Zhu JY, Park T, Isola P, Efros AA. Unpaired Image-to-Image Translation Using Cycle-Consistent Adversarial Networks. Image Translation Using Cycle-Consistent Adversarial Networks. In: IEEE/CVF International Conference on Computer Vision; 22-29 October 2017; Venice, Italy.

[9] Choi Y, Choi M, Munyoung K, Ha JW, Kim S, Choo J. StarGAN: Unified Generative Adversarial Networks for Multi-Domain Imageto-Image Translation. In: IEEE/CVF Conference on Computer Vision and Pattern Recognition; 18-23 June 2018. pp. 8789-8797.
[10] Thies J, Zollhöfer M, Stamminger M, Theobalt C, Niebner M. Face2face: Real-Time Face Capture and Reenactment of RGB Videos. In: IEEE/CVF Conference on Compute Vision and Pattern Recognition; 27-30 June 2016. pp. 2387 – 2395.
[11] Khatri N, Borar V, Garg R. A Comparative Study: Deepfake Detection Using Deep-learning. In: 13th International Conference on Cloud Computing, Data Science & Engineering; 19-20 January 2023.
[12] Pipin SJ, Purba R, Pasha MF. Deepfake Video Detection Using Spatiotemporal Convolutional Network and Photo Response Non Uniformity. In: IEEE International Conference of Computer Science and Information Technology (ICOSNIKOM); 19-21 October 2022.
[13] Zhang J, Cheng K, Sovernigo G, Lin X. A Heterogeneous Feature Ensemble Learning based Deepfake Detection Method. In: IEEE International Conference on Communications; 16-20 May 2022. pp: 2084 - 2089
[14] Budhiraja R, Kumar M, Das MK, Bafila AS, Singh S, MeDiFakeD: Medical Deepfake Detection using Convolutional Reservoir Networks. In: IEEE Global Conference on Computing, Power and Communication Technologies (GlobConPT); 23-25 September 2022.
[15] Li Y, Zhang C, Sun P, Ke L, Ju Y, Qi H, Lyu S. DeepFake-o-meter: An Open Platform for DeepFake Detection. In: IEEE Security and Privacy Workshops (SPW); 27 May 2021; China. pp. 277-281.
[16] Jia S, Li X,Siwei L. Model Attribution of Face-Swap Deepfake Videos. In: IEEE International Conference on Image Processing (ICIP), 16-19 October 2022. pp: 2356 - 2360.
[17] Yang X, Li Y, Lyu S. Exposing deep fakes using inconsistent head poses. In: IEEE Int. Conf. Acoust., Speech and Signal Process. (ICASSP*)*, 25-30 March 2012. pp. 8261 –8265.
[18] Ataş S, İlhan İ, Karaköse M. An Efficient Deepfake Video Detection Approach with Combination of EfficientNet and Xception Models Using Deep Learning. In: 26th International Conference on Information Technology (IT); 13-15 December 2023.
[19] Bar NF, Yetis H, Karakose M. An efficient and scalable variational quantum circuits approach for deep reinforcement learning. Quantum Information Processing 2023; 22(8): 300.
[20] Srivastava N, Salakhutdinov RR. Multimodal Learning with Deep Boltzmann Machines. Advances in Neural Information Processing Systems 25 (NIPS 2012); 3-8 December 2012.
[21] Krizhevsky A, Sutskever I,Geoffrey EH. ImageNet Classification with Deep Convolutional Neural Networks. Adv.Neural Inf. Process. Syst. 2012; *25*: 1–9.
[22] Deng J, Dong W, Socher R, Li LJ, Li K, Fei LF. Imagenet: A large-scale hierarchical image database. In: IEEE Conference on Computer Vision and Pattern Recognition; 20-25 June 2009. pp. 248-255.
[23] Rajput, SK, Patni JC, Alshamrani SS, Chaudhari V, Dumka A, Singh R, Rashid, M, Gehlot A, AlGhamdi AS. Automatic Vehicle Identification and Classification Model Using the YOLOv3 Algorithm for a Toll Management System. Sustainability 2022; 14(15): 9163.
[24] Salih ZA, Thabit R, Zidan KA, Khoo Be. A new face image manipulation reveal scheme based on face detection and image watermarking. In: IEEE International Conference on Artificial Intelligence in Engineering and Technology (IICAIET); 13-15 September 2022.
[25] Chang X, Wu J, Yang T, Feng G. DeepFake Face Image Detection based on Improved VGG Convolutional Neural Network. In: 39th Chinese Control Conference; 27-29 July 2020.
[26] Belhi A, Gasmi H, Al-Ali AK, Bouras A, Foufou S, Yu X, Zhang H. Deep Learning and Cultural Heritage: The CEPROQHA Project Case Study. In: International Conference on Software, Knowledge Information, Industrial Management and Applications (SKIMA); 26-29 August 2019.
[27] Concas S, Perelli G, Marcialis GL, Puglisi G. Tensor-Based Deepfake Detection in Scaled and Compressed Images. In: IEEE International Conference on Image Processing (ICIP); 16-19 October 2022. pp. 3121 – 3125.
[28] Rahman A, Siddique N, Moon MJ, Tasnim T, Islam M, Shahiduzzaman Md, Ahmed S. Short and Low Resolution Deepfake Video Detection using CNN. In: IEEE Region 10 Humanitarian Technology Conference (R10-HTC) 16-19 September 2022. pp. 259 - 264.
[29] Afchar D, Nozick V, Yamagishi J, Echizen I. MesoNet: a Compact Facial Video Forgery Detection Network. In: IEEE International Workshop on Information Forensics and Security (WIFS), 11-13 December 2018.

Turkish Journal of Science & Technology
19(2), 325-338, 2024

Research Paper
https://doi.org/10.55525/tjst.1411197

PneumoNet: Automated Detection of Pneumonia using Deep Neural Networks from Chest X-Ray Images

Zehra KADIROGLU[1*], Erkan DENIZ[2], Mazhar KAYAOGLU[3], Hanifi GULDEMIR[4], Abdurrahman SENYIGIT[5], Abdulkadir SENGUR[6]

[1,2,4,6] Department of Electrical and Electronics Engineering, Faculty of Technology, Fırat University, Elazıg, Turkey
[3] Department of Informatics, Bingol University, Bingol, Turkey
[5] Department of Chest Diseases and Tuberculosis, Faculty of Medicine, Dicle University, Diyarbakır, Turkey
[*1] zehrakad@gmail.com, [2] edeniz@firat.edu.tr, [3] mkayaoglu@bingol.edu.tr, [4] hguldemir@firat.edu.tr,
[5] drasenyigit@gmail.com, [6] ksengur@firat.edu.tr

(Geliş/Received: 28/12/2023; Kabul/Accepted: 18/04/2024)

Abstract: Pneumonia is a dangerous disease that causes severe inflammation of the air sacs in the lungs. It is one of the infectious diseases with high morbidity and mortality in all age groups worldwide. Chest X-ray (CXR) is a diagnostic and imaging modality widely used in diagnosing pneumonia due to its low dose of ionizing radiation, low cost, and easy accessibility. Many deep learning methods have been proposed in various medical applications to assist clinicians in detecting and diagnosing pneumonia from CXR images. We have proposed a novel PneumoNet using a convolutional neural network (CNN) to detect pneumonia using CXR images accurately. Transformer-based deep learning methods, which have yielded high performance in natural language processing (NLP) problems, have recently attracted the attention of researchers. In this work, we have compared our results obtained using the CNN model with transformer-based architectures. These transformer architectures are vision transformer (ViT), gated multilayer perceptron (gMLP), MLP-mixer, and FNet. In this study, we have used the healthy and pneumonia CXR images from public and private databases to develop the model. Our developed PneumoNet model has yielded the highest accuracy of 96.50% and 94.29% for private and public databases, respectively, in detecting pneumonia accurately from healthy subjects.

Key words: Pneumonia detection, medical image classification, chest x-ray imaging, transformer, deep neural networks.

PneumoNet: Göğüs Röntgeni Görüntülerinden Derin Sinir Ağları Kullanarak Pnömoninin Otomatik Tespiti

Öz: Pnömoni, akciğerlerdeki hava keseciklerinin şiddetli iltihaplanmasına neden olan tehlikeli bir hastalıktır. Dünya genelinde tüm yaş gruplarında yüksek morbidite ve mortaliteye sahip bulaşıcı hastalıklardan biridir. Göğüs röntgeni (CXR), düşük iyonize radyasyon dozu, düşük maliyeti ve kolay erişilebilirliği nedeniyle pnömoni teşhisinde yaygın olarak kullanılan bir teşhis ve görüntüleme yöntemidir. Çeşitli tıbbi uygulamalarda klinisyenlere CXR görüntülerinden pnömoni tespit ve teşhisinde yardımcı olmak için birçok derin öğrenme yöntemi önerilmiştir. CXR görüntülerini kullanarak pnömoniyi doğru bir şekilde tespit etmek için evrişimsel sinir ağı (ESA) kullanan yeni bir PneumoNet önerilmiştir. Doğal dil işleme (NLP) problemlerinde yüksek performans sağlayan dönüştürücü tabanlı derin öğrenme yöntemleri son zamanlarda araştırmacıların ilgisini çekmektedir. Bu çalışmada, CNN modelini kullanarak elde ettiğimiz sonuçlar dönüştürücü tabanlı mimarilerle karşılaştırılmıştır. Bu dönüştürücü mimariler görüntü dönüştürücü (ViT), kapılı çok katmanlı algılayıcı (gMLP), MLP-mikser ve FNet'tir. Bu çalışmada, modeli geliştirmek için kamu ve özel veri tabanlarından sağlıklı ve pnömoni CXR görüntüleri kullanılmıştır. Geliştirdiğimiz PneumoNet modeli, sağlıklı bireylerden pnömoniyi doğru bir şekilde tespit etmede özel ve kamu veri tabanları için sırasıyla %96,50 ve %94,29'luk en yüksek doğruluğu sağlamıştır.

Anahtar kelimeler: Pnömoni tespiti, tıbbi görüntü sınıflandırma, göğüs röntgeni görüntüleme, transformatör, derin sinir ağları.

1. Introduction

Pneumonia is inflammation of the lung parenchyma caused by infective or non-infective causes [1]. People of all ages can have mild to severe diseases. The prevalence and mortality rates are highest in children younger than five years and persons over 70 years worldwide [2]. Depending on the severity of the disease: cough, shortness of breath, fever, sweating and chills, chest pain, nausea, vomiting and diarrhea can be seen. Factors such as unhealthy climatic conditions, pollution, passive smoking, and malnutrition increase the risk of this disease [3]. Other lung diseases also present similar symptoms like pneumonia. Hence it is challenging to diagnose it by symptoms and a medical examination [4]. Various medical imaging modalities and diagnostic tools are used in clinics to diagnose pneumonia. Due to its low cost, faster imaging time, and ease of access, CXR is the most common medical imaging technique used to detect pneumonia worldwide [5]. Chest radiographs contain

[*] Corresponding author: zehrakad@gmail.com. ORCID Number of authors: [1] 0000-0002-2696-8138, [2] 0000-0002-9048-6547, [3] 0000-0002-5807-9781, [4] 0000-0003-0491-8348, [5] 0000-0001-9603-2231, [6] 0000-0003-1614-2639

significant amount of information about the patient's condition. However, even for very experienced radiologists, distinguishing similar lesions or detecting and interpreting very indistinct nodules can be difficult [6]. Therefore, manual reading of CXR radiographs is tedious, time-consuming, and prone to human errors. Hence, accurate processing and analysis of medical images are crucial for a faster and more reliable diagnosis. In recent years, studies on the precise detection of diseases using deep learning techniques have been employed for computer-aided diagnosis (CAD) [3-6]. As a decision support system, deep learning-based CAD systems assist clinicians and radiologists in making accurate and rapid diagnoses, reducing the rate of misdiagnosis, and improving healthcare quality at lower costs [7]. Convolutional neural network (CNN), one of the deep learning architectures is considered as the most advanced architecture in image classification and computer vision problems, as it effectively extracts features from low to deep convolution layers in the network [8]. In further studies, researchers sought successful recognition and performance improvement without convolution functions in deep learning models for computer vision applications [9]. Transformer models, which are attention mechanism-based architectures and widely used in natural language processing (NLP), have been adapted to solve this problem, and remarkable results have been obtained [10, 11]. Vision transformer (ViT), the image model of the transformer architecture, represents an input image as a fixed-size array of image patches and predicts image class tags, similar to the sequence of word embedding used in NLP applications [12]. In the literature, pneumonia is currently detected using transformer-based architectures.

Ukwuoma et al. [15] designed a hybrid deep learning framework to diagnose pneumonia. The designed hybrid framework is developed by combining both convolutional networks and transformer encoder mechanisms. The method was trained and evaluated using Mendeley [13] and chest x-ray [14] datasets for binary and multiple classification tasks. Their hybrid framework produced over 95% accuracy and F1 score values for classification tasks. Cha et al. [7] developed a transfer learning framework based on the attention mechanism for effective pneumonia detection on CXR images. First, as a feature extractor, features were collected from three pre-trained models, namely ResNet152, DenseNet121, and ResNet18. Then, the attention mechanism was implemented as a feature selection operation. The proposed approach achieved a 96.63% accuracy score, a 97.3% F1-score, a 96.03% area under the curve (AUC), a 96.23% precision and a 98.46% sensitivity. Singh et al. [16] combined a deep neural network (DNN) with an attention mechanism to detect pneumonia disease using CXR images. The proposed network is built to generate attention-sensitive features by combining channel and spatial attention modules in the DNN architecture. They studied a public CXR dataset with the proposed network [13]. The proposed network yielded a classification accuracy of 95.47% and an F1-score of 0.92. Tyagi et al. [17] proposed an auto-detection model for the early detection of pneumonia. Three models, namely CNN, VGG16, and Vision Transformer, were used in their study. In addition, they studied a publicly available CXR dataset to develop their models [13]. The ViT method used in experimental studies showed an accuracy performance of 96.45% in identifying pneumonia.

Ma et al. [18] used the Swin transformer as the pneumonia recognition model in CXR images and optimized them according to the characteristics of CXR images. After comparative experiments on two different datasets [13, 14], the experimental results showed that the model's accuracy increased from 76.3% to 87.3% and from 92.8% to 97.2%, respectively. Jiang et al. [19] proposed the multi-level patch merger vision transformer (MP-ViT) to automatically diagnose pneumonia from CXR images. They performed their experiments on a publicly available dataset [13]. Their proposed model achieved 0.91 accuracy, 0.92 precision, 0.89 sensitivity, and 0.90 F1-score. Wei et al. [20] proposed a deep learning architecture called Deep Pneumonia to recognize pneumonia lesions. The authors proposed a feature learning mechanism based on the mask-driven intense attention and comparative editing strategies. These strategies were applied to the attention map and the extracted features to draw more attention to the lesion area with more distinctive features and guide the model. Their proposed model achieved an accuracy of 83.85%. Okolo et al. [21] evaluated the performance of a new deep-learning model based on a transformer network for the CXR image classification task. They examined the ViT performance and then proposed and evaluated the input-enhanced vision transformer (IEViT). Experiments on four CXR image datasets containing various pathologies (pediatric pneumonia, tuberculosis, viral pneumonia, COVID-19) showed that the developed IEViT architecture produced a higher accuracy score than the ViT model for all datasets. Mabrouk et al. [22] proposed a computer-assisted tool for detecting pneumonia, using ensemble learning using CXR images. Their suggested ensemble learning model comprised three well-known CNN models, namely DenseNet169, MobileNetV2, and ViT. These models were trained on the CXR dataset using fine-tuning [13]. The proposed ensemble learning model outperformed other state-of-the-art methods, achieving 93.91% accuracy and a 93.88% F1 score. Ar et al. [23] proposed an ensemble framework for pneumonia detection using chest X-ray images. The proposed framework has been tested and evaluated using the CXR dataset [13]. VDSNet and CAPSNet models were used for the proposed pneumonia detection framework. Their proposed ensemble (combined) model reached 98% accuracy.

The aim of this study is to produce a new CXR dataset as an alternative to the pneumonia datasets in the literature. The new data set was created for binary classification tasks as pneumonia and healthy classes. Our study uses CXR images of healthy and pneumonia patients obtained from a private and public database. We also

developed a new CNN-based PneumoNet model in this study. It is about designing a network that can be compared to pre-trained networks. Additionally, we compared the model developed in this study with four transformer-based models, namely ViT, FNet, gMLP and MLP mixers, for pneumonia detection using CXR images. The proposed models were compared in terms of classification performances such as recall, precision, F1-score, and accuracy. Our developed PneumoNet model yielded 96.50% and 94.29% accuracy for private and public databases, respectively, detecting pneumonia accurately from healthy subjects. The organization of this paper is as follows. In this section, medical information about pneumonia is given in detail. Literature studies on pneumonia detection using transformer-based models are mentioned and the purpose of this study is also explained. Section 2 provides detailed information about the datasets used for pneumonia detection in this study, the developed deep learning-based pneumonia detection model, transformer-based models, and performance evaluation metrics. In Section 3, the steps followed in experimental studies and the results of experimental studies are mentioned. The discussion is described in Section 4. In Section 5, the results obtained in the study are evaluated.

2. Material and Method

2.1. Private database

The private database used in this study consists of pneumonia and healthy CXR images obtained from Dicle University Medical Faculty Chest Diseases and Tuberculosis clinic, intensive care unit, and chest polyclinic. The study on 2000 subjects, 1000 subjects were diagnosed with pneumonia on Poster Anterior (PA) chest X-ray and 1000 subjects had normal PA chest X-ray. All images were in different sizes and RGB. Figure 1 shows typical pneumonia and healthy CXR images obtained from the private database.

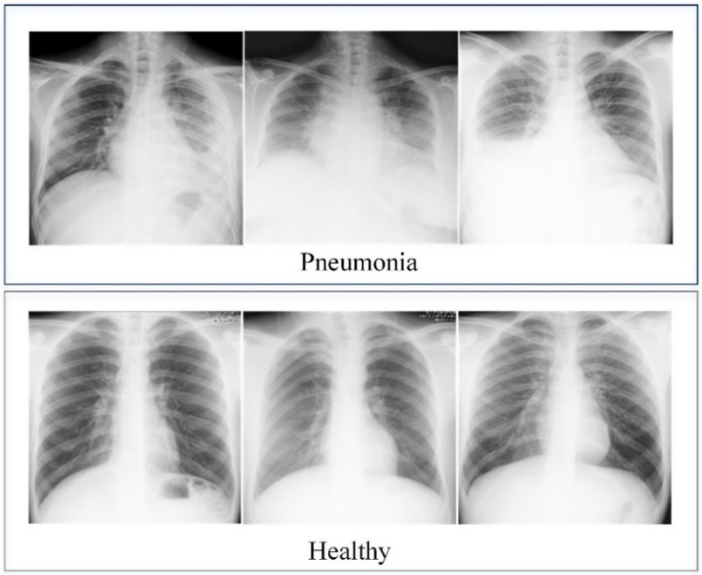

Figure 1. Typical healthy and pneumonia CXR images collected from our private dataset.

2.2. Public database

In order to test the effectiveness of the developed pneumonia detection network, experimental studies were carried out with CXR image datasets, which are the most used in the literature for pneumonia detection [13, 14]. To avoid class imbalance problems, equal numbers of CXR images from both classes in the datasets were randomly selected and used. In this study, 3500 images were used, 1750 of which were from the healthy class and the other 1750 from the pneumonia class.

2.3. PneumoNet model

A new PneumoNet model is developed and trained end-to-end for pneumonia classification. The developed PneumoNet model consists of 21 layers, as shown in Figure 2. The new CNN architecture starts with an input layer. It continues with the batch normalization and ReLU layer, which then follows each convolution layer. Among the pooling operations, the max operator function was used in the pooling layers. There are five

convolution layers in the 21-layer CNN architecture. Two pool layers, pool_1, and pool_2, come after the ReLu_1 and ReLu_2 layers. The last three layers of the proposed new network are used for classification purposes. The proposed PneumoNet architecture for pneumonia detection is shown in Figure 2. Besides, Table 1 shows the various setting parameters of the developed PneumoNet model.

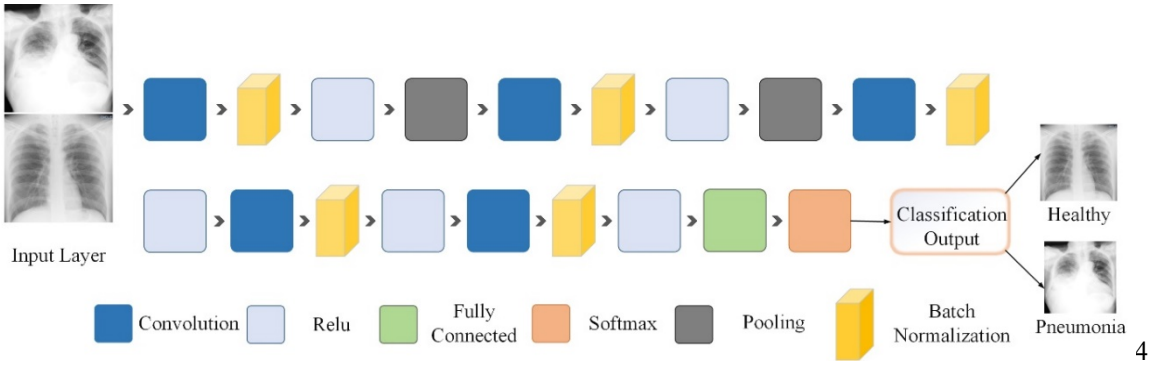

Figure 2. Architecture of PneumoNet for pneumonia detection.

Table 1. Hyperparameters used to develop the PneumoNet model.

Type	Activations	Learnable
Image input	224×224×3	-
Convolution	224×224×64	Weights 3×3×3×64 Bias 1×1×64
Batch Normalization	224×224×64	Offset 1×1×64 Scale 1×1×64
ReLu	224×224×64	-
Max Pooling	112×112×64	-
Convolution	112×112×32	Weights 3×3×3×64 Bias 1×1×64
Batch Normalization	112×112×32	Offset 1×1×32 Scale 1×1×32
ReLu	112×112×32	-
Max Pooling	56×56×32	-
Convolution	56×56×16	Weights 3×3×3×64 Bias 1×1×64
Batch Normalization	56×56×16	Offset 1×1×16 Scale 1×1×16
ReLu	56×56×16	-
Convolution	56×56×8	Weights 3×3×3×64 Bias 1×1×64
Batch Normalization	56×56×8	Offset 1×1×8 Scale 1×1×8
ReLu	56×56×8	-
Convolution	56×56×4	Weights 3×3×3×64 Bias 1×1×64
Batch Normalization	56×56×4	Offset 1×1×4 Scale 1×1×4
ReLu	56×56×4	-
Fully Connected	1×1×2	Weights 2×12544 Bias 2×1
Softmax	1×1×2	-
Classification Output	-	-

2.4. Vision Transformer (ViT)

ViT [12], is a computer vision-adapted version of attention mechanism-based transformer models that have been successfully performed in NLP applications. When classifying an image, ViT treats it as a patch sequence, similar to a sequence of word embedding generated by the NLP transformer. The working principle of the ViT model consists of the following steps. The ViT splits an input image into sequences of patches or visual tokens. Each 2D image patches are flattened. Then, the flattened patches are embedded linearly, called patch embedding.

Learnable position embeddings are added to each image patch. An embedded image patch is combined with extra learnable class tokens to predict the class of the new image. Finally, the resulting sequence is given to the transformer encoder block. While the standard transformer takes 1D token embedding sequences as input to handle a 2D image as a 1D sequence in ViT; $x \in \mathbb{R}^{H\times W\times C}$ input image is reshaped $x_p \in \mathbb{R}^{N\times(P^2.C)}$ as a sequence of flattened 2D patches. The number of patches is calculated using Equation (1).

$$N = HW/P^2 \tag{1}$$

Where (H, W) is the size of each original image, i.e., the height and width values, C is the number of image's channels, (P, P) is the size of each square image patch. The following equations explain the handling of images in the ViT. Flattening the patches and mapping them to the D dimension with a trainable linear projection is calculated as shown in Equation (2).

$$z_0 = \left[x_{class}; x_p^1\mathrm{E}; x_p^2\mathrm{E}; \ldots; x_p^N\mathrm{E}\right] + \mathrm{E}_{pos}, \qquad \mathrm{E}\in\mathbb{R}^{(P^2.C)\times D}, \mathrm{E}_{pos}\in\mathbb{R}^{(N+1)\times D} \tag{2}$$

The sum size of the flattened patches (x_p) can be determined using Equation (3).

$$x_p = N \times (P^2.C) \tag{3}$$

In Equation (4,5), there are MLP (Multilayer Perceptron) and MSA (Multi-head self-attention) blocks of the transformer encoder layer (L). The outputs of the ℓ.th layer are calculated as in the equations. In Equation (6), the image representation of the encoder's output (z_L^0) is denoted by y [12]. The illustration of the developed ViT architecture is given in Figure 3.

$$z'_\ell = MSA\big(LN(z_{\ell-1})\big) + z_{\ell-1}, \qquad \ell = 1 \ldots L \tag{4}$$
$$z_\ell = MLP\big(LN(z'_\ell)\big) + z'_\ell, \qquad \ell = 1 \ldots L \tag{5}$$
$$y = LN(z_L^0) \tag{6}$$

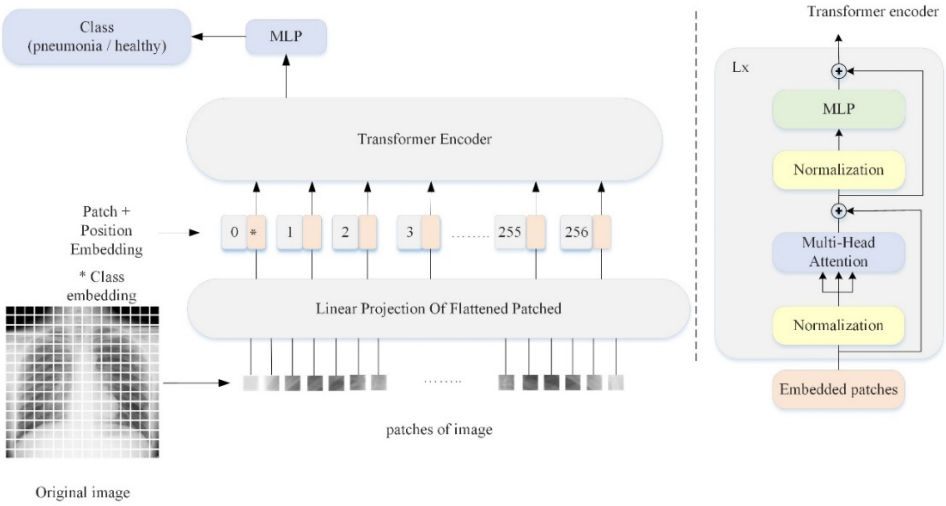

Figure 3. Illustration of the ViT model for pneumonia detection.

2.5. MLP mixer

The basic architecture of the developed MLP-mixer is given in Figure 4. As can be seen, the input colour image has a size of 512×512, and a non-overlapping window of size 32×32 is used for patch extraction. After all, patches are extracted, each patch is initially flattened, and a linear projection layer is employed to reduce the number of samples in each flattened patch. The linear projection layer is formulated using Equation (7).

$$y = x\omega^T + b \tag{7}$$

Where x is the input vector, ω, and b are the weights vector and bias value, respectively. The length of a flattened patch is 3072; after linear projection, the length of each patch vector becomes 2048. Similarly, after the linear projection layer, a patch embedding matrix of size 256×1024 is obtained for all patches. Next, these patches embedding of shape 256×1024 of an input image goes through mixer layers before being fed to the MLP Head for classification [24].

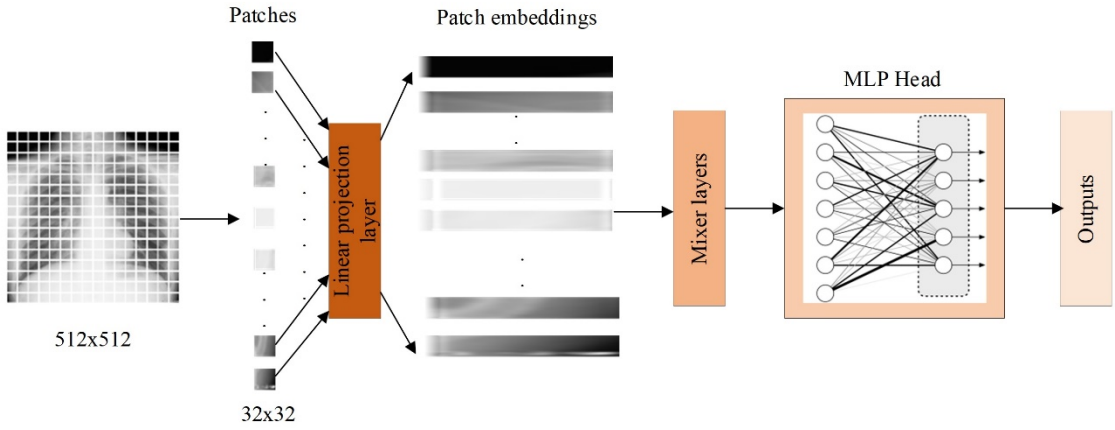

Figure 4. Illustration of the MLP-mixer architecture.

2.6. FNet

In the model introduced by Lee-Thorp et al., the Fourier transform is used as the token mixing mechanism [25]. With this model, simple linear transforms, including Fourier transforms, have been shown to be competent in modeling various relationships in text data. The advantage of FNet hybrid models, which contain only two self-attention sublayers, over other transformer models, is that they run faster and perform better at longer input lengths. In addition, this model has shown that the attention mechanism affects increasing accuracy, but it is not necessary to use it in every layer. As shown in Equation (8), based on FNet, the attention sublayer has been replaced with a Fourier sublayer that implements 2D DFT. Here $\mathcal{F}_{seq}$ is the sequence length, $\mathcal{F}_h$ is the hidden dimension. The developed FNet architecture for this study is given in Figure 5.

$$y = \Re(\mathcal{F}_{seq}(\mathcal{F}_h(x))) \tag{8}$$

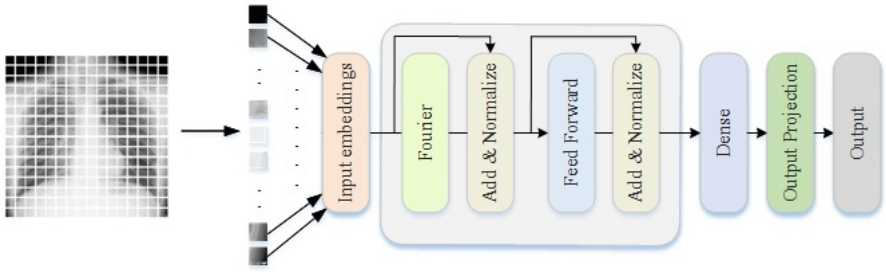

Figure 5. An illustration of the FNet architecture.

2.7. GMLP

The gMLP proposed by Liu et al. is a without self-attention MLP-based transformer model [26]. It was designed by combining basic MLP layers with gating to research the necessity of attention mechanisms in transformer architectures. The innovation in gMLP uses a spatial gating unit (SGU), which learns the complex spatial interactions between sequence elements, as an alternative to attention mechanisms. SGU does not require encoding for element positions because such information is held in the $s(\cdot)$ layer, which captures spatial interactions. gMLP uses fewer trainable parameters than other transformer models. The basic working principle of gMLP for the initial matrix $X \in \mathbb{R}^{n \times d}$ with the length of the token sequence n and the size of the token, d are shown in the following equations. Where σ is an activation function like Gaussian Error Linear Unit (GeLU), U

and V are matrices that describe linear projections along the channel dimension, $s(\cdot)$ is the layer that captures spatial interactions. Y is the output of the block. The illustration of the proposed gMLP architecture is given in Figure 6. Each block can be defined as in the equations (9) to (11).

$$\mathrm{Z} = \sigma(XU) \tag{9}$$
$$\check{\mathrm{Z}} = s(\mathrm{Z}) \tag{10}$$
$$Y = \check{\mathrm{Z}}V \tag{11}$$

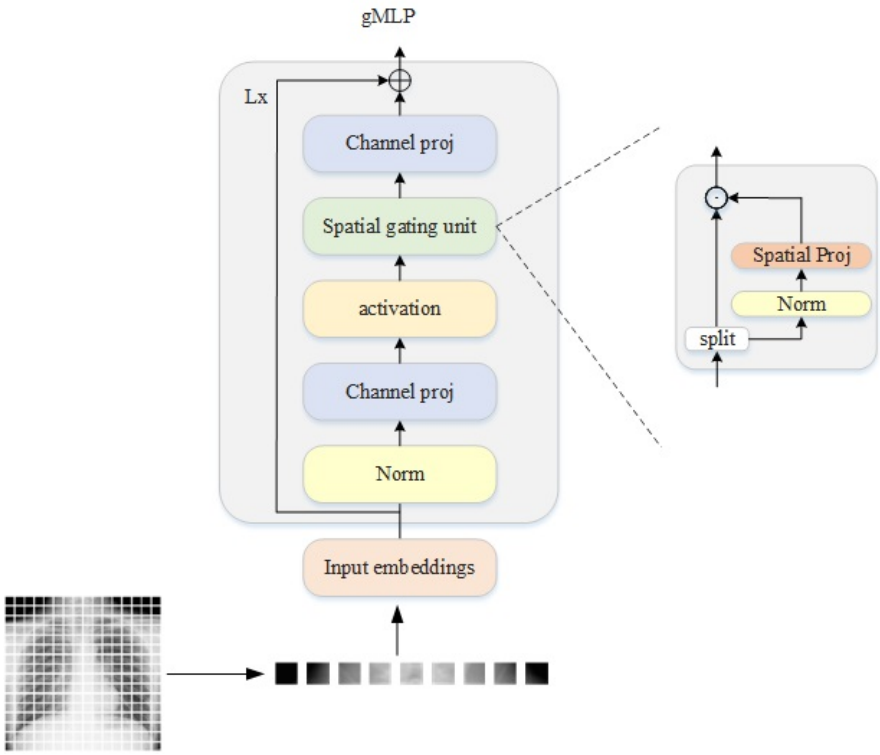

Figure 6. Illustration of the gMLP architecture.

2.8. Performance Metrics

Various evaluation metrics, i.e., accuracy, precision, recall, and F1 score, were used to assess the performance of the proposed methods in the study. Accuracy, as in Equation 12, refers to the number of data samples correctly identified out of the total number of data samples given [27,28].

$$Accuracy = \frac{TP+TN}{TP+TN+FP+FN} \tag{12}$$

Precision/positive predictive value, is the ratio of correctly detected positive cases to all expected positive cases, as shown in Equation 13.

$$Precision = \frac{TP}{TP+FP} \tag{13}$$

The sensitivity/recall/true positive ratio, is the number of samples correctly identified as positive cases compared to all true positive cases, as shown in Equation 14.

$$Recall = \frac{TP}{TP+FN} \tag{14}$$

F1 Score is defined as the harmonic mean of sensitivity and precision, also indicates the overall accuracy of the method and is calculated as shown in Equation 15.

$$F_1 = \frac{2*(Precision*Recall)}{Precision+Recall} \quad (15)$$

True Positive (TP) is the pneumonia image being classified as pneumonia by the model. True Negative (TN) labels the non-pneumonia image, the healthy image, as healthy by the post-classification model. False Positive (FP) is when the model labels the healthy image as pneumonia. False Negative (FN) is the model's classification of the pneumonia image as a healthy image.

3. Experimental Results

This section presents experimental evaluations of proposed pneumonia detection methods. All experiments were conducted on Python and MATLAB, using a computer with an A5000 GPU with 45 GB RAM. During the pre-processing stage of the study, since the CXR images in the dataset are of different sizes, they are resized to 512×512 to meet the minimum input dimensions of the transformer-based models. The CXR images are resized to 224×224 for the PneumoNet model additionally. Then each image was divided into a total of 256 patches of size 32×32 pixels. Adam optimizer was considered in training the mentioned methods. Besides, hold-out validation was used to split the dataset into the training and test data, where the division ratio was 90% for training and 10% for testing [29, 30]. For the developed PneumoNet model, the learning rate was 0.0001, the batch size was 10, and the number of epochs was 8. Stochastic gradient descent with momentum (SGDM) optimizer was considered in training the mentioned methods.

The transformer-based models' parameters were assigned heuristically while running each code. For the ViT model, the learning rate was set to 0.001, weight decay was set to 0.0001, and batch size, number of epochs, projection dimension, number of heads and number of transformer layers were set to 64, 400, 64, 4 and 8, respectively. For FNet, MLP-mixer and gMLP models, weight decay was set to 0.0001, batch size, number of epochs, embedding dimension, number of MLP-mixer layers and dropout rate were set to 64, 400, 256, 4, and 0.2, respectively. The learning rate was set to 0.005 for the MLP mixer, 0.001 for FNet and 0.003 for gMLP. The flowchart of the proposed method is given in Figure 7. The flowchart of the proposed method is given in Figure 7. Classification of pneumonia and healthy CXR images with transformer-based models and 21-layer CNN. Performance metrics such as accuracy, precision, sensitivity, and F1-measure were used to evaluate the effectiveness of the proposed methods.

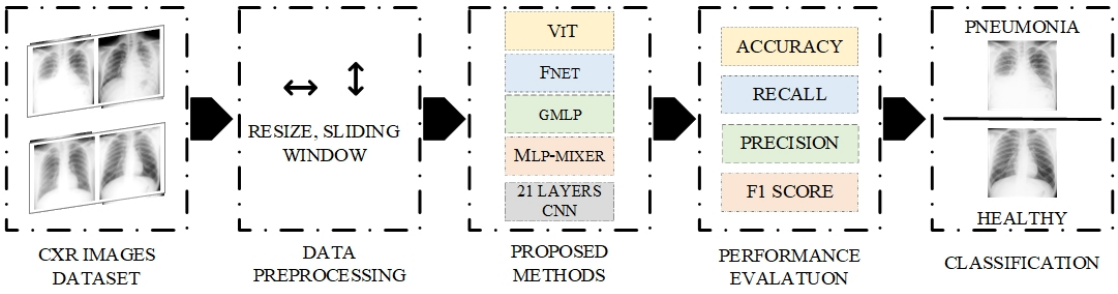

Figure 7. Flowchart of the proposed method.

Table 2 gives the evaluation metrics of the classification obtained for each method. The rows in Table 2 show the type of model, and the columns show the classification performance parameters obtained. As seen in Table 2, the ViT and FNet models produced identical accuracy, precision, recall and F1-scores values. The produced evaluation scores were 96.43%, 97.98%, 95.10% and 96.52%, respectively. Besides, MLP-mixer produced a 95.41% accuracy score, 96.04% precision value, 95.10% recall value and 95.57% F1-score, respectively. Finally, 94.39% accuracy score, 97.89% precision, 91.18% recall and 94.42% F1-score values were obtained by the gMLP approach. As the calculated evaluation metrics were observed, it was seen that ViT and FNet achievements were the highest among the examined transformer-based approaches. The MLP-mixer model produced the second-best evaluation scores (F1-scores, recall, and accuracy). gMLP produced the second-best precision score, where the calculated precision was 97.89%. However, the proposed PneumoNet outperformed all the transformer-based models and reported an accuracy of 96.50%, precision rate of 100%, recall of 93.46 and F1 score of 96.62% using the private database with a hold-out strategy. Considering the small amount of data in this study and the use of

transformer-based models as the basic architecture during experimental studies, it is considered reasonable that their performance is relatively low.

Table 2. Summary of classification performances obtained for used models.

Model	F1 score (%)	Recall (%)	Precision (%)	Accuracy (%)
ViT	96.52	**95.10**	97.98	96.43
FNet	96.52	95.10	97.98	96.43
MLP-mixer	95.57	95.10	96.04	95.41
gMLP	94.42	91.18	97.89	94.39
PneumoNet	**96.62**	93.46	**100.00**	**96.50**

Figure 8. Confusion matrix obtained using our PneumoNet model.

The confusion matrix acquired by the developed PneumoNet model is illustrated in Figure 8. While the rows of the confusion matrix show the number of instances of the true classes, the columns show the number of instances of the predicted classes. As can be seen from Figure 8, the healthy class was 100% correctly classified, and 7 pneumonia samples were misclassified. The summary of performance obtained using the PneumoNet model is included in Table 3. As indicated in the Table 3, the developed PneumoNet model produced 96.50% accuracy score, 100% precision, 93.46% recall, and 96.62% F1 score values for the private database with a hold-out validation strategy. In addition, the PneumoNet model yielded precision, F1-score, recall and accuracy values were 93.33%, 92.15%, 91.00% and 92.25%, respectively, using a private database with a ten-fold cross-validation strategy.

Table 3. Summary of performance obtained using the PneumoNet model for the private database.

Model	Data Partition	Accuracy (%)	Precision (%)	Recall (%)	F1 score (%)
PneumoNet	Hold-out Validation (90% training and 10% test)	96.50	100.00	93.46	96.62
PneumoNet	Ten-fold cross validation	92.25	93.33	91.00	92.15

3.1. Explainable Transformer models with the Grad-CAM technique

Figure 9 shows the heat maps obtained for healthy and pneumonia classes employing the Grad-CAM method for the PneumoNet. It helps to delineate the problematic region of the input image for the clinicians and helps to detect pneumonia from healthy classes. In this work, we have used the well-known Grad-CAM approach [31,32]. Grad-CAM enables viewing every model layer and examining each feature map layer, both of which are required to understand how input values influence model categorization. In this work, we also used Grad-CAM on the output of the PneumoNet model. Figure 9 shows the Grad-CAM illustrations for pneumonia and healthy classes. As seen in Figure 9, the images in the first-row show pneumonia, and the images in the second row show the healthy subjects.

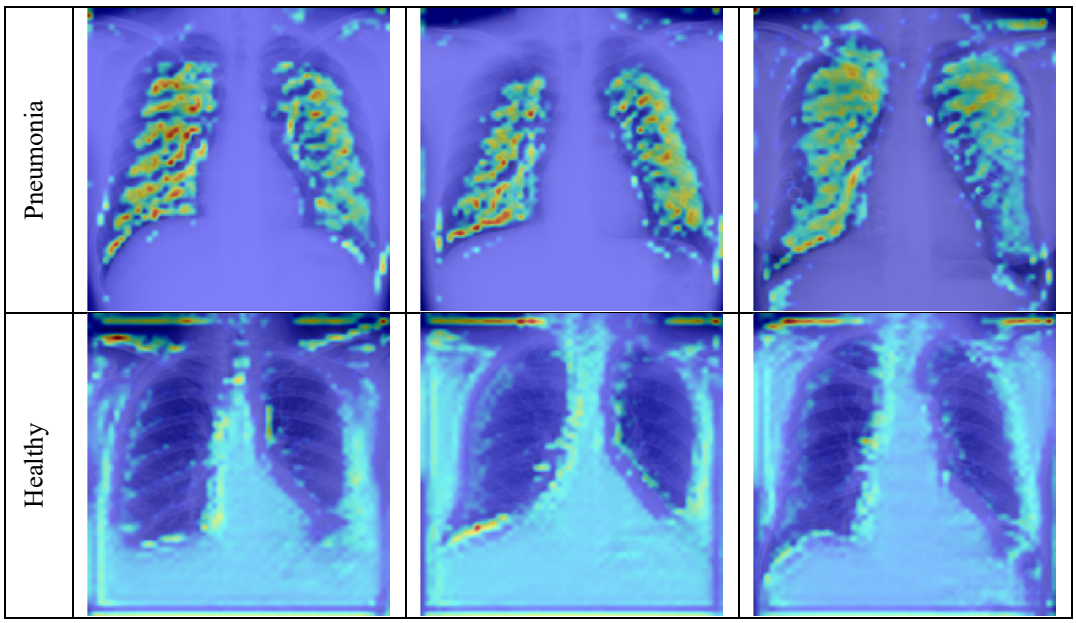

Figure 9. Heat maps obtained for healthy and pneumonia classes using the Grad-CAM technique for the PneumoNet model.

As illustrated in Figure 9, for the pneumonia class, the PneumoNet model mostly considered the left lung blob for pneumonia detection and has not concentrated on lung blobs for the health class for the public database.

The performance evaluation obtained using a 10-fold cross-validation test for the public databases is given in Table 4. We have obtained a precision value of 94.46%, an accuracy of 94.29 %, an F1 score of 94.27, and a recall rate of 94.10%.

Table 4. Summary of performance matrices obtained using our PneumoNet model on CXR image datasets with ten-fold cross-validation strategy.

Model	Data Partition	Accuracy (%)	Precision (%)	Recall (%)	F1 score (%)
PneumoNet	Cross Validation (10-fold)	94.29	94.46	94.10	94.27

4. Discussion

This study has proposed a novel PneumoNet model and compared its performance with various transformer-based approaches to classify CXR images to detect pneumonia. In this study, the novel model was developed using private and public databases. The obtained results showed that the proposed CNN-based model is effective and accurate in detecting pneumonia using the CXR dataset collected for this study. As presented in Table 2, classification accuracy of the developed model is 96.5% and 94.29% for private and public databases, respectively

in detecting pneumonia. Table 5 lists previous studies published to detect pneumonia using publicly available CXR datasets. It can be noted that most of the studies used different CNN techniques and transformer-based ensemble CNN frameworks for pneumonia detection. As shown in Table 5, when studies in the literature were reviewed for the detection of pneumonia, a dataset containing 5856 CXR images was widely used in the literature in binary classification tasks [13]. The Kaggle Pneumonia dataset is divided into subfolders for each image category (Pneumonia/Normal) and is arranged into three folders: training, testing, and validation. However, we did not use the data set in this form in our study. We combined the same class images in the training and test folders to ensure similarity to the data set we created. To make a two-class classification as normal and pneumonia. Additionally, an extra data set was used, and the CXR images were selected randomly.

As seen in Table 5, the best accuracy score of 99.21% in binary classification was obtained by Ukwuoma et al. [15] using a hybrid transformer encoder-based deep learning model. Authors in [21] obtained a 98.08% accuracy score using the input-enhanced vision transformer model, and Ar et al. [23] obtained 98.0% using a transformer-based ensemble framework on the same CXR pneumonia image database. Our study is the first work to use private and public databases for pneumonia detection using CXR images accurately (Table 5).

Table 5. Comparison of the classification performance of our work with the latest techniques developed using CXR images for pneumonia detection.

Authors	Dataset	Method	Compared techniques	Acc %
Ukwuoma et al. [15]	Kermany [13] Chest X-ray [14]	Hybrid Deep Learning Framework	Ensemble A (DenseNet201, VGG16, GoogleNet) Ensemble B(DenseNet201, InceptionResNetV2, Xception)	[13] 99.21 [14] 98.19
Cha et al. [7]	[13]	Attention-Based Transfer Learning Framework	ResNet152 ResNet18 DenseNet	96.63
Singh et al. [16]	[13]	Deep Attention Network	ResNet, ResNet with attention	95.47
Tyagi et al. [17]	[13]	CNN Based Framework	CNN, VGG16, ViT	96.45
Ma et al. [18]	[13] [14]	Transformer Backbone Network	Swin Transformer	[13] 97.2 [14] 87.3
Jiang et al. [19]	[13]	Multisemantic Level Patch Merger Vision Transformer	Baseline (ResNet50), ViT, ViT + Patch Merger	91.18
Wei et al. [20]	20,012 CXR images	Attention Based Contrastive Learning	ResNet18 (backbone)	83.85
Okolo et al. [21]	[13]	Input Enhanced Vision Transformer	IEViT variants	98.08
Mabrouk et al. [22]	[13]	Ensemble Of Deep CNN	DenseNet169, MobileNetV2, ViT	93.91
Ar et al. [23]	[13]	Ensembling Framework	CAPSNet, VDSNet, Ensemble Scheme	98.0
This work	Own dataset	CNN-Based	PneumoNet	96.50
This work	Public dataset [13,14]	CNN-Based	PneumoNet and XAI	94.29

In this study, a 21-layer CNN architecture is proposed to separate and classify input images into two classes. This network was created and trained from scratch using the end-to-end training method. Its purpose is to compare its performance with other pre-trained networks. The reason why our model gives low results when compared to studies in the literature is that the models we compare in the literature are generally in ensemble structures. Both the transformer models and the new 21-layer CNN are backbones.

The advantages of this study are given below:

1- A new dataset was created for the automated detection of pneumonia.
2- Our novel PneumoNet model has yielded an accuracy of 96.5% and 94.29% for private and public databases, respectively, in detecting pneumonia accurately from healthy subjects.
3- Our proposed model yielded higher classification performance than the recently developed transformer-based models for pneumonia detection.
4- Shown typical heatmaps for the healthy and pneumonia classes to develop confidence in clinicians by showing the regions of interest.
5- A new PneumoNet was proposed for pneumonia detection.

5. Conclusion

Chest X-ray is a promising imaging modality for diagnosing pneumonia as it is economical, fast, and readily available. The adoption of deep learning-based methods for pneumonia detection provides significant benefits for improving the interpretation, usability, accuracy, and consistency of CXR images. This study proposed a new model called PneumoNet for detecting pneumonia using CXR images and compared classification performance with recently transformer networks. Our developed model has yielded 96.5% and 94.29% accuracy for private and public databases, respectively, in detecting pneumonia accurately from healthy subjects. The limitation of this study is that we only used two datasets for this work. We plan to evaluate the model's performance using more chest X-ray images from diverse races. Also, we intend to explore the possibility of using this developed model to detect other pulmonary disorders using CXR images.

Acknowledgements

Ethics approval

This article is derived from the PhD thesis of the corresponding author Zehra Kadiroğlu. This study was performed in line with the principles of the Declaration of Helsinki. Approval was granted by the Ethics Committee of University of Dicle. Date: 13.10.2021, Number: 421. We would like to thank Dicle University Faculty of Medicine, Department of Chest Diseases and Tuberculosis for their contribution to the study. The dataset used for pneumonia detection during this study is available from the corresponding author upon reasonable request.

Author Contribution

Conceptualization Abdulkadir Sengur, Zehra Kadiroglu, and Erkan Deniz; investigation, Abdulkadir Sengur, Zehra Kadiroglu, Mazhar Kayaoglu and Erkan Deniz; methodology, Abdulkadir Sengur, Zehra Kadiroglu, Mazhar Kayaoglu and Hanifi Guldemir; software, Zehra Kadiroglu, and Mazhar Kayaoglu; project administration, Abdurrahman Senyigit, and Hanifi Guldemir ; resources, Abdurrahman Senyigit, and Hanifi Guldemir; supervision; Hanifi Guldemir, and Abdurrahman Senyigit; visualization, Abdulkadir Sengur, Zehra Kadiroglu, and Mazhar Kayaoglu; writing—original draft, Abdulkadir Sengur, Zehra Kadiroglu, Mazhar Kayaoglu; All authors have read and agreed to the published version of the manuscript.

References

[1] World Health Organization. "Pneumonia." Erişim: 9 Aralık 2022. [Online]. Available: https://www.who.int/news-room/fact-sheets/detail/ pneumonia
[2] Torres A, Cilloniz C, Niederman MS, Menéndez R, Chalmers JD, Wunderink RG, van der Poll T. Pneumonia. Nat Rev Dis Primers 2021;7(1):25.
[3] Kumar S, Singh P, Ranjan M. A review on deep learning based pneumonia detection systems. In: 2021 International Conference on Artificial Intelligence and Smart Systems (ICAIS), 2021, Coimbatore, India: IEEE.pp. 289-296.

[4] Kwon T, Lee SP, Kim D, Jang J, Lee M, Kang SU, Kim H, Oh K, On J, Kim YJ, Yun SJ, Jin KN, Kim EY, Kim KG. Diagnostic performance of artificial intelligence model for pneumonia from chest radiography. PLoS One 2021;16(4):e0249399.
[5] Mujahid M, Rustam F, Álvarez R, Luis Vidal Mazón J, Díez IT, Ashraf I. Pneumonia Classification from X-ray Images with Inception-V3 and Convolutional Neural Network. Diagnostics 2022;12(5):1280.
[6] Govindarajan A, Govindarajan A, Tanamala S, Chattoraj S, Reddy B, Agrawal R, Iyer D, Srivastava A, Kumar P, Putha P. Role of an Automated Deep Learning Algorithm for Reliable Screening of Abnormality in Chest Radiographs: A Prospective Multicenter Quality Improvement Study. Diagnostics 2022; 12(11):2724.
[7] Cha S-M, Lee S-S, Ko B. Attention-Based Transfer Learning for Efficient Pneumonia Detection in Chest X-ray Images. Appl Sci 2021; 11(3):1242.
[8] Al Mamlook RE, Chen S, Bzizi, HF. Investigation of the performance of machine learning classifiers for pneumonia detection in chest X-ray images. In: 2020 IEEE International Conference on Electro Information Technology (EIT); 2020, Chicago, IL, USA, IEEE: pp. 98-104.
[9] Bai Y, Mei J, Yuille A L, Xie C. Are transformers more robust than cnns?. Advances in Neural Information Processing Systems, 2021; 34:26831-26843.
[10] Usman M, Zia T, Tariq A. Analyzing Transfer Learning of Vision Transformers for Interpreting Chest Radiography. J Digit Imaging 2022;35(6):1445-1462.
[11] Vaswani A, Shazeer NM, Parmar N, Uszkoreit J, Jones L, Gomez AN, Kaiser L, Polosukhin I. Attention is All you Need. In: Advances in Neural Information Processing Systems 30: Annual Conference on Neural Information Processing Systems 2017, USA, 2017, pp. 5998-6008.
[12] Dosovitskiy A, Beyer L, Kolesnikov A, Weissenborn D, Zhai X, Unterthiner T, Dehghani M, Minderer M, Heigold G, Gelly S, et al. An image is worth 16x16 words: Transformers for image recognition at scale. In: 9th International Conference on Learning Representations (ICLR); 2021, Virtual Event, Austria, *arXiv:2010.11929*.
[13] Kermany DS, Goldbaum M, Cai W, Valentim CCS, Liang H, Baxter SL, et al. Identifying medical diagnoses and treatable diseases by image-based deep learning. Cell 2018;172(5):1122-1131.e9.
[14] Wang X, Peng Y, Lu L, Lu Z, Bagheri M, Summers RM. ChestX-ray8: hospitalscale chest X-ray database and benchmarks on weakly-supervised classification and localization of common thorax diseases. In: 2017 IEEE Conference on Computer Vision and Pattern Recognition (CVPR); 2017; Honolulu, HI, USA: IEEE, pp. 3462-3471
[15] Ukwuoma CC, Qin Z, Belal Bin Heyat M, Akhtar F, Bamisile O, Muaad AY, Addo D, Al-Antari MA. A hybrid explainable ensemble transformer encoder for pneumonia identification from chest X-ray images. J Adv Res 2023; 48: 191-211.
[16] Singh S, Rawat S, Gupta M, Tripathi B, Alanzi F, Majumdar A, Khuwuthyakorn P, Thinnukool O. Deep attention network for pneumonia detection using chest x-ray ımages. Comput Mater Contin 2023; 74(1): 1673-1691.
[17] Tyagi K, Pathak G, Nijhawan R, Mittal A. Detecting pneumonia using vision transformer and comparing with other techniques. In: 2021 5th International Conference on Electronics, Communication and Aerospace Technology (ICECA), 2021; Coimbatore, India, IEEE: pp. 12-16.
[18] Ma Y, Lv W. Identification of Pneumonia in Chest X-Ray Image Based on Transformer. Int J Antennas Propag 2022; 2022(1): 5072666.
[19] Jıang Z, Chen L. Multisemantic level patch merger vision transformer for diagnosis of pneumonia. Comput Math Methods Med 2022; 2022(1): 7852958.
[20] Wei X, Niu X, Zhang X, Li Y. Deep Pneumonia: Attention-Based Contrastive Learning for Class-Imbalanced Pneumonia Lesion Recognition in Chest X-rays. In: 2022 IEEE International Conference on Big Data (Big Data); 2022; IEEE. pp. 5361-5369.
[21] Okolo GI, Katsigiannis S, Ramzan N. IEViT: An Enhanced Vision Transformer Architecture for Chest X-ray Image Classification. Comput Methods Programs Biomed 2022; 226:107141.
[22] Mabrouk A, Díaz Redondo RP, Dahou A, Abd Elaziz M, Kayed M. Pneumonia Detection on Chest X-ray Images Using Ensemble of Deep Convolutional Neural Networks. Appl Sci 2022; 12(13):6448.
[23] Gokul AG, Kumaratharan N, Rani PL, Devi N. Ensembling Framework for Pneumonia Detection in Chest X-ray images. In: 2022 International Conference on Smart Technologies and Systems for Next Generation Computing (ICSTSN); 2022; Villupuram, India: IEEE, pp. 1-5.
[24] Tolstikhin IO, Houlsby N, Kolesnikov A, Beyer L, Zhai X, Unterthiner T, Yung J, Keysers D, Uszkoreit J, Lucic M, & Dosovitskiy A. MLP-Mixer: An all-MLP Architecture for Vision. In NeurIPS 2021, 34: 24261-24272.
[25] Lee-Thorp J, Ainslie J, Eckstein I, Ontanon S. FNet: Mixing tokens with Fourier transforms. In: Proceedings of the 2022 Conference of the North American Chapter of the Association for Computational Linguistics: Human Language Technologies; 2022; Seattle, United States: Association for Computational Linguistics, pp. 4296-4313.
[26] Liu H, Dai Z, So D, Le QV. Pay attention to mlps. In NeurIPS 2021; 34:9204-9215.
[27] Visuña L, Yang D, Garcia-Blas J, Carretero J. Computer-aided diagnostic for classifying chest X-ray images using deep ensemble learning. BMC Med Imag 2022; 22(1): 1-16.
[28] Jain DK, Singh T, Saurabh P, Bisen D, Sahu N, Mishra J, Rahman H. Deep Learning-Aided Automated Pneumonia Detection and Classification Using CXR Scans. Comput Intell Neurosci 2022;2022(1): 7474304.
[29] Şengür D. Investigation of the relationships of the students' academic level and gender with Covid-19 based anxiety and protective behaviors: A data mining approach. Turkish J Sci Technol 2020; 15(2): 93-99.

[30] Şengür D, Siuly S. Efficient approach for EEG-based emotion recognition. Electron Lett 2020; 56(25): 1361-1364.
[31] Loh HW, Ooi CP, Seoni S, Barua PD, Molinari F, Acharya UR. Application of explainable artificial intelligence for healthcare: A systematic review of the last decade (2011–2022). Comput Methods Programs Biomed 2022; 226:107161.
[32] Sobahi N, Atila O, Deniz E, Sengur A, Acharya UR. Explainable COVID-19 detection using fractal dimension and vision transformer with Grad-CAM on cough sounds. Biocybern Biomed Eng 2022; 42(3):1066-1080.

Turkish Journal of Science & Technology
19(2), 339-350, 2024

Research Paper
https://doi.org/10.55525/tjst.1427300

PLC Controlled Fuzzy Logic-Based Egg Hatching Machine

Muhammed ELTALEB[1*], Hakan ÇELİK[2]
[1,2] Department of Mechatronics Engineering, Faculty of Engineering, Fırat University, Elazığ, Türkiye.
[*1] m1.6alab@gmail.com, [2] hakancelik@firat.edu.tr

(Geliş/Received: 29/01/2024; Kabul/Accepted: 17/09/2024)

Abstract: In response to the increasing food demand due to the growing global population, this study has designed a fully automated incubator machine based on a Programmable Logic Controller (PLC) to enhance efficiency in the egg production sector. To align with Industry 4.0 technologies, this machine controls temperature and humidity using fuzzy logic, one of the artificial intelligence methods. The incubator is capable of meeting the specific temperature and humidity needs for the incubation processes of various types of bird eggs. It has been tested under different conditions, and its performance has been examined in detail. The analysis results show that the fuzzy logic-based temperature and humidity control systems on the PLC successfully reached the set reference values and maintained them continuously and stably after initial fluctuations. In conclusion, the design and control of an automated incubation machine with a PLC-based fuzzy logic controller were successfully accomplished.

Key words: Programmable logic controller, fuzzy logic, Industry 4.0, temperature control, humidity control.

PLC Kontrollü Bulanık Mantık Tabanlı Kuluçka Makinesi

Öz: Artan dünya nüfusu ile birlikte artan yiyecek ihtiyacına cevap vermek ve yiyecek endüstrisinde önemli bir yere sahip olan yumurta üretimini daha verimli hale getirmek amacıyla, bu çalışmada PLC (Programlanabilir Mantık Denetleyicisi) tabanlı tam otomasyonlu bir kuluçka makinesi tasarlanmıştır. Endüstri 4.0 teknolojileriyle uyumu sağlamak amacıyla bu makinenin, sıcaklık ve nem kontrolünü, yapay zekâ yöntemlerinden biri olan bulanık mantığı kullanarak gerçekleştirmektedir. Farklı türdeki kuş yumurtalarının kuluçka süreçleri için gereken özel sıcaklık ve nem değerlerini karşılayabilen bu tam otomatik kuluçka makinesi, çeşitli sıcaklık ve nem koşullarında test edilmiş, makinenin performansı detaylı olarak incelenmiştir. Analiz sonuçları, PLC üzerinde bulanık mantık tabanlı sıcaklık ve nem kontrol sistemlerinin belirlenen referans değerlerini başarıyla yakaladığını ve belirli bir süre dalgalanmadan sonra referans değerleri sürekli ve kararlı bir şekilde takip ettiğini göstermektedir. Sonuç alarak, PLC tabanlı bulanık mantık kontrollü otomatik bir kuluçka makinesinin tasarımı ve kontrolü başarıyla gerçekleştirilmiştir.

Anahtar kelimeler: Programlanabilir mantık denetleyicisi, bulanık mantık, sıcaklık, nem, Endüstri 4.0.

1. Introduction

Food production has been one of the fundamental tasks since the presence of humans on Earth. fact, it has been the main reason for the emergence of other sectors such as agriculture, trade, and industry. The food production process is constantly evolving and its development is seen as an indispensable need. Poultry meat and eggs, which are among the most important elements of food and nutrition, are essential food items on the table. Therefore, the production of eggs and poultry meat has become a major food industry worldwide. This production begins with the hatching of chicks. Every year, billions of layer chicks hatch from eggs under industrial conditions worldwide. The incubation process in hatcheries has been highly standardized and does not differ significantly between countries. In short, when they reach the hatchery, the eggs are placed in large-scale incubators (each containing tens of thousands of eggs) and are incubated in the dark, with temperature and humidity controlled in a highly controlled manner [1].

Recently, industrial automation systems have been rapidly advancing and evolving into more intelligent forms, such as Industrial Internet of Things (IIoT), paving the way for the concept of Industry 4.0 [2].

Meanwhile, due to its simple software logic and robust, rugged nature, PLCs remain valuable devices capable of meeting the requirements of IIoT. This is attributed to their modularity (ability to be used in any purpose), ability to support numerous communication protocols, and connectivity with field devices such as sensors and actuators [3]. The literature generally features numerous studies on MCU-based incubator control, primarily using non-industrial controllers and materials [4],[5]. In the other hand, studies on PLC-based temperature control, primarily employing PID based controllers as a control method. In Jakub's study [6], a FOPID was utilized to control temperature under laboratory conditions, employing the S7-1200 PLC as the hardware controller. Meanwhile, Jasmin's study [7] describes simple incubator temperature control using PLC and PID, but it does not

[*] Corresponding author: m1.6alab@gmail.com ORCID Number of authors: [1] 0000-0003-3461-0360, [2] 0000-0002-2861-3269

provide any information about controlling humidity levels. On the other hand, most PLC-controlled humidity systems are predominantly associated with air quality control rather than incubation machines [8]. In conclusion, while there are many studies on applying adaptive controllers to other systems, the literature lacks a study that addresses a PLC-based adaptive controller for an incubation machine controlling both temperature and humidity.

Recent studies, such as the one discussed in [9], explore the integration of IoT for more precise control of incubation environments, highlighting the potential for improved efficiency and adaptability in industrial applications. Therefore, in this article, the aim is to control the temperature and humidity conditions in an incubator machine using PLC, without the need for a computer or computer-based software like Matlab. Differing from studies in the existing literature, a FLC structure has been established in the PLC environment, and the temperature and humidity values of the incubator machine have been controlled. As a result, the design and control of an artificial intelligence-based incubator compatible with Industry 4.0 systems have been successfully achieved.

1.1 Incubation and Hatching

The process of providing the necessary humidity, temperature, and turning conditions for a healthy hatch of a chick from an egg is called incubation [10]. This process naturally occurs as mother hens instinctively sit on the eggs. The incubation process also takes place artificially in incubators and hatcheries, which can provide the necessary humidity and temperature conditions [11]. Despite improvements in incubation conditions and technology, the success rate for hatching young brood from the eggs of modern high-yield poultry breeds has not significantly increased, and about 20% of expensive breeding eggs are still lost as incubation waste. The potential for improving hatchability lies not only in enhancing the biological qualities of the eggs but also in organizing effective incubation [12]. Generally, the incubation and hatching conditions are shown in Table 1 [13],[14].

Table 1. Incubation and hatching conditions.

Chicken	Incubation	Hatching
Days	18	3-5
Temperature °C	37.8	36.8-37.3
Humidity %RH	55-60	65-75
Turning	1 turn per hour	No turning

2. Material and Method

In this study, an S7-1200 PLC was utilized to regulate the temperature and humidity conditions of an egg incubation machine. The use of a PLC as the control hardware aims to enhance the accuracy and modularity of incubation machines [15]. A fuzzy logic controller (FLC) was developed in MATLAB for the control algorithm, and its code was implemented in TIA Portal using SCL and Ladder languages. The FLC is preferred in this study due to its simplicity and effectiveness [16].

The heating system's hardware configuration includes a 300-watt resistance heater integrated with a circulation fan, serving as the heating actuator. This heater is regulated by an AC dimmer, which is controlled by a Pulse Width Modulation (PWM) signal from the PLC. The control aligns with the FLC's duty cycle, ensuring precise temperature regulation. However, since the AC dimmer requires a 5-volt logic signal, it cannot directly use the PLC's PWM signal. To resolve this, a Microcontroller Unit (MCU) is employed to convert the PLC signals into a format compatible with the AC dimmer.

On the other hand, for the humidifier, a manually assembled setup has been utilized due to the unavailability of a suitable analog humidifier for purchase. This setup comprises scold mist nozzles placed within a specific container. The amount of mist produced and introduced into the incubation environment is controlled by a snail fan blower. This manual approach allows for precise regulation of humidity levels, essential for the incubation process.

For sensing purposes, the system employs an HT-2 humidity and temperature transmitter, which have outputs with 0-10 V DC analog signal compatible with the PLC. This sensor is crucial for real-time monitoring of the incubation conditions and giving feedback to the FLC function blocks. Additionally, to facilitate the monitoring and control of the machine's operational conditions, a Human Machine Interface (HMI) was developed using TIA Portal software and implemented in a Siemens KTP 700 HMI unit. This interface allows for efficient interaction and management of the machine's functions. In Figure 1, the block diagram representing the architecture of the

system is presented, whereas Figure 2 illustrates the incubator machine, highlighting its design and control mechanisms as developed in this project.

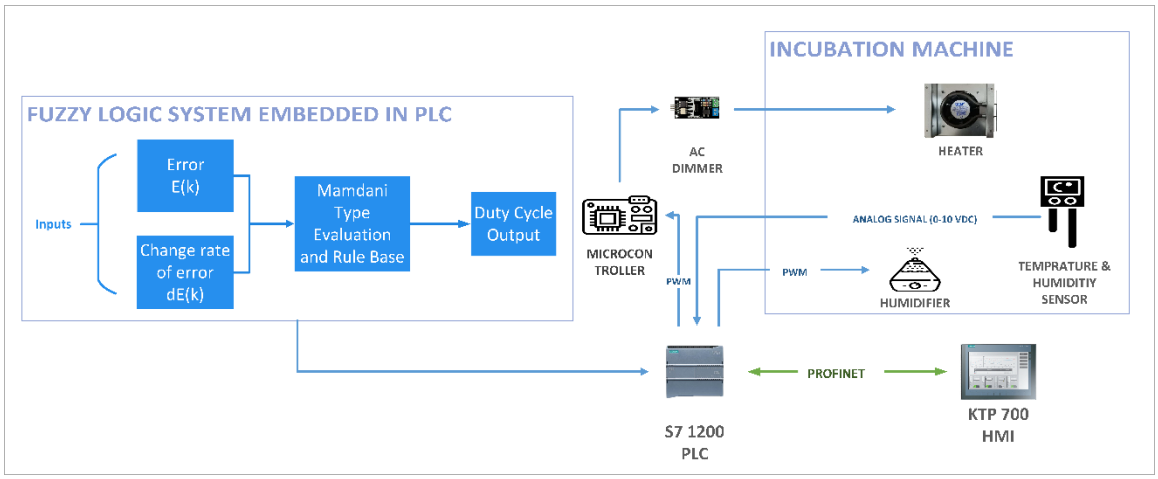

Figure 1. Block diagram of the system.

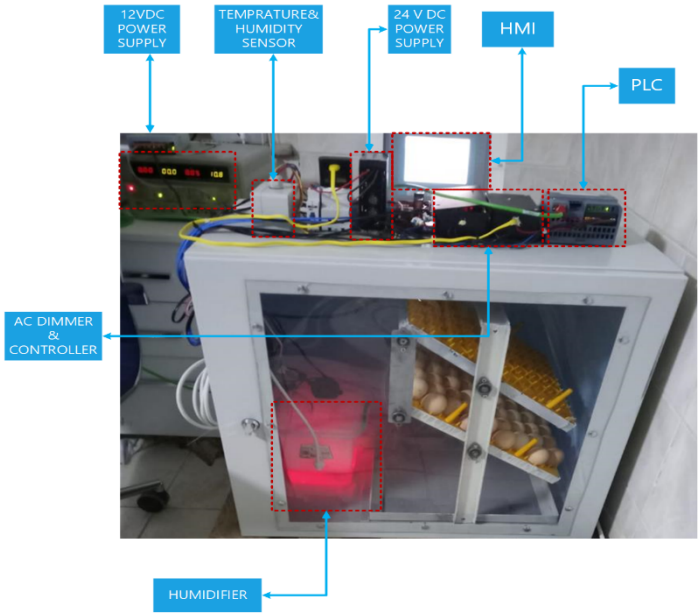

Figure 2. Designed system.

In the conclusion of the study, the control method was tested under both preset temperature and humidity conditions as well as varying conditions.

2.1. Fuzzy Logic Controller Design

Due to the nonlinear nature of humidity and temperature control systems, traditional methods like PID controllers often prove insufficient. The adaptive nature and simple mathematical structure of FLCs present them as a more effective alternative [17]. FLCs offer an advanced method for regulating temperature and humidity in closed boundary systems. Unlike traditional controllers, FLCs utilize fuzzy set theory to handle imprecise and variable environmental conditions typically encountered in temperature and humidity control processes.

In this study, as shown in Figure 3, separate FLC's have been developed for managing humidity and temperature. Each controller is designed with two inputs and one output. This configuration allows for a more nuanced and responsive control mechanism in environmental management systems.

Initially, the membership functions were determined based on previous works in the literature. After conducting a few experiments, the membership functions were adjusted according to the obtained actuators' response.

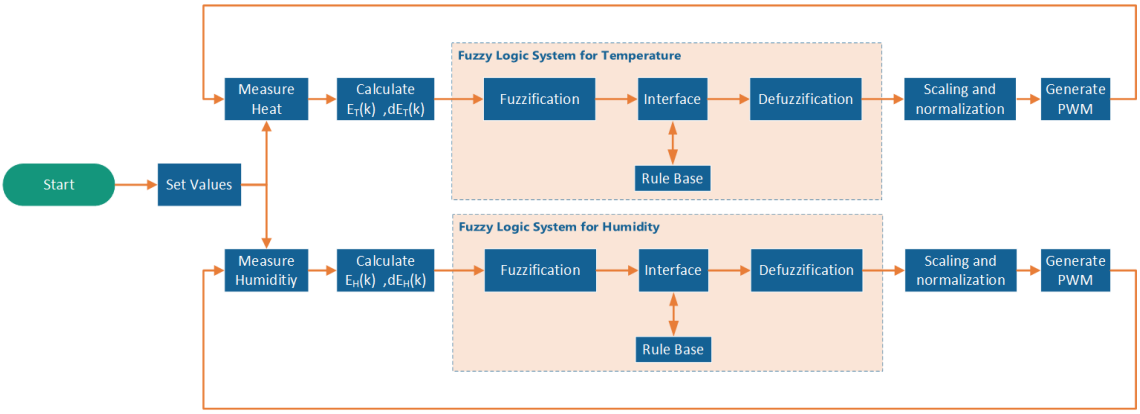

Figure 3. FLC structure.

2.2. Main components of the fuzzy logic system:

Fuzzification: This initial phase involves converting real-time temperature and humidity readings into analog values, which are essential for calculating the error and the rate of change in error, as shown in Equations (1) and (2).

$$E(k) = Referance\ value - Measured\ value \tag{1}$$

$$dE(k) = E(k) - E(k-1) \tag{2}$$

Calculated values serve as the inputs for the FLC. The fuzzification process then maps these inputs onto five distinct membership functions, known as fuzzy sets. These fuzzy sets are organized as NB (Negative Big), NS (Negative Small), ZE (Zero), PS (Positive Small), and PB (Positive Big), corresponding to the error range from -10 to 10 and the change rate of error range from -1 to 1. This step is crucial for enabling the FLC to handle the nuances of environmental variability with greater accuracy. The membership functions are shown in Figures 4 and 5 for temperature and Figures 6 and 7 for humidity.

Rule Base and Evaluation: The controller's operation is governed by a structured set of if-then rules, typically formulated based on empirical knowledge and experience. These rules are designed to interpret the fuzzified inputs and make appropriate control decisions. For example, a rule might state: "If E(k) is Positive Big (PB) and dE(k) is Negative Small (NS), then increase the duty output rapidly." Such rules are crucial for generating fuzzy output decisions that accurately respond to environmental changes. Given two inputs with five fuzzy sets each, the system requires a comprehensive 5x5 rule matrix, shown in Table 2, to cover all possible scenarios.

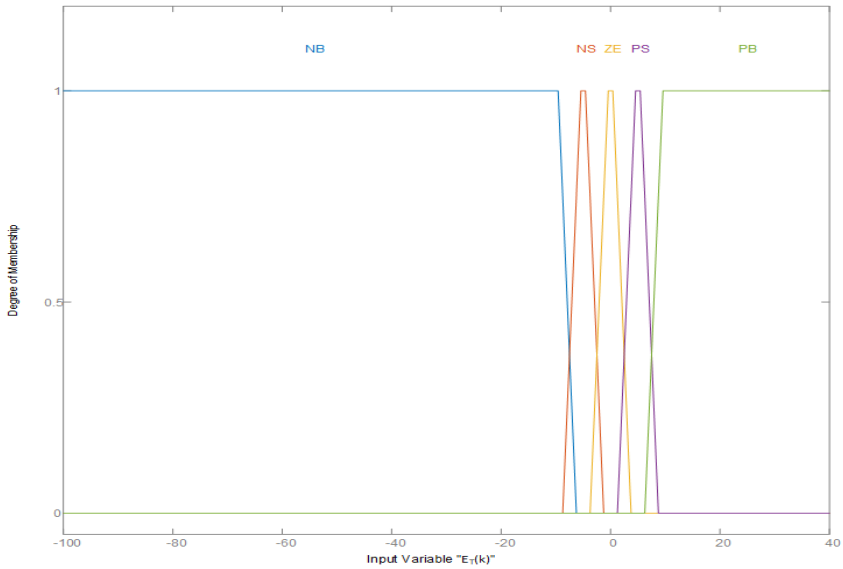

Figure 4. Temperature error membership functions.

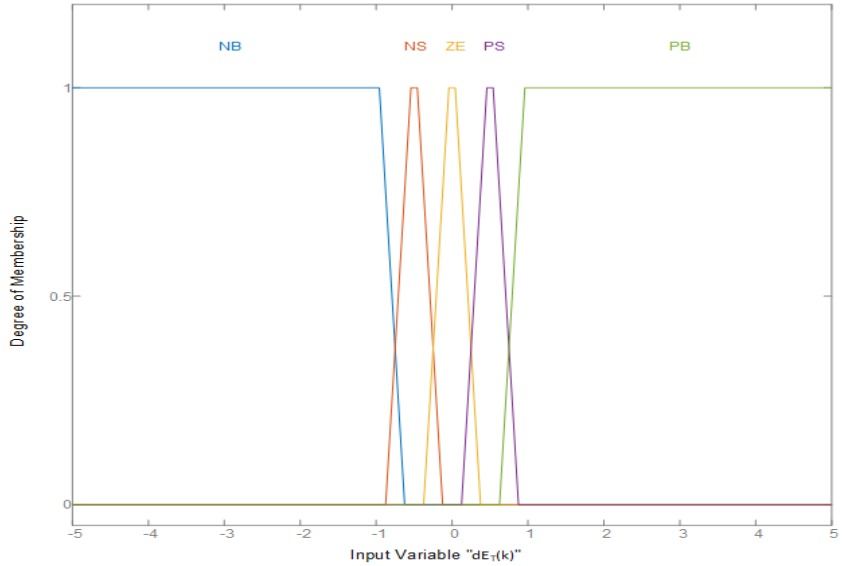

Figure 5. Temperature change rate of error membership functions.

Table 2. Rule Matrix.

E / dE	NB	NS	ZE	PS	PB
NB	VS	VS	VS	S	M
NS	VS	VS	S	M	B
ZE	VS	S	M	B	VB
PS	S	M	B	VB	VB
PB	M	B	VB	VB	VB

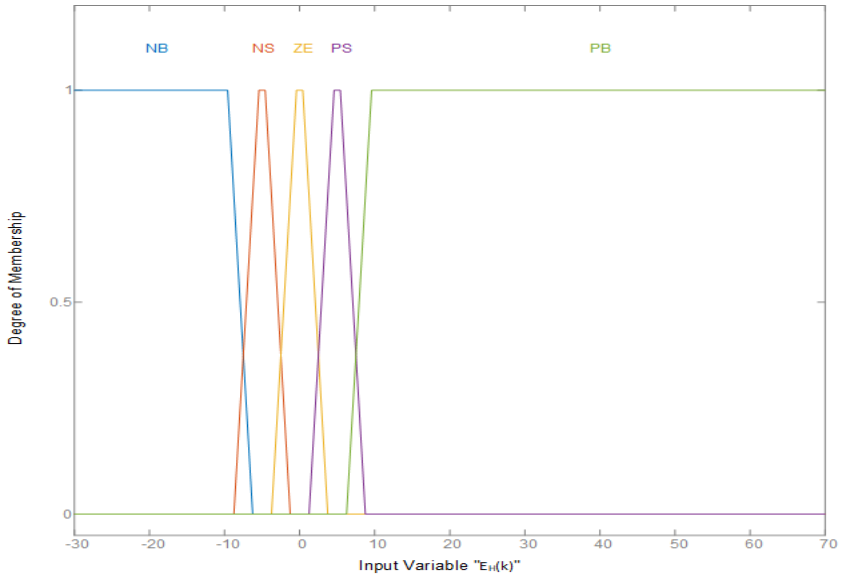

Figure 6. Humidity error membership functions.

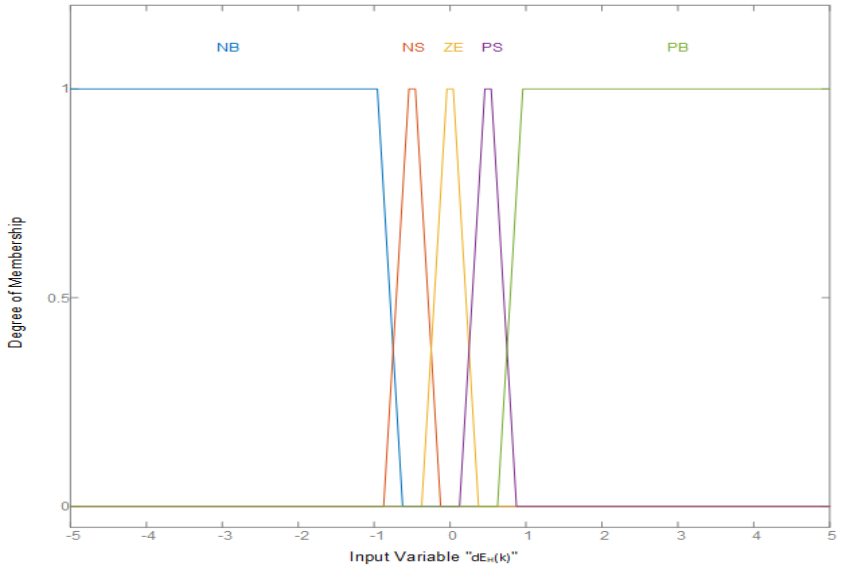

Figure 7. Humidity change rate of error membership functions.

While the rule base determines the controller's response in a verbal (qualitative) manner, it is imperative to convert this verbal data into a quantifiable mathematical form for application in the fuzzification layer. This conversion process is known as evaluation. Various evaluation methods are discussed in the literature, but the preferred approach in this study is the Mamdani method. With this method, the control of systems is successfully carried out based on expert knowledge without relying on a data set [18]. This method relies on the Min-Max principle for evaluation and aggregation. For the defuzzification, the centroid method was applied, as shown in Equation (3).

$$y^* = \frac{\sum_{k=1}^{n} y_k \cdot \mu_c(y_k)}{\sum_{k=1}^{n} \mu_c(y_k)} \tag{3}$$

In this equation, is the crisp output, y^* represents the discrete output values, and $\mu_c(y_k)$ is the membership degree for y_k. The sum over k applies to all discrete points in the output domain. The specifics of the Mamdani method and its reliance on the Min-Max approach are further elucidated in Figure 8 [1]. The control surface of the FLC system is also shown in Figure 9.

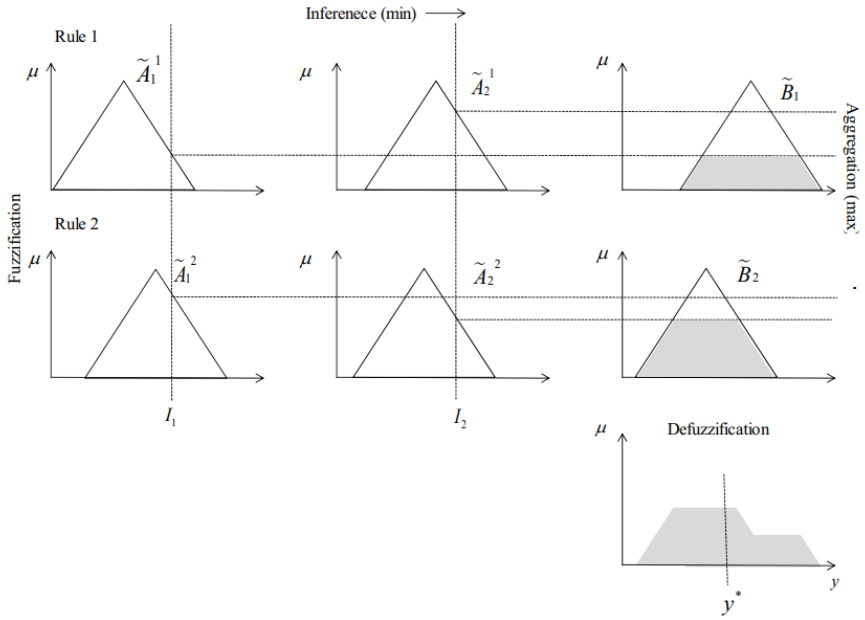

Figure 8. Min-Max Evaluation.

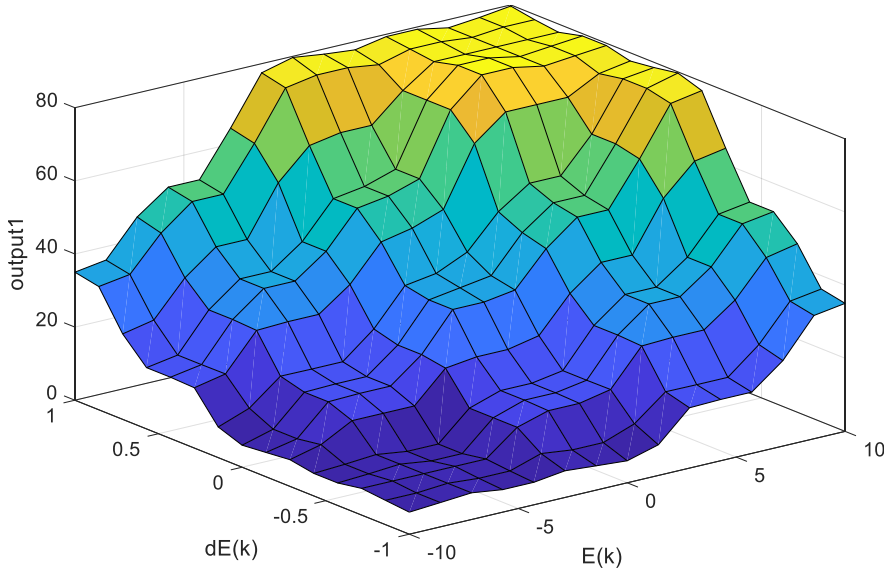

Figure 9. Control surface of the FLC system.

Defuzzification: The evaluation process yields an output that is still a fuzzified value, typically ranging between [0,1]. To make this output applicable to the actuators of the system, it must be converted into a different quantity. In this system, actuators are controlled by a PWM signal, which varies between 0 and 100. Due to the operational differences between the humidifier and the heater, their respective defuzzification member functions

are distinct. The specific defuzzification functions for both the heater and the humidifier are depicted in the respective Figures (10-11). These functions are critical for translating the fuzzy evaluation output into a precise and actionable control signal for each actuator.

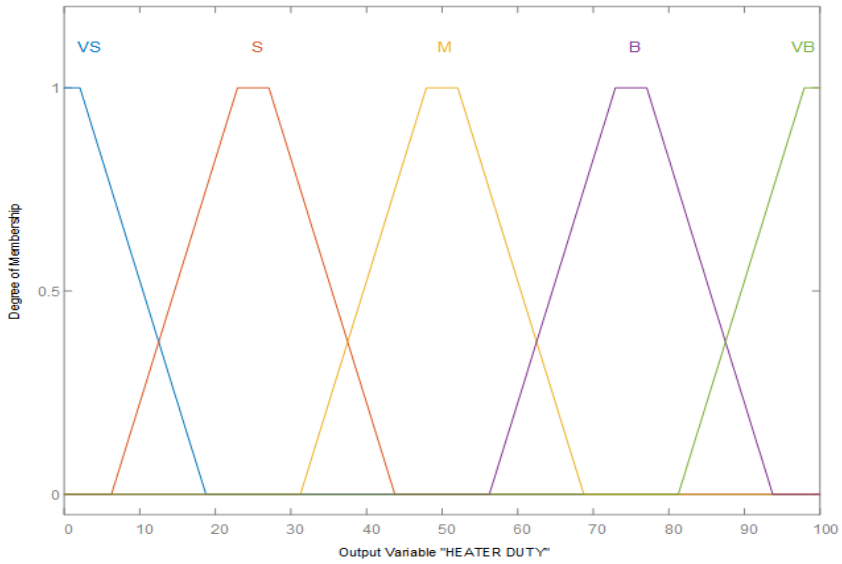

Figure 10. Heater duty cycle membership functions.

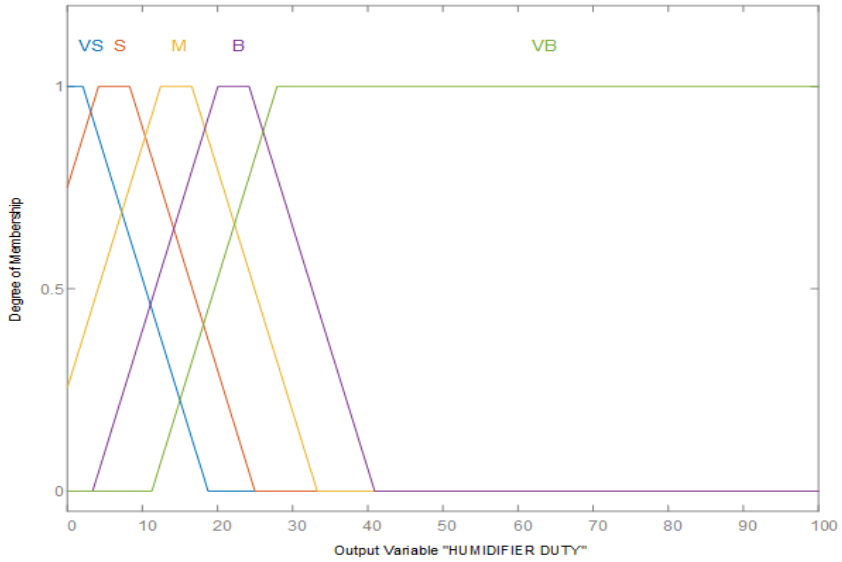

Figure 11. Humidifier duty cycle membership functions**.**

2.3. Implementation of Fuzzy logic controller in S7-1200 PLC

The S7-1200 PLC system offers the flexibility and capability to control a wide variety of devices, supporting diverse automation needs. Its compact design, along with flexible configuration and command sets, has made the S7-1200 widely used in various control applications. The S7-1200 integrates a microprocessor, an integrated PROFINET communication circuit, digital input and output units, and, in some series, an analog input and output unit, all within a compact structure. In this project, both LADDER diagrams and Structured Control Language (SCL) have been employed for programming the control blocks within the TIA Portal project. The program blocks are arranged and presented in a chronological sequence shown in Figure 12, reflecting the block calls in the control part of the project.

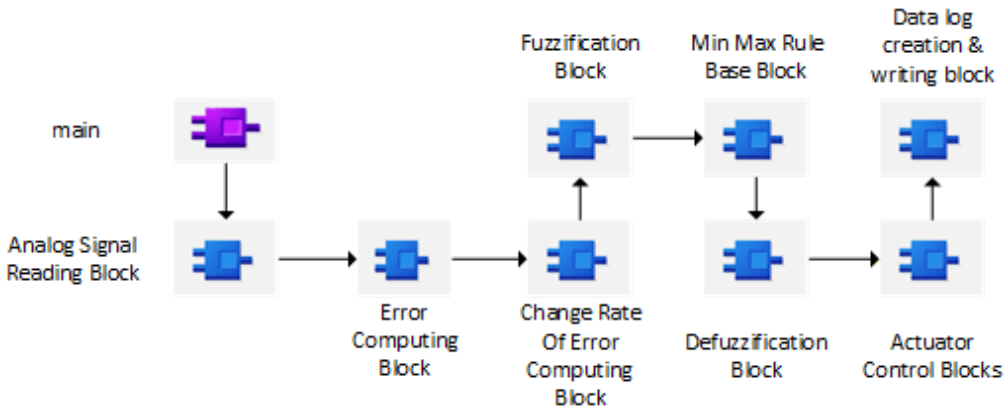

Figure 12. Chronological sequence of the PLC program.

To obtain continuous feedback from the incubation environment and convert the analog signals into digital signals, the S7-1200 PLC's Analog-to-Digital Converter (ADC) module is utilized. This module effectively converts the analog signal on a scale from 0 to 27.648. To make the digital signal meaningful for the control system, normalization and scaling blocks are employed, adjusting the input from 0 to 100, which aligns with the transmitter's actual measuring range. Subsequently, the processed digital signals are fed into error and derivative error blocks, which are configured based on the mathematical equations previously presented. In the next stage, the error and derivative error signals are applied to the fuzzification block, as shown in Figures 12 to 14, which is written in SCL and parameterized according to the design that was executed in the MATLAB environment.

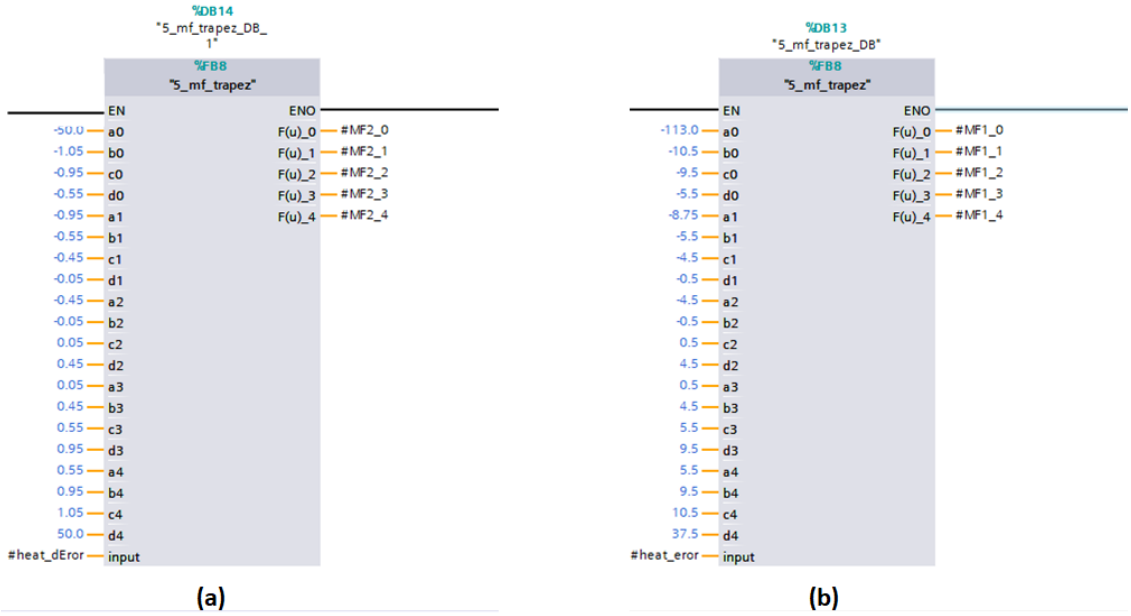

Figure 13. a) Error fuzzification block, b) Change rate of error fuzzification block.

The subsequent block, depicted in Figure 015, represents the rule base and the evaluation stage of the FLC. This stage is developed using both LADDER and SCL.

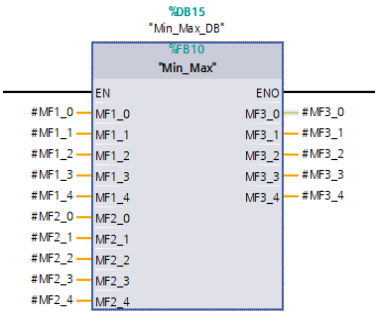

Figure 14. Rule base and the evaluation block.

The fuzzy quantities generated by the min-max block are then fed into the defuzzification blocks, which produce the desired duty cycle needed for the control system. The humidifier and heater actuators are controlled by PWM signals. For this purpose, actuator control blocks containing PWM control blocks are meticulously designed to meet the specific requirements of each actuator.

3. Results and Discussion

The automated incubator machine designed has been operated for poultry incubation, requiring a temperature of 37.8°C and a humidity reference of 60%. The results obtained are presented in Figures 15, 16, 17, and 18. When examining the temperature change shown in Figure 15, it is observed that the temperature of the experimental setup is successfully controlled with the FLC created in the PLC, and the desired temperature value is achieved. Figure 16 presents the variation of the duty cycle value produced by the temperature FLC controller. Upon examining this variation, it is noted that the duty cycle value changes until the desired reference temperature is reached and then remains constant in the steady state.

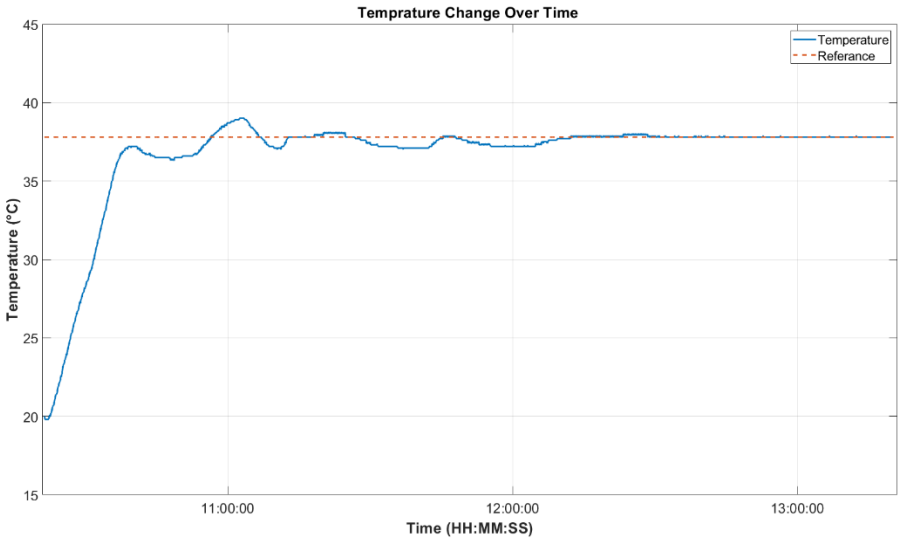

Figure 15. Temperature change over time**.**

When analyzing the humidity change presented in Figure 17, fluctuations and steady-state errors are observed in the humidity control with the FLC, due to the influence of temperature on the humidity experimental setup. However, when the temperature value reaches the reference value, it is observed that the humidity value approaches the reference value and follows it with an acceptable error. Figure 18 presents the variation of the duty cycle value produced by the humidity FLC controller. Similar to temperature control, this variation shows that the duty cycle value changes until the desired humidity value is achieved and then remains constant in the steady state.

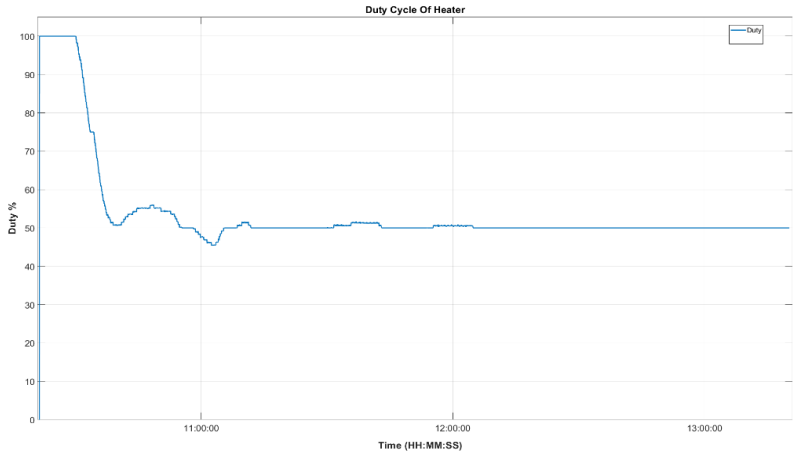

Figure 16. Duty Cycle of Heater.

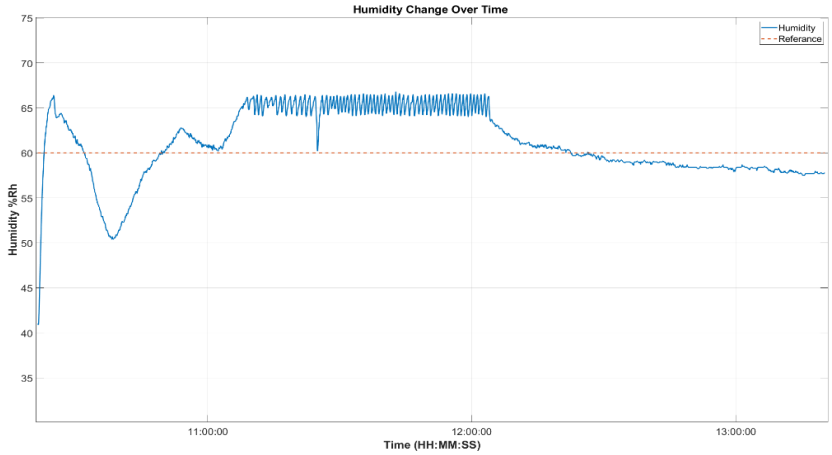

Figure 17. Humidity change over time.

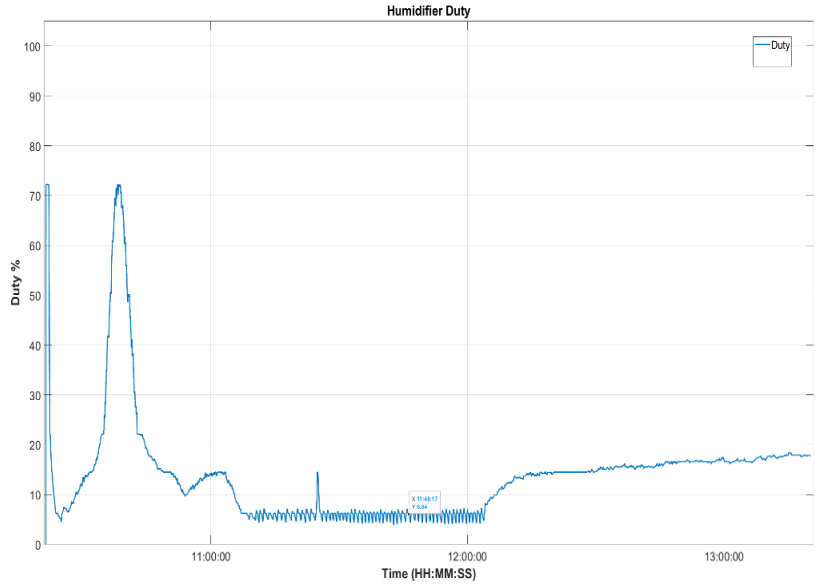

Figure 18. Duty Cycle of Humidifier.

4. Conclusion

As the global population continues to rise, and with it the increasing need for food, this study presents the design of a fully automated incubation machine controlled by PLC-based fuzzy logic to improve efficiency in egg production, a significant sector in the food industry. This study contributes to the literature by demonstrating the successful integration of a FLC within a PLC environment for the precise control of temperature and humidity in an industrial incubation machine, which is compatible with Industry 4.0 standards. This approach not only enhances the efficiency of egg production but also offers a novel solution by utilizing a PLC-based control system instead of traditional microprocessor-based systems. According to the results obtained from the experimental setup created for the temperature and humidity control of the incubation machine, it has been observed that the fuzzy logic-based temperature and humidity controller implemented in the PLC environment successfully controls the temperature and humidity values.

Better performance can be obtained by optimizing the fuzzy logic membership function limits with a suitable optimization method based on the data obtained from the machine. In addition, the actuators used in this project are non-industrial, so to improve the responses, there is a need to purchase a PLC-compatible humidifier.

Inspired by this study, future research could focus on implementing Fractional-Order PID, 2-DOF PID, and other artificial intelligence-based control structures in the PLC environment to enhance the performance of automated incubation machines.

Acknowledgement

This manuscript is the culmination of research conducted under project number 1919B012111329, which was funded by the Scientific and Technological Research Council of Turkey (TÜBITAK) as part of the 2209-A Research Projects Support Program for University Students. We extend our sincere appreciation to TÜBITAK for their invaluable moral and financial support throughout the course of this study.

References

[1] Hedlund L, Jensen P. Effects of stress during commercial hatching on growth, egg production and feather pecking in laying hens. PLoS One 2022; 17(1): 1-11.
[2] Azarmipour M, Elfaham H, Gries C, Epple U. PLC 4.0: A Control System for Industry 4.0. 45th Annual Conference of the IEEE Industrial Electronics Society (IECON); Oct. 2019; Lisbon, Portugal: IEEE. pp. 5513-5518.
[3] Sehr M, et al. Programmable Logic Controllers in the Context of Industry 4.0. IEEE Trans Ind Inf 2020; 17(5): 3523-3533.
[4] Shafiudin S, Kholis N. Monitoring System and Temperature Controlling on PID Based Poultry Hatching Incubator. IOP Conf. Ser.: Mater Sci Eng 2018; 336(1): 012007.
[5] Iskandar J., Alrasyid S., Nurhaqiqi E., Andria F., and Tosida E. T. Optimisation of electronics and mechanics system of automatic egg incubator machine. IOP Conference Series: Materials Science and Engineering 2019; 621(1): 012004.
[6] Możaryn J, Petryszyn J, Ozana S. PLC based fractional-order PID temperature control in pipeline: design procedure and experimental evaluation. Meccanica 2021; 56(4): 855-871.
[7] Velagic J, Osmic N, Lutvica K, Kadic N. Incubator system identification and temperature control with PLC & HMI. Proceedings ELMAR-2010; Sep. 2010; Zadar, Croatia: pp. 309-312.
[8] Rizescu C. I, Rizescu D. Smart Home Air Quality Control System Controlled with a PLC. Int J Mechatron Appl Mech 2022; 2022(12): 99-103.
[9] Nugraha S., Patawaran N., Wayangkau I. H., Suwarjono, and Nurcholis. Implementation of Internet of Things for Egg Incubation Control System. IOP Conference Series: Earth and Environmental Science 2024, 1341(1): 1-10.
[10] Boleli I. C, Morita V. S, Matos Jr J. B, Thimotheo M, Almeida V. R. Poultry Egg Incubation: Integrating and Optimizing Production Efficiency. Braz J Poult Sci 2016; 18(spe2): 1-16.
[11] French N. A. Modeling incubation temperature: the effects of incubator design, embryonic development, and egg size. Poult Sci 1997; 76(1): 124-133.
[12] Korsheva I. A, Trotsenko I. V, The influence of incubator design features on the incubation result. IOP Conference Series: Earth Environ Sci 2022; 954(1): 012039.
[13] Gregory S. Archer and A. Lee Cartwright. Incubating and Hatching Eggs. Texas A&M Agrlife Extension Service, Accessed: Nov 08, 2023.
[14] Brinsea's Incubation Handbook - Brinsea. Accessed: Nov. 08, 2023.
[15] Ioannides M. G, Design and implementation of PLC-based monitoring control system for induction motor. IEEE Trans Energy Convers 2004; 19(3): 469-476.
[16] Deng Y, Zhao D, Chen B, Gong M. Double-channel event-triggered adaptive tracking control of nonstrict-feedback nonlinear systems. J Franklin Inst 2022; 359(13): 7219-7232.
[17] Tang K. S, Man K. F, Chen G, Kwong S. An optimal fuzzy PID controller. IEEE Trans Ind Electron 2001; 48(4): 757-765.
[18] Torun H, Uçal Sarı İ, Kahraman C. Multicriteria Evaluation of Environmentally Conscious Manufacturers Under Fuzzy Environment. J Mult-Valued Log Soft Comput 2012; 18: 457-477.

Turkish Journal of Science & Technology
19(2), 351-362, 2024

Research Paper
https://doi.org/10.55525/tjst.1438741

A Practical Approach for Estimating Drag Increase due to Volume Increase in the Center Body of a High-Speed UAV

Ugur Ozdemir[1*]
[1] Department of Flight Training, Faculty of Aeronautics And Astronautics, Eskisehir Technical Universtiy, Eskisehir
[*] ugurozdemir@eskisehir.edu.tr

(Geliş/Received: 17/02/2024; Kabul/Accepted: 03/09/2024)

Abstract: High-speed unmanned aerial vehicles are used for many purposes in aviation. High-speed aircraft do not only fly at supersonic speed, but their subsonic flight performance is also important. Aircraft design is an iterative process in which many disciplines work together. The design process is updated by the negotiation of different disciplines. There may be a demand for a body volume increase in the interior design process. The increase in volume can be achieved by the elongation or expansion of the body. A volume increase in the center body causes an increase in drag. The aim of this study is to predict the effect of the elongation or expansion of the center body on drag in a practical way. It is investigated using a structure proposed with MATLAB and DATCOM. The results in both subsonic and supersonic regimes are formalized separately and compared. It is shown that in case of providing the same volume increase in both subsonic and supersonic regimes, the elongation of the aircraft center body causes less drag compared to widening.

Keywords: Drag estimation, Digital DATCOM, high-speed UAV.

Yüksek Hızlı İHA'nın Gövde Hacim Artışı Nedeniyle Sürükleme Kuvvetinin Artışının Tahmininde Pratik Bir Yaklaşım

Öz: Yüksek hızlı insansız hava araçları havacılıkta birçok amaç için kullanılmaktadır. Hızlı uçaklar sadece süpersonik hızda uçmazlar, aynı zamanda süpersonik altı uçuş performansı da önemlidir. Uçak tasarımı, birçok disiplinin birlikte çalıştığı iteratif bir süreçtir. Tasarım süreci, farklı disiplinlerin müzakeresiyle güncellenir. İç tasarım sürecinde gövde hacminde bir artış talebi olabilir. Hacim artışı, gövdenin uzatılması veya genişletilmesiyle elde edilebilir. Merkezi gövde hacmindeki bir artış, sürüklemede kuvvetinde bir artışa neden olur. Bu çalışmanın amacı, merkezi gövdenin uzatılması veya genişletilmesinin sürükleme kuvveti üzerindeki etkisini pratik bir şekilde öngörmektir. MATLAB ve DATCOM yazılımları kullanılarak oluşturulan bir yapı ile bu durum incelenmiştir. Süpersonik ve süpersonik altı rejimlerde elde edilen sonuçlar ayrı ayrı formalize edilmiş ve karşılaştırılmıştır. Aynı hacim artışının süpersonik ve süpersonik altı rejimlerde sağlanması durumunda, uçağın merkezi gövdesinin uzatılmasının genişlemeye kıyasla daha az sürükleme kuvvetine neden olduğu gösterilmiştir.

Anahtar Kelimeler: Sürükleme kuvveti kestirimi, Digital DATCOM, yüksek hızlı İHA.

1. Introduction

Currently, the principal ways to obtain aerodynamic parameters are a wind tunnel test, Computational Fluid Dynamics (CFD) analysis, and semi-empirical methods [1]. Wind tunnels are assuring and classical ways to determine the derivatives. However, they are time-consuming and costly processes. Therefore, they are not recommended for the initial phase [1-3]. CFD software can model aircraft with a more complex structure. However, the software parameters are intricate, and its computer processor demands are immense [1,4]. Different aerodynamic flow models can be applied to obtain flow field properties. The Navier–Stokes equations are the main flow models representing viscous, rotational, and compressible flows [5,6]. Different approaches can be listed as follows: DATCOM, XFLR, TORNADO, AVL, PANAIR, ANSYS, etc. Each software has its restrictions limiting its application areas. The results obtained by TORNADO are precise only for slight angles of attack. It cannot cope with high Mach number conditions properly [7]. Athena Vortex Lattice (AVL) software is suitable for thin airfoils. Moreover, it is not convenient for small angles of attack and sideslip. ANSYS includes two modules, FLUENT and CFX, and it is a successful way to reveal stability and control characteristics. On the other hand, it includes a complex mesh generation process and lasts for many hours [5]. Alternatively, the commonly used technique in the early phase of aerodynamic estimations is semi-empirical methods [1]. These methods use datasheets, linear aerodynamic theory, and empirical equations to obtain aerodynamic parameters. DATCOM [8,9], also known as Missile DATCOM, is a widely used one. It was created by the US Air Force Research Laboratory and is now in the public domain. In academia, it has found a place as one of the trustworthy instruments to determine the stability and control derivatives of an aircraft [5]. It has been consistently modified with new test

[*] Corresponding author: ugurozdemir@eskisehir.edu.tr ORCID Number of author: [1] 0000-0001-7969-7717

data and novel computational analysis options [10-12]. DATCOM is extensively employed for aircraft planes, airships, projectiles, missiles, etc. The software combines the wind tunnel test data with durable flexibility and high accuracy [12]. Although this kind of methods cannot entirely replace wind tunnel tests and CFD analysis, they can lower time costs enormously [1]. Aerodynamic calculations on individual wings, aircraft body and wing-body [13-17], and deformable wing or a swept-wing aircraft [18-22] are executed using DATCOM. A new approach for aerodynamic shape optimization is used in Ref. [23], where CFD and DATCOM are used together. In this way, the researchers manage to decrease the necessary CFD calls by over 62.5%.

An empirical method to estimate the hydrodynamic derivatives of streamlined undersea vehicles is used in Ref. [24]. They show that DATCOM outputs are compatible with the results from other sources. The state-space model extraction of a high wing design UAV is proposed in Ref. [25] using DATCOM for a fairly accurate plant model.

The longitudinal dynamic system modeling of a fixed-wing UAV is performed using both flight test data and DATCOM calculations in Ref. [26], which demonstrates that both approaches provide a similar result. DATCOM is used in several studies and validated with flight test data [26-27]. Unguided rolling projectiles at varying Mach numbers are studied in Ref. [28] using DATCOM. Digital DATCOM is also used to obtain the aerodynamic characteristics of UAV for the development of a pitch control subsystem for a fixed-wing UAV in Ref. [29]. Moreover, it is used to analyze the aerodynamic performance during the folding process of wing-tip [30].

Aircraft design is an iterative process in which many disciplines work together [33]. The design process is updated by the negotiation of different disciplines. There may be a demand for a body volume increase in the interior design process. The increase in volume can be achieved by the elongation or expansion of the body.
In addition, this volume increase should be in the center body, which is convenient to equip the system and place useful loads. A volume increase in the center body will cause an increase in drag. This directly changes the required thrust-available thrust graph and may cause the need for a new engine.

The effect of the elongation and expansion of the aircraft center body on drag in both subsonic and supersonic regimes can be addressed by methods such as the flight test and CFD mentioned above. However, these methods are time-consuming and not economical. Methods that will produce fast and reliable results are required, especially in projects with time constraints. The purpose of this study is to provide a structure to meet the aforesaid need.
DATCOM software, which is especially validated for classical aircraft configurations, was used in this study.
Investigating the reliability of DATCOM software is beyond the scope of this article, as it has been researched in many studies before. This article is built on the knowledge in the literature that DATCOM software is reliable for classical geometries. The input files required by DATCOM software for each geometry change were automatically created with the code developed using MATLAB software. At the same time, DATCOM output files were drawn by the program developed using MATLAB software. First, the creation of a reference UAV geometry in DATCOM was given. Then, three different volume increases were considered as both the elongation of the center body and the widening of the center body. Each geometry change was analyzed with the proposed MATLAB-DATCOM structure. As a result, an approach was put forward to predict the drag increase.

2. Materials and Methods

Wind tunnel and flight testing, CFD, and semi-empirical methods can be used to calculate aerodynamic parameters. Digital DATCOM was used in this paper. It was first introduced in 1960 and improved in 1978. It is an approach combining theoretical and experimental procedures and provides reliable results for standard aircraft configurations. DATCOM has an algorithm to obtain aerodynamic parameters, i.e., stability and control derivatives, either by the extrapolation or interpolation of data from the US Air Force for years [5,43]. The structure of DATCOM is as follows: 1) Defining an input file: aircraft shapes and the flight environment, 2) Executing the main function to trigger DATCOM, 3) The software creates an output file by detecting the wind tunnel test data and a theoretical approach suitable for input parameters. It is often used in the first phase of aircraft development to evaluate different shape schemes [1].

In this study, the unmanned aerial vehicle geometry in Fig. 1 was used to show the effect of the elongation or expansion of the center body on drag.

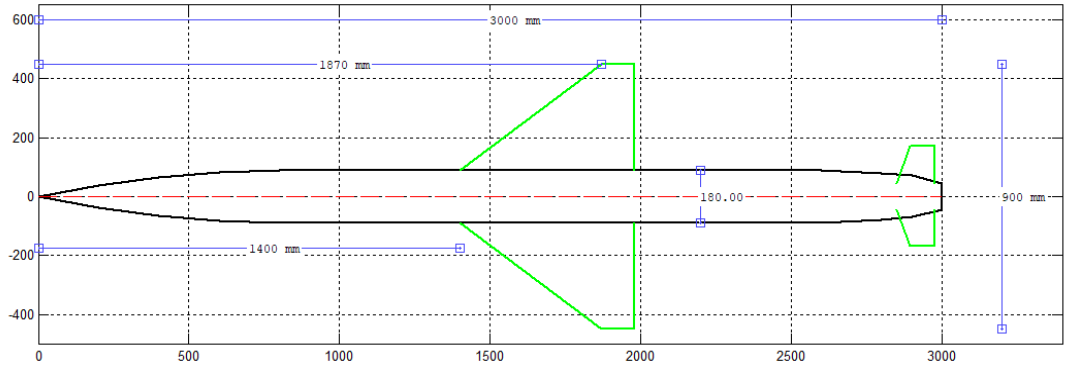

Figure 1. Top view of the UAV model.

The geometric parameters, along with flight conditions, are the basic and most important requirements for modeling an aircraft in any software.

Table 1 lists the flight conditions to be analyzed.

Table 1. Flight Conditions.

	Subsonic	**Supersonic**
Mach Number	M = 0.6	M= 1.4
Altitude	h= 3000 m	h= 3000 m
Angle of attack	$-6° < \alpha < 20°$	$-6° < \alpha < 20°$

While some geometric properties of the UAV are given in Table 2, the definitions of these sizes are given in Table 3.

Table 2. Flight Conditions.

SREF	234000 mm^2
CBARR	255 mm
BLREF	900 mm
XCG	1748 mm
ZCG	0 mm
BNOSE	BNOSE = 2 ogive nose
BLN	800 mm
BLA	1800 mm

Table 3. Definition of the geometric abbreviations used in the analysis.

Variable Name	**Definition**
SREF	Planform area used as a reference area
CBARR	Value of the theoretical wing mean aerodynamic chord
BLREF	Value of the wingspan
XCG	Longitudinal distance of CG from the nose
ZCG	Vertical location of CG relative to the reference plane
BNOSE	BNOSE=1 conical nose; BNOSE = 2 ogive nose
BLN	Length of the body nose
BLA	Length of the cylindrical afterbody segment

In the DATCOM program, the body geometry is created by dividing it into segments. Accordingly, the airframe is divided into segments as in Fig. 2 using the values in Table 4.

Table 4. Dimensions of the body segments.

Station	1	2	3	4	5	6	7	8	9	10
X (mm)	0	200	400	600	800	1500	2600	2800	2900	3000
S (mm^2)	0	4257	13454	21021	25447	25447	25447	20106	15394	6362
P (mm)	0	231.28	411.17	513.96	565.48	565.48	565.48	502.65	439.82	282.74
R (mm)	0	36.81	65.44	81.80	90	90	90	80	70	45

where X: Longitudinal distance measured from the arbitrary location; S: Cross-sectional area; P: Periphery at station x(i); R: Planform half width

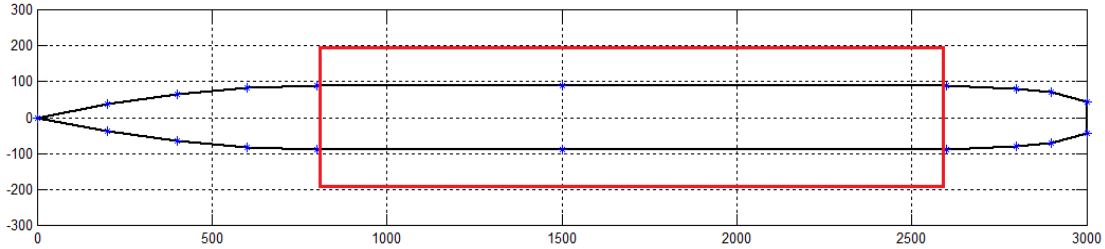

Figure 2. Segmentations of the body.

The cross-sectional area between segments 5 and 7 shown in the red box in Fig. 2 is equal. The distance between these two segments, which we call the center body, is 1800 mm, and values of the radius, circumference, and area remain constant between these two segments (Fig. 3). The center body is the most useful part of the aircraft fuselage as an interior layout. In this work, the elongation or expansion of the body will be performed in this region to create an additional volume. However, when analyzing the center body expansion, it will be taken into account that the front and rear parts will expand in proportion to this part.

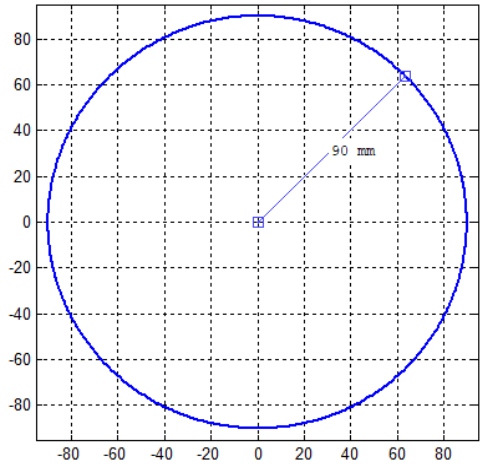

Figure 3. Cross-section on the constant body section.

The volume increase to be provided by the elongation or expansion of the center body (shown in Fig. 2 by the red rectangular) is calculated in Table 5. Accordingly, the 270-mm elongation of the body and the 6.51-mm increase in the radius of the body provide the same volume increase (4580 cm^3). Hence, a 270-mm elongation corresponds to an extension of 6.51 mm in the radius. The same calculations were made in 15%, 25%, and 35%

increments of the center body length (the part with a fixed cross-sectional area of 1800 mm in length) and given in Table 5.

Table 5. Volume increase caused by the center body elongation or expansion.

Percent increase in the body (extension)	Equivalent increase in the radius to sustain the same volume	Volume increase
15% (270 mm)	7.24% (6.51 mm)	6871 cm^3
25% (450 mm)	11.80% (10.62 mm)	11451 cm^3
35% (630 mm)	16.16% (14.57 mm)	16032 cm^3

To investigate whether the center body elongation or enlargement providing the same volume increase will be better, the conditions given in Table 4 should be analyzed and compared separately. This investigation will be made for both subsonic and supersonic flight regimes.

Figure 4. Digital DATCOM analysis process

First, the input file containing the flight geometry and flight conditions given in Tables 1 and 3 is prepared. After the Digital DATCOM program is run, the output file is created.

While the subsonic and supersonic analyses of a single geometry are performed as shown in Fig. 4, a different input file should be prepared for each of the different geometry changes, as in our problem.

As seen in Fig. 5, the MATLAB program was used to create the Input File as an iterative for each geometry change, to call the Digital DATCOM and to create the graphics from the output files.

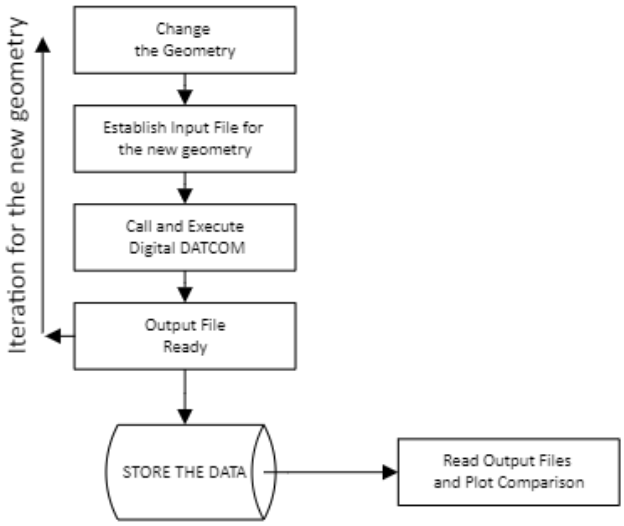

Figure 5. Iterative Digital DATCOM analysis process.

3. Results and Discussion

The following graphs were drawn using the data in the output files obtained for each geometry. The drag coefficient versus attack angle of the aircraft body given in Fig. 1 is drawn in Fig. 6. In Fig. 6, the change in the drag coefficient at both 0.6 Mach and 1.4 Mach according to the angle of attack is given. As expected, the drag coefficient is higher at supersonic speed than subsonic speed. Furthermore, while the variation in the drag coefficient with respect to the angle of attack (C_{D_α}) is more linear at subsonic speeds (C_{D_α}) (almost constant), it continues to increase in the supersonic regime. It is larger, especially at high angles of attack. Therefore, in supersonic drag calculations, C_{D_α} should be taken depending on the angle of attack.

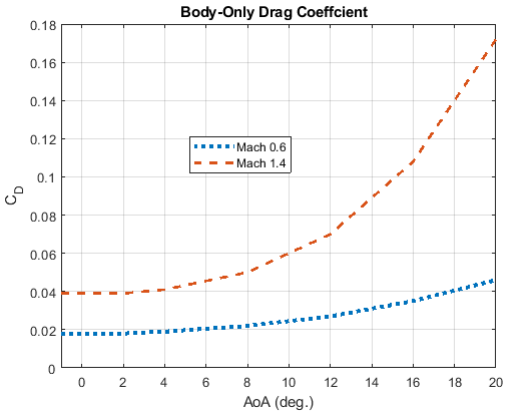

Figure 6. Body-only drag coefficient versus the angle of attack in the subsonic and supersonic regimes.

First, the effects of the elongation of the body with a constant cross-sectional area are shown in Fig. 7.

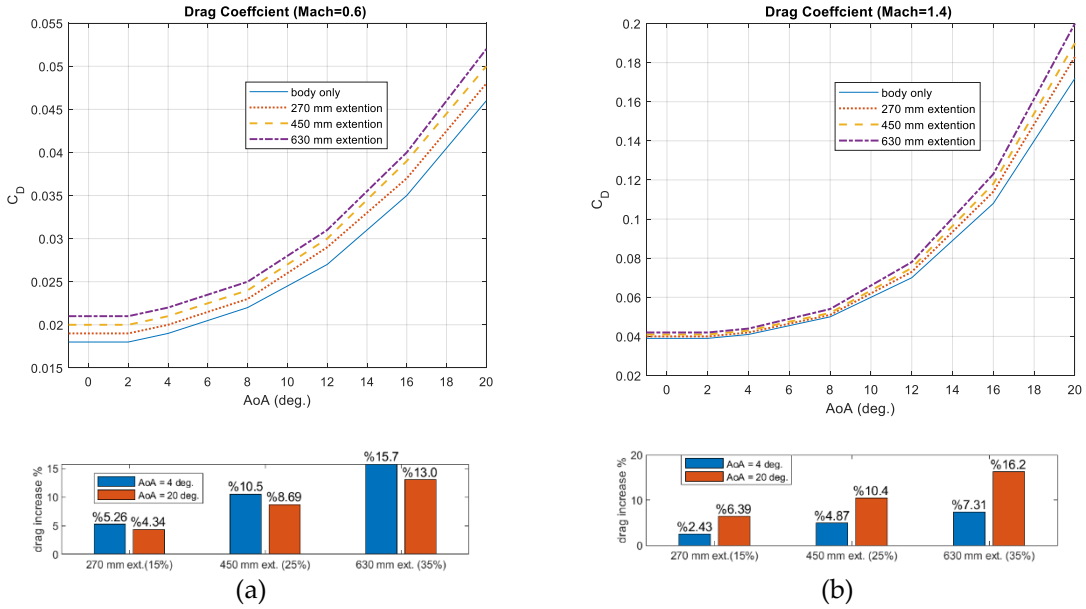

Figure 7. Body extension effect on the body-only drag coefficient in: (**a**) Subsonic regime (Mach=0.6), (**b**) Supersonic regime (Mach=1.4)

The effects of 270 mm (15%), 450 mm (25%), and 630 mm (35%) elongations of the center body are shown on the same graph, respectively. These elongations resulted in an increase in drag of 5.26%, 10.5%, and 15.5%, respectively, at a low angle of attack in the subsonic regime. Using these values, the drag effect of the percent elongation in the center body at a low angle of attack in the subsonic regime can be expressed as a 3rd-order equation as in Eq. 1:

$$\%\delta D = -0.0002\ \ \%\delta L^3 + 0.0162\ \%\delta L^2 + 0.1595\ \ \%\delta \mathrm{L} \tag{1}$$

where
$\%\delta D$: percent drag increase, i.e., the result value of 5 means a 5% increase
$\%\delta L$: percent elongation of the center body, between 0 and 35

They also resulted in an increase in drag of 4.34%, 8.69%, and 13%, respectively, at a high angle of attack in the subsonic regime. Using these values, the drag effect of the percent elongation in the center body at a high angle of attack in the subsonic regime can be expressed as a 3rd-order equation as in Eq. 2:

$$\%\delta D = -0.0002\ \ \%\delta L^3 + 0.0127\ \ \%\delta L^2 + 0.1374\ \%\delta \mathrm{L} \tag{2}$$

These elongations resulted in an increase in drag of 2.43%, 4.87%, and 7.31%, respectively, at a low angle of attack in the supersonic regime. Using these values, the drag effect of the percent elongation in the center body at a low angle of attack in the supersonic regime can be expressed as a 3rd-order equation as in Eq. 3:

$$\%\delta D = -0.0001\ \ \%\delta L^3 + 0.0070\ \%\delta L^2 + 0.0777\ \ \%\delta \mathrm{L} \tag{3}$$

We can conclude an increase in drag of 6.39%, 10.40%, and 16.20%, respectively, at a high angle of attack in the supersonic regime. Using these values, the drag effect of the percent elongation in the center body at a high angle of attack in the supersonic regime can be expressed as a 3rd-order equation as in Eq. 4:

$$\%\delta D = -0.0003\ \ \%\delta L^3 - 0.0124\ \%\delta L^2 + 0.5476\ \%\delta \mathrm{L} \tag{4}$$

The effect of body elongation on drag is similar in the subsonic regime at both low and high angles of attack (i.e., percent drag increases at low and high angles of attack are close to each other). On the other hand, the percent drag increase values at low and high angles of attack in the supersonic regime are different.

In the supersonic regime, the percent drag increase at low angles of attack is almost half the increase at high angles of attack. For instance, while the 630-mm elongation of the center body at Mach 1.4 (a 35% increase in the body length) causes a 7.31% increase in drag at a low angle of attack, it causes a 16.2% increase at a high angle of attack (AoA = 20 deg.).

On the other hand, the percentage drag increase in the subsonic regime is 15.7% and 13.0% at low and high angles of attack, respectively. In the subsonic regime, in contrast to the supersonic regime, the percentage drag increase at high angles of attack is lower than the increase at low angles of attack. In case of a 630-mm (35%) body extension, the maximum body drag coefficient (C_D= 0.2) is reached in the supersonic regime at an angle of attack of 20 deg. In case of body elongation, the most significant percent drag increase occurs at a high angle of attack in the supersonic regime. The effect of increasing the radius of the center body to drag is shown in Fig. 8. The effect of increasing the body radius of 6.51 mm (7.24%), 10.62 mm (11.80%), and 14.57 mm (16.16%) is shown on the same graph, respectively.

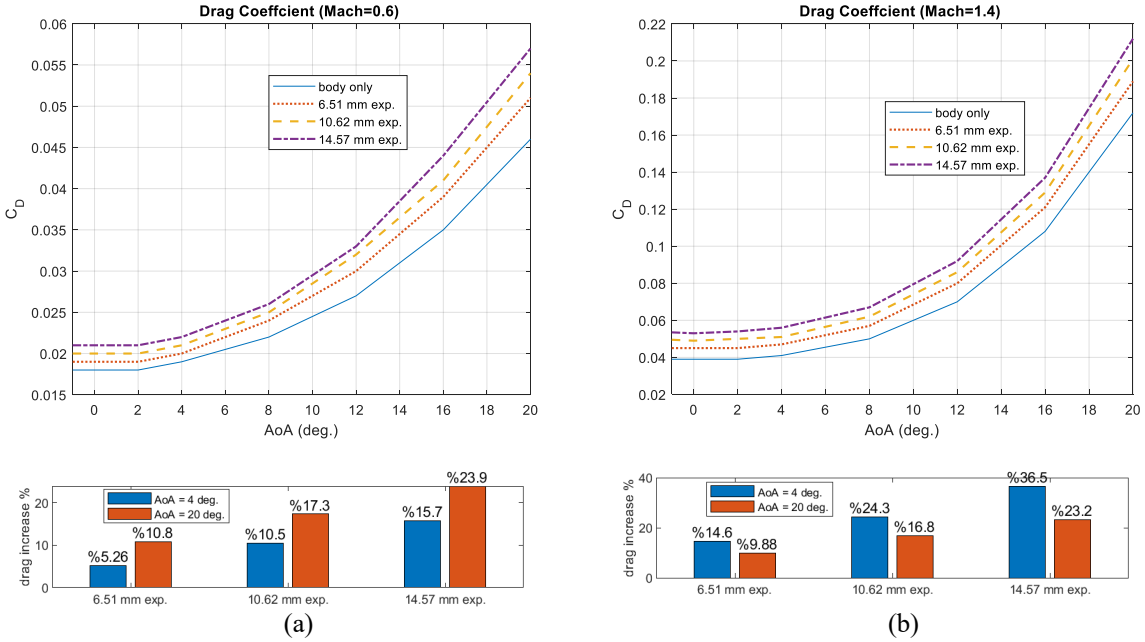

Figure 8. Body expansion effect on the body-only drag coefficient in: (**a**) Subsonic regime (Mach=0.6), (**b**) Supersonic regime (Mach=1.4)

These expansions resulted in an increase in drag of 5.26%, 10.5%, and 15.7%, respectively, at a low angle of attack in the subsonic regime. Using these values, the drag effect of the percent increase in the radius of the center body at a low angle of attack in the subsonic regime can be expressed as a 3rd-order equation as in Eq. 5:

$$\%\delta D = -0.0019\ \ \%\delta r^3 + 0.0723\ \%\delta r^2 + 0.3037\ \%\delta \mathrm{r} \tag{5}$$

where
%δD: percent drag increase, i.e., the result value of 5 means a 5% increase
%δr: percent elongation of the center body, between 7.24 and 16.16

These expansions in the center body also resulted in an increase in drag of 10.80%, 17.30%, and 23.90%, respectively, at a high angle of attack in the subsonic regime. Using these values, the drag effect of the percent increase in the radius of the center body at a high angle of attack in the subsonic regime can be expressed as a 3rd-order equation as in Eq. 6:

$$\%\delta D = 0.0010\ \ \%\delta r^3 - 0.0239\ \%\delta r^2 + 1.6144\ \%\delta \mathrm{r} \tag{6}$$

This resulted in drag increases of 14.60%, 24.30%, and 36.50%, respectively, at low angles of attack in the supersonic regime. Using these values, the drag effect of the percent increase of the body radius at a low angle of attack in the supersonic regime can be expressed as a 3rd-order equation (Eq. 7):

$$\%\delta D = 0.0041\ \ \%\delta r^3 - 0.0682\ \%\delta r^2 + 2.2968\%\delta \mathrm{r} \tag{7}$$

This resulted in drag increases of 9.88%, 16.80%, and 23.20%, respectively, at high angles of attack in the supersonic regime. Using these values, the drag effect of the percent increase of the body radius at a high angle of attack in the supersonic regime can be expressed as a 3rd-order equation (Eq. 8):

$$\%\delta D = -0.0011\ \ \%\delta r^3 + 0.0348\ \%\delta r^2 + 1.1729\ \%\delta \mathrm{r} \tag{8}$$

The effect of body expansion on drag at low and high angles of attack differs in both subsonic and supersonic regimes. In case of body expansion, the most significant percent drag increase occurs at a low angle of attack in the supersonic regime (Fig. 8b). When the body radius was widened by 14.51 mm, the maximum body drag coefficient reached $C_D = 0.21$ at a 20-deg angle of attack in the supersonic regime. Equations 1-8 can be used to predict the drag effect of the elongation of the fuselage geometry or the increase in the radius of its cross-section, especially for aircraft with a similar geometry. To increase the volume of the aircraft fuselage by 6871 cm^3, an extension of 6.51 mm in the fuselage length or 6.51 mm in the radius of the fuselage is required. The drag effect of these geometry changes, which will provide the same volume increase, is shown in Fig. 9.

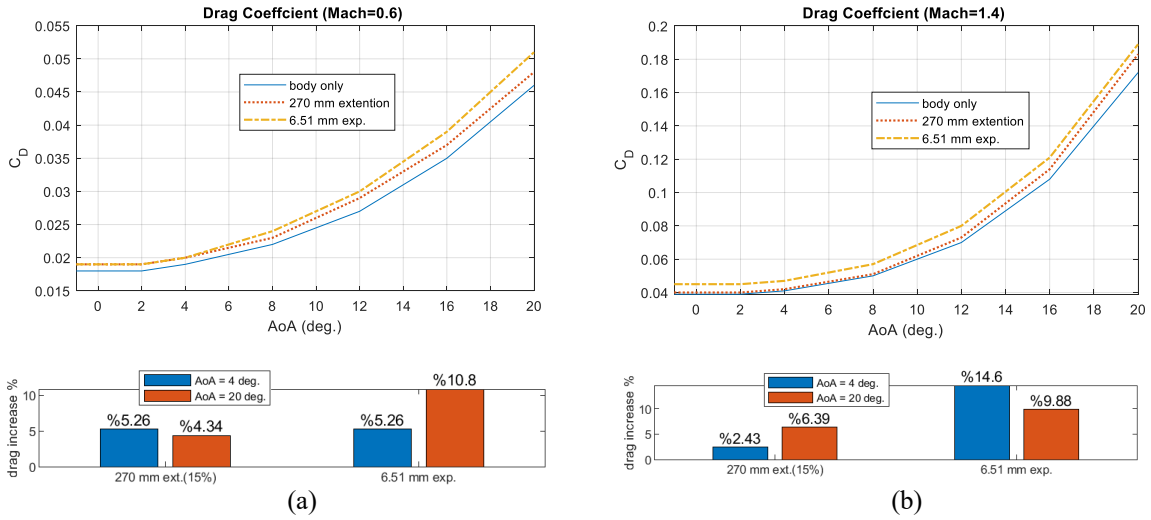

Figure 9. The influence of the 270-mm extension of the body length or the 6.51-mm expansion of the cross-section radius on the body-only drag coefficient in: (**a**) Subsonic regime (Mach=0.6), (**b**) Supersonic regime (Mach=1.4)

In the subsonic regime, while the 270-mm (15%) elongation of the center body at low angles of attack causes a 5.26% increase in body drag, the 6.51-mm widening of the radius of the center body cross-section causes an increase of 5.26% in body drag. At a high angle of attack, while body elongation causes a 4.34% drag increase, body expansion causes a 10.80% drag increase. Therefore, in the subsonic regime, while body expansion and elongation at a low angle of attack cause an equal drag increase, elongation at a high angle of attack provides a significant advantage over widening. In the supersonic regime, while a 270-mm (15%) elongation in the fuselage at low angles of attack causes a 2.43% increase in body drag, the 6.51-mm widening of the radius of the center body cross-section causes a 14.60% increase in body drag. At a high angle of attack, while body elongation causes a 6.39% drag increase, center body widening causes a 9.88% body drag increase. As seen from Fig. 9, body elongation is more advantageous than body enlargement at both low and high angles of attack in both flight regimes. This advantage becomes dominant at high angles of attack, especially in the subsonic regime, and at low angles of attack in the supersonic regime. To increase the volume of the aircraft center body by 11451 cm^3, an extension of the center body length by 450 mm or an increase in its radius by 10.62 mm is required. The effect of these geometry changes, which will provide the same volume increase, on body drag is calculated separately and shown in Fig. 10.

To increase the volume of the aircraft center body by 16032 cm^3, an extension of the center body length by 630 mm or an increase in its radius by 14.57 mm is required. The effect of these geometry changes, which will provide the same volume increase, on body drag is calculated separately and shown in Fig. 11.

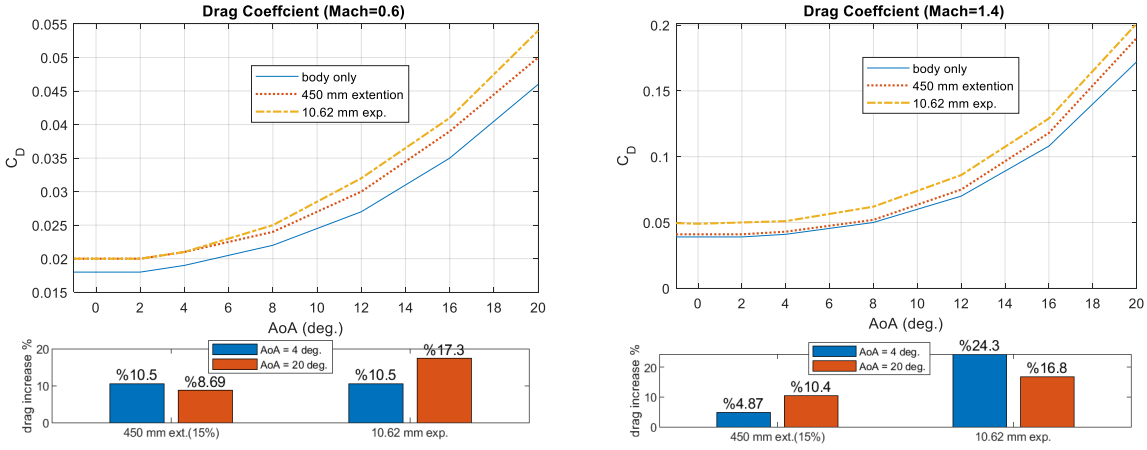

Figure 10. The influence of the 450-mm extension of the body length or the 10.62-mm expansion of the cross-section radius on the body-only drag coefficient in: (**a**) Subsonic regime (Mach=0.6), (**b**) Supersonic regime (Mach=1.4)

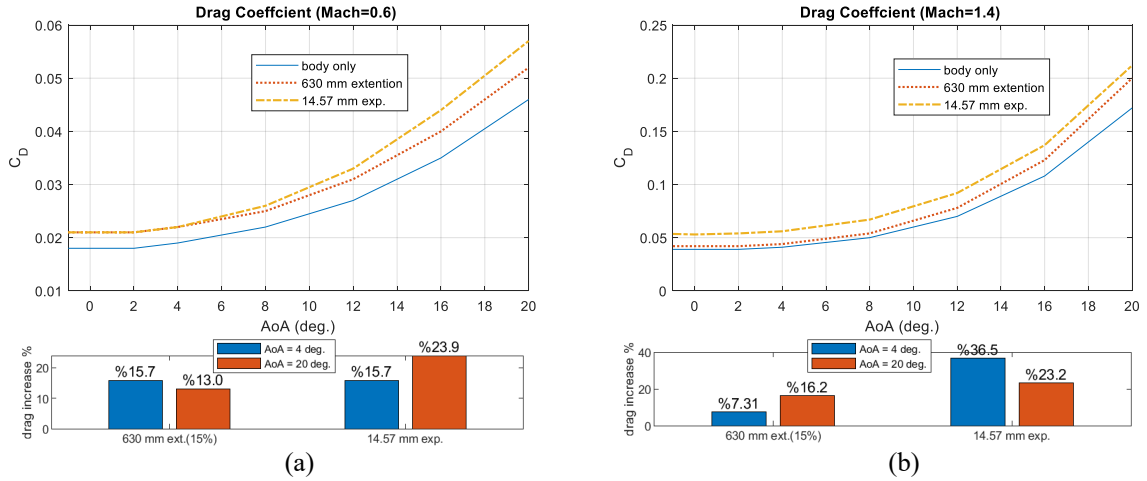

Figure 11. The influence of the 630-mm extension of the body length or the 14.57-mm expansion of the cross-section radius on the body-only drag coefficient in: (**a**) Subsonic regime (Mach=0.6), (**b**) Supersonic regime (Mach=1.4)

The results in Figs. 10 and 11 are in parallel with Fig. 9. In both flight regimes, center body elongation at low and high angles of attack outperforms its widening. This advantage becomes dominant at high angles of attack, especially in the subsonic regime, and at low angles of attack in the supersonic regime.

4. Conclusions

In this study, a practical and low-cost approach is developed to predict the drag cost of volume increase in various ways during the aircraft design process using MATLAB and DATCOM software. The lengthening of the center body and the increase in its radius are considered the same volume increases. Owing to this approach, body drag coefficient values are calculated and plotted in seconds for both subsonic and supersonic regimes for 3 different volume increases with 6 different geometry changes. According to the results, the effect of the center body percent elongation and the percentage increase of its cross-section radius on the body drag coefficient is expressed as second-order equations for both low and high angles of attack. These equations can be used to give

quick ideas for aircraft with similar geometries and missions, especially at the early design stages. The 35% elongation of the center body results in a 16.2% increase in the maximum drag coefficient, while the 16.16 % increase in the center body section radius results in a 36.5% increase in the maximum drag coefficient. This would roughly mean the need for an engine producing 16.2% and 36.5% more thrust, respectively, than intended to be used in the design. It can be inferred from the results that when an increase in the volume is required, increasing the center body length causes less body drag increase according to increasing its section radius. While it is already expected that elongation causes more drag than expansion, the magnitude of the drag difference is also important. If the drag disadvantage caused by widening will not cause a change in engine selection in the aircraft design, body widening may also be preferred due to the advantage it provides in terms of placement in the body. Therefore, it requires such a comparative analysis approach. The systematic approach made on the aircraft fuselage in this study can also be used to analyze the effects of changes on the aircraft's surfaces such as wings and tail. Especially the performance effects of aircraft in the morphing aircraft category, which can change their geometry during flight, can be analyzed using the same approach.

Code Availability

The MATLAB code used in this study is available at:
https://drive.google.com/drive/folders/1TxFMq3h2x67A3-FDsiyNfVv6s06zx-3b?usp=sharing

References

[1] Wu H, Gao M, Song X, Xu J, Wang Y, Zhao J. Accuracy Analysis of Aerodynamic Calculation of 2-Dimensional Trajectory Correction Projectile Based on DATCOM. Curr Eng Lett Rev 2019; 27 (4).

[2] Sun D, Wu H, Zhu R, Hung LC. Development of Micro Air Vehicle Based on Aerodynamic Modeling Analysis in Tunnel Tests. In: Proceedings of the 2005 IEEE International Conference on Robotics and Automation; Barcelona, Spain, 2005, pp. 2235-2240.

[3] Haque AU, Asrar W, Omar AA, Sulaiman E, Ali MJS. Preliminary Aerodynamic and Static Stability Analysis for Hybrid Buoyant Aerial Vehicles at Low Speeds Using Digital DATCOM. Can Aeronaut Space J 2015; 61 (3).

[4] Sahu J. Time-Accurate Aerodynamic Modeling of Synthetic Jets for Projectile Control. In: 2004 Users Group Conference (DOD UGC'04), Williamsburg, VA, USA, 2004. pp. 144–150.

[5] Ahmad M, Hussain ZL, Shah SIA, Shams TA. Estimation of Stability Parameters for Wide Body Aircraft Using Computational Techniques. Appl Sci-Basel 2021; 11 (5), 2087.

[6] Anderson, J. D. Computational Fluid Dynamics. McGraw-Hill Professional: New York, NY, 1995.

[7] Melin T. User's Guide and Reference Manual for Tornado. Royal Inst of Technology KTH: Stockholm, Sweden, 2000.

[8] Sooy TJ, Schmidt RZ. Aerodynamic Predictions, Comparisons, and Validations Using Missile DATCOM (97) and Aeroprediction 98 (AP98). J Spacecr Rockets 2005; 42 (2), 257–265.

[9] Zhang W, Wang Y, Liu Y. Aerodynamic Study of Theater Ballistic Missile Target, Aerosp Sci Technol 2013; 24 (1), 221–225.

[10] Grasmeyer J. Stability and Control Derivative Estimation and Engine-Out Analysis, Virginia Polytechnic Institute and State University, Blacksburg, VA, USA, 1998.

[11] Anton N, Botez R, Popescu D. New Methodologies for Aircraft Stability Derivatives Determination from its Geometrical Data. In: AIAA Atmospheric Flight Mechanics Conference; American Institute of Aeronautics and Astronautics: Reston, Virginia, 2009.

[12] Maurice AF. Aerodynamic Performance Predictions of a SA-2 Missile Using Missile DATCOM. M.Sc. Thesis, University of Florida, 2009.

[13] Blake WB. Missile DATCOM: 1997 Status and Fluent Plans. American Institute of Aeronautics and Astronautics 1997, AIAA-97-2280, 538–548.

[14] Nguyen NV, Kim WS, Lee JW, Byun YH. Validations, Prediction, and Aerodynamic Optimization of Short and Medium Range Missile Configurations. In: KSAS-JSASS Joint International Symposium 2008, 146–152.

[15] Shistik E, Sigal A. The Interaction between Canards and Thick Bodies: Implementation in the Missile Datcom Code. In 20th AIAA Applied Aerodynamics Conference; American Institute of Aeronautics and Astronautics: Reston, Virginia, 2012.

[16] Nicolosi F, Vecchia PD, Ciliberti D. An Investigation on Vertical Tailplane Contribution to Aircraft Sideforce. Aerosp Sci Technol 2013; 28 (1), 401–416.

[17] Bakar MRA, Basuno B, Hasan S. Aerodynamics Analysis on Unsymmetrical Fuselage Models. Applied Mechanics and Materials 2013; 315, 273–277.

[18] Li T, Yan P, Jiang RM, Zhou J. Calculation and Analysis of High-Speed Missile's Aerodynamic Characteristic with Asymmetric Morphing Wings. Journal of Ordnance Equipment Engineering 2017; 2017, 51–56.

[19] Zhang GP, Duan ZY, Liao ZZ, Zhang Y. Multi-Body Dynamics of Tactical Missile with Morphing Wing. Journal of Projectile, Rockets, Missile and Guidance 2011; 31, 149–151, 158.
[20] Wei DH, Chen WC, Li NY, Xu P. Morphing Theory and Control Approaches of a Morphing Missile. Tactical Missile Technology 2016; 2, 10–15.
[21] Zheng MM. Modeling and Flight Control of the Variable-Sweep Aircraft in the Whole Morphing. Nanjing University of Aeronautics and Astronautics the Graduate School, 2015.
[22] Guo SJ. Research on Cooperative Control of the Morphing Aircraft. Nanjing University of Aeronautics and Astronautics the Graduate School College of Automation Engineering, 2012.
[23] Yan X, Zhu J, Kuang M, Wang X. Aerodynamic Shape Optimization Using a Novel Optimizer Based on Machine Learning Techniques. Aerosp Sci Technol 2019; 86, 826–835.
[24] Nahon M. Determination of Undersea Vehicle Hydrodynamic Derivatives Using the USAF Datcom. In: Proceedings of OCEANS '93, Victoria, BC, Canada, 1993.
[25] Rauf A, Zafar MA, Ashraf Z, Akhtar H. Aerodynamic Modeling and State-Space Model Extraction of a UAV Using DATCOM and Simulink. In: 2011 3rd International Conference on Computer Research and Development, Shanghai, China, 2011.
[26] Triputra FR, Trilaksono BR, Sasongko RA, Dahsyat M. Longitudinal Dynamic System Modeling of a Fixed-Wing UAV towards Autonomous Flight Control System Development: A Case Study of BPPT Wulung UAV Platform. In 2012 International Conference on System Engineering and Technology (ICSET), Bandung, Indonesia, 2012, pp. 1-6.
[27] Jamil MA, Ahsan M, Ahsan MJ, Choudhry MA. Time Domain System Identification of Longitudinal Dynamics of a UAV: A Grey Box Approach. In: 2015 International Conference on Emerging Technologies (ICET), Peshawar, Pakistan, 2015, pp. 1-6.
[28] Bashir M, Khan SA, Udayagiri L, Noor A. Dynamic Stability of Unguided Projectile with 6-DOF Trajectory Modeling. In: 2017 2nd International Conference for Convergence in Technology (I2CT), Mumbai, India, 2017, pp. 1002-1009.
[29] Jeevan HL, Narahari HK, Sriram AT. Development of Pitch Control Subsystem of Autopilot for a Fixed Wing Unmanned Aerial Vehicle. In: 2018 2nd International Conference on Inventive Systems and Control (ICISC), Coimbatore, India, 2018, pp. 1233-1238.
[30] Yang J, Wen L, Jiang B, Wang Z. Dynamic Modeling and Flight Simulation of a Folding Wing-Tip UAV. In: 2020 Chinese Control And Decision Conference (CCDC), Hefei, China, 2020, pp. 1814-1819.
[31] Turevskiy A, Gage S, Buhr C. Model-Based Design of a New Light-Weight Aircraft. In: AIAA Modeling and Simulation Technologies Conference and Exhibit; American Institute of Aeronautics and Astronautics: Reston, Virginia, 2007.
[32] Anton N, Popescu D, Botez RM. Estimation of Stability Derivatives from Aircraft Geometrical Data for Use in Simulator Applications, Conference: American Romanian Academy ARAAt: Boston, MI, USA, 2007.
[33] Raymer DP. Aircraft Design: A Conceptual Approach; American Institute of Aeronautics & Astronautics: Reston, VA, 2012.

Turkish Journal of Science & Technology
19(2), 363-372, 2024

Research Paper
https://doi.org/10.55525/tjst.1446242

A Multifunctional Project Study for Elazig: Botanic Park, Pumped Irrigation Line, and Solar-Hydroelectric Power Plant

Ayca AYTAC[1*]
[1] Department of Civil Engineering, Dogus University, İstanbul, Turkey
[*1] aaytac@dogus.edu.tr

(Geliş/Received: 02/03/2024; Kabul/Accepted: 07/08/2024)

Abstract: Urban centers serve as more than just hubs of economic activity; they are also focal points of community life and social interaction. It is incumbent upon local authorities to elevate the standard of living within these urban environments by establishing communal spaces conducive to enhancing the well-being of residents. To this end, botanical gardens and recreational areas have been established in numerous developed cities worldwide. These amenities not only enrich the lives of inhabitants and local fauna but also constitute significant contributors to the municipal economy. Recognizing their pivotal role in urban economies, the imperative lies in implementing projects that optimize the utilization of available water resources. The prospect of establishing such a facility in the heart of Elazig holds promise. This study undertakes a preliminary assessment of the feasibility of establishing a botanical garden within the designated area, exploring avenues such as tapping into the Keban Dam reservoir, constructing a micro-hydroelectric power plant utilizing downstream water, and other potential initiatives.

Key words: Hydrology, micro-hydroelectric power plant, pumped transmission, recreation area.

Elazığ için Çok Fonksiyonlu Bir Proje Çalışması: Botanik Park, Pompa Sulama Hattı ve Güneş-Hidroelektrik Santrali

Öz: Kentsel merkezler, sadece ekonomik faaliyetlerin merkezleri olmakla kalmaz; aynı zamanda topluluk yaşamı ve sosyal etkileşimin odak noktalarıdır. Bu kentsel ortamlardaki yaşam standartlarını yükseltmek, yerel yönetimlerin sorumluluğundadır. Bu amaçla, birçok gelişmiş şehirde botanik bahçeleri ve rekreasyon alanları kurulmuştur. Bu tesisler, sadece yerel halkın ve faunanın yaşamını zenginleştirmekle kalmaz, aynı zamanda yerel ekonomiye de önemli katkılarda bulunurlar. Kent ekonomilerindeki bu önemli rolü tanıyarak, Elazığ'ın merkezinde böyle bir tesis kurma gerekliliği ortaya çıkmaktadır. Bu çalışma, belirlenen alan içinde bir botanik bahçesi kurulmasının fizibilitesinin ön değerlendirmesini yapmakta olup, Keban Barajı rezervuarından su kullanımı, aşağı akış sularını değerlendiren mikro-hidroelektrik santral inşası gibi çeşitli projeleri incelemektedir.

Anahtar kelimeler: Hidroloji, mikro-hidroelektrik santral, pompa iletimi, rekreasyon alanı.

1. Introduction

In cities, green areas are decreasing and disappearing due to overpopulation, developing industry, new roads and settlements. Therefore, it is extremely important to protect the green areas in the centers of settlements and to increase them if possible [1]. Despite the possibility of creating artificial water surfaces for recreational purposes in landlocked settlements, nearby reservoirs or rivers are also important resources that can be used for this purpose [2]. Recently, due to the increasing interest in recreation and sports activities in lakes and reservoirs and the opportunity to relax away from the stress of the city, especially in seaside cities, the arrangements to be made in these areas and their surroundings have started to be emphasized [3]. The first modern designed botanical park was built in Italy in 1545. Currently, there are around 2500 botanical gardens in the world [4]. These botanical gardens play a central role in the conservation and research of plant biodiversity [5]. This role is likely to become more important as the effects of global warming become more severe [6].

It is important to develop planning policies that produce solutions to the problems of society and for maximum benefit for recreation areas to be built in reservoirs and their surroundings in order to ensure the use of society's resources that cannot be used efficiently [7].

Botanical parks, which function as special recreational areas in cities, are open-air museums or plant collections where a wide variety of plant species are brought together and are a part of the outdoor system open to the public [8]. Botanical parks not only promote the importance of plants, habitats, and conservation awareness but also provide visitors with experiences that influence their movement, behavior, and social values [9].

Botanical parks are versatile recreational facilities with different qualified units such as walking paths, seating and viewing areas, water surfaces, organised plant collections, cafeterias and restaurants, zoos and playgrounds

[*] Corresponding author: aaytac@dogus.edu.tr. ORCID Number of authors: [1] 0000-0002-2108-6363

[10]. People live in an environment and the qualities of this environment affect their activities [11, 12]. It has been determined that environments intertwined with nature and designed landscapes in cities produce very positive effects on people [13, 14]. Botanical gardens are facilities with significant plant collections, and access to sufficient water is essential for healthy and well-maintained plants as well as daily organizational needs. Nevertheless, this also entails significant water consumption. The need for water, which is an indispensable source of life for humans and all other living things, is increasing day by day. Since this source of life is not unlimited and even decreasing, the available water should be used more efficiently to some studies.

Urban water management is recognized for its high energy intensity. Therefore, engineers are looking for ways to recover the energy contained in water networks and their treatment plants that collect water from drinking water, sewage, and recreational facilities [15-18]. This potential remains largely unexplored. Recently, the increasing need for energy worldwide and rising energy costs are compelling engineers to exploit this alternative energy source.

In this study, the construction possibilities of a botanical facility with benefits such as drinking water, recreation, and energy production for the city with the ponds to be built on the Calgan Stream flowing in the North-South direction from Nurali Village in the upper part of the Firat University campus area located in the city center of Elazig were investigated. Through this multi-purpose vision project, it was evaluated that benefits such as positive social contribution, energy and tourism income, and flood protection could be provided.

1.1. Environmental effects

It is known that green areas such as botanical parks contribute positively to climate and hydrological processes, reduce pollutants [19], and significantly reduce the heat island effect frequently encountered in urban areas. In addition to providing shelter for living things, they also have important effects on increasing biodiversity. Erosion control, dust stabilisation and noise pollution reduction are other important environmental benefits [20].

According to a study conducted by Xinian in Beijing, a natural green area of 20.000 ha absorbs 4 million tonnes of CO_2 and returns about 400 million tonnes of water vapour to the atmosphere annually [21]. This contributes to reducing the effects of global warming and climate change [19].

Despite the positive environmental impacts mentioned here, a detailed environmental impact assessment report should be prepared in order to minimise the negativities to be experienced during the construction process of the botanical parks. This detailed report, which should be prepared according to the characteristics of plants, insects and other living things living in the region where the park is planned to be built, will minimize the possible negativities during the construction process.

2. Materials and Methods

The project area is located in the city center of Elazig (Turkey). It consists of a valley with elevations ranging from 1.000 m to 1.500 m above sea level (see Figure 1). The park area of approximately 20 km^2 is divided into a core and a buffer zone, accounting for 66% and 34% of the area respectively. The primary ecosystem components within the park area comprise forests (34%), grass-covered landscapes (31%), and rocky terrain (35%). The project location is shown below.

2.1. Hydrology

Generally, continental climate conditions are valid in Elazig province. The rainfall area of the basin is completely characterized by the Eastern Anatolian climate. Summer months exhibit hot and arid conditions, while winters are marked by snowfall, and spring experiences increased precipitation. The average annual temperature in the basin is 12.9 °C. Basin parameters are shown in Table 1.

2.2. Rainfall-runoff modeling

The watershed model is derived from a Digital Elevation Model (DEM). The discretization is based both on the spatial distribution of physiographic factors (i.e., lithology, soils, cover type, hydrological conditions and slope) that determine a homogeneous hydrological response, and on control sections where dendro-geomorphological data are available. The use of simulation methods for the various processes involved is based on the information available for the basin. The curve number method (CN 89) was utilized to estimate initial water abstractions, considering land use, land cover type, and hydrological soil group.

The storage coefficient was calculated assuming it represents 0.6 tc. The Muskingum-Cunge method was applied for flood wave routing due to the lack of observed flow data. Muskingum-Cunge parameters were calculated based on flow and channel characteristics.

Figure 1. General view of the project site.

Table 1. Basin parameters.

Basin area (A)	8.7 km^2
Max. and min. heights of the basin (h_{max} / h_{min})	1395m/1100m
Basin direction	South-North
Basin average elevation (h_{ort})	1170 m
Basin harmonic slope (S)	0.0729
Hydrological soil type [CN (Hydrological soil type)]	89
Main sleeve length (L)	3.6 km
Distance from the projection of the basin center of gravity on the main tributary to the basin outlet (L_c)	1.75 km

2.3. Precipitation

According to the observation values in Elazig province, the average annual rainfall is around 600 mm. Precipitation is irregular according to the months, with the wettest month being April and the driest month being August. All three types of precipitation are observed in the region: convective, orographic, and frontal. There are precipitation observations at the meteorological stations in the Project area. The 60-year extreme distributions of the daily maximum precipitation of the precipitation stations in the vicinity of the project area were investigated, suitability tests were performed, and the recurring precipitation was calculated according to the appropriate distribution type.

Previous studies have advocated for the utilization of exceedance series to estimate the frequencies of extreme precipitation [22-24] that better fit the high range of the frequency function [25, 26] and have been applied to both runoff and precipitation forecasts. These exceedance series were derived from 24-hour rainfall events recorded in the day before and the day after the extreme rainfall event. On the basis of the results of the goodness of fit test (Kolmogorov-Smirnov test and Mean Square Error test), the function of the fit parameters estimated by the L-Moments method applied to the exceedance series above the threshold was selected. The Kolmogorov-Smirnov

test shows very similar values for all distribution functions, with the Log Pearson 3 distribution having the lowest error value. The results are given in Table 2.

Table 2. Repeated rainfall calculation.

Distribution Type	2 Year	5 Year	10 Year	25 Year	50 Year	100 Year	Acceptance
Normal Distribution	26.26	52.77	66.64	81.43	90.97	99.56	
Log-Normal (2 Parameters)	16.81	37.22	56.39	87.86	116.94	151.27	
Log-Normal (3 Parameters)	23.02	51.08	67.85	87.54	101.30	114.47	
Pearson Type-3 (Gama Type-3)	21.10	50.15	68.48	90.62	106.33	121.45	
Log-Pearson Type-3	29.98	40.37	47.02	55.22	61.19	67.02	****
Gumbel	15.23	51.19	74.99	105.07	127.38	149.53	

Repeated rainfall was calculated with the hourly pluviograph rates of the Elazig DMI (Turkish State Meteorological Service) meteorological station which has a pluviograph. In the calculation of the recurrent flood flows of Calgan Stream, which was selected according to the hydrological conditions of the drainage area from these rainfall, flow and incremental flows were calculated with the CN II (89) condition curve number and superposed with the unit hydrograph and recurrent flood hydrographs were drawn. The results of the DSI (General directorate of state hydraulic works) synthetic method were accepted for the project flood hydrograph and the unit hydrograph is given in Figure 2.

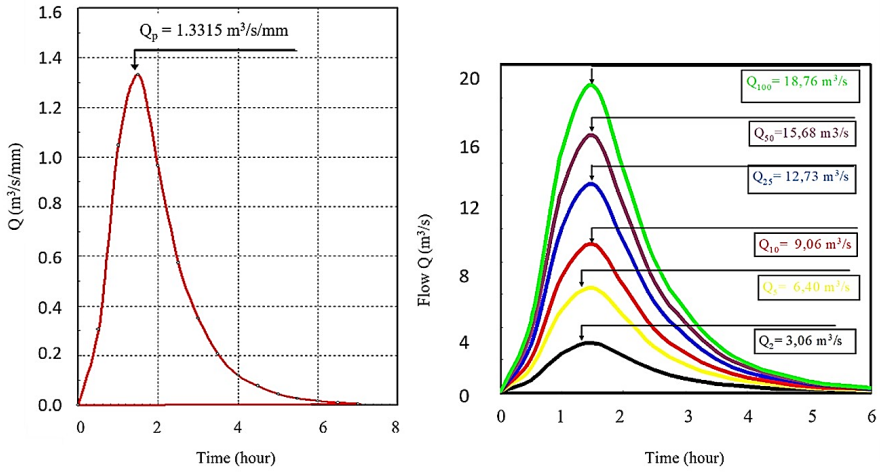

Figure 2. Unit and recurrence of flood hydrograph.

The only surface water source in the Project area is the Calgan Stream. There is no current observation station SGS (Stream gauging station) operated by any institution on the Calgan Stream. However, sporadic measurements were made by DSI. These measurements were utilized in the water potential studies of the regulator location. Monthly averages of these measurements were taken, and total flows are shown in Figure 3.

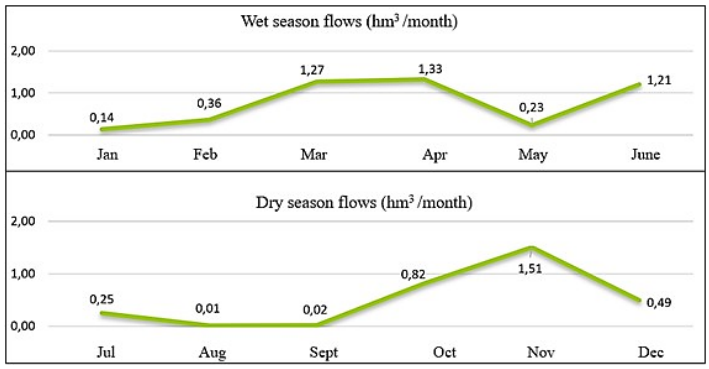

Figure 3. Monthly average flow rates of Calgan Stream.

2.4. Pumped from Keban Dam reservoir and botanical park

The sporadic measurements conducted by DSI indicate a natural annual flow of approximately 1 million m^3 in the Calgan Stream. As depicted in Figure 4, it is feasible to transport the required volume of water from the Keban reservoir to the Calgan Stream through a pumped transmission line spanning roughly 10 km in length. The water intake structure of the project draws from the Keban Dam Lake and features a reservoir capable of continuous water retention. Notably, the Keban Dam reservoir ranks among the largest in the country, boasting a storage capacity of approximately 30 billion m^3. The water extracted via the intake structure will be conveyed to the pumping station and subsequently to the regulation pool through penstock pipes. From there, it will be conveyed to the Calgan Stream basin via the transmission tunnel. The pipeline and reservoir are illustrated in the figure.

Figure 4. Pump station and Keban dam resorvoir.

As depicted in the Figure 4, the regulation pond at the terminus of the penstock transmission system will be designed with ample capacity to facilitate the necessary water regulation. It will store water during the operational hours of the solar power plant and will be adequately sized for this purpose. With the stored water, it will be feasible to procure water without the need to operate the pump during other periods.

The electrical energy required for the pumping process will be supplied by the solar power plant slated for installation in the area. An SPP (solar power plant) plant generating approximately 5 MW of power will be sufficient for each 1 m^3/s flow rate, given the region's favorable solar radiation conditions. According to the pvsyst simulation outlined in Table 3, a 1 MW AC power plant in the region is projected to produce 1752.6 MWh per

year. Consequently, the total energy output from the proposed 5 MW power plant in the area is estimated to be approximately 10 million kWh.

Table 3. Project area 1 MW pvsyst energy simulation.

Time	Radiation	Temperature °C	Energy
Jan	55.8	-1.10	74.4
Feb	73.4	0.40	94.7
Mar	130.5	5.40	146.8
Apr	155.1	11.20	149.8
May	209.9	16.40	187.3
June	245.4	22.30	203.2
Jul	253.0	26.80	209.7
Aug	227.2	27.10	203.1
Sep	177.3	21.90	182.3
Oct	127.4	15.20	156.3
Nov	77.4	7.20	106.1
Dec	54.9	1.10	73.6
TOTAL	1787.2	12.86	1787.2

2.5. Electric power of the PV power plant

The hourly output power of solar PV array (Equation 1);

$$P_{pv} = \eta_{pv}.N_{pvp}.N_{pvs}.V_{pv}.I_{pv} \quad (1)$$

where ηpv the conversion efficiency of a PV module, V_{pv} the module operating voltage, Ipv the module operating current, N_{pvp}; N_{pvs}, the number of parallel and series solar cells, respectively.

2.6. Energy consumed by the pump

The calculation of energy consumed by the pump is shown in Equation 2

$$E_p = \frac{2.72.Q.H_{net}}{1000} \quad (2)$$

where Q is the average water flow (m^3/day) pumped from the Keban Dam reservoir into the Calgan Stream, and Hnet is the total head (water level difference in Calgan Stream and Keban reservoir, including losses) in meters.

To pump water from the Keban reservoir to the project site, a total head of 500 meters is required, necessitating a power input of 5.45 MW. This pumping operation will occur during the summer months, when water is scarce, for approximately 4300 hours per year.

With this project, water from the Keban Dam Lake will be redirected to the Calgan Stream basin, enabling the creation of one of the largest botanical parks and oasis valley projects in our country, located in the forested land above the university. The region's natural riches, such as waterfalls, enhance its suitability for this venture. Social amenities like promenades and restaurants around the pond will provide economic benefits to the municipality.

Since the reservoir area, body axis, and other structures will be situated entirely within public land, there will be no expropriation issues or costs. Additionally, the initial construction expenses are expected to be recouped in a short period through the development of social facilities around the pond, making the water infrastructure project highly profitable. The project area, already covered with pine trees, will gain even more aesthetic appeal with the addition of the pond and botanical park.

2.7. Tailwater and city wastewater micro HEPP

In the subsequent phase of the project, the downstream segment, an innovative wastewater hydroelectric power plant (HEPP) can be constructed, representing a pioneering initiative in Turkey, inspired by similar endeavors in many developed nations worldwide. The effluent from the downstream section of the botanical park project will be reintroduced into the Keban Dam Lake via the Sorsor Stream. Notably, the wastewater line discharge from the Elazig city center also traverses this area. These combined waters, sourced from the cemetery ridges at an elevation of 980 m, can be channelized and utilized to generate energy in the hydroelectric power plant to be erected, facilitated by a transmission conduit. Subsequently, the tailwater from the hydroelectric power plant can be reintegrated into the Keban Dam reservoir. It is estimated that the total wastewater volume from the city, in conjunction with the Calgan Stream, will amount to approximately 2-3 m^3/s. All elements and locations of this multifunctional project are shown in Figure 5.

Figure 5. Study area.

2.8. Hydroelectric plant power calculation

Hydropower generation depends on two basic inputs in addition to plant characteristics. Flow and head. Under these conditions, Equation 3 shows the total power (Watts) that can be generated as a function of water density, where: density ρ (kg/m^3); gravitational acceleration g (m/s^2); plant efficiency η (constant); water head, H (m); and flow through the turbines Q (m^3/s). The product of these values gives the installed power in watts.

$$\text{Power} = \rho.g.\eta.H.Q \tag{3}$$

Power multiplied by time, t (hours), gives the energy production (kWh) in a given period, ΔT (Equation 4).

$$\text{Energy} = \int_0^T \rho g \eta H(t) Q(t) dt \tag{4}$$

If the amount of energy produced is multiplied by the energy price, p(t) ($/kWh) hydroelectric revenue ($) will be obtained.

The water from the botanic park's tailwater and city wastewater is diverted by a weir to a transmission canal and then directed through a penstock to the turbines, with a total installed power of 3.06 MW and an annual energy generation of 20.80 GWh (14.2 GWh firm and 6.6 GWh secondary) in the HEPP powerhouse, located at an elevation of 840.00 m. Subsequently, the water is discharged back into the Keban Dam reservoir. The gross head of the project is 180 m, and the design flow is selected as 2.0 m^3/s.

2.9. Economic analysis

The levelized cost of energy (LCOE) is a unit of measurement used to compare electricity from renewable energy sources with other fossil-based electricity generating systems (Equation 5). This cost calculation includes the installation cost of the system, maintenance and operation costs, and country-specific fiscal rates. LCOE (The cost to value of energy) is also referred to as the ratio of the PV plant cost incurred during the system lifetime to the electrical energy generated during this period.

$$\text{LCOE} = \frac{\text{Installation cost over the total system life}}{\text{Total energy generated during system life}} \quad (5)$$

The system life cycle costs comprise four main components: initial project costs, depreciation, annual operating costs, and residual value. The total system life cycle costs typically range between $15-18 per kW per year, depending on the system size. In power plants, the cost of in-house insulators constitutes approximately 9.5% of the initial investment cost, with an average lifespan of 10-13 years. Additionally, when considering depreciation and financial aspects, the initial installation cost of the system is multiplied by 1.4 to calculate the average system life cost. Losses within the system are estimated at 20%. Photovoltaic module manufacturers typically specify a module efficiency loss rate of 10% over 25 years.

For the calculation of energy revenue in 2023, an assumed average sales value in the Turkish market of $0.073 per kWh is utilized. Based on these calculations, the hybrid power plant (solar+hydro) is projected to generate an annual average of 30.8 GWh of electricity, with 10 GWh generated by the solar power plant alone. The initial investment cost for the plants and pumps to be installed is estimated at $9.500.000. Consequently, the total energy revenue of the hybrid power plant is assessed as $3.500.400, and the annual solar energy gain is projected at $684.000. The energy expended for annual pumping amounts to 13 million kWh, with a monetary equivalent of $949.000. Various factors, including depreciation, operation and maintenance costs, and interest, are factored into the calculation of annual costs. The amortization period of the system is determined to be 3.8 years, based on calculations considering the annual return over the retail electricity sales price and the initial installation price. These calculations underscore the significant cost-effectiveness of the project's energy investments alone.

3. Results

The drinking water supply for Elazig city center currently relies on the Hamzabey Dam and wells located in Uluova. However, with the anticipated increase in global warming and climate change, there is growing uncertainty regarding the security of supply from these sources. The recent water cuts in our city serve as a stark reminder of this vulnerability. With the proposed project, water will be sourced from the Keban Dam reservoir, providing a much safer water supply for the city center and mitigating potential water shortages.

Currently, water from Hamzabey is pumped from the treatment plant at approximately 950-1000 m to higher neighborhoods at elevations of 1250-1300 m, incurring significant energy costs. In the project, energy expended for pumping will be offset by the energy produced in the micro-hydroelectric power plant (HEPP) utilizing wastewater. Moreover, the presence of water in the region presents significant recreational potential.

Establishing a botanical park in the Calgan Stream basin requires a significant amount of water, particularly during the summer months. The inclusion of social amenities such as restaurants and cafeterias in the surrounding area will also contribute substantially to the region's economy.

Furthermore, since the proposed recreational area will be situated on treasury land, there will be no land acquisition or expropriation costs. The profitability of the facilities is evident, as construction expenses are expected to be recouped quickly with the establishment of social amenities around the botanical park.

4. Conclusion

The multifunctional project proposed for Elazig, including the establishment of a botanical park, a pumped irrigation line, and a solar-hydroelectric power plant, presents a promising solution to several pressing issues faced by the city. By harnessing the potential of existing water resources and integrating renewable energy sources, this project aims to enhance the quality of life for residents while also addressing challenges related to water supply, energy generation, flood protection, and recreation.

The botanical park planned for the Calgan Stream basin promises to be a valuable asset for the city, offering not only recreational opportunities but also contributing to the conservation of biodiversity and environmental education. With careful planning and efficient water management, the park can provide a sustainable source of irrigation water for landscaping and agriculture, reducing dependence on scarce resources.

The integration of a pumped irrigation line from the Keban Dam reservoir to the botanical park demonstrates a creative approach to water supply management. By utilizing solar energy to power the pumping process, the project not only reduces reliance on fossil fuels but also generates additional revenue through the sale of excess energy. Furthermore, the inclusion of a micro-hydroelectric power plant downstream of the botanical park offers a further opportunity to harness renewable energy and offset operational costs.

In addition to the environmental and economic benefits, the project also addresses pressing issues related to water security and flood management in Elazig. By diversifying the city's water sources and implementing measures to protect against floods, the project enhances resilience to climate change and ensures the long-term sustainability of water resources.

Overall, the multifunctional project proposed for Elazig represents a holistic approach to urban development, integrating environmental conservation, renewable energy generation, and social welfare. By leveraging the synergies between different components of the project, it has the potential to transform the city's landscape and improve the quality of life for its residents, while also serving as a model for sustainable development in similar urban contexts.

References

[1] Ivahova LI, Fesuk SS, Samoylov VS. Modern Earth Design. Arhangelsk: Adelant Press, 2009.

[2] Surat H, Eminağaoğlu Z, Yavuz Özalp A, Yaman YK. Determination of the Borcka Dam Reservoir Recreational Area Usage. Kastamonu Univ. J For Fac 2016; 16(2).

[3] Sabaz M. Türkiye'de Kent Gelişimi ve Açık Alan Gereksinimi. Doktora Tezi, Münih Teknik Üniversitesi, 1986.

[4] Golding J, Güsewell S, Kreft H, Kuzevanov VY, Lehvävirta S, Parmentier I, Pautasso M. Species-richness patterns of the living collections of the world's botanic gardens: a matter of socio-economics. Ann Bot 2010; 105: 689-696.

[5] Mounce R, Smith P, Brockington S. Ex situ conservation of plant diversity in the world's botanic gardens. Nat Plants 2017; 3: 795-802.

[6] Ren H, Duan ZY. The Theory and Practice on Construction of Classic Botanical Garden. Beijing: Science Press 2017.

[7] Oruckaptan A. Su Parkı Planlama Kriterlerinin Saptanması ve Ankara Susuz Göleti Örneğinde Değerlendirilmesi Üzerine Bir Araştırma. Doktora Tezi, Ankara Üniversitesi Fen Bilimleri Enstitüsü, Ankara, 2002.

[8] Ozkan B, Küçükerbaş E, Kaplan A, Hepcan Ş, Yiğit EM, Sönmez H. Muğla kenti kamusal dış mekânları bağlamında master plan çalışması. İzmir, 2003; pp. 3-15.

[9] Willison J. Botanic gardens as agents for social change. In: Kings Park and Botanic Garden Conservation into the 21st Century: Proceedings of the Fourth International Botanical Gardens Conservation Congress; 25-29 September 1997.

[10] Uzun G. Çukurova Üniversitesi Botanik Bahçesi Peyzaj Planlama İlkelerinin Saptanması Üzerine Bir Araştırma. Doçentlik Tezi, Çukurova Üniversitesi Fen Bilimleri Enstitüsü, Adana, 1997.

[11] Akten M, Akoğlu M. The effect on place perception of the artificial lighting in the landscape design. J Curr Res Soc Sci 2017; 7(1): 479-488.

[12] Yilmaz S, Mutlu E, Yilmaz H. Alternative scenarios for ecological urbanizations using ENVI-met model. Environ Sci Pollut Res 2018; 25(26): 26307-26321.

[13] Sachs NA, Rakow DA, Sheple M.M, Peditto K. The potential correlation between nature engagement in middle childhood years and college undergraduates' nature engagement, proenvironmental attitudes, and stress. Front Psychol 2020; 11: 2919.

[14] Tarsitano E, Posca C, Giannoccaro RA, Borghi C, Trentadue C, Romanazzi G, Colao MA. Park to Live between environmental education and social inclusion through a landsense ecology approach. Int J Sustain Dev World Ecol 2021; 28(2): 166-178.

[15] Beltran H, Vidal R, Basiero L, Santos JM, Basiero JA, Belenguer E. Micro hydro installation analysis in a wastewater treatment plant. Renew Energy Power Qual J 2014; 12: 15–20.

[16] Bousquet C, Samora I, Manso P, Rossi L, Heller P, Schleiss AJ. Assessment of hydropower potential in wastewater systems and application to Switzerland. Renew Energy 2017; 113: 64–73.

[17] Llácer-Iglesias R, Pérez J, Satorre-Aznar J, López-Jiménez P, Pérez-Sánchez, M. Energy recovery in wastewater treatment systems through hydraulic micro-machinery. Case study. J Appl Res Technol Eng 2020; 1: 15.

[18] Diaz-Elsayed N, Rezaei N, Ndiaye A, Zhang Q. Trends in the environmental and economic sustainability of wastewater-based resource recovery: A review. J Clean Prod 2020; 265: 121598.

[19] Nowak DJ, Stevens JC, Sisinni SM, Luley CJ. Effects of urban tree management and species selection on atmospheric carbon oxide. J Arboric 2002; 28(3): 113-122.

[20] O'Keefe B. Trees on track to save millions. The Australian Newspaper, Higher Education Supplement, 14 June 2006; p. 30.

[21] Xinian Z. Quantitative evaluation of environmental benefits of urban greenland in Beijing City. In: Proceedings of IFPRA-Asia/Pacific Congress; September 1999; Hangzhou, China. pp. 315-323.

[22] Wang QJ. The POT model described by the generalized Pareto distribution with Poisson arrival rate. J Hydrol 1991; 129: 263–280.
[23] Wilks DS. Comparison of three-parameter probability distributions for representing annual extreme and partial duration precipitation series. Water Resour Res 1993; 29: 3543–3549.
[24] Coles S, Pericchi LR, Sisson S. A fully probabilistic approach to extreme rainfall modelling. J Hydrol 2003; 273: 35-50.
[25] Cunnane C. A particular comparison of annual maxima and partial duration series methods of flood frequency prediction. J Hydrol 1973; 18: 257–271.
[26] Madsen H, Pearson CP, Rosbjerg D. Comparison of annual maximum series and partial duration methods for modelling extreme hydrologic events. 1. At-site modelling. Water Resour Res 1997; 33: 759–769.

Turkish Journal of Science & Technology
19(2), 373-378, 2024

Research Paper
https://doi.org/10.55525/tjst.1444667

The Antimicrobial and Antioxidant Effects of *Equisetum arvense* Extracts

Ayşe EREN[1*], Şule İNCİ[2] , Sevda KIRBAĞ[3]
[1] Molecular Biology and Genetics Department, Faculty of Science, Dicle University, 21280 Diyarbakır, Turkey
[2] Health Services Vocational School, Department of Medical Services and Techniques, Medical Laboratory Techniques Program, T.C. Istanbul Rumeli University, Istanbul, Turkey
[3]Fırat University, Science Faculty, Department of Biology, 23270, Elazığ, Turkey

[*1]flow.eren@hotmail.com, [2]sule.inci@rumeli.edu.tr, [3]skirbag@firat.edu.tr

(Geliş/Received: 29/02/2024 Kabul/Accepted: 28/09/2024)

Abstract: *Equisetum arvense* L, also known as horsetail, is a medicinal plant used in traditional medicine. Especially, it is used in the treatment of bleeding, antiseptic, anti-inflammatory, urethritis, jaundice and hepatitis. In the study, the antimicrobial and antioxidant activities of extracts obtained from different solvents of *E. arvense* were investigated. Antimicrobial activity of *E. arvense* extracts was determined using the disc diffusion method. The antimicrobial activity was determined utilizing the pathogenic microorganisms *Staphylococcus aureus*, *Klebsiella pneumoniae*, *Escherichia coli*, *Bacillus megaterium*, *Candida albicans* and *Candida glabrata*. In the results obtained, it was determined that the ethanol extract of *E. arvense* at 500 µg concentration showed antimicrobial activity at different rates (14.3-28.0). Ethanol extract showed the highest antimicrobial activity against *Candida glabrata* (28.0 mm) at the same concentration. It was detected that the chloroform extract showed antimicrobial activity (7.3-10.6 mm) against the microorganisms used. The antioxidant activity of the aerial parts of *E. arvense* at different concentrations of methanol extract was determined according to the 2,2-diphenyl-1-picrylhydrazil radical scavenging capacity method. The highest radical scavenging capacity of the methanol extract was observed at a concentration of 10mg/mL (91.5%). The IC_{50} value of the methanol extract of *E. arvense* was calculated as 3.13 mg/mL.

Key words: *Equisetum arvense*, antimicrobial, antioxidant, medicinal plant.

Equisetum arvense Ekstraktlarının Antimikrobiyal ve Antioksidan Etkileri

Öz: Atkuyruğu olarak bilinen *Equisetum arvense* L. geleneksel tıpta kullanılan tıbbi bir bitkidir. Özellikle; kanama, antiseptik, antiinflamatuar, üretrit, sarılık ve hepatit tedavisinde kullanılır. Çalışmada *E. arvense*'nin farklı solventlerinden elde edilen ekstraktların antimikrobiyal ve antioksidan aktiviteleri araştırılmıştır. *E. arvense* ekstraktlarının antimikrobiyal aktivitesi disk difüzyon yöntemi kullanılarak tespit edilmiştir. Antimikrobiyal aktivite patojenik mikroorganizmalar *Staphylococcus aureus*, *Klebsiella pneumoniae*, *Escherichia coli*, *Bacillus megaterium*, *Candida albicans* ve *Candida glabrata* kullanılarak belirlendi. Elde edilen sonuçlarda *E. arvense*'nin 500 µg konsantrasonda etanol ekstraktının farklı oranlarda (14,3-28,0) antimikrobiyal aktivite gösterdiği belirlendi. Etanol ekstraktı aynı konsantrasyonda *Candida glabrata*'ya (28,0 mm) karşı en yüksek antimikrobiyal aktivite göstermiştir. Kloroform ekstraktının kullanılan mikroorganizmalara karşı antimikrobiyal aktivite gösterdiği (7,3-10,6 mm) tespit edilmiştir. *E. arvense*'nin toprak üstü kısımlarının metanol ekstraktının farklı konsantrasyonlarındaki antioksidan aktivitesi, 2,2-diphenyl-1-picrilhydrazyl radikal temizleme kapasitesi yöntemine göre tespit edilmiştir. Metanol ekstraktının en yüksek radikal temizleme kapasitesi 10mg/mL (%91,5) konsantrasyonda görülmüştür. *E. arvense*'nin metanol ekstraktının IC_{50} değeri 3,13 mg/mL olarak hesaplandı.

Anahtar kelimeler: *Equisetum arvense*, antimikrobiyal, antioksidan, tıbbi bitki.

1. Introduction

Medicinal aromatic plants have been used since the existence of humanity to prevent and cure diseases and to maintain health. In addition, it is used in many industries such as food, perfume and cosmetics, and the importance given to medicinal plants is increasing [1, 2]. For this reason, the majority of the population in the world finds herbal medicines more reliable [3]. Studies on the antimicrobial and antioxidant effects of some components in herbal sources are increasing rapidly [3-4]. Today, considering that bacteria have important power over antibiotics, different alternative ways are sought. In particular, thanks to the secondary metabolites of plants, this can be prevented [5, 3]. In addition, plants protect the organism against oxidation thanks to these components. For this reason, plants, which are one of the natural antioxidant sources, have started to be used more than synthetic antioxidants [2-4].

* Corresponding author: flow.eren@hotmail.com. ORCID Number of authors: [1]0000-0002-5601-6808, [2]0000-0002-4022-5269,[3]0000-0002-4337-8236

Equisetum arvense (field horsetail) L. belongs to the *Equisetaceae*. It is a northern hemisphere herbaceous perennial plant that has long been utilized for medicinal reasons. This species are found across Canada, Europe, the United States (except for the southeast) southern Asia, and Africa, including Turkey, the Himalayas, Iran, Japan, China (except for the southeast), and Korea [6-8]. The horsetail has been used as an anti-inflammatory agent in Europe, Asia and America, as well as an antiseptic agent in Turkey and in the United States for years [9-12].

Thanks to its anti-inflammatory effect, *E. arvense* is known to be used in kidney stones, gout, and prostate disease. Additionally, its tea is good for mouth and gum infections [7]. In addition, it is used among the public as a hemostatic agent in the treatment of tuberculosis and menstrual bleeding [8]. Studies have confirmed various biological effects of *E. arvense*, such as sedative, anticonvulsive, hepatoprotective, antioxidant, antibacterial and antifungal activity [13-16]. *E. arvense* is used in food supplements and alternative medicine thanks to the phytochemicals it contains. Its biological activity is related to the content of various classes of secondary metabolites such as phenolics (flavonoids, styryl pyrones and phenolic acids), alkaloids (equisetin, nicotine, palustrine), phytosterols (campesterol), and minerals (silica, calcium, magnesium, selenium, iron, potassium, zinc, etc.) [8, 15-16].

The aim of the present study was to evaluate the antimicrobial effect of ethanol, methanol and chloroform extraction of the aerial parts of *E. arvense* and to evaluate the 2,2-diphenyl-1-picrylhydrazine (DPPH) radical scavenging effect of methanol extract.

2. Material and Method

2.1. Collecting and Obtaining of Sample

E. arvense plant was obtained from herbalists in 2020. Taxonomic description of plant material was carried out by the systematics-botany expert Prof. Dr. Şemsettin Civelek of Fırat University using the book Flora of Turkey. The powdered dry plant material weighed 0.5 g. 100 mL of solvent 96% methanol (MeOH), ethanol (EtOH) and chloroform were added to the weighed plant. It was then stirred on a rotary shaker in a dark environment at room temperature for 72 hours and filtered using Whatman filter paper. The prepared extracts were stored at +4°C.

2.2. Antimicrobial Assay

The antimicrobial activities of *Equisetum arvense*'s chloroform, ethanol and methanol extracts were performed according to the method specified by Collins and Lyne [17]. Prepared broth cultures yeast (*Candida albicans* and *Candida glabrata*) and bacterial (*Staphylococcus aureus* ATCC25923, *Klebsiella pneumoniae* ATCC 700603, *Escherichia coli* ATCC25322, *Bacillus megaterium* DSM32) were cultured on Sabouraud Dextrose Agar (Difco) and Müeller Hinton Agar (Difco), respectively inoculated at 1% (10^6 bacteria/mL, 10^4 yeast/mL) and placed in sterile petri dishes. Antimicrobial discs (6 mm diameter), each impregnated with 100 µl (500 µg) of different extracts, were gently transferred on agar medium. Following incubation for 1.5-2 hours at 4°C, the bacteria and yeast were transferred onto plates and incubated for 24 hours at 37 ± 0.1°C, and for 72 hours at 25 ± 0.1°C, respectively. Nystatin (30 µg/disc) (for yeast) and Streptomycin sulfate (10 µg/disc) (for bacteria) were used as standard discs. The zones (mm) were then measured.

2.3. Antioxidant Assay

The antioxidant assay was found by using 2,2-diphenyl-1-picrylhydrazine (DPPH) radical scavenging capacity of [18,19]. Plant extracts were prepared in methanol at concentrations of 1.25, 2.5, 5, and 10 mg/mL. 3 ml of the DPPH solution (0.004%) was prepared before the study was taken and 30 µL of plant extracts were added to it and left in the dark for 30 minutes. The activity was measured spectrophotometrically at 517 nm. Antioxidant activity was performed in triplicate. Methanol and butylated hydroxyanisole (BHA) were utilized as control. The percent scavenging effect of the DPPH radical was measured using the formula (1).

$$\%\text{DPPH inhibit} = [(\text{Abs Control} - \text{AbsSample}) \div \text{AbsControl}] \times 100 \quad (1)$$

2.4. Statistical Analysis

SPSS Statistics (version 22) was used to perform the statistical analysis and generate the figures. Analysis of variance (ANOVA) and Student's t-test were performed, and $p < 0.01$ was considered significant.

3. Results and Discussion

3.1. Antimicrobial Assay

The antimicrobial effects of the aerial parts of *E. arvense* are shown in Table 1. In the results obtained, the inhibition zones of methanol extract against *B. megaterium*, *K. pneumoniae*, *S. aures*, *E. coli*, *C. glabrata* and *C. albican*s were determined 20.3, 20.3, 20.3, 20.0, 21.6 and 20.6, respectively. Ethanol extract showed antimicrobial effect against the same microorganisms at different rates (14.3-28.0 mm). It was detected that the chloroform extract showed antimicrobial activity (7.3-10.6 mm) against *C. glabrata*, *C. albicans*, *S. aureus*, *E. coli* and *B. megaterium*, but not against *K. pneumoniae* (Table 1).

Table 1. Inhibition zones of *E. arvense* extracts (mm).

		Extracts		
Microorganisms	**Control**	***E. arvense*-M***	***E. arvense*-E***	***E. arvense*-C***
E. coli	10.6 ± 0.33	20.0 ± 0.57	15.3 ± 0.66	7.6 ± 0.33
K. pneumoniae	17.0 ± 0.57	20.3 ± 0.33	15.0 ± 0.57	-
C. albicans	9.6 ± 0.33	20.6 ± 0.34	14.3 ± 0.66	7.3 ± 0.33
C. glabrata	22.6 ± 0.33	21.6 ± 0.33	28.0 ± 0.57	9.6 ± 0.33
S. aureus	14.6 ± 0.34	20.3 ± 0.33	18.3 ± 0.33	10.6 ± 0.34
B.megaterium	9.6 ± 0.33	20.3 ± 0.34	20.3 ± 0.33	7.6 ± 0.33

**E. arvense*-M: methanol extract of *Equisetum arvense*; *E. arvense*-E: ethanol extract of *Equisetum arvense*; *E. arvense*-C: chloroform extract of *Equisetum arvense.*

In the previous study, while the water extract of *E. arvense* showed an antimicrobial effect against *S. aureus*, *S. pneumoniae* and *S. pyogenes* at a concentration of 100 mg/mL (8mm-11mm), it did not show an antimicrobial effect against *C. albicans* and *E. coli* [20]. Kukrić et al.[15] determined that the methanol extract of *E. arvense* L. had the highest antibacterial activity against *S. aureus* with MIC and MBC (11.14 and 22.28 mg/mL). Inhibition zones of hydro-alcoholic extracts of *E. arvense* against *E. coli*, *K. pneumoniae*, *S. aureus* and, *C. albicans*, were reported as 12.1 mm, 11.3 mm, 11.7 mm and 13.1 mm, respectively [21]. Ethyl acetate, aqueous extracts and chloroform from the same plant did not show antimicrobial activity against *E. coli*. However, ethyl acetate and chloroform extracts created a 9 mm zone of inhibition against *S. aureus* [22]. The ethanol extracts of *E. arvense* at 1000 µg concentration were reported as 11 mm, 18 mm,14 mm and 18 mm zones of inhibition against *P. aeruginosa, K. pneumoniae*, *S. aureus* and *E. faecalis,* respectively [23]. The methanol extract of *E. arvense* showed antimicrobial activity against *E. coli* at a concentration of 1mg/mL [24]. The zone diameters of 4 different extracts of *E. arvense* (hexane, ethyl acetate, ethanol and methanol) were determined to be 9-15 mm. The highest antimicrobial activity of the plant extracts was observed against 15 mm *C. albicans* yeasts [25]. It was determined that *E. arvense* ethanol extracts did not have an antimicrobial effect against *E. coli* at concentrations of 5 µL and 10 µL [26]. The minimum concentration values of *E. arvense* shoots methyl and ethyl extracts against clinical isolates *S. aureus* and *S. aureus* were determined in the range of (20.58, 15.5 mg/mL), respectively. It has been reported that the minimum concentration values of methyl and ethyl extracts against *E. coli* are in the range of 15.41- 12.58 mg/mL [27]. It was reported that the essential oil of *E. arvense* had the highest antimicrobial effect against *K. pneumoniae* (37 mm) and *S. enteritidis* (35 mm) [28]. The same species formed 14.67 mm, 15.33 mm and 14.33 mm inhibition zones against *E. coli*, *Y. enterocolitica* and *S. enterica*, respectively [29]. When the results obtained are compared with previous studies, it is seen that the results obtained show similarities with literature studies [21, 23, 25, 26, 28, 29] It is seen that the results vary depending on the solvents and concentrations used.

3.2. Antioxidant Assay

The DPPH radical scavenging activities of the aboveground parts of the methanol extract of *E. arvense* at concentrations of 1.25 mg/mL, 2.5 mg/mL, 5 mg/mL and 10 mg/mL are shown in Figure 1. Methanol extract showed a DPPH radical scavenging effect of 24.5% at 1.25 mg/mL concentration, 46.6% at 2.5 mg/mL concentration, 81.7% at 5 mg/mL concentration and 91.5% at 10 mg/mL concentration. It was observed that the DPPH radical scavenging effect of *E. arvense* increased with increasing concentrations. The IC_{50} value of the methanol extract of *E. arvense* was calculated as 3.13 mg/mL. The DPPH radical scavenging activity of the aerial parts of the methanol extracts of *E. arvense* at different concentrations is shown in Figure 1.

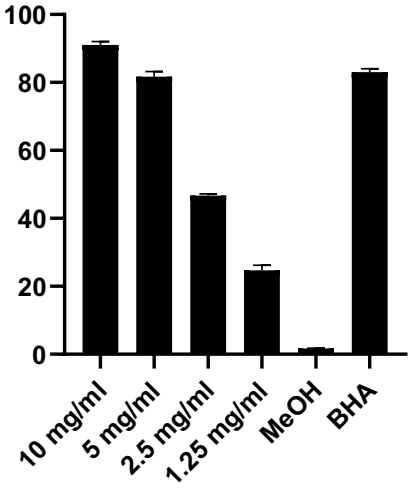

Figure 1. Percent inhibition of the DPPH radical of *E.arvense*.

In previous studies, it was reported that the EtOAc extract of *E. arvense* has a scavenging effect on DPPH radicals of 2.37 µg/mL, and the water extract is 37.20 µg/mL. Ethanol extract has a higher antioxidant effect than water extract in this study.This is explained by the fact that ethanol extract contains significant amounts of quercetin 3-*O*-glucoside (isoquercitrin), apigenin 5-*O*-glucoside, and kaempferol 3-*O*-glucoside [30]. It was determined that the pectins obtained from the stems of *E. arvense* have a 63% scavenging effect on the DPPH radical [31]. It was reported that the antioxidant effect of *E. arvense* sterile stem extracts was 87.30%. In the same study, epicatechin, which is known to have antioxidant effects, was detected in *E. arvense* sterile stem extracts [16]. Free radical scavenging effects of *E. arvense*'s foliage and central stalk were determined as 71.37%-96.22% mg/mL at different concentrations. In the same study, scavenging activity for rhizomatous stem and root was reported as 70.55-94.66% mg/mL [32]. The horsetail n-butanol extract has been reported to DPPH (EC_{50}=0.65 mg/mL) and hydroxyl radical scavenging activities (EC_{50}=0.74 mg/mL) respectively. It has been reported that there may be a relationship between the high phenolic content of n-Butanol extract and its antioxidant effect. [14]. Wang et al. [33] determined that the IC_{50} value of the antioxidant effect of *E. arvense* extract was 12.3 µg/ml. In the antioxidant study of the essential oil of *E. arvense* using RSA and FIC methods, IC_{50} values were found to be 952.7 and 1, 282.7 µg/mL, respectively. It was determined that the IC_{50} value of the scavenged DPPH of *E. arvense* extract was 15.2 µg/mL [34]. The scavenging effect of methanol, ethanol and water extracts of *E. arvense* on DPPH radical was calculated as 1847, 2217 and 374 µmol TE g^{-1}, respectively. Ethanol extract was found to be rich in flavonoids, flavonoid-*O*-glycosides, phytosterols, phenolic and fatty acids, as well as in minerals and mainly in K, Ca, Mg, Si and P [35]. The highest DPPH radical scavenging effect of *E. arvense* was found in the ethanol extract (IC_{50}=2.37 µg/mL) [30]. The IC_{50} value of the antioxidant effect of *E. arvense* was reported as 13.5 µg/mL [15]. The percent inhibition of the DPPH radical scavenging effect of *E. arvense* was calculated as 87.50 [16]. The results obtained are compared with previous studies. [16, 30-33], [14], it is known that the results differ depending on the methods used, the concentrations used, the solvent used, and the phytochemicals they contain and their amounts.

4. Conclusion

The antimicrobial and DPPH radical scavenging effects of the aerial parts of *E. arvense* on some pathogenic microorganisms were investigated. It was found that the methanol extract different solvents 20.3, 20.3, 20.3, 20.0, 21.6 and 20.6, and mm inhibition zones against *B. megaterium*, *S.aureus*, *K.pneumoniae*, *E.coli, C.glabrata* and *C.albicans*. *E. arvense*'s ethanol extract showed the highest antimicrobial activity against *C. glabrata* (28.0 mm). The highest DPPH radical scavenging effect of methanol extract was at 10mg/ml (%91.5) concentration. Considering that *E. arvense* is responsible for the bioactivity of the biochemicals it contains, the results of the study may be important in terms of the literature.

Acknowledgements

The results are included in the abstract book of the 4th International Conference on Physical Chemistry and Functional Materials Congress (08-09 April 2021, Firat University/Elâzığ).

References

[1] Güler HK, Dönmez İE, Aksoy SA. Antibacterial activity of medicinal and aromatic plants and utilization in textile industry. Süleyman Demirel Üni Fac Arts Sci J Sci 2015; 10 (2): 27-34.
[2] Faydaoğlu E, Sürücüoğlu MS. Medical and aromatic plants antimicrobial, antioxidant activities and use opportunities. Erzincan Uni J Sci Technol 2013; 6(2): 233-265.
[3] Orçan İ, Bülbül AS, Kara Y. Determination of antimicrobial, antibiofilm, antioxidant activity and phenolic profile of *Alyssum filiforme.* Çanakkale Onsekiz Mart Uni J Adv Res Nat Appl Sci 2023; 9(1) :48-55.
[4] Çağlak E, Kara B, Karslı B, Öğretmen ÖY Gürdal AA, Kara A. Determination of antimicrobial and antioxidant activities of wastes (Tea Seed, Orange, and Mandarin Peel) of some local product grown in Rize province. Atatürk Uni. J Agric Fac 2022; 53 (3): 166-177.
[5] Essawi T, Srour M. Screening of some palestinian medicinal plants for antibacterial activity. J Ethnopharmacol 2000; 70(3) :343-349.
[6] Sandhu NS, Kaur S, Chopra D. *Equisetum Aervens*: Pharmacology and phytochemistry-a review. Asian J Pharm Clin Res 2010; 3(3): 146-150.
[7] Adhikari A, Bhandari S, Pandey DP. Anti-inflammatory compounds camphor and methylsalicylate from traditionally used pain curing plant *Equisetum arvense* L. J Nepal Chem Soc 2019; 40, 1-4.
[8] Makia R, Al-Halbosiy MM, Al-Mashhadani MH. Phytochemistry of the genus *Equisetum* (*Equisetum arvense*). Biol Pharm Sci 2022;18(2): 283-289.
[9] Ody P, Kindersley D. The complete medicinal herbal. New York: DK Publishing; 1993.
[10] Hoffman D. The new holistic herbal. Shaftesbury: Element; 1990.
[11] Ismail AM, Al-Khasreji TO, Maulood BK. Flavonoids content in methanolic extract of *Equisetum arvense* L. (Horsetail) from Kurdistan region-Iraq. J Biotechnol Res Cent 2020; 14(1), 47-51.
[12] Do Monte FHM, dos Santos Jr JG, Russi M, Lanziotti VMNB, Leal LKAM, de Andrade Cunha G.M. Antinociceptive and anti-inflammatory properties of the hydroalcoholic extract of stems from *Equisetum arvense* L in mice. Pharmacol Res 2004; 49(3): 239-243.
[13] Guimaraes R, Barros R, Carvalho A, Sousa M, Morais J, Ferrira ICFR. Aromatic plants as a aource of important phytochemicals: vitamins, sugars and fatty acids in cistus ladanifer, cupressus lusitanica and eucalyptus gunnii leaves. Ind Crops Prod 2009; 30(3): 427-430.
[14] Canadanovic-Brunet JM, Cetkovic GS, Djilas SM, Tumbas VT, Savatovic SS, Mandic AI, Markov SL, Cventkovic DD.Radical scavenging and antimicrobial activity of horsetail (*Equisetum arvense* L) extractsInt. Int J Food Sci Technol 2009; 44(2): 269-278.
[15] Kukrić Z, Topalić-Trivunović L, Pavičić S, Žabić M, Matoš S, Davidović A. Total phenolic content, antioxidant and antimicrobial activity of *Equisetum arvense* L. Chem Ind Chem Eng Q 2013; 19 (1): 37-43.
[16] Pallag A, Jurca T, Pasca B, Sirbu V, Honiges ANA, Costuleanu M. Analysis of phenolic compounds composition by HPLC and assessment of antioxidant capacity in *Equisetum arvense* L extracts. Rev Chim 2016; 67(8), 1623-1627.
[17] Collins CH, Lyne PM, Grange JM, Flkinham III JO. Microbiological Methods, pp. 140, 2004; London, Arnold.
[18] Sharma OP, Bhat TK. DPPH antioxidant assay revisited. Food Chem 2009; (113): 1202-1205.
[19] Dimitrova DZ, Nedialkov P, Kitanov. Radical scavenging and antioxidant activities of methanolic extracts from *Hypericum* species growing in Bulgaria. Pharmacogn Mag 2010; (6): 74-78.
[20] Pallag A, Filip GA, Olteanu D, Clichici S, Baldea I, Jurca T, Micle O, Vicaş L, Marian E Soriţău O, Cenariu M, Mureşan M. *Equisetum arvense* L extract induces antibacterial activity and modulates oxidative stress, inflammation, and apoptosis in endothelial vascular cells exposed to hyperosmotic stress. Oxid Med Cell Longevity 2018; 14.

[21] Milovanovic V, Radulovic N, Todorovic Z, Stankovic M, Stojanovic G. Antioxidant, antimicrobial and genotoxicity screening of hydro-alcoholic extracts of five serbian *Equisetum* species. Plant Foods Hum Nutr 2007 (62): 113-119.
[22] Lotfipour F, Mazemiyeh H, Fathi-Azad F, Garaei N, Arami S, Talat S, Sadegpour F, Hasanpour R. Evaluation of antibacterial activities of some medicinal plants from North-West Iran. Iran J Basic Med Sci 2008;11: 80-85.
[23] Geetha RV, Lakshmi T, Roy A. In vitro evaluation of antibacterial activity of *Equisetum arvense linn on* urinary tract pathogens. Int J Pharm Pharm Sci 2011;(3): 323-325.
[24] Uslu ME, Erdogan I, Oguzbayraktar O, Ates M. Optimization of extraction conditions for active components in *Equisetum arvense* extract. Rom Biotechnol Lett 2013; (18): 8115-8131.
[25] Acet T, Özcan K. Investigation of some biological activities of horsetail (*Equisetum arvense*) plant used for medicinal purposes in Gümüşhane province. Turkish J Agric Food Sci Technol 2017; 5 (13): 1810-1814.
[26] Gülmez Ö, Algur ÖF. Determination of antimicrobial properties of ethyl alcohol extracts of some plants. J Nat Appl Sci East 2019; 2 (2): 54-60.
[27] Kryvtsova M, Koscova J, Kouhuch T, Savenko M, Spivak, N. Antimicrobial, antibiofilm-forming properties of *Equisetum arvense* L. shoot extracts. Curr Perspec Med Aromat Plants 2021; 4(1), 50-57.
[28] Radulović N, Stojanović G, Palić R. Composition and antimicrobial activity of *Equisetum arvense* L. essential oil. Phytother Res 2006*;*20(1): 85-88.
[29] Kačániová M, Žiarovská J, Kunová S, Rovná K, Savistkaya T, Hrinshpan D, Veronika V, Lucia G, Petra B, Ivanišová E. Antimicrobial potential of different medicinal plants against food industry pathogens. Potravinarstvo Slovak J Food Sci 2020; 14: 494-500.
[30] Mimica-Dukic N, Simin N, Cvejic J, Jovin E, Orcic D, Bozin B. Phenolic compounds in field horsetail (*Equisetum arvense* L) as natural antioxidants. Mol 2008; 13 (7): 1455-1464.
[31] Patova OA, Smirnov VV, Golovchenko VV, Vityazev FV, Shashkov AS, Popov SV. Structural, rheological and antioxidant properties of pectins from *Equisetum arvense* L. and *Equisetum sylvaticum* L. Carbohydr Polym 2019; 209: 239-249.
[32] Huh MK, Han MD. Inhibitory effect of hyaluronidase and dpph radical scavening activity using extraction of *Equisetum arvens*. Eur J Adv Res Biol Life Sci 2015; 3(2).
[33] Wang L, Zhang L, Zheng G, Luo H, El-kott AF, El-kenawy AE. *Equisetum arvense* L aqueous extract: a novel chemotherapeutic supplement for treatment of human colon carcinoma. Arch Med Sci 2023 19(5): 1472-1478.
[34] Gu H, Yi T, Lin P, Hu J. Study on essential oil, antioxidant activity, anti-human prostate cancer effects, and induction of apoptosis by *Equisetum arvense*. Open Chem 2022; 20 (1): 1187-1195.
[35] Dormousoglou M, Efthimiou I, Antonopoulou M, Fetzer DL, Hamerski F, Corazza ML, Papadaki M, Santzouk S, Dailianis S, Vlastos D. Investigation of the genotoxic, antigenotoxic and antioxidant profile of different extracts from *Equisetum arvense* L. Antioxid 2022; 11(7): 1393.

Turkish Journal of Science & Technology
19(2), 379-386, 2024

Research Paper
https://doi.org/10.55525/tjst.1447886

Effect of Dietary Zinc on the Antioxidant Parameters of Juvenile Common Carp (*Cyprinus carpio*)

Shokri Omar Mustafa MUSTAFA[1], Muzaffer Mustafa HARLIOĞLU[2*], Önder AKSU[3], Zahra BATOOL[4]

[1, 2, 4] Department of Fish Cultivation, Fisheries Faculty, Firat University, 23200 Elazığ, TÜRKİYE
[3] Department of Fish Cultivation Fisheries Faculty, Munzur University, 62000 Tunceli, TÜRKİYE
[1] shokri.mustafa@uqconnect.edu.au, [2*] mharlioglu@firat.edu.tr, [3] onderaksu@munzur.edu.tr,
[4] mushhood4@gmail.com

(Geliş/Received: 06/03/2024; Kabul/Accepted: 26/07/2024)

Abstract: Zinc (Zn) is an essential micro mineral needed for the proper growth and immune function of fish. This investigation was designed to examine the antioxidant role of a fortified diet with different Zn levels in the muscle and liver tissues of carp fry. A four-iso-nitrogen (35% crude protein) practical diet was produced that included graded levels of dietary zinc sulphate as a nutritional zinc resource in the fundamental diet supplemented with increased zinc levels (T1, control, 85 mg Zn kg^{-1}, T2 105 mg Zn kg^{-1}, T3, 125 mg Zn kg^{-1} and T4, 145 mg Zn kg^{-1}). Even though the SOD and CAT analysis results did not show a linear increase in the increasing Zn ratio in the diets, higher values were obtained compared to the control groups. SOD highest values in T3 for the liver (0.713 ± 0.220 U/ml) and T1 for muscle (0.751 ± 0.144 U/ml), CAT values were highest in T2 for the liver (0.849 ± 0.115 nmol/dk/m) and T2 for muscle (1.059 ± 0.148 nmol/dk/m) was obtained. MDA values were completely higher for the muscle than for the control group, and for the liver, a lower value was obtained in the T2 trial group than in the control group (1.671 ± 0.230 µM). The results of the study showed that Zn contributed significantly to the nutrition of carp fish. It can be concluded that the findings of SOD and CAT analysis endorse the positive contributions of using 105 mg Zn in the diets to promote the antioxidant defense of juvenile carp fish.

Keywords: Antioxidant, catalase, liver, muscle, superoxide dismutase.

Diyetsel Çinkonun Yavru Sazanların (*Cyprinus carpio*) Antioksidan Parametreleri Üzerine Etkisi

Öz: Çinko (Zn), balığın dengeli büyümesi ve metabolizması için gerekli olan önemli bir mikromineraldir. Bu araştırma, sazan yavrularının kas ve karaciğer dokularında farklı Zn düzeylerine sahip zenginleştirilmiş bir diyetin antioksidan rolünü incelemek üzere tasarlanmıştır. Artan çinko seviyeleri ile desteklenen temel diyette besinsel bir çinko kaynağı olarak kademeli seviyelerde diyet çinko sülfat içeren dört izo-nitrojenli (%35 ham protein) pratik bir diyet üretildi (T1, kontrol, 85 mg Zn kg^{-1}, T2 105 mg Zn kg^{-1}, T3, 125 mg Zn kg^{-1} ve T4, 145 mg Zn kg^{-1}). Çalışma sonunda rasyonlarda artan Zn oranında SOD ve CAT analiz sonuçları doğrusal bir artış göstermese de kontrol gruplarına göre daha yüksek değerler elde edilmiştir. En yüksek SOD değerleri karaciğer için T3'te (0,713±0,220 U/ml) ve T1'de kas için (0,751±0,144 U/ml), CAT değerleri en yüksek karaciğer için T2'de (0,849±0,115 nmol/dk/m) ve T2'de kas için (1,059±0,148 nmol/dk/m) elde edildi. MDA değerleri kas için kontrol grubuna göre tamamen yüksekti ve karaciğer için T2 deneme grubunda kontrol grubuna göre daha düşük bir değer elde edildi (1,671 ± 0,230 µM). SOD ve CAT analiz bulgularının, yavru sazan balıklarının antioksidan savunmasını geliştirmek için rasyonlarda 105 mg Zn kullanımının olumlu katkılarını desteklediği sonucuna varılabilir.

Anahtar Kelimeler: Antioksidan, katalaz, karaciğer, kas, süperoksit dismutaz.

1. Introduction

In the production of cultured fish, feed is very important in decisive the quality and quantity of the product obtained. Excess minerals in feeds in dense culture systems are an important problem causing eutrophication. In order to prevent this situation, the establishment of mineral-balanced pellets according to the needs of the produced fish is necessary to minimize mineral overload in aquatic habitats. Zinc (Zn) is also very important for appropriate growth rate, metabolism activity and immune system in fish [1,2]. Moreover, it has role in antibacterial actions, health-improving, and preventive outcomes in living animals [3] and is necessary for favourable somatic development [4]. On the other hand, zinc deficiency in fish causes problems in hormone system, growth (i.e.,

* Corresponding author: mharlioglu@firat.edu.tr. ORCID Number of authors: [1] 0000-0003-3290-1092, [2] 0000-0001-8288-0571, [3] 0000-0003-3735-6732, [4] 0000-0002-4393-3527.

reduces survival rates) and accelerates the formation of cataracts in the eye [5-7]. Considering their significant potential in the food industry and human health, antioxidants are gaining popularity all over the world. Antioxidants are defined as substances that can prevent or delay the oxidation of easily oxidized substances, even in small quantities. An antioxidant is also defined as a substance that can inhibit a certain oxidizing enzyme or react with oxidizing agents before damaging other molecules, or a substance that traps metal ions or even repairs the system, such as an iron carrier protein [8]. The living body contains enzymatic and non-enzymatic antioxidant systems such as superoxide dismutase (SOD), catalase (CAT) and glutathione peroxidase (GPX). These systems govern the stability between antioxidants and reactive oxygen species (ROS) [9]. The major mechanism involved in the oxidative cell injury is lipid peroxidation which is a complex process of the breakdown of polyunsaturated fatty acids [10]. Malondialdehyde (MDA), the end product of peroxidation and oxidative damage caused by reactive oxygen species, has been reported to be a vital marker [11]. Antioxidants can protect living things from free radicals and the harmful effects of ROS and prevent the progression of lipid peroxidation [12]. Due to these effects, interest in natural additives with potential antioxidant contents is increasing [13]. Zinc is a necessary microelement demanded for the structure and function of enzymes and many macromolecules that regulate cellular processes. It exhibits antimicrobial, antioxidant, and anti-inflammatory activity by modulating the immune response. It delays oxidative processes for an extended duration by causing the definition of metallothionein [14]. It is an important nutrient that helps the normal development of the living thing and better development of the immune system [15]. Zinc conserves the membranes of cells from iron-commenced lipid oxidation by covering negatively debited areas with possible iron-binding power. However, the interdependent effects of zinc with water-soluble antioxidants and lipids prevent lipid oxidation [16]. In addition, zinc improves the mobilization of antioxidant proteins and enzymes (i.e., catalase and glutathione). It can also replace redox-active elements (i.e., iron and copper) at specific linking locations [14], and can decrease the inflammatory feedback of the body's branchial and viscera by enhancing the body's antioxidant and anti-stress protection abilities [17]. Furthermore, the potential of zinc for delaying oxidative manner is known for a long time. The antioxidant mechanism can be divided into acute and chronic. Although there are substantial verifications on the antioxidant effects of zinc, these processes have not yet been fully clarified. Future research investigating these processes can be possibly identified contemporary antioxidant properties and employs for zinc [18].

The purpose of the present investigation was to determine the antioxidant enzyme activities in the liver and muscle tissue of juvenile *C. carpio* fed diets containing different levels of zinc (T1, control, 85 mg Zn kg^{-1}, T2, 105 mg Zn kg^{-1}, T3, 125 mg Zn kg^{-1} and T4, 145 mg Zn kg^{-1}).

2. Materials and methods

2.1. Experimental protocol.

The Fırat University Ethics Committee's established rules for conducting experiments were followed for this study. In this study, a basal meal consisting of 4,300 kcal/kg gross energy, 6% crude fat, and 35 ± 0.02% crude protein was used (Table 1). The nutritional needs of juvenile common carp fish were taken into consideration when creating the criteria [19]. Then, the experimental meals (T1, control, 85 mg Zn kg^{-1}, T2, 105 mg Zn kg^{-1}, T3, 125 mg Zn kg^{-1} and T4, 145 mg Zn kg^{-1}) containing varied amounts of zinc sulphate monohydrate ($ZnSO_4 \bullet H_2O$, 35% Zn) were created. The proportions of the experimental meals and the control diets for dry matter are listed in (Table 1), crude protein, crude fat, gross energy (kcal/kg), crude ash, crude cellulose, lysin, methionine, calcium, and phosphorus. Also shown in (Table 2) are the percentages of fish meals, soybean meals, yellow maize, wheat flour, oil, vitamin and mineral mix in the control diet that was employed in this study.

In total, 240 juvenile carps (11.7 ± 0.4 g and 9 ± 03 cm in length) were used for this study. Carp juveniles were provided by The Government Water Management Affairs of IX. Area Directory, Keban, Elazığ, Türkiye. Three replicates were used in conducting this study. Each glass aquarium contained 20 juvenile carp (143 cm X 37 cm X 30 cm). The fish were exposed to the experimental conditions for two weeks to get used to the experimental environment. Throughout the period of acclimatization, fish were fed commercial feed. The experiment was set up in 158 L of water with 12 aquariums, one for each treatment, receiving 7 weeks of well-aerated, dechlorinated tap water. 240 juveniles (11.8 ± 0.1 g) were randomly assigned to 4 treatment groups, each with a replicate.

Table 1. The proximate composition of the basal diet in %.

Diet Items	%
Dry Matter	92.4
Crude protein	35
Crude Fat	6
Gross Energy (kcal/kg)	4.300
Raw Ash	7
Raw Cellulose	3.5
Lysine	1.9
Methionine	0.7
Calcium	1.5
Phosphorus	1.2
Zinc (mg/kg)	85

Table 2. Composition of the basal diet in %.

Ingredients	%
Fish Meal	20.0
Soybean Meal	35.0
Yellow Corn	21.5
Wheat flour	20
Fish oil	2.0
Vitamin Mix	1.0
Mineral Mix	0.5
Total	100

Vitamin Mix: Vitamin A 3.22 (I.U/100 g fillet), Vitamin D 208.40 (I.U/100 g fillet), Vitamin E 0.16 (I.U/100 g fillet), Vitamin K 0.16 (I.U/100 g fillet), and Vitamin C 1200 mg/kg. Minerla Mix mg/g: Fe 50, Cu 3, Co 0.01, Mn 20, I 0.1 and Se 0.1

The water was kept at a constant temperature of 27°C with a pH of 7-8, DO of 6 mg/L, total ammonia of 0.6 mg/L, and water Zn of 2.2 mg/L. The experiment was conducted as the sun went through its daily cycle, with each tank being continuously aerated. The amount of food that should be provided to the young each day was calculated using the formula below. It was administered twice daily in equal portions for 60 days.

The daily Feed Amount= Feeding Coefficient x Total Fish Weight / 100 considering water temperature [20]. Feeding coefficient values for 60 days were 2.058 for control, 1.431 for T1, 1.984 for T2 and 2.030 for T3. A commercial juvenile carp feed manufacturer (GÜRDAL YEM, Kahramanmaraş http://www.gurdalyem.com.tr/) provided the basic diet. "Kahramanmaraş Sütçü İmam Üniversitesi Üniversite-Sanayi-Kamu İşbirliği Geliştirme Uygulama ve Araştırma Merkezi (ÜSKM) Laboratuvarlar" conducted the content analysis of the experimental pellets.

The proportionate elements were mixed together until the dough was completely homogeneous, and then water was added in a 1/1 ratio to the dough. The pulp material was pelletized using the mincing equipment. The generated pellets were placed on trays and allowed to dry for 24 hours at 60°C in a feed oven. When determining the size of the pellets, consideration for the fish's weight was made. The rations were maintained in polypropylene storage containers to be used at 4°C.

2.2. Dissection and tissue preparation procedures

The bioengineering laboratories of Munzur University performed the dissection and processing of tissues for analysis. The carp that had been maintained in a deep freezer at -85°C for one day was removed and left to defrost for five hours in order to measure the enzyme activity in the tissues. The bioengineering laboratories of Munzur University performed tissue dissection and preparation for analysis. With sharp scissors, the fish's bellies were separated from the anus and cut all the way to the gills. A little piece of the liver, which is located right below the air sac, was excised, and weighed on a precise balance. Using a phosphate-buffered salt solution with a pH of 7.4 at a rate of 1/5 w/v, the blood was then extracted after the liver had been removed. The solution's pH was adjusted using diluted glucose. The homogenization process was followed by the placement of the liver pieces in Eppendorf tubes. To stop the enzymes from degrading as the homogenizer's cycle temperature increased, ice moulds were

utilized. The CAT underived homogenizer was used for homogenization. After homogenization, the tubes were cooled down and spin at 17000 rpm for 15 minutes in a Nuve 800 R centrifuge to produce supernatants.

2.3. Making analysis

Antioxidant kits were used to process the produced supernatants before being read by the microplate reader. Sunred kits were utilised for MDA and CAT, while BT-Lab kits were used for SOD activity. The kits were used for fish. Using automated micropipettes, samples from the supernatants were transferred to the 96 well plate that was included in the antioxidant kit box. The prepared plates were read in the microplate reader attached to the computer after following the instructions in the kit.

2.4. Statistical analysis

The SPSS 22.0 package programme was used to apply the ANOVA Duncan's test for the evaluation of this data collection. The letters "a, b" are used to represent the outcomes. The data distribution was subjected to a test.

3. Result

When the antioxidant analysis results were examined, it was determined that the SOD values of the liver were 0.623 ± 0.097 U/ml in the control group, decreased to 0.546 ± 0.033 U/ml in the T1 group, increased to 0.651 ± 0.084 U/ml in the T2 group, and attained the greatest value at 0.713 ± 0.220 U/ml in the T3 group. Although numerical differences were detected between the values, no statistically significant difference was found ($p > 0.05$). SOD values for the muscle showed a different situation than the liver, and while it was 0.607 ± 0.146 U/ml in the control group, it increased to 0.751 ± 0.144 U/ml in the T1 group. It started to decrease again with 0.690 ± 0.142 U/ml in the T2 group and 0.646 ± 0.170 U/ml in the T3 group ($p > 0.05$). Muscle and liver results did not show a parallel situation compared to the experimental groups (Table 3).

In the CAT results, while the value of the control group was 0.876 ± 0.067, this value decreased to 0.818 ± 0.117 nmol/dk/m in the T1 group, 0.849 ± 0.115 nmol/dk/m in the T2 group and suddenly decreased to 0.728 ± 0.127 nmol/dk/m in the T3 group ($p < 0.05$). When examined for muscle, the CAT value was 0.724 ± 0.157 nmol/dk/m in the control group, increased to 0.874 ± 0.184 nmol/dk/m in the T1 group, reached the highest value with 1.059 ± 0.148 nmol/dk/m in the T2 group, and 0.854 ± 0.142 nmol/dk/m with a sudden decrease in the T3 group ($p < 0.05$). Muscle and liver results did not show a parallel situation compared to the experimental groups (Table 3).

In the liver analysis of malondialdehyde (MDA), the value in the control group was 1.866 ± 0.255 µM, with a slight increase in the T1 group, it became 1.888 ± 0.419 µM, then suddenly decreased to 1.671 ± 0.230 µM in the T2 group and again reached a value close to 1.868 ± 0.567 µM in the T3 group. ($p > 0.05$). When the muscle data were examined, it was 1.313 ± 0.124 µM in the control group, while it increased to 1.428 ± 0.238 µM in the T1 group, with a slight increase in the T2 group, a value of 1.498 ± 0.207 µM was obtained, and then again with a rapid increase, it reached the highest value of 1.620 ± 0.124 µM ($p < 0.05$). Muscle and liver results did not show a parallel situation compared to the experimental groups (Table 3).

Table 3. SOD, CAT and MDA values (average ± SD) in liver and muscle tissues of carp fish.

	Control (T1)	T2	T3	T4
	SOD values (average ± SD) in liver and muscle tissues of carp fish) (U/ml)			
Liver	0.623±0.097[a]	0.546±0.033[a]	0.651±0.084[a]	0.713±0.220[a]
Muscle	0.607±0.146[a]	0.751±0.144[a]	0.690±0.142[a]	0.646±0.170[a]
	CAT values (average ± SD) in liver and muscle tissues of carp fish (nmol/dk/m)			
Liver	0.876±0.067[a]	0.818±0.117[ab]	0.849±0.115[ab]	0.728±0.127[b]
Muscle	0.724±0.157[a]	0.874±0.184[ab]	1.059±0.148[b]	0.854±0.142[a]
	MDA values (average ± SD) in liver and muscle tissues of carp fish) (µM)			
Liver	1.866±0.255[a]	1.888±0.419[a]	1.671±0.230[a]	1.868±0.567[a]
Muscle	1.313±0.124[a]	1.428±0.238[ab]	1.620±0.124[b]	1.498±0.207[ab]

4. Discussion

Humans can easily absorb and digest important micro and macro elements and proteins in fish meat [21]. On the other hand, it is a challenge for public health to deal with Zn water contamination by industrial expansion [22]. It has been found that Zn accumulates greater amounts in fish feces, creating critical problems in humans [23]. In addition, Zn storing gives rise to nourishing diseases and oxidative stress in animals [24]. For this reason, it is important to develop water treatment technologies to eliminate Zn toxicity [25] as shown in recent studies.

Like other vertebrates, fish have an antioxidant system to deal with oxidation and oxidation reactions occur in the organism through enzymes containing metals such as iron (Fe), copper (Cu) and Zn [26]. In order to alleviate the damage caused by oxidative stress, antioxidant molecules containing glutathione (GSH) undertake the first line of defence [27]. Secondary defence systems consist of antioxidant enzymes such as SOD, which detoxifies superoxide anions, and CAT radical scavenger, which reduces H_2O_2 [27,28]. Dawood et al. [29] indicated that feeding rabbitfish with dietary ZnMet (30 mg/kg) for 49 days showed increased protein utilization, development rate, CAT, SOD, GPx, phenol oxidase activities, and lysozyme. It is also known that MDA is a good biomarker to measure oxidative stress [30]. Lipid peroxidation is the oxidative degradation process of lipids, in which free radicals cause cell damage, especially by taking electrons from polyunsaturated fatty acids (PUFA) in cell membranes [31]. It was found that supplementing diets with excellent levels of zinc extremely improves the antioxidant actions of fish [32,33].

Ibrahim et al. [34] found that growth and the immune system improved, and the amount of growth and antioxidant enzymes (SOD and CAT) increased, at the end of the study in which they fed a fish with antioxidant feed. Furthermore, as a result of a study conducted to evaluate the antioxidant effect of dietary Zn levels on juvenile yellow catfish (*Pelteobagrus fulvidraco*), a significant decrease in MDA level was observed [33], In addition, it was observed that SOD activity rose and malondialdehyde (MDA) amount decreased with the increase in nutritional Zn amounts reached the required level. Hepatic CAT activity did not differ significantly between treatments. The SOD and CAT values of the finding obtained in this investigation are unchanging with the above studies. Only the muscle values of the MDA analysis were quite different from these studies, and the liver values were not very different from the control group, even if the liver values were not as low as desired. The best value for MDA was obtained in the T2 muscle trial group.

Excessive absorption of Zn adversely affects reproductive performance in fish and may limit the uptake and use of other minerals [34]. Furthermore, it can disrupt the metabolic activities that cause both ion balance and oxidative destruction in fish [35,36]. As a result of ZnO toxicity studies in fish, an average dose value was found [37,38]. Depending on this situation, it is recommended to use ZnONPs in average amounts to diminish the harmful effects on the toxicity range and development rate [39,40].

Wu et al. [41] mentioned that fed young grass carp (*Ctenopharyngodon idella* Val.) with Zn-added feeds. The weight gain, specific growth rate, feed intake, feed conversion rate, SOD and CAT activities increased significantly up to a point and then decreased with increasing Zn levels. Malondialdehyde (MDA), on the other hand, decreased significantly with increasing zinc level up to a point and then increased again. Although muscle values in the results obtained from SOD analyses revealed values similar to the above study, liver results on the contrary showed a continuous increase. CAT analysis studies, whereas, revealed values more compatible with the above study. MDA values, on the other hand, gave more similar results to the above study.

Musharraf [42] indicated that in the study on the nutritional zinc demand for Indian major carp, serum superoxide dismutase, GPX, CAT, and alkaline phosphatase actions returned certainly, at the same time as malondialdehyde amount was 51.42 mg kg^{-1} nutritional zinc gave a negative response. Similar results were obtained in this study as well. While the recommended Zn ratio in fish for Zn is 35 mg kg^{-1}, the use of much higher amounts of Zn in the above study and in the feed used in this study may be the reason why the results are similar.

Huang et al. [7] conducted a study to observe the nutritional Zn demand of adult Nile tilapia and to assess its impacts on antioxidant responses. The weight gain (%) of the fish developed with accelerating nutritional Zn from 15.9 to 53.5 mg/kg for more than a period of 84 days and then fell over these amounts. It revealed that the activities of total superoxide dismutase content increased significantly, while catalase activities reduced remarkably with the expansion of nutritional Zn grade.

Feng et al. [43] studied the influences of nutritional Zn on lipid peroxidation, amino acid oxidation, and antioxidant defence of juvenile Jian carp by nourishing them with increased Zn amounts. The findings indicated that the content of malondialdehyde (MDA) in the serum was lowest in the food having 15.3 mg zinc kg^{-1}. SOD and CAT were increased with escalating nutritional Zn up to 40.8 mg zinc kg^{-1} food and then stabilized. The findings of the present investigation showed that ZN reduces lipid peroxidation and amino acid oxidation and improves antioxidant defence in carp juveniles. Although it could not reach the desired values, Zn showed positive effects on antioxidant values SOD and CAT and MDA values in this research.

Saddick et al. [44] informed that the lethal concentrations (LC50) of Zinc nanoparticles (ZnNPs (500 and 2000 μg L^{-1})) on *Oreochromis niloticus* and *Tilapia zillii*. As a result of the study, while SOD and CAT values decreased, MDA values increased significantly. The reason why the analysis results are not completely perfect in Zn feeding may be due to the fact that the Zn ratio is slightly higher, as we have mentioned before.

Mohammadya et al. [45] found that with higher Zn availability than the ZnSO4 form, it promoted growth, modulated digestive enzymes, improved serum biochemical response and immune antioxidant enzyme capacity in Nile tilapia. In addition, they found that iinsufficient zinc consumption in a short time may show harmful symptoms and its effect may become evident. However, the bone mineralization and growth performance of fish might be badly affected by using the huge level of Zn consumption [34], Moreover, [34], stated that high zinc consumption may negatively affect the bone mineralization and growth performance of fish.

Kumar et al.; Alvarez et al. [46,47], studied the influence of Zn on the development rate and cellular metabolic stress of fish maintained to various stresses affected by the high temperature due to climate change. Yu et al. [48] at the end of research indicated that where they fed *Oncorhynchus kisutch* puppies with Zn-added feeds, found that as the amount of Zn in the feeds increased. The results showed that the feed conversion ratio (FCR) was improved in the Pb and high temperature–maintained fish. On the other hand, zinc supplementation in the carp fish diet has enhanced weight gain (%), FCR, PER, and SGR. Compared to the study of [46,49], the results obtained in our study are better, especially in feed conversion ratio.

5. Conclusion

Based on the results of the present research, it is possible to significantly improve antioxidant defense by using convenient level of zinc in carp fish juvenile diet (105 mg/kg). Especially the results of SOD and CAT analysis confirm the positive effects of using 105 mg Zn in the diets to increase the growth performance of juvenile carp in this study. Further researches are required to investigate the zinc demands of different juvenile size of carps. In addition, the differences in dietary Zn demands among fish species can be due to the adaptive mechanism of metal absorption and utilization in their habitats when the results obtained in this study are compared with the results of other studies in the literature. Therefore, further research is needed on the characteristics and structures of the developmental adaptation of fish to mineral demand. The findings suggest that supplementing the diet of common carp fry with appropriate levels of zinc can have positive effects on antioxidant enzyme activities in their muscle and liver tissues. This indicates that zinc plays a significant role in the nutrition and overall health of carp fish. However, it is important to avoid excessive zinc supplementation, as it may lead to adverse effects on fish health and growth.

References

[1] National Research Council (NRC). Nutrient requirements of fish and shrimp. National Academies Press, Washington, DC 2011; (376 + XVI p).
[2] Moazenzadeh K, Islami HR, Zamini A, Soltani M. Dietary zinc requirement of Siberian sturgeon (*Acipenser baerii*, Brandt 1869) juveniles, based on the growth performance and blood parameters. Int Aquat Res 2017; 9: 25-35.
[3] Wang B, Feng W, Wang M, Wang T, Gu Y, Zhu M. Acute toxicological impact of nano- and submicro-scaled zinc oxide powder on healthy adult mice. J Nanopart Res 2008; 10(2): 263-276.
[4] Paski SC, Xu Z. Labile intracellular zinc is associated with 3T3 cell growth. J.Nutr Biochem 2001; 12(11): 655-661.
[5] Clegg MS, Keen CL, Donovan SM. Zinc deficiency induced anorexia influences the distribution of serum insulin-like growth factor binding proteins in the rat. Metab 1995; 44(11): 1495-1501.
[6] Ekinci D, Ceyhun SB, Aksakal E, Erdoğan O. IGF and GH mRNA levels are suppressed upon exposure to micromolar concentrations of cobalt and zinc in rainbow trout white muscle. Comp Biochem Physiology Part - C Toxicol Pharmacol 2011; 153(3): 336-341.
[7] Huang F, Jiang M, Wen H, Wu F, Liu W, Tian J, Yang C. Dietary zinc requirement of adult Nile tilapia (*Oreochromis niloticus*) fed semi-purified diets, and effects on tissue mineral composition and antioxidant responses. Aquacult 2015; 439: 53-59.
[8] Brewer MS. Natural Antioxidants: Sources, Compounds, mechanisms of action, and potential applications. J Food Sci Educ 2011; 10(4): 221-247.
[9] Salehi B, Martorell M, Arbiser JL, Sureda A, Martins N, Maurya PK, Sharifi-Rad M, Kumar P, Sharifi-Rad J. Antioxidants: positive or negative actors? Biomol 2018; 8(4): 124.
[10] Meriç, İ. Evaluation of sunflower seed meal in feeds for carp: Antinutritional effects on antioxidant defense system, JFAE 2013: 11(2): 1128-1132.
[11] Nielsen F, Mikkelsen BB, Nielsen JB, Andersen HR, Grandjean P. Plasma malondialdehyde as biomarker for oxidative stress: reference interval and effects of life-style factors. Clin Chem 1997; 43: 1209-1214.
[12] Kalaiselvi T, Panneerselvam C. Effect of L-carnitine on the status of lipid peroxidation and antioxidants in aging rats. JNB 1998; 9: 575-581.

[13] Ma JJ, Xu ZR, Shao QJ, Xu JZ, Hung Silas SO, Hu WL, Zhuo LY. Effect of dietary supplemental L-carnitine on growth performance, body composition and antioxidant status in juvenile black sea beram, *Sparus macrocephalus*. Aquac Nutr 2008; 14: 464-471.
[14] Jarosz M, Olbert M, Wyszogrodzka G, Młyniec K, Librowski T. Antioxidant and anti-inflammatory effects of zinc zinc-dependent NF-κB signalling. Inflammopharma 2017; 25: 11-24.
[15] Fazil DM, Hamdi H, Al-Barty A, Zaid AA, Parashar SKS, Das B. Selenium and zinc oxide multinutrient supplementation enhanced growth performance in zebra fish by modulating oxidative stress and growth-related gene expression. Front Bioeng Biotechnol 2021; 9: 1-12.
[16] Zagoa MP., Oteiza PI. The antioxidant properties of zinc: interactions with iron and antioxidants. Free Radic Biol Med 2001; 31(2): 266-274.
[17] Ren HT, An HY, Du MX, Zhou J. Effects of zinc adaptation on histological morphology, antioxidant responses, and expression of immune-related genes of grass carp (*Ctenopharyngodon idella*). Biol Trace Elem Res 2022; 200(12): 5251-5259.
[18] Powell SR. The antioxidant properties of Zinc. J Nutr 2000; 130(5): 1447-1454.
[19] National Research Council (NRC) (1993). Nutrient Requirements of Fish, Washington, D.C, USA, National Academies Press. 114 p.
[20] Song-bo CH, Wei-xing CH, Zhao-ting F. Effect of water temperature on feeding rhythm in common carp (*Cyprinus carpio*) haematopterus Temminck Schlegel. J Northeast For Univ 2012; 19(1): 57-61.
[21] Wang N, Yin Y, Xia C, Li Y, Liu J, Li Y. Zn-enriched *Bacillus cereus* alleviates Cd toxicity in mirror carp (*Cyprinus carpio*): Intestinal microbiota, bioaccumulation, and oxidative stress. Biol Trace Elem Res 2021; 200: 1-10.
[22] Liu F, Li M, Lu J, La, Z, Tong Y, Wang M. Trace metals (As, Cd, Cr, Cu, Hg, Ni, Pb, Zn) and stable isotope ratios (δ13C and δ15N) in Fish from Wulungu Lake, Xinjiang, China. IJERPH 2021; 18: 9007.
[23] El-Moselhy KM, Othman A, Abd El-Azem H, El-Metwally M. Bioaccumulation of heavy metals in some tissues of fish in the Red Sea. Egypt J Basic Appl Sci 2014; 1: 97-105.
[24] Connolly M, Fernández M, Conde E, Torrent F, Navas JM, Fernández-Cruz ML.Tissue distribution of zinc and subtle oxidative stress effects after dietary administration of ZnO nanoparticles to rainbow trout. Sci Total Environ 2016; 551: 334-343.
[25] Loro VL, Jorge MB, da Silva KR, Wood CM. Oxidative stress parameters and antioxidant response to sublethal waterborne zinc in a euryhaline teleost *Fundulus heteroclitus*: protective effects of salinity. Aquat Toxicol 2012; 110: 187-193.
[26] Yapici M, Meriç Turgut İ. Farklı doz ve sürelerde levonorgestrel uygulamasının zebra balıklarında (D*anio rerio*, Hamılton, 1822) antioksidatif metabolizma üzerine etkileri, Ankara Üniversitesi Fen Bilimleri Enstitüsü, 2023, Ankara. PhD thesis, 80 p.
[27] Roberts AP, Oris JT. Multiple biomarker response in rainbow trout during exposure to hexavalent chromium. Comp Biochem Physiol Part - C Toxicol Pharmacol 2004; 138: 221-228.
[28] Bagnyukova V, Chahrak OI, Lushchak V. Coordinated response of goldfish antioxidant defences to environmental stress. Aquat Toxicol 2006; 78: 325-331.
[29] Dawood MAO, Alagawany M, Sewilam H. The role of zinc microelement in aquaculture: a Review. Biol Trace Elem Res 2021; 200(8): 3841-3853.
[30] Wang J, Xiao J, Zhang J, Chen H, Li D, Li L, Cao J, Xie L, Luo Y. Effects of dietary Cu and Zn on the accumulation, oxidative stress and the expressions of immune-related genes in the livers of Nile tilapia (*Oreochromis niloticus*). Fish Shellfish Immunol 2020; 100: 198-207.
[31] Kanazawa K. Tissue injury induced by dietary products of lipid peroxidation. In: Corongiu, F. (Ed.), Free Radicals and Antioxidants in Nutrition. Richelieu Press, London, 1993; 383-399.
[32] Jiang N, Wu F, Huan F, Wen H, Liu W, Tian J, Yang C, Wang W. Effects of dietary Zn on growth performance, antioxidant responses, and sperm motility of adult blunt snout bream, *Megalobrama amblycephala*. Aquacult 2016; 464: 121-128.
[33] Luo Z, Tan XY, Zheng JL, Chen QL, Liu CX. Quantitative dietary zinc requirement of juvenile yellow catfish *Pelteobagrus fulvidraco*, and effects on hepatic intermediary metabolism and antioxidant responses. Aquacult 2011; 319(1-2): 150-155.
[34] Ibrahim MS, Mohammady EY, El-Erian MA, Ragaza JA, El-Haroun ER, Hassaan MS. Dietary zinc oxide for growth and immune stimulation of aquatic animal species: A Review. Proc Zool Soc 2023; 76: 59-72.
[35] Shiau SY, Jiang C. Dietary zinc requirements of grass shrimp, *Penaeus monodon*, and effects on immune responses. Aquacult 2006; 254: 476-482.
[36] Shyong JS, Sun LT. Effects of dietary zinc levels on zinc concentrations in tissues of common carp. J Nutr 1981; 111: 134-140.
[37] Wehmas LC, Anders C, Chess J, Punnoose A, Pereira CB, Greenwood JA. Comparative metal oxide nanoparticle toxicity using embryonic zebrafish. Toxicol Rep 2015; 2: 702-715.
[38] Verma SK, Mishra AK, Suar M, Parashar SKS. In vivo assessment of impact of titanium oxide nanoparticle on zebrafish embryo. AIP Conference Proceedings 2017; 1832, 040030.
[39] Franklin NM, Rogers NJ, Apte SC, Batley GE, Gadd GE, Case PS. Comparative toxicity of nanoparticulate ZnO, bulk ZnO, and ZnCl2to a freshwater microalga (*Pseudokirchneriella subcapitata*): The importance of particle solubility. ESST 2007; 41: 8484-8490.
[40] Lin D, Xing B. Phytotoxicity of nanoparticles: Inhibition of seed germination and root growth. Envir Pollut 2007;150: 243-250.

[41] Wu YP, Feng L, Jiang WD, Liu Y, Jiang J, Li SH, Tang L, Kuang SY, Zhou XQ. Influence of dietary zinc on muscle composition, flesh quality and muscle antioxidant status of young grass carp (*Ctenopharyngodon idella* Val.). Aquac Rep 2015; 45(10): 2360-2373.
[42] Musharraf M, Khan MA. Dietary zinc requirement of fingerling Indian major carp, *Labeo rohita* (Hamilton). Aquac Rep 2019; 503: 489-498.
[43] Feng F, Tan LN, Liu Y, Jiang J, Jiang WD, Hu K, Li SH, Zhou XQ. Influence of dietary zinc on lipid peroxidation, protein oxidation and antioxidant defence of juvenile Jian carp (*Cyprinus carpio* var. Jian). Aquac Nutr 2011; 17(4): 875-882.
[44] Saddick S, Afifi M, Abu Zinada OA. Effect of zinc nanoparticles on oxidative stress-related genes and antioxidant enzymes activity in the brain of *Oreochromis niloticus* and *Tilapia zillii*. Saudi J Biol Sci 2017; 24(7): 1672-1678.
[45] Mohammadya EY, Soaudyb MR, Abdel-Rahmanc A, Abdel-Tawwabd M, Hassaan MS. Comparative effects of dietary zinc forms on performance, immunity and oxidative stress-related gene expression in Nile tilapia, *Oreochromis niloticus*. Aquacult 2021; 532: 1-11.
[46] Kumar N, Krishnani KK, Singh NP. Effect of zinc on growth performance and cellular metabolic stress of fish exposed to multiple stresses. Fish Physiol Biochem 2020; 46: 315-329.
[47] Alvarez RM, Morales AE, Sanz A. Antioxidant defences in fish: biotic and abiotic factors. Rev Fish Biol Fish 2005; 15: 75-88.
[48] Yu, HR, Li LY, Shan LL, Gao J., Ma CY, Li X. Effect of supplemental dietary zinc on the growth, body composition and anti-oxidant enzymes of coho salmon (*Oncorhynchus kisutch*). Aquac Rep 2021; 20: 100744.
[49] Avila-Nava A, Pech-Aguilar AG, Lugo R, Medina-Vera I, Guevara-Cruz M, Gutiérrez-Solis A. Oxidative stress biomarkers and their association with mortality among patients infected with SARS-CoV-2 in Mexico. Oxidative Med Cell Longev 2022: 1-8.

Turkish Journal of Science & Technology
19(2), 387-396, 2024

Research Paper
https://doi.org/10.55525/tjst.1448314

High-Precision Angle Measurement for Position Control in Industrial Drives Systems with Shaft Resolver

Reşat ÇELİKEL[1], Ahmet GÜNDOĞDU[2*]
[1] Dept. of Mechatronics Engineering, Faculty of Technology, Fırat University, Elazığ, Türkiye
[2] Dept. of Electrical and Electronics Engineering, Faculty of Engineering and Architecture, Batman University, Batman, Türkiye
[1] rcelikel@firat.edu.tr, [2*] ahmet.gundogdu@batman.edu.tr

(Geliş/Received: 07/03/2024; Kabul/Accepted: 20/09/2024)

Abstract: Resolver is a shaft angle sensor, which is mechanically connected to the motor shaft and operates according to the induction principle. A high frequency sinusoidal signal is applied to its input and produces two signals in the form of sine and cosine at its output. The output signals include the angle information of the motor shaft. Using these signals, the shaft angle of the motor is determined. In the study, a sinusoidal signal at the 5 kHz frequency was applied to an input resolver as the conventional method. After, the fact that applied to two PWM signals which has a duty ratio d=0.5 at 20 kHz and 100 kHz frequency is proposed as different from the conventional method. These PWM signals are the input signals of the resolver. Thus, complex equipment will not be needed to produce the high frequency sinusoidal signal. With only a simple amplifier circuit, a high frequency input signal will be produced. More sensitive angle information will be obtained with high frequency stimulation. A simulation study of conventional and proposed methods has been performed in MATLAB/Simscape environment. As a result of the simulation study, the information on the motor angle obtained from both methods was compared by using figures and details. By increasing the applied PWM signal from 20 kHz to 100 kHz, measurement errors related to shaft angle change were minimized and more precise position information was obtained.

Key words: Shaft resolver, position control, ındustrial drives, robotic.

Mil Resolver'li Endüstriyel Sürücü Sistemlerde Pozisyon Kontrolü İçin Yüksek Hassasiyetli Açı Ölçümü

Öz: Resolver motor miline mekanik olarak bağlanan ve indükleme prensibine göre çalışan mil açısı algılayıcısıdır. Girişine yüksek frekanslı sinusoidal sinyal uygulanır ve çıkışında sinus ve cosinus formunda iki adet sinyal üretir. Bu çıkış sinyalleri, motor milinin pozisyon bilgisini içerir. Bu sinyaller kullanılarak motorun mil açısının tespiti yapılır. Bu çalışmada resolver'in girişine önce geleneksel yöntem olarak 5 kHz frekansında bir sinusoidal sinyal uygulanmıştır. Daha sonra bu geleneksel yöntemden farklı olarak resolver'in davranışını analiz etmek amacı ile girişine 20 kHz ve 100 kHz frekansında d=0,5 görev periyoduna sahip iki ayrı PWM sinyalinin uygulanması önerilmiştir. Bu PWM sinyalleri resolveri'n giriş sinyallerini oluşturmaktadır. Böylece yüksek frekanslı sinusoidal sinyali üretmek için karmaşık donanıma ihtiyaç duyulmayacaktır. Sadece basit bir yükselteç devresi ile yüksek frekanslı giriş sinyali üretilmiş olacaktır. Yüksek frekanslı uyartım ile daha hassas açı bilgisi elde edilecektir. Geleneksel yöntem ile önerilen yönteme ilişkin benzetim çalışmaları MATLAB/Simscape ortamında gerçekleştirilmiştir. Benzetim çalışmaları sonucunda her iki yöntemden elde edilen motor açı bilgisi verilen grafikler yardımı ile detaylı olarak karşılaştırılmıştır. Uygulanan PWM sinyalinin 20 kHz 'den 100 kHz 'e yükseltilmesi ile birlikte mil açı değişimine ait ölçüm hataları minimize edilerek daha hassas konum bilgisi elde edilmiştir.

Anahtar kelimeler: Mil resolver, konum kontrolü, endüstriyel sürücüler, robotik.

1. Introduction

A stable measurement of speed and position is required in many industrial applications. Electric motors are used for position control in many industrial applications such as robotic systems, machine tools, telescopes, and radars [1]. Resolvers, on the other hand, are preferred for detecting the angular displacement of the motor shaft due to their high stability, mechanical durability, stable behavior in transient states, and lack of common mode noise [2, 3]. Resolvers are electrical machines with three windings that work based on Faraday's principle of electromagnetic induction and are mechanically connected to the motor shaft. The second and third windings are mechanically placed in the body at an angle of 90°. By applying a high-frequency sinusoidal signal to the first winding, signals varying depending on the shaft angle of the motor are obtained from the second and third windings. The signals obtained from the second and third windings are converted into sine and cosine signals by using modulation techniques. Using these obtained signals and with the help of mathematical operations, the determination of the shaft angle of the motor is easily made [4, 5]. To achieve this, many different Resolver-to-Digital (R/D) converter circuit applications have been performed in the literature. The main purpose of these R/D

* Corresponding author: ahmet.gundogdu@batman.edu.tr. ORCID Number of authors: [1] 0000-0002-9169-6466, [2] 0000-0002-8333-3083

converters is to reduce the cost and error amount [6, 7]. Here, the input signal applied to the first winding of the resolver is generated by Digital Signal Processors (DSPs). The output signals of the Resolver are measured using the analog inputs of DSP. Thus, DSP, which is used for motor control applications, is also used for determining the shaft angle. As a result, the reduction of the total cost has been ensured. On the other hand, tables have been used for the purpose of realizing simpler software [8-10]. In recent years, quite a lot of studies have been conducted on the realization of R/D converters through software instead of being realized by circuit design [11-13]. In many other studies, nonlinear state observers, dq transformations, and modified angle tracking observers have been used to reduce the measured angle error [14-15]. With the help of FPGA, which has been widely used in motor control applications in recent years, resolver signals have been measured, and shaft angle has been obtained. Thus, it has been shown that high-level processors can be used to measure resolver signals [16-17]. Artificial Neural Networks (ANNs) used for speed estimation in motor control applications have been used to reduce noise in resolver signals and errors in signal measurement [18-19].

The fact that the excitation signal of the first winding, which is the input winding of the resolver, is in sinusoidal form and has high frequency makes it difficult to apply from the point of view of microprocessors. In addition, making an analog circuit makes it difficult to implement. To eliminate this problem, a square wave excitation signal was applied to the first winding of the resolver. Thus, the process was simplified considerably, and operation with low error amounts at high speeds was achieved by applying high frequency [20]. In a very recent study, a PCB-based axial intelligent resolver was developed. Square wave excitation is used in the resolver decoder. Thus, excitation at a frequency of 10 kHz is provided and motor control is also realized at the same time [21]. A trapezoidal excitation system derived from square wave excitation was developed to reduce measurement errors. Thus, output signals with lower harmonic content could be produced [22]. Considering the studies related to measuring the resolver signal with the help of DSP and determining the shaft angle, it is seen that additional circuits or filters are needed for the excitation of the first winding of the resolver. In this study, a Pulse-Width Modulation (PWM) signal with a duty period of d=0.5 was used as the resolver input signal. Thus, it is envisaged that the resolver operating with the logic of a transformer will act as a pulse transformer, and the shaft angle can be determined by regular sampling. With this method, it was aimed to generate the resolver input signal directly using hardware PWM blocks of DSP without using any additional signal circuit. The proposed method offers significant improvements in terms of software and hardware. The simulation study of the proposed method was carried out with MATLAB/Simscape blocks.

2. Material and Method

2.1. Resolver

Resolver is a motor shaft position-measuring sensor that is mechanically connected to the motor shaft and operates based on the principle of induction. The resolver is comprised of one first winding and two second windings placed with a 90° angle difference, as shown in Figure 1. A high-frequency sinusoidal voltage between 1 kHz and 10 kHz is applied to the first winding. Depending on the displacement of the motor shaft, sine and cosine signals are obtained from the second windings. These obtained signals include both the signal of the first winding and vary depending on the change of the shaft angle. From these signals, sine and cosine signals, from which the shaft angle will be calculated using different modulation techniques, are obtained. The expression of the first winding voltage and the second winding voltages of the resolver are given in Equations (1), (2), and (3).

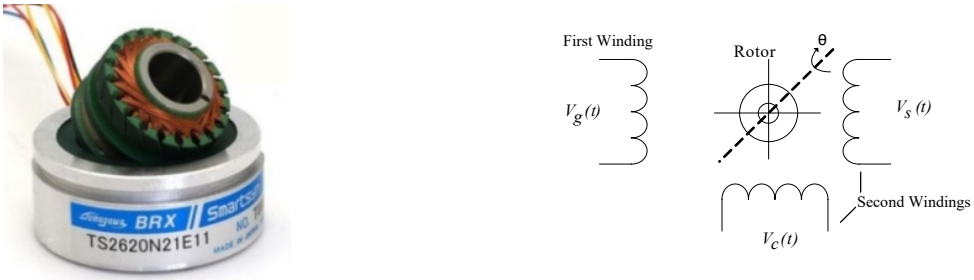

Figure 1. Mechanical and electrical structure of Resolver.

$$V_g(t) = V_m \times sin\,(\omega_e t) \tag{1}$$

$$V_s(t) = K_i \times V_m \times sin\,(\omega_e t) \times \sin\,(\theta) \tag{2}$$

$$V_c(t) = K_i \times V_m \times sin\,(\omega_e t) \times \cos\,(\theta) \tag{3}$$

where ω_e is the angular velocity of the input voltage and has a high frequency. K_i is the resolver constant, V_m is the maximum value of the first winding voltage, and θ is the shaft angle. The maximum values of the second winding voltages change depending on the input voltage in each period, and by sampling them in each period, sine and cosine signals, from which the motor angle will be calculated, are obtained. The waveforms of the resolver's first winding voltage and second winding voltages are seen in Figure 2.

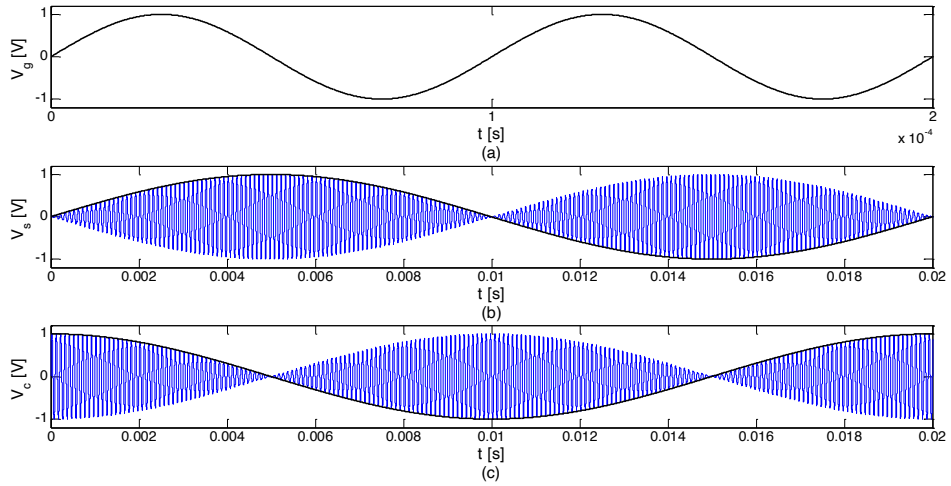

Figure 2. a) First winding voltage, b) Sinus voltage of first winding, c) Cosine voltage of second winding.

The motor shaft angle is calculated using these sine and cosine signals with the help of the equation given in Equation 4.

$$\theta = atan\,(\frac{V_s}{V_c}) \tag{4}$$

2.2. Applied Signals to the Resolver Input

In conventional methods, a sinusoidal voltage is applied to the resolver input as shown in Figure 3(a). An analog circuit design is being made to obtain this sinusoidal signal. This analog circuit design adds cost and difficulty to the system. In the newly developed methods, as shown in Figure 3(b), a bidirectional square wave signal with positive and negative amplitude is applied to the resolver input to increase the frequency of the resolver input signal and thus to perform angle measurement more effectively and with a lower error rate in high-speed applications. However, in this method, it is necessary to make an additional circuit design to produce the input signal. On the other hand, in the method proposed in this article, a unidirectional square wave signal with only positive amplitude obtained from the output of the PWM block of the DSP, as shown in Figure 3(c), was applied to the resolver input.

In this study, the positive part of the hysteresis curve is used because the input voltage is used in the range between + Vmax and 0 V. Since -Vmax is not used, the resolver has been thought of as a pulse transformer that triggers in a positive direction. In the secondary windings in pulse transformers, there will be short-term voltage changes on the rising edge and falling edge of the pulse on the primary side. The reason for these tensions is a short-term magnetic flux change. If it is in the steady state, the induced voltage will be zero. In this study, the maximum values of short-term voltage changes were sampled.

Microprocessors have been extensively used in recent years for processing resolver signals and obtaining angle information. However, high frequency sine input cannot be produced directly with a microprocessor. Additional circuits are needed here. With the proposed study, a +5V logic signal to be generated by the microprocessor can be applied to resolver with a simple amplifier. On the other hand, producing the sinusoidal input signal requires a complex and well-designed structure. As mentioned in the literature, if it is desired to generate a sinusoidal input signal with a microprocessor, this can be accomplished using high-grade filters and additional circuits.

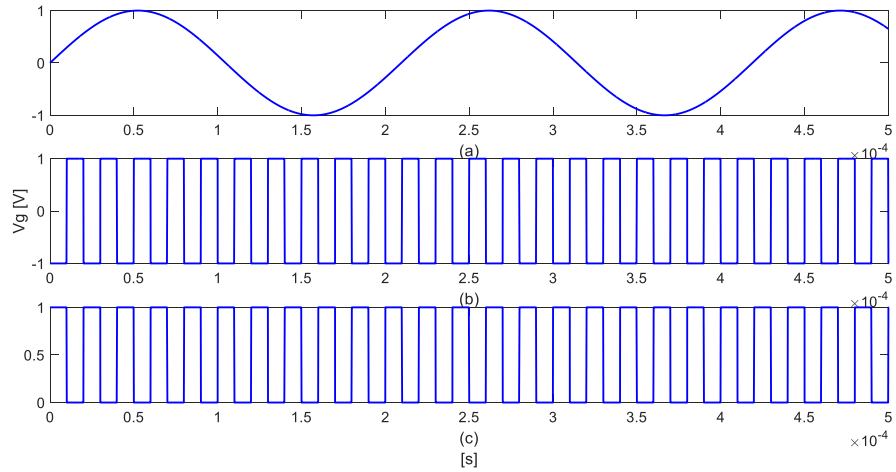

Figure 3. Different input signals to resolver a) Conventional method, b) Square wave, c) Proposed method.

In addition, delays caused by filters must also be compensated with software. High-frequency excitations are challenging situations for magnetic circuits. In the literature, there are experimental studies carried out at a frequency of 40 kHz. However, the developing material technology has brought about significant improvements in the technical properties of magnetic cores. With these developments, these levels of stimulation are now possible.

The expression of the input signal belonging to the conventional method is given in Equation 1. The frequency of the signal used in the proposed method and its transmission time are given in Equations (5) and (6).

$$f_s = \frac{1}{T_p} \tag{5}$$

$$T_{on} = dxT_p \tag{6}$$

f_s is the switching frequency, T_p is the period of the input signal, T_{on} is the duration of the transmission, and d is the duty cycle. Duty cycle (d) is calculated as in Equation 7 and varies between 0 and 1.

$$d = \frac{T_{on}}{T_{on} + T_{off}} \tag{7}$$

where T_{off} is the time passing during the off period. The duty cycle was taken as constant d=0.5 in this study. The use of a fixed duty cycle significantly reduces the operational load density required for the production of the PWM mark. Thus, higher frequency PWM signals can be obtained from the PWM outputs of the DSP. If the value of the duty cycle d is too small, voltage induction in the opposite direction occurs without the desired level of induction event occurring. To induce positive and negative voltages and to equal the slope going toward zero, d=0.5 was chosen.

Sampling of the voltage waveform obtained from the second side windings is performed on the rising and falling edges of the input signal. Depending on the amplitude and rate of change of the ∅ flux generated by the input voltage at these points, a voltage is induced in the secondary windings on the second side in accordance with Equation 8. This induced voltage is a short-term impulse voltage formed at the rising and falling edges of the primary winding voltage.

$$e = -N\frac{d\emptyset}{dt} \tag{8}$$

where N is the winding number, ∅ and is the magnetic flux. Since the sampling process is performed in a very short time, this voltage can be considered as a DC voltage. Instead of the input signals seen in Equations 2 and 3,

the output voltages given in Equations 9 and 10, which can be sampled in a short time, can be written. Here, V_{m2} also includes the voltage component.

$$V_s(t) = K_i \times V_{m2} \times \sin(\theta) \tag{9}$$

$$V_c(t) = K_i \times V_{m2} \times \cos(\theta) \tag{10}$$

3. Results

In this study, the input and output signals of the resolver connected to the shaft of a DC motor were examined. For this purpose, a simulation study was carried out using MATLAB/Simscape blocks. In the simulation study, the sinusoidal input signal of the conventional method given in Figure 3(a) was applied to the resolver input first, and then the unidirectional square wave positive input signal of the proposed method given in Figure 3(c) was applied. The simulation model is given in Figure 4. The shaft angle information obtained for both cases was compared in detail. High sampling rate comparisons were made with fewer errors, especially in the high-speed region.

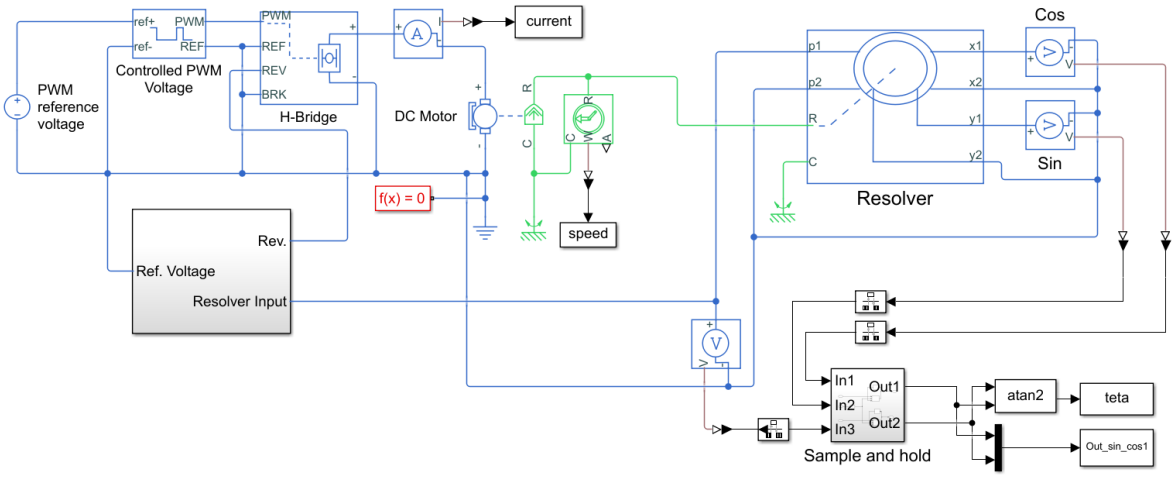

Figure 4. Simulation model consisting of DC motor, resolver, and drivers.

In this simulation study, a *TS2620N21E11* coded resolver belonging to Smartsyn company and a DC motor with the no-load operating speed of 10700 rpm were preferred. An H-bridge driver was used for the bidirectional operation of the motor. The sampling frequency of the simulation study was 1µs. The motor was operated at ±10700 rpm without load. The speed and current graphs of the motor are shown in Figure 5. While a sinusoidal voltage at a frequency of 5 kHz was applied as the resolver input signal in the conventional method, a PWM with a frequency of 20 kHz and a duty cycle of d=0.5 was applied first in the proposed method. While the sampling process is performed at the peak values of the sinusoidal signal in the conventional method, it was performed at each rising edge in the proposed method. Since the reading speeds of the analog inputs of DSPs are very high today, there will not be any problems during the reading process. The most important point in the proposed method is that the analog measurement to be made works synchronously with the rising edge of the input signal. The resolver output signals related to the conventional method in which a sinusoidal input voltage of 5 kHz is applied are shown in Figure 6(a), and the sampled resolver output signals at the maximum points of the input signals in sine form are shown in Figure 6(b).

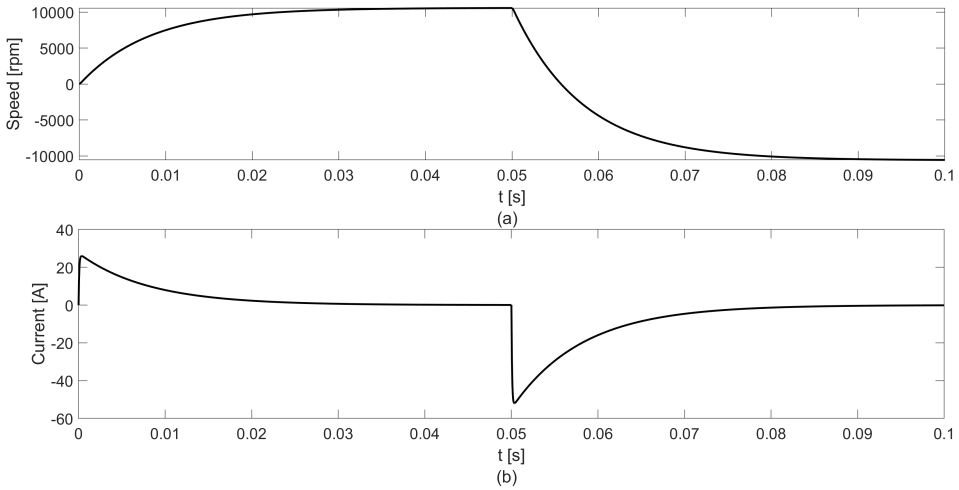

Figure 5. a) DC motor speed curve, b) DC motor current curve.

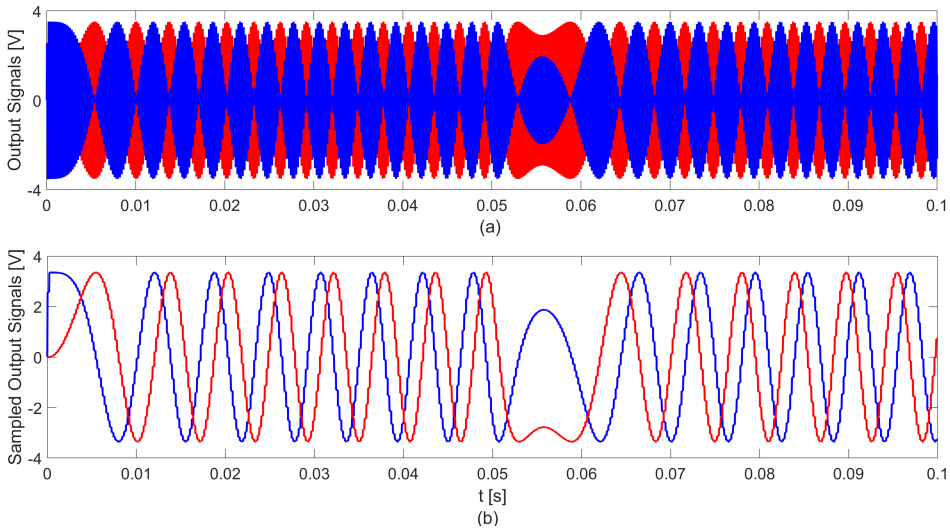

Figure 6. The Conventional Method - for 5 kHz a) Resolver output signals, b) Resolver output signals sampled at maximum points.

In Figure 7(a) and Figure 7(b), the variation of the output signals obtained by the conventional method and the output signals sampled at the maximum points of the input sine signal over a time interval of 0.02s to 0.024s is observed. The resolver output signals obtained by the 20 kHz input PWM signal related to the proposed method are seen in Figure 8(a), while the resolver output signals sampled on the rising edge of the input PWM wave are seen in Figure 8(b). In Figure 9(a) and Figure 9(b), the change in the time interval of 0.02s to 0.024s of the output signals obtained in Figure 8 is observed. In order to see the advantage of the proposed method, sampled sine and cosine signals can be compared using conventional and recommended methods. In addition, it is possible to increase the frequency of the PWM resolver input signal by hardware. Therefore, examining the resolver output signals at an input frequency of 100 kHz will be useful to better understand the advantage of the proposed method.

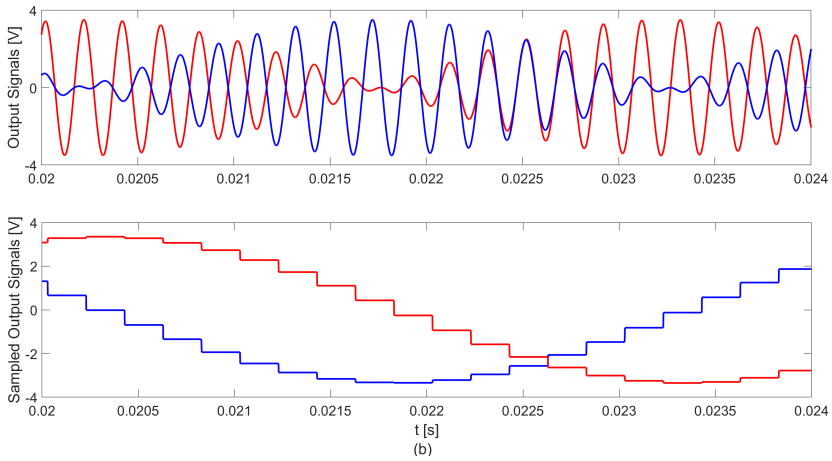

Figure 7. The Conventional Method - for 5 kHz (at an interval of 0.02-0.024 s) a) Resolver output signals, b) Resolver output signals sampled at maximum points.

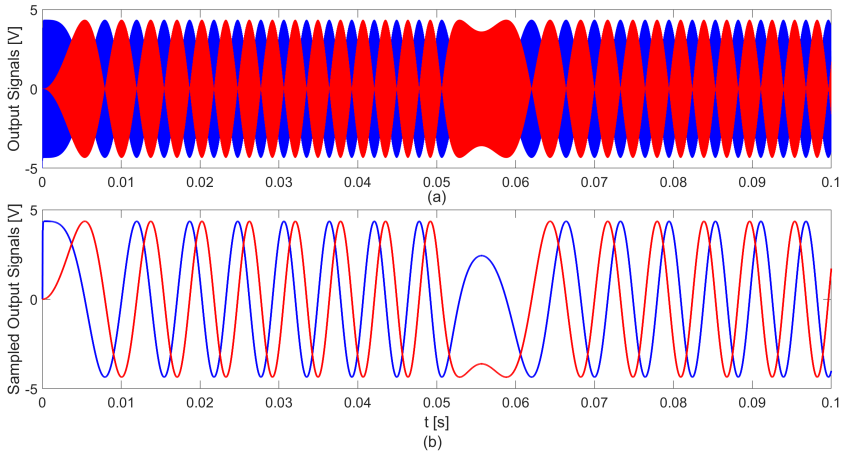

Figure 8. The Proposed Method - for 20 kHz a) Resolver output signals, b) Resolver output signals sampled on the PWM rising edge.

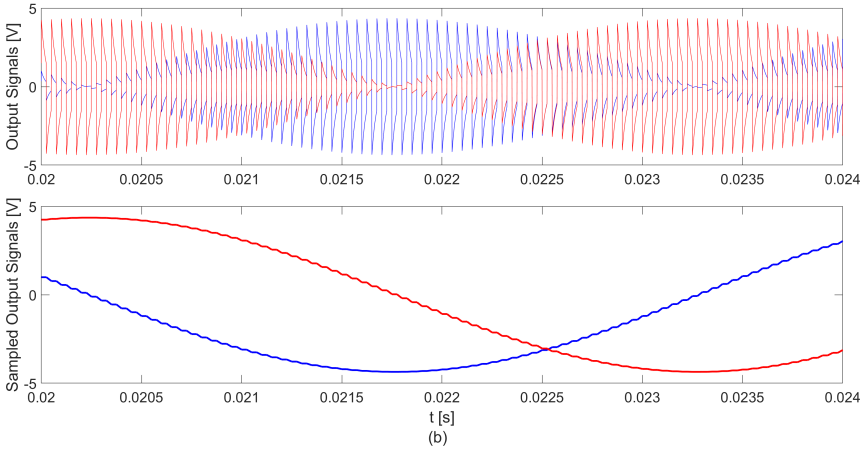

Figure 9. The Proposed Method - for 20 kHz (at an interval of 0.02-0.024 s) a) Resolver output signals, b) Resolver output signals sampled on the PWM rising edge.

Regarding the proposed method, the resolver output signals obtained by the 100 kHz input PWM signal are seen in Figure 10(a), while the resolver output signals sampled on the rising edge of the input PWM wave are seen in Figure 10(b). In Figure 11(a) and Figure 11(b), the change in the time interval of 0.02s to 0.024s of the output signals obtained in Figure 10 is shown.

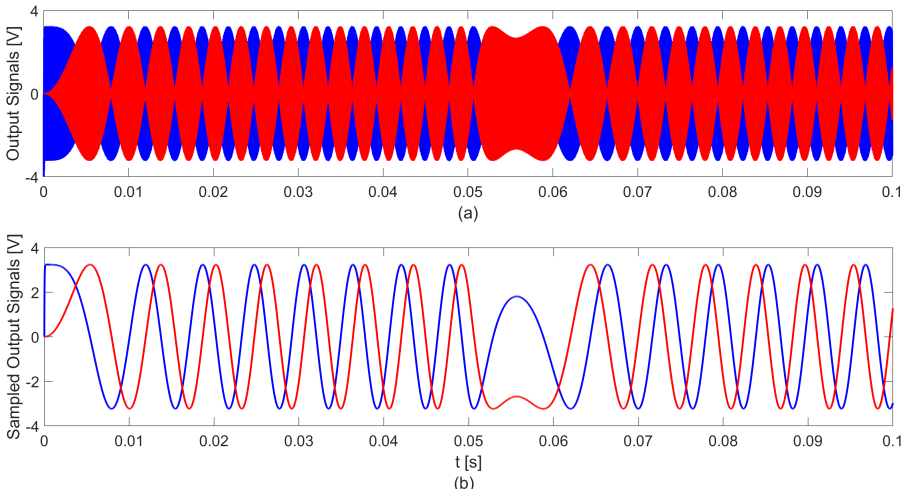

Figure 10. The Proposed Method - for 100 kHz a) Resolver output signals b) Resolver output signals sampled on the PWM rising edge.

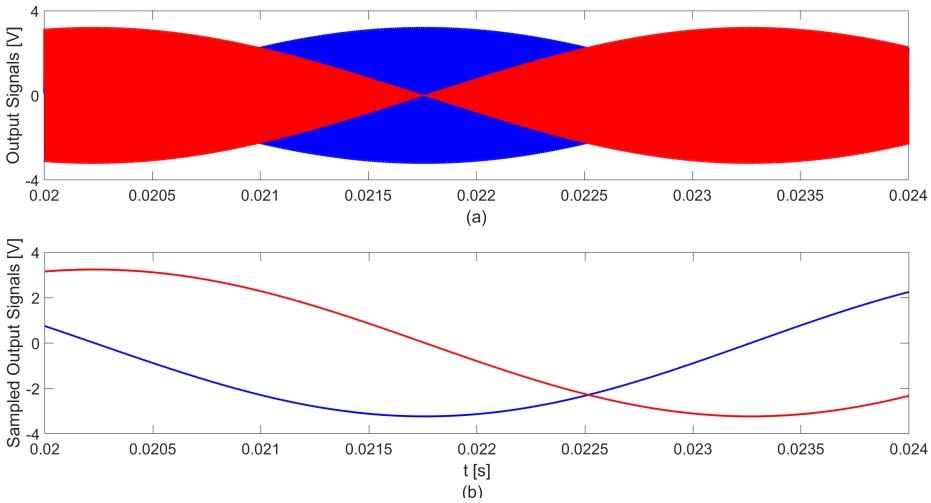

Figure 11. The Proposed Method - for 100 kHz (at an interval of 0.02-0.024 s) a) Resolver output signals, b) Resolver output signals sampled on the PWM rising edge.

The resolver shaft angle changes obtained from simulation studies carried out with 5 kHz, 20 kHz, and 100 kHz input signals are given comparatively in Figure 12. The shaft angle change was obtained by sampling the sine and cosine signals at the resolver output. As seen in Figure 12, the measurement error that may occur due to the shaft angle change obtained by the proposed method with an input signal of 100 kHz is the lowest. On the other hand, the measurement error that may occur due to the shaft angle change obtained by the traditional method with a 5 kHz input signal is higher because the sampling time is low. The proposed method performs the motor control based on software while, at the same time, it generates the resolver input signal and measures the output signal.

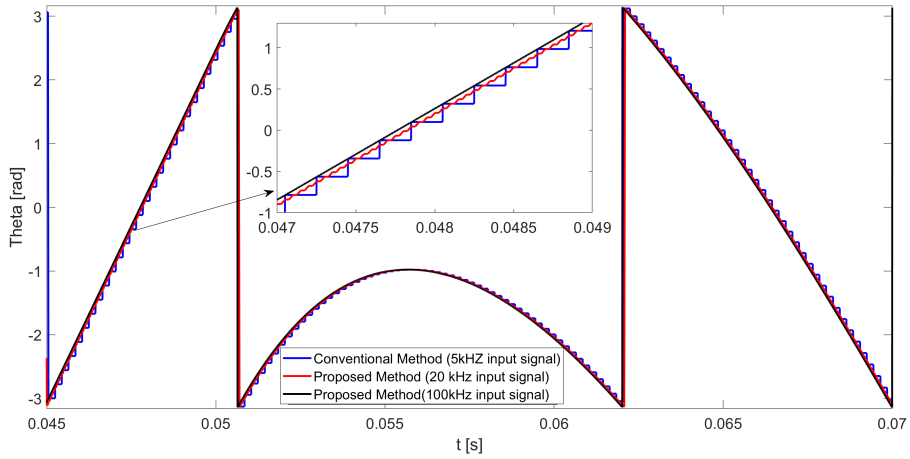

Figure 12. Resolver shaft angle changes obtained from simulation studies carried out with resolver input signals of 5 kHz, 20 kHz, and 100 kHz.

Generating a sinusoidal excitation signal is both a costly process and has difficulties in application. For this reason, square wave excitation based resolver decoders have been developed in recent years. Thus, excitation signals can be generated more easily at higher frequencies. H bridge circuits are used to provide this excitation. In this study, resolver excitation was performed with the microcontroller PWM output using only one power switch. Thus, both the cost was reduced and high frequency excitation was provided. A microcontroller will be able to generate angle information from resolver signals and also perform motor control at the same time. Almost exactly linear angle information was obtained at an excitation frequency of 100 kHz. This precise angle measurement information is very important, especially in high speed applications. Thus, it will be easier to create systems that operate with lower errors, especially in industrial robotic applications.

4. Discussion

High-level processors are used in motor control applications. The measurement and use of Resolver signals for control purposes can also be performed with these processors. Thus, as the software of the resolver application becomes simple, it will also pave the way for its use on the same processor. More precise motor control can be performed using the high-accuracy shaft position information obtained by the proposed method. Both the conventional and the proposed methods require filtering against noise for more precise control. However, since software-based measurement is preferred instead of analog card design in the proposed method, digital filtering techniques can be used instead of analog filtering.

5. Conclusion

Resolver is used to measure the shaft angle of electric motors for making position control in industrial applications. Resolver directly changes the waveform of the input signals and the frequency of the output signals. In this study, a sinusoidal input voltage with a frequency of 5 kHz was used in the conventional method. In the proposed method, on the other hand, a unidirectional PWM input signal with a duty cycle of d=0.5 and a positive amplitude at frequencies of 20 kHz and 100 kHz was used. Generating high-frequency sinusoidal input signals in the conventional method is both difficult and poses some problems in terms of card and system design. In order to eliminate these problems, both a high-frequency input signal was obtained using the proposed method and a high-accuracy measurement process was performed by sampling only without making an analog card design. As a result, with this study, two significant advantages have been obtained reducing the cost of the system and measurement errors. It is estimated that higher performance can be achieved by obtaining a high-accuracy shaft angle in control systems where position and position control are performed using the proposed method. In the continuation of this study, the advantages of the proposed method will be shown experimentally by performing the position control on a real system.

References

[1] Benammar M, Ben-Brahim L, and Alhamadi MA, A high precision resolver-to-DC converter, IEEE Trans Instrum Meas 2005;5, 2289–2296.

[2] Benammar M, Ben-Brahim L, and Alhamadi MA, A Novel Resolver-to-360° Linearized Converter. IEEE Sens J 2004; 4, 96–101.

[3] Erbahan OZ, Alışkan I, Diagnostics of a Broken Rotor Bar Faults of Three-phase Squirrel Cage Induction Motor Using Acoustic Signals, Düzce Üniversitesi Bilim ve Teknoloji Dergisi 2019; 7(3), 935–950.

[4] Ben-Brahim L, Benammar M, and Alhamadi MA, A resolver angle estimator based on its excitation signal, IEEE Trans Ind Electron 2009; 56:574–580.

[5] Attaianese C, Tomasso G, Position measurement in industrial drives by means of low-cost resolver-to-digital converter, IEEE Trans Instrum Meas 2007;56: 2155–2159.

[6] Pecly L, Schindeler R, Cleveland D, and Hashtrudi-Zaad K, High-Precision Resolver-to-Velocity Converter, IEEE Sens J 2017; 66(11): 2917–2928.

[7] Ben-Brahim L, Benammar M, Alhamadi MA, Al-Emadi NA, and Al-Hitmi MA, A new low cost linear resolver converter, IEEE Sens J 2008; 8: 1620–1627.

[8] Sarma S, Agrawal VK, and Udupa S, Software-based resolver-to-digital conversion using a DSP, IEEE Trans Ind Electron 2008; 55:371–379.

[9] Sarma S, Agrawal VK, Udupa S, and Parameswaran K, Instantaneous angular position and speed measurement using a DSP based resolver-to-digital converter, Measurement 2008; 41(7): 788–796.

[10] Khaburi DA, Software-based resolver-to-digital converter for DSP-based drives using an improved angle-tracking observer, IEEE Trans Instrum Meas 2012;61: 922–929.

[11] Qamar NA, Hatziadoniu CJ, and Wang H, Speed error mitigation for a DSP-basedresolver-to-digital converter using autotuning filters, IEEE Trans Ind Electron 2015; 62: 1134–1139.

[12] Wu Z, and Li Y, High-accuracy automatic calibration of resolver signals via two-step gradient estimators, IEEE Sensors Journal 2018; 18(7): 2883-2891.

[13] Qin H, and Wu Z, Angle Tracking Observer with Improved Accuracy for Resolver-to-Digital Conversion, Symmetry 2019; 11(11): 1347.

[14] Zhang J, and Wu Z, Composite state observer for resolver-to-digital conversion, Meas Sci Technol 2017;28: 1-10.

[15] Kim YH, and Kim S, Software resolver-to-digital converter for compensation of amplitude imbalances using d-q transformation, J Electr Eng Technol 2013; 8: 1310-1319.

[16] Celikel R, and Aydogmus O, A FPGA-Based Position Calculation for Shaft Resolvers, International Advanced Technologies Symposium (IATS'17), 2017; 368–374.

[17] Karabeyli FA, and Alkar AZ, Enhancing the Accuracy for the Open-loop Resolver to Digital Converters, J Electr Eng Technol 2018;13: 192-200.

[18] Celikel R and Aydogmus O, ANN-Based Noise Reduction for Shaft Resolver in Robotic Applications, 1st International Engineering and Technology Symposium, 2018;561–568.

[19] Celikel R, ANN based angle tracking technique for shaft resolver, Measurement 2019;148: 1-10.

[20] Shi T, Hao Y, Jiang G, Wang Z, and Xia C, A Method of Resolver-to-Digital Conversion Based on Square Wave Excitation, IEEE Trans Ind Electron 2018; 65(9): 7211-7219.

[21] Sun L, Kong T, Wu C, Zhang L, Wang W, and Ding S, The Leaf-Style Axial Field Variable Reluctance Resolver With an Efficient Decoding System, IEEE Trans on Ind Electron 2024; 71(9): 11581-11591.

[22] Hwang Y, and Jang P, New RDC Method Using Trapezoidal Excitation Signal Considering Resolver Nonliearity, IEEE Transactions on Instrumentation and Measurement 2023; 72: 9000709.

Turkish Journal of Science & Technology
19(2), 397-405, 2024

Research Paper
https://doi.org/10.55525/tjst.1452146

Comparison of Fourier and Trigonometric Transform based Multicarrier Modulations for Visible Light Communication

Selva Muratoğlu ÇÜRÜK[1*]
[1] Elektrik Elektronik Mühendisliği, Mühendislik ve Doğa Bilimleri Fakültesi,
İskenderun Teknik Üniversitesi, Hatay, Türkiye
[*1] selva.curuk@iste.edu.tr

(Geliş/Received: 13/03/2024; Kabul/Accepted:07/08/2024)

Abstract: It is predicted that the radio frequency spectrum will be insufficient in the near future due to the increase in wireless data. Visible Light Communication (VLC) is an alternative solution, which promises high speeds. Similar to other wireless communication systems, VLC systems prefer Multicarrier Modulation (MCM), but the signals are converted to be real and unipolar before transmission for optical communication. In this paper, two optical MCM groups that utilize Discrete Fourier Transform (DFT) and Discrete Trigonometric Transform (DTT) are questioned with respect to Bit Error Rate (BER), spectral efficiency and complexity. DFT based techniques use complex mapped signals together with their Hermitian symmetries to obtain real output signals, while DTT based techniques already output real signals when the input signal is real mapped. It is seen that DFT based techniques have lower BERs because of used mapping. DTT based techniques improve spectral efficiency, but they are limited to real mappings with higher error rates. For both transformations, the real signals are made unipolar by adding a bias (DCO-MCM), by asymmetrically clipping (ACO-MCM) or by sending positive and negative values separately (UnO-MCM). It is shown that, adding a dc bias (DCO-MCM) increases BERs, where ACO-MCM and UnO-MCM have close performances with lower BERs.

Key words: Bit error rate, discrete Fourier transform, discrete trigonometric transform, multicarrier modulation, visible light communication.

Görünür Işık Haberleşmesi için Fourier ve Trigonometrik Dönüşüm Tabanlı Çok Taşıyıcılı Modülasyonların Karşılaştırılması

Öz: Kablosuz verideki artış nedeniyle yakın gelecekte radyo frekans spektrumunun yetersiz kalması ön görülmektedir. Görünür Işık Haberleşmesi (VLC) yüksek hız vaat eden alternatif bir çözümdür. VLC sistemleri, diğer kablosuz haberleşme sistemlerine benzer şekilde, Çoklu Taşıyıcılı Modülasyon (MCM) tercih ederler, ancak optik iletişim için iletimden önce sinyaller gerçek ve tek kutuplu olacak şekilde dönüştürülürler. Bu makalede, Ayrık Fourier Dönüşümü (DFT) ve Ayrık Trigonometrik Dönüşümü (DTT) kullanan iki optik MCM grubu Bit Hata Oranı (BER), spektral verimlilik ve karmaşıklık açısından sorgulanmaktadır. DFT tabanlı teknikler, gerçek çıkış sinyali elde etmek için karmaşık eşlemeli sinyaller ve onların Hermit simetrilerini kullanırlar, DTT tabanlı tekniklerde ise giriş sinyali gerçek eşlenmiş ise çıkış zaten gerçek olacaktır. DFT tabanlı tekniklerin kullanılan eşleme nedeniyle daha düşük BER'lere sahip oldukları görülmektedir. DTT tabanlı teknikler spektral verimliliği arttırır ancak bu teknikler daha yüksek hata oranlarına sahip gerçek eşlemelerle sınırlıdırlar. Her iki dönüşüm için de gerçek sinyaller, bir öngerilim eklenerek (DCO-MCM), asimetrik olarak kırpılarak (ACO-MCM) veya pozitif ve negatif değerleri ayrı ayrı göndererek (UnO-MCM) tek kutuplu hale getirilir. Dc bileşen eklemek (DCO-MCM) BER'leri arttırırken, ACO-MCM ve UnO-MCM in daha düşük BER'lerle yakın performanslara sahip oldukları gösterilmiştir.

Anahtar kelimeler: Bit hata oranı, ayrık fourier dönüşüm, ayrık trigonometrik dönüşüm, çok taşıyıcılı modülasyon, görünür ışık haberleşmesi.

1. Introduction

There is a tremendous amount of increase in wireless data traffic due to the rise in the number of users with demands of high speed communication for services such as social media, video streaming, cloud storage and game streaming. Thus, wireless systems using radio frequency bands become more and more saturated every day. Visible Light Communication (VLC), a kind of optical communication, seems to be a strong candidate for future wireless communication. VLC systems use already existing Light Emitting Diode (LED) based illumination infrastructure for communication, and as LEDs become widespread, VLC systems seem to increase rapidly. The health friendly, low cost VLC has many advantages such as wide band, high data rate, high security and no interference to the radio frequency band. Therefore, many interesting indoor and outdoor applications have come into view. i.e., high speed data transmission in houses and offices, communication in hospitals and airplane cabins, traffic management and underwater communication.

* Selva Muratoğlu ÇÜRÜK: selva.curuk@iste.edu.tr. ORCID 0000-0002-2195-7827[1]

VLC systems, as well as other optical communication systems, use the Intensity Modulation / Direct Detection (IM/DD) technique [1]. Thus, the intensity of light is modulated with the LED's input current which is controlled by modulated signal. After transmission of the signal, the demodulation process is carried out in the receiver by an optical detector, generally a photodiode, which outputs an electrical signal related to the detected light intensity.

Multicarrier Modulation (MCM) is attractive in wireless communication for high data rates and its resilience to Intersymbol Interference. MCM schemes are divided into two groups: Discrete Fourier Transform (DFT) based techniques (they are also named Orthogonal Frequency Division Multiplexing, OFDM) and Discrete Trigonometric Transform (DTT) based techniques. MCM is also used in optical communication but with modifications. The output signals of MCM are complex and/or bipolar, but the input of IM/DD block should be real and unipolar [2] because light intensity cannot be complex and bipolar. Various approaches are proposed in the literature to solve this problem. For real outputs, techniques implement DFT input symbols together with their Hermitian symmetries, whereas techniques that use DTT already output real signals in case of real input. Following, real signals are made unipolar, by adding a bias, by clipping, or positive and negative values are sent separately.

In the literature, these optical MCM techniques are investigated. For example, the authors of [3] survey the evolution of Optical OFDM (O-OFDM) designed for both VLC and optical fiber. In [4], Direct Current O-OFDM and Asymmetrically Clipped O-OFDM are analyzed in terms of signal clipping under the constraints of maximum and non-negative optical power. In [5], an innovative unipolar transceiver system is proposed and the authors enhance the data rate, system complexity, power and spectrum efficiency. The authors in [6] investigate optical MCM systems based on discrete Hartley transform for VLC. Spectral and energy efficiency of Asymmetrically Clipped O-OFDM is investigated in [7]. In [8], an enhanced OFDM scheme is proposed for VLC. A hybrid O-OFDM scheme for VLC with adaptive bias is proposed in [9] to improve spectral efficiency and power efficiency.

In this paper, Bit Error Rate (BER) performances of DFT and DTT based techniques are investigated under additive white Gaussian Noise (AWGN) channel assumption, together with their complexity and spectral efficiency. The remainder of this paper is organized as follows. First, DFT and DTT based optical MCM techniques are introduced in Section 2. Then BER performances of these techniques are demonstrated by simulations in Section 3. Finally, the conclusions of the study are given.

2. Optical Multicarrier Modulation

A block diagram of an optical MCM system is given in Figure 1. Note that, the receiver side is the same as the conventional ones, but two steps are added to the transmitter. For obtaining real signals, if Inverse Discrete Fourier Transform (IDFT) is used, mapped complex signals together with their Hermitian symmetries are fed to the block. If Inverse Discrete Trigonometric Transform (IDTT) is used, real mapping is preferred and Hermitian symmetries are not needed. Following, parallel to serial conversion is done and cyclic prefix (CP) is appended to the signal to mitigate the effect of Intersymbol Interference. Next, to obtain unipolar signals, one of the three methods is applied: An appropriate dc bias is added and negative peaks are clipped at zero, or after mapping zero padding is done and asymmetrically clipping is performed, or positive and negative values are sent separately.

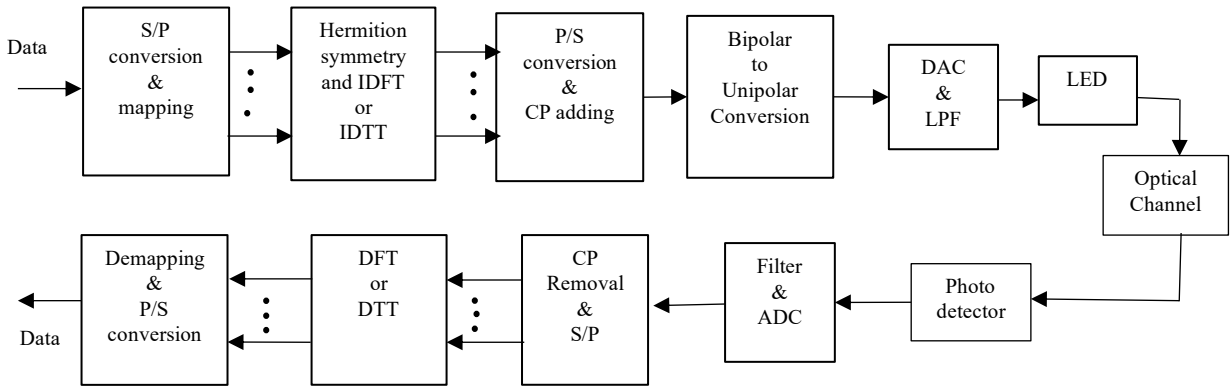

Figure 1. Optical MCM system block diagram.

2.1. Real MCM signals

The used mapping in DFT based MCM generally outputs complex values. To obtain real signals, the IDFT block is fed with complex mapped symbols together with their Hermitian symmetries [10], as given in Equation 1:

$$X_{DFT,(N-k)} = X^*_{DFT,k} \qquad k = 1, 2, \dots, \frac{N}{2} - 1 \tag{1}$$

where $X_{DFT,k}$ is the input of IDFT block and N denotes the subcarrier number. Then the input vector of IDFT is given in Equation 2:

$$\boldsymbol{X_{DFT}} = [0,\ X_{DFT,1},\ X_{DFT,2},\ \dots\ ,\ X_{DFT,\frac{N}{2}-1},\ 0,\ X^*_{DFT,\frac{N}{2}-1},\ \dots\ ,\ X^*_{DFT,2},\ X^*_{DFT,1}] \tag{2}$$

The output of IDFT is given by Equation 3 [10]:

$$x_{DFT,n} = \frac{1}{\sqrt{N}} \sum_{k=0}^{N-1} X_{DFT,k} \exp\left(\frac{j2\pi kn}{N}\right), \quad n = 0, 1, 2, \dots, N-1 \tag{3}$$

Where n is subcarrier indices. Then, DFT equation is known to be as given in Equation 4:

$$X_{DFT,k} = \frac{1}{\sqrt{N}} \sum_{n=0}^{N-1} x_{DFT,n} \exp\left(\frac{-j2\pi kn}{N}\right), \quad k = 0, 1,2, \dots, N-1 \tag{4}$$

Note that because of the Hermitian symmetry given in Equation 1, it can easily be shown that Equation 3 simplifies to Equation 5 [11]:

$$x_{DFT,n} = \frac{1}{\sqrt{N}} \left[\sum_{k=1}^{\frac{N}{2}-1} 2X_{DFT,real,k} \cos\left(\frac{2\pi nk}{N}\right) \right], \ n = 0, 1,2, \dots, N-1 \tag{5}$$

Thus, the output of IDFT block is real so that it can be transferred via IM/DD after bipolar to unipolar conversion.

The second group of optical MCM techniques uses one of the well-known DTTs, namely Discrete Hartley Transform (DHT), Discrete Sine Transform (DST) and Discrete Cosine Transform (DCT) [11-15]. DTT already outputs real valued signals when input signals are real. Thus, DTT based MCM techniques are limited to real mappings.

N point Inverse DST (IDST) can be expressed as Equation 6 [11],

$$x_{DST,n} = \sqrt{\frac{2}{N}} \sum_{k=0}^{N-1} X_{DST,k} \, sin\left(\frac{\pi(2n+1)(2k+1)}{4N}\right) \quad n = 0, 1, 2, \dots, N-1 \tag{6}$$

where $X_{DST,k}$ is output of mapping and it is clear that the output of IDST block $x_{DST,n}$ is going to be real in case of real mapping. DST equation is given in Equation 7:

$$X_{DST,k} = \sqrt{\frac{2}{N}} \sum_{n=0}^{N-1} x_{DST,n} \, sin\left(\frac{\pi(2n+1)(2k+1)}{4N}\right) \quad k = 0, 1, 2, \dots, N-1 \tag{7}$$

DCT also outputs real valued signals when input is real. Inverse DCT (IDCT) is expressed as Equation 8 [14],

$$x_{DCT,n} = \sqrt{\frac{2}{N}} \sum_{k=0}^{N-1} \varepsilon_k \, X_{DCT,k} \, cos\left(\frac{\pi k(2n+1)}{2N}\right) \quad n = 0, 1, 2, \dots, N-1 \tag{8}$$

The coefficient ε_k is defined in Equation 9:

$$\varepsilon_k = \begin{cases} \sqrt{0.5}, & k = 0 \\ 1, & k = 1, 2, \dots, N-1 \end{cases} \tag{9}$$

DCT equation (Equation 10) can be expressed as:

$$X_{DCT,k} = \sqrt{\frac{2}{N}} \sum_{n=0}^{N-1} \varepsilon_n \, x_{DCT,n} \, cos\left(\frac{\pi k(2n+1)}{2N}\right) \quad k = 0, 1, 2, \dots, N-1 \tag{10}$$

The output of Inverse DHT (IDHT) is given by Equation 11 [15],

$$x_{DHT,n} = \frac{1}{\sqrt{N}} \sum_{k=0}^{N-1} X_{DHT,k} \left[\sin\left(\frac{2\pi nk}{N}\right) + \cos\left(\frac{2\pi nk}{N}\right)\right], n = 0,1,2, \dots, N-1 \tag{11}$$

where $X_{DHT,k}$ is the output of mapping. Then, DHT equation is (Equation 12)

$$X_{DHT,k} = \frac{1}{\sqrt{N}} \sum_{n=0}^{N-1} x_{DHT,n} \left[\sin\left(\frac{2\pi nk}{N}\right) + \cos\left(\frac{2\pi nk}{N}\right)\right], k = 0,1,2, \dots, N-1 \tag{12}$$

Note that the equations of DHT and IDHT are identical, as in DST and DCT. Thus, same digital signal processing unit may be used both in the transmitter and in receiver which reduces system complexity [15-17].

2.2. Unipolar MCM signals

Real but bipolar MCM signals should be made unipolar before IM. Three basic techniques are found in the literature: The first one is adding a bias, (Direct Current Biased Optical MCM, DCO-MCM), the second one is clipping (Asymmetrically Clipped Optical MCM, ACO-MCM) and the third is sending positive and negative values separately (UnO-MCM).

DCO-MCM is one of the popular approaches that is used in VLC. In DCO-MCM, an appropriate dc bias is added to the bipolar MCM signal with a cyclic prefix and then all remaining negative peaks are clipped at zero [18, 19]. Thus, dc bias addition is given in Equation 13,

$$x_{DC}(t) = x_{cp}(t) + B_{DC} \tag{13}$$

where $x_{cp}(t)$ is the cyclic prefix added MCM signal and B_{DC} is the dc bias. Adding a constant dc bias is a choice but selecting a dc bias related to the power of the signal will be more appropriate, i.e. [20]:

$$B_{DC} = k\sqrt{E\{(x_{cp}(t)^2\}} \tag{14}$$

Where in Equation 14 k is the proportional constant of clipping factor and E{} denotes statistical expectation. The approximate increase in energy dissipation of DCO-MCM in decibels is given in Equation 15 [20]:

$$B_{DC,dB} = 10\log_{10}(k^2 + 1) \tag{15}$$

Note that, all negative parts may not be eliminated even after adding the dc bias, therefore clipping at zero should be applied as in Equation 16:

$$x_{DCO}(t) = \begin{cases} x_{DC}(t), & x_{DC}(t) \geq 0 \\ 0, & x_{DC}(t) < 0 \end{cases} \tag{16}$$

DCO-MCM is easy to implement, but deciding to the dc bias is critical because high dc bias may result with the clipping of the signal peaks which are out of the led dynamic range. Further, high positive peaks may be observed which requires high power. Thus, Peak to Average Power Rate increases which lowers the power efficiency [21]. But low dc bias selection also results with high clipping noise.

ACO-MCM is introduced as a power efficient technique, where only odd subcarriers are used for data transmission and even subcarriers are set to zero [21]. Then, for example in an ACO-DFT system, the input vector of IDFT is expressed as in Equation 17:

$$\boldsymbol{X} = [0, X_1, 0, X_2, \dots, X_{\frac{N}{2}-1}, 0, X^*_{\frac{N}{2}-1}, 0, X^*_{\frac{N}{2}-3}, \dots, 0, X^*_1] \tag{17}$$

Finally, negative parts are clipped to ensure nonnegativity (Equation 18):

$$x_{ACO}(t) = \begin{cases} x_{cp}(t), & x_{cp}(t) \geq 0 \\ 0, & x_{cp}(t) < 0 \end{cases} \quad (18)$$

Note that all the intermodulation caused by clipping is on the even subcarriers because only the odd subcarriers are modulated. Thus, the data-carrying odd subcarriers are not affected.

In UnO-MCM, for unipolarization, the time-domain real signal (one bipolar frame) is transformed into two separate frames and then transmitted one after the other [19, 22]. The first frame includes the positive samples where the places of negative ones are set to zero. Similarly, the second frame holds the absolute values of the negative samples with zeros in the places of positive ones. At the receiver, the negative frame is subtracted from the positive frame to obtain the original bipolar frame. Indeed, this may combine the noise in both frames.

The illustrations of MCM symbol structures of related schemes for the same amount of sending data are given in Figure 2.

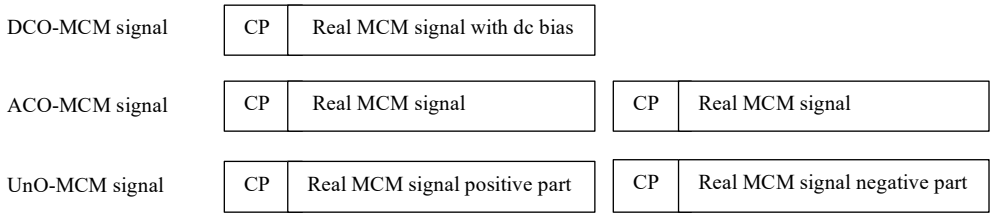

Figure 2. Illustration of the transmitted signals for DCO-MCM, ACO-MCM and UnO-MCM.

The spectral efficiency of DCO-MCM with *M* level of mapping is calculated by Equation 19 [23],

$$\eta_{DCO-MCM} = l\frac{N-2}{(N+N_{cp})}log_2(M) \quad (19)$$

Where N_{cp} is the length of the cyclic prefix. The constant l is equal to 0.5 for DFT based MCM (Half of the subcarriers is allocated to Hermitian symmetry which halves the data carrying subcarriers.) and 1 for the DTT based MCM. Thus, DTT based MCM spectral efficiency is better than DFT based MCM.

In ACO-MCM, the use of only odd subcarriers results in $N/2$ independent complex input values, then spectral efficiency of ACO-OFDM is given in Equation 20 [23],

$$\eta_{ACO-MCM} = l\frac{N-2}{2.(N+N_{cp})}log_2(M) \quad (20)$$

In UnO-MCM, transformation of positive and negative parts halves the achievable data rate, i.e., the spectral efficiency becomes as Equation 21 [22]:

$$\eta_{UnO-MCM} = l\frac{N-2}{2.(N+N_{cp})}log_2(M) \quad (21)$$

As seen, spectral efficiency is halved in ACO-MCM and UnO-MCM compared to DCO-MCM. However, they have a significant energy advantage over DCO-MCM [24].

3. Results and Discussion

For the BER performances, numerical results are obtained using computer based Monte Carlo simulations with MATLAB software. In the simulations, AWGN channel is assumed, i.e., a robust line-of-sight path exists, which is commonly the case for indoor and outdoor optical wireless systems. The number of subcarriers is 1024 and guard interval subcarriers are 96. The most popular mapping are selected for both transformations, i.e., Quadrature Amplitude Modulation (QAM) mapping for DFT based MCMs and Pulse Amplitude Modulation (PAM) mapping for DTT based MCMs.

Comparing the speeds of Fast Fourier Transform (FFT) algorithm proposed in [25] and Fast Hartley Transform (FHT) proposed in [26], FFT needs a few less operations [26]. However since FFT based MCM needs

to calculate Hermitian symmetry, FHT based MCM has less computational complexity. Further, DTT based MCM systems use same digital signal processing unit for both receiver and transmitter due to self-inverse property, therefore complexity and cost are reduced compared to DFT based MCM systems.

In the simulations, the effect of selected dc bias is investigated first. The BER graphs of DCO-DHT for 2, 4 and 8 PAM mapping levels as a function of Signal to Noise Ratio (SNR) are given in Figure 3. The added dc biases are selected to be the minimum of the signal (solid lines without markers), the proportional constant of clipping factor k=1.5 (lines with circle) and k=5 (lines with stars). As seen from the figure, adding larger dc biases increases the BERs, especially for low SNRs. But note that adding small bias values results with small BERs, if clipping noise is tolerable, as in 2-PAM. But low dc bias results with high BERs for SNR values greater than 25 dB for 4-PAM and 8-PAM. This is because of insufficient dc bias which results in high clipping noise. It is interesting that especially for lower modulation levels, adding the minimum of the signal as dc bias may result in higher BER, especially for low SNR values.

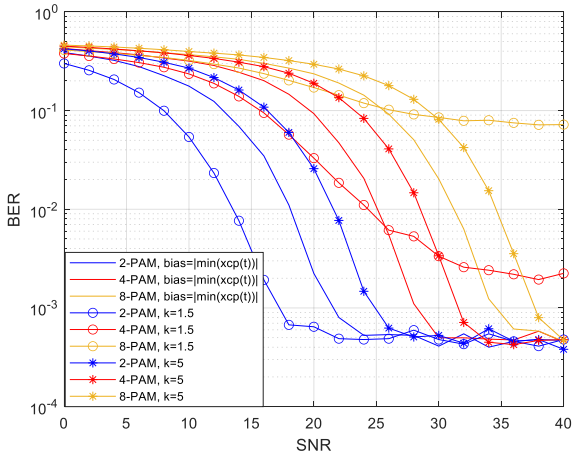

Figure 3. BER of DCO-DHT, effect of dc bias selection.

The BER graphs of DCO-DFT are given in Figure 4, for 2, 4 and 8 QAM levels. The added dc biases are the same as in the case of DCO-DHT. As seen from the figure, adding larger dc biases increases the BERs, especially for low SNRs. Clipping noise is observed for 8-QAM when SNR is larger than 25 dB only. It is concluded that the added bias is critical for the performance of DCO-MCMs. Maximum bias should be the minimum value of the signal, indeed lower values can be found for decreasing the power but care is needed for clipping noise, especially for high SNRs. The optimum k value depends on modulation level and SNR, obtaining the value is out of the scope of this study. The dc bias is selected to be the minimum of the signal power in the following simulations.

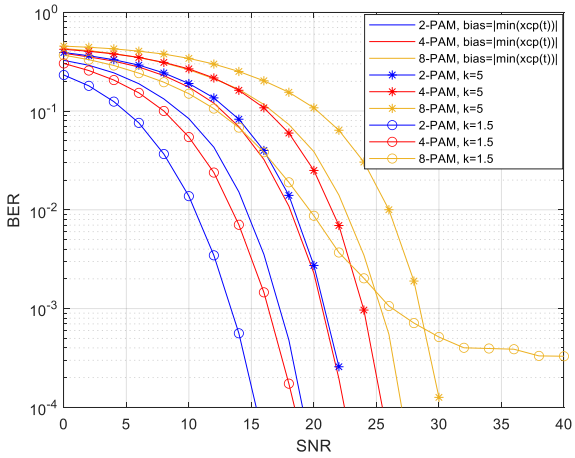

Figure 4. BER of DCO-DFT, the effect of dc bias selection.

BER performances of DCT, DHT and DFT based MCMs for three unipolarization schemes are given in Figure 5, Figure 6 and Figure 7, respectively. Mapping levels are selected to be 2, 4 and 8, for both PAM and QAM. In all figures, solid lines are used for DCO-MCM (dc bias is selected to be the minimum of the signal power), dashed line is for ACO-MCM and starred line is used for UnO-MCM schemes. For all MCM techniques, ACO-MCMs and UnO-MCMs give very close results (two curves overlap on the graphs) and DCO-MCMs result with higher BER values compared to ACO-MCMs and UnO-MCMs. For all O-MCM techniques, as the modulation level increases, the BER also increases, as expected. Comparing the BER graphs, DCT-MCM and DHT-MCM have very close performances, but DFT-MCM performance is better because of the used mapping.

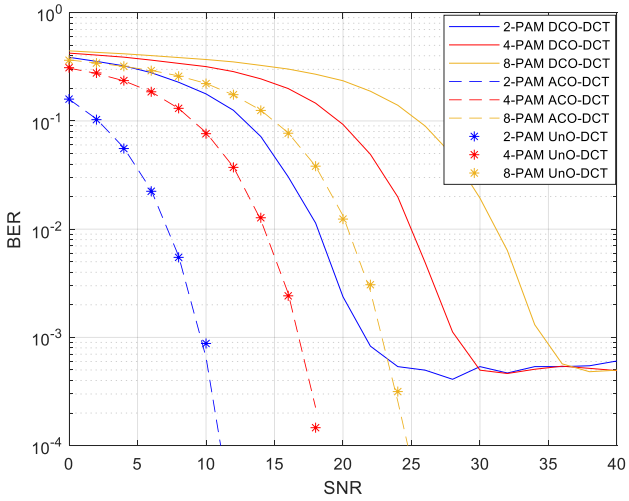

Figure 5. BERs of DCO-DCT, ACO-DCT and UnO-DCT.

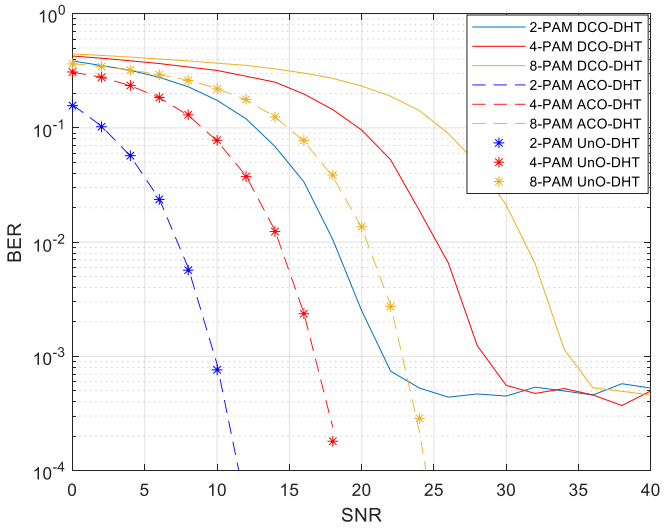

Figure 6. BERs of DCO-DHT, ACO-DHT and UnO-DHT

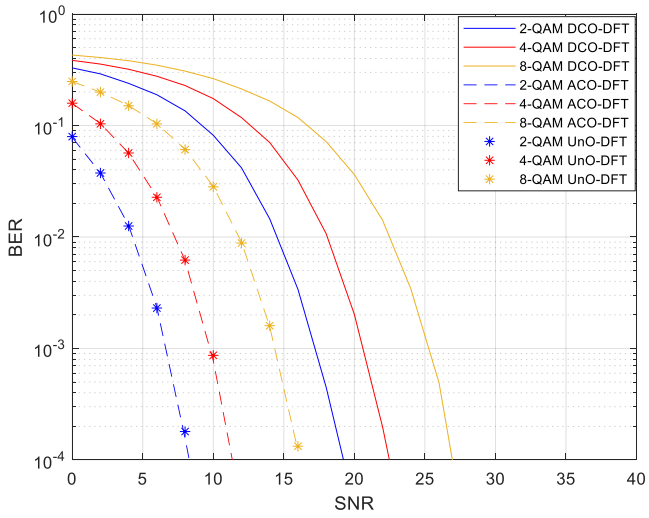

Figure 7. BERs of DCO-DFT, ACO-DFT and UnO-DFT

4. Conclusion

VLC systems use optical MCM techniques, where the complex and bipolar MCM signals are made real and unipolar so that they can be transmitted over optical channels by intensity modulation. In this paper, optical MCM schemes that use DFT and DTT with various unipolarization schemes are compared in terms of their spectral efficiency, complexity and BERs. DTT-MCM has reduced complexity, but these systems are limited to using real mappings only which results in poor BER performance. BER performance of DFT-MCM is shown to be better, because of the mapping used. Comparing unipolarization techniques, namely DCO_MCM, ACO-MCM and UnO-MCM, DCO-MCM has the best spectral efficiency with a simple structure but requires higher power. Furthermore, the BER performance of DCO-MCM is poor compared to the others. Arranging the bias is also a critical task, i.e., high dc bias increases the power but reduces the clipping noise or vice versa. ACO-MCM and UnO-MCM have similar performances in means of spectral efficiency and BER. Finally, as an optimum decision, ACO-DTT systems come forward with their relatively simple structures and acceptable BER performances.

References

[1] Çürük SM. Alignment of transmitters in indoor Visible Light Communication for flat channel characteristics. ETRI J 2022; 44(1): 125–134.
[2] Chen C, Zhong WD, Wu D. Non-Hermitian Symmetry Orthogonal Frequency Division Multiplexing for multiple-input multiple-output Visible Light Communications. J Opt Commun Netw 2017; 9(2): 36-44.
[3] Zhang X, Babar Z, Petropoulos P, Haas H, Hanzo L. The Evolution of optical OFDM. IEEE Commun Surv Tut 2021; 23(3): 1430-1457.
[4] Xia L, Wang X, Sun Z, Cheng Z, Jin J, Yuan Y, Liu G, Jiang T, Huang Y. Signal clipping at transmitter and receiver of O-OFDM for VLC under optical power constraint. China Commun 2022; 19(6): 154-168.
[5] Farid SM, Saleh MZ, Elbadawy HM, Elramly SH. Novel unipolar optical modulation techniques for enhancing Visible Light Communication systems performance. IEEE Access 2022; 10: 67925-67939.
[6] Xu XY, Zhang Q, Yue DW. Orthogonal Frequency Division Multiplexing with index modulation based on discrete Hartley transform in Visible Light Communications. IEEE Photonics J 2022; 14(3): 1-10.
[7] Ma S, Yang R, Deng X. Spectral and energy efficiency of ACO-OFDM in Visible Light Communication systems. IEEE Trans Wirel Commun 2022; 21(4): 2147-2161.
[8] Niu S, Wang P, Chi S, Liu Z, Pang W, Guo L. Enhanced optical OFDM/OQAM for Visible Light Communication systems. IEEE Wirel Commun Lett 2021; 10(3): 614-618,
[9] Hong H, Li Z. Hybrid adaptive bias OFDM-based IM/DD Visible Light Communication system. Photonics 2021; 8(7): 257-267.
[10] Armstrong J, Lowery AJ. Power efficient optical OFDM. Electron Lett 2006; 42(6): 370-372.
[11] Vappangi S, Mani VV. Performance analysis of DST-based Intensity Modulated / Direct Detection (IM/DD) systems for VLC. IEEE Sens J 2018; 19(4): 1320-1337.
[12] Azim AW, Le Guennec Y, Maury G. Spectrally augmented Hartley transform precoded asymmetrically clipped optical OFDM for VLC. IEEE Photonics Technol Lett 2018; 30(23): 2029-2032.

[13] Che M, Kuboki T, Kato K. Dimmable optical OFDM based on discrete Hartley transform for indoor visible light illumination and communication. In: 23rd Opto-Electronics and Communications Conference (OECC); 2018, Jeju island, Korea, IEEE, 1-2.
[14] Narmanlıoğlu Ö, Uysal M. DCT-OFDM based Visible Light Communications. In: 24th Signal Processing and Communication Application Conference (SIU); 2016, Zonguldak, Turkey, IEEE, 521-524.
[15] Zhao H, Liu J, Liang K, Zhang Y, Yi D, Zhong C, Liu S. DHT-based IM/DD optical OFDM system for power data transmission. In: 6th International Conference on Information Engineering for Mechanics and Materials, 2016, Inner Mongolia, Atlantis Press, 20-24
[16] Moreolo MS, Muñoz R, Junyent G. Novel power efficient optical OFDM based on Hartley transform for Intensity-Modulated Direct-Detection systems. J Lightwave Technol 2010; 28(5): 798-805.
[17] Moreolo MS. Performance analysis of DHT-based optical OFDM using large-size constellations in AWGN. IEEE Commun Lett 2011; 15(5): 572-574.
[18] Dissanayake SD, Armstrong J. Comparison of ACO-OFDM, DCO-OFDM and ADO-OFDM in IM/DD systems. J Lightwave Technol 2013; 31(2): 1063-1072.
[19] Godwin RJ, Veena K, Kumar DS. Performance analysis of direct detection Flip-OFDM for VLC system. In: International Conference on Emerging Trends in Engineering, Technology and Science (ICETETS); 2016, India, IEEE, 442-446.
[20] Armstrong J, Schmidt BJC. Comparison of asymmetrically clipped optical OFDM and DC-biased optical OFDM in AWGN. IEEE Commun Lett 2008; 12(5): 343-345.
[21] Sharifi AA, A new post-coding approach for PAPR reduction in DC-biased optical OFDM systems. Optoelectron Lett 2019; 15(4): 302-305.
[22] Tsonev D, Haas H. Avoiding spectral efficiency loss in unipolar OFDM for optical wireless communication. In: IEEE International Conference on Communications; 2014, 3336–3341.
[23] Bhadoria MP, Pandey G, Dixit A. Performance evaluation of Visible Light Communication for DCO and ACO optical OFDM techniques. In: National Conference on Communications (NCC); 2019, Bangalore, India, IEEE, 1-6.
[24] Çürük SM. Comparison of optical OFDM techniques in Visible Light Communication. In: International Conference on Engineering Technologies; 2021, 227-231.
[25] Johnson SG, Frigo M. A modified split-radix FFT with fewer arithmetic operations. IEEE Trans Signal Process 2006; 55(1): 111-119.
[26] Skodras AN, Aburdene MF, Nandi AK. Two-band fast Hartley transform. Electron Lett 2015; 51(1): 57-59.

Turkish Journal of Science & Technology
19(2), 407-414, 2024

Research Paper
https://doi.org/10.55525/tjst.1459356

Variations in Diffusion Coefficients on Equinox Days at Specified Critical Heights of the Ionosphere at the Equator

Kadri KURT[1*], Ali YEŞİL[2]

[1]Elektrik ve Enerji Bölümü, Beşiri OSB Vocational School, Batman University, Batman, Turkey
[2] Yüksek Enerji ve Plazma Fiziği Bölümü, Fen Fakültesi, Fırat Üniversitesi, Elazığ, Turkey
[*1]kadridewani@gmail.com, [2]ayesil@firat.edu.tr

(Geliş/Received: 26/03/2024; Kabul/Accepted: 10/09/2024)

Abstract: This study investigates the local time diffusion coefficient for stable and unstable ($\omega = 0$, $\omega \neq 0$) states at the equator (0^0), "the geographical latitude where the first peak of the magnetic equatorial trough in the ionosphere occurs," during the spring and fall equinoxes (March 21 and September 23). The findings show that the diffusion tensor in a steady state is completely real and has a magnitude equal to the speed of light in a steady state. But in the unsteady state, the diffusion tensor consists of two parts, real and imaginary. The diagonal elements of the real part tensor are of the size of the conductivity in the ionosphere and the elements of the imaginary part are of the size of the speed of sound with about the same magnitude. Furthermore, for all assumed conditions, the diffusion elements form the first peak of the magnetic equatorial trough at 6.00 am local time.

Key words: Diffusion tensor, ionospheric plasma, diffusion coefficient.

Ekvatorda Iyonosferin Bazı Kritik Yüksekliklerinde Difüzyon Katsayılarının Ekinoks Günlerinde Değişimi

Öz: Bu çalışmada, ilkbahar ve sonbahar ekinoksları (21 Mart ve 23 Eylül) sırasında "iyonosferdeki manyetik ekvatoral çukurun ilk zirvesinin meydana geldiği coğrafi enlem" olan ekvatorda (0^0) kararlı ve kararsız ($\omega = 0$, $\omega \neq 0$) durumlar için yerel zaman zaman difüzyon katsayısı araştırılmıştır. Bulgulara göre, kararlı durumda difüzyon tensörünün tamamen gerçek olduğunu ve sabit bir durumda ışık hızına eşit bir büyüklüğe sahip olduğunu göstermektedir. Fakat kararsız durumda difüzyon tensörü; reel ve sanal olmak üzere iki kısımdan oluşmaktadır. Reel kısım tensörününün köşegen elemanları iyonosferdeki büyüklüğü iletkenlik boyutunda, sanal kısmının elamanları yaklaşık aynı büyüklükte ses hızı boyutundadır. Bunun yanı sıra bütün kabul edilen şartlarda difüzyon elemanları sabah 6.00'da yerel zamanda manyetik ekvator çukurun ilk tepesini oluşturmaktadır.

Anahtar kelimeler: Difüzyon tensörü, iyonosferik plazma, difüzyon katsayıları.

1. Introduction

A section of Earth's upper atmosphere that lies between 50 and 1000 kilometers above the surface of the Earth is known as the ionosphere. Solar energy, especially ultraviolet (UV) rays, ionizes this area [1,2]. The transmission and propagation of radio waves depend heavily on the ionosphere. The D, E, and F layers are among the layers that make up the ionosphere [3,4]. Ionized particles, also known as ions, are present in these layers and are produced when solar radiation removes electrons from neutral atoms and molecules [5]. Radio communication, satellite operations, and space weather prediction are just a few of the uses that depend on understanding the ionosphere and its fluctuations. To track and investigate the behavior of the ionosphere and its interactions with solar radiation, scientists and researchers utilize equipment like satellites and ionosondes. Neutral winds, geomagnetic activity, solar radiation, and other factors all have an impact on the complicated phenomenon of electron density change in the magnetic equatorial trough of the ionosphere. There are significant variations in the electron density profile of the ionosphere in the magnetic equatorial trough during the day, with daytime and nighttime differences being particularly noticeable [6]. The strong ultraviolet (UV) radiation from the Sun ionizes the neutral particles in the ionosphere's F region during the day, releasing free electrons and ions. The overall electron density in the F region is influenced by this process [7]. A major contributor is the eastward-directed electric current known as the Equatorial Electrojet, which flows close to the magnetic equator. Higher altitudes of ionized particles are transported by the upward **E**×**B** drift, which is facilitated by the electrojet. This may cause the electron density in the F region to increase, resulting in the formation of a peak near the magnetic equator [8]. One important driver is the **E**×**B** drift, which is caused by the interaction of the ionospheric magnetic field (**B**) and

* Corresponding author:kadridewani@gmail.com ORCID Number of authors: [1]0000-0002-6507-8234, [2]0000-0003-2997-897X

the Earth's electric field (**E**) [9]. The plasma moves vertically as a result of this drift and in some circumstances, it may cause the electron density profile to trough close to the magnetic equator. The electron density distribution is also influenced by the meridional (north-south) wind patterns. Meridional winds and the **E**x**B** drift can push ionized particles away from the magnetic equator, which can aid in the creation of the trough [10]. At night, when solar ionization is lower, recombination activities take center stage. Electron density decreases as a result of electron-neutral collisions. The trough may also occur as a result of loss processes such as gravity settling and ambipolar diffusion.

The electron density profile might trough at proximity to the magnetic equator as a result of it. The meridional (north-south) wind patterns have an impact on the electron density distribution as well. The trough may form as a result of ionized particles being pushed away from the magnetic equator by meridian winds and the **E**x**B** drift [11]. Nighttime brings more prominence to recombination events due to decreased solar ionization. Electron-neutral collisions result in a drop in electron density. Additionally, loss processes including ambipolar diffusion and gravity settling may cause a decrease.

2. **Diffusion Equations for Steady(ω=0) and Unstable State(ω≠0) Ionosphere Plasma**

Given that the ionosphere's density inhomogeneity causes very minor departures from the equilibrium state and that these density instabilities are first-order, the velocity distribution can be roughly regarded as isotropic [12]. Density in this instance has the following definition. On the other hand, the medium is said to be anisotropic when **B** (magnetic field)≠0. There is not an isotropic velocity distribution. The ionospheric plasma is anisotropic because the magnetic field in the ionosphere plasma differs from zero [13,14]. As seen in Figure 1, the Earth's magnetic field takes on three dimensions when its true geometry is applied.

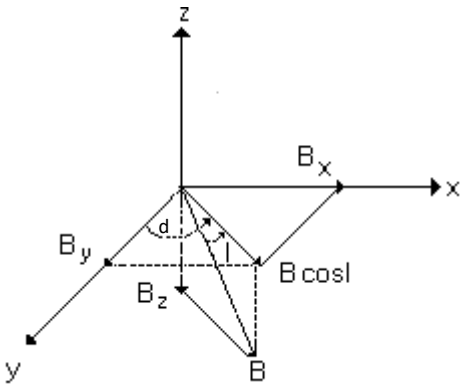

Figure 1. Geometry of the Earth's magnetic field (for the Northern Hemisphere) [2,14,15].

Here, $B_x = BCosISind$, $B_y = BCosICosd$ and, I is the magnetic dip and d is the magnetic declination angle. Other rotations to be used in this study are as follows:

ω_c: Electron Cyclotron (rotation) frequency. These frequencies depend on plasma parameters; is given as [2,14,15]

$$\omega_{cx\alpha} = \frac{eB_x}{m},\ \omega_{cy\alpha} = \frac{eB_y}{m} \text{ ve } \omega_{cz\alpha} = \frac{eB_z}{m}$$

If the geometry of the Earth's magnetic field is used in the flux density for the northern hemisphere, the diffusion equation can be written as follows;

$$\mathbf{\Gamma} + \frac{n_\alpha}{\nu_\alpha}\frac{D\mathbf{U}}{Dt} = \mu_\alpha(\mathbf{\Gamma}\times\mathbf{B} + n_\alpha E) - D_\alpha \nabla n_\alpha \quad (1)$$

Here, α=±e ($\mu_\alpha = \frac{q_\alpha}{m_\alpha \nu_\alpha}$) is the mobility of electrons, ions and charged particles. Also, Γ shows the electron flux density. From the solution of this expression, the diffusion tensor is obtained as follows,

$$D = \begin{bmatrix} D_{xx\alpha} & D_{xy\alpha} & D_{xz\alpha} \\ D_{yx\alpha} & D_{yy\alpha} & D_{yz\alpha} \\ D_{zx\alpha} & D_{zy\alpha} & D_{zz\alpha} \end{bmatrix}. \tag{2}$$

For electrons and ions the elements of the tensor are as follows;

$$D_{xx\alpha} = K^{-1} D_\alpha \left[\omega_{cx\alpha}^2 + \nu_\alpha^2 \right] \qquad D_{xy\alpha} = K^{-1} D_\alpha \left[\omega_{cx\alpha}\omega_{cy\alpha} - \omega_{cz\alpha}\nu_\alpha \right]$$

$$D_{xz\alpha} = K^{-1} D_\alpha \left[-\omega_{cx\alpha}\omega_{cz\alpha} + \omega_{cy\alpha}\nu_\alpha \right] \quad D_{yx\alpha} = K^{-1} D_\alpha \left[\omega_{cx\alpha}\omega_{cy\alpha} - \omega_{cz\alpha}\nu_\alpha \right]$$

$$D_{yy\alpha} = K^{-1} D_\alpha \left[\omega_{cy\alpha}^2 + \nu_\alpha^2 \right] \qquad D_{yz\alpha} = -K^{-1} D_\alpha \left[\omega_{cy\alpha}\omega_{cz\alpha} + \omega_{cx\alpha}\nu_\alpha \right]$$

$$D_{zx\alpha} = -K^{-1} D_\alpha \left[\omega_{cx\alpha}\omega_{cz\alpha} + \omega_{cy\alpha}\nu_\alpha \right] \quad D_{zy\alpha} = K^{-1} D_\alpha \left[-\omega_{cy\alpha}\omega_{cz\alpha} + \omega_{cx\alpha}\nu_\alpha \right]$$

$$D_{zz\alpha} = K^{-1} D_\alpha \left[\omega_{cz\alpha}^2 + \nu_\alpha^2 \right] \qquad K = \left[\omega_{cx\alpha}^2 + \omega_{cy\alpha}^2 + \omega_{cz\alpha}^2 + \nu_\alpha^2 \right]$$

For ionosphere plasma, depending on the geometry of the Earth's magnetic field, if Eq. (1) is solved, the diffusion equations for unstable cases are given by including real and imaginary components;

$$D = \begin{bmatrix} D_{xxR} & D_{xyR} & D_{xzR} \\ D_{yxR} & D_{yyR} & D_{yzR} \\ D_{zxR} & D_{zyR} & D_{zzR} \end{bmatrix} + i \begin{bmatrix} D_{xxI} & D_{xyI} & D_{xzI} \\ D_{yxI} & D_{yyI} & D_{yzI} \\ D_{zxI} & D_{zyI} & D_{zzI} \end{bmatrix} \tag{3}$$

We can write the elements of this matrix in explicit form, step by step, in Eq. (4):

$$D_{xx\alpha R} = \frac{(\upsilon_\alpha^3(\upsilon_\alpha^2 + \omega_{c\alpha}^2 + \omega_{cx\alpha}^2 + 2\omega^2) + \upsilon_\alpha[\omega_{cx\alpha}^2(\omega_{c\alpha}^2 - 3\omega^2) + \omega^2(\omega_{c\alpha}^2 + \omega^2)]}{(\omega^2 + \upsilon_\alpha^2)[(\omega_{c\alpha}^2 + \upsilon_\alpha^2 - \omega^2) + 4\upsilon_\alpha^2\omega^2]}$$

$$D_{xx\alpha I} = \left[\frac{\upsilon_\alpha^2\omega\left(\upsilon_\alpha^2 - \omega_{c\alpha}^2 + 3\omega_{cx\alpha}^2 + 2\omega^2\right) + \omega\left(\omega_{c\alpha}^2 - \omega^2\right)\left(\omega_{cx\alpha}^2 - \omega^2\right)}{\left(\omega^2 + \upsilon_\alpha^2\right)\left[\left(\omega_{c\alpha}^2 + \upsilon_\alpha^2 - \omega^2\right) + 4\upsilon_\alpha^2\omega^2\right]} \right] \tag{4}$$

$$D_{xy\alpha R} = \frac{(\omega_{cx\alpha}\omega_{cy\alpha}\upsilon_\alpha\left(\omega_{c\alpha}^2+\upsilon_\alpha^2-3\omega^2\right)-\omega_{cz\alpha}\left(\upsilon_\alpha^2+\omega^2\right)\left(\omega_{c\alpha}^2+\upsilon_\alpha^2-\omega^2\right)}{(\omega^2+\upsilon_\alpha^2)[(\omega_{c\alpha}^2+\upsilon_\alpha^2-\omega^2)+4\upsilon_\alpha^2\omega^2]}$$

$$D_{xy\alpha I} = \left[\frac{(\omega_{cx\alpha}\omega_{cy\alpha}\omega\left(\omega_{c\alpha}^2+3\upsilon_\alpha^2-\omega^2\right)-2\omega_{cz\alpha}\upsilon_\alpha\omega\left(\upsilon_\alpha^2+\omega^2\right)}{\left(\omega^2+\upsilon_\alpha^2\right)\left[\left(\omega_{c\alpha}^2+\upsilon_\alpha^2-\omega^2\right)+4\upsilon_\alpha^2\omega^2\right]}\right]$$

$$D_{xz\alpha R} = \frac{-\omega_{cx\alpha}\omega_{cz\alpha}\upsilon_\alpha\left(\omega_{c\alpha}^2+\upsilon_\alpha^2-3\omega^2\right)-\omega_{cy\alpha}\left(\upsilon_\alpha^2+\omega^2\right)\left(\omega_{c\alpha}^2+\upsilon_\alpha^2-\omega^2\right)}{(\omega^2+\upsilon_\alpha^2)[(\omega_{c\alpha}^2+\upsilon_\alpha^2-\omega^2)+4\upsilon_\alpha^2\omega^2]}$$

$$D_{xz\alpha I} = \left[\frac{-\omega_{cx\alpha}\omega_{cz\alpha}\omega\left(\omega_{c\alpha}^2+3\upsilon_\alpha^2-\omega^2\right)-2\omega_{cy\alpha}\upsilon_\alpha\omega\left(\upsilon_\alpha^2+\omega^2\right)}{\left(\omega^2+\upsilon_\alpha^2\right)\left[\left(\omega_{c\alpha}^2+\upsilon_\alpha^2-\omega^2\right)+4\upsilon_\alpha^2\omega^2\right]}\right]$$

$$D_{yx\alpha R} = \frac{(\omega_{cx\alpha}\omega_{cy\alpha}\upsilon_\alpha\left(\omega_{c\alpha}^2+\upsilon_\alpha^2-3\omega^2\right)-\omega_{cz\alpha}\left(\upsilon_\alpha^2+\omega^2\right)\left(\omega_{c\alpha}^2+\upsilon_\alpha^2-\omega^2\right)}{(\omega^2+\upsilon_\alpha^2)[(\omega_{c\alpha}^2+\upsilon_\alpha^2-\omega^2)+4\upsilon_\alpha^2\omega^2]}$$

$$D_{yx\alpha I} = \left[\frac{(\omega_{cx\alpha}\omega_{cy\alpha}\omega\left(\omega_{c\alpha}^2+3\upsilon_\alpha^2-\omega^2\right)-2\omega_{cz\alpha}\upsilon_\alpha\omega\left(\upsilon_\alpha^2+\omega^2\right)}{\left(\omega^2+\upsilon_\alpha^2\right)\left[\left(\omega_{c\alpha}^2+\upsilon_\alpha^2-\omega^2\right)+4\upsilon_\alpha^2\omega^2\right]}\right]$$

$$D_{yy\alpha R} = \frac{(\upsilon_\alpha^3(\upsilon_\alpha^2+\omega_{c\alpha}^2+\omega_{cy\alpha}^2+2\omega^2)+\upsilon_\alpha[\omega_{cy\alpha}^2(\omega_{c\alpha}^2-3\omega^2)+\omega^2(\omega_{c\alpha}^2+\omega^2)]}{(\omega^2+\upsilon_\alpha^2)[(\omega_{c\alpha}^2+\upsilon_\alpha^2-\omega^2)+4\upsilon_\alpha^2\omega^2]}$$

$$D_{yy\alpha I} = \left[\frac{\upsilon_\alpha^2\omega\left(\upsilon_\alpha^2-\omega_{c\alpha}^2+3\omega_{cy\alpha}^2+2\omega^2\right)+\omega\left(\omega_{c\alpha}^2-\omega^2\right)\left(\omega_{cy\alpha}^2-\omega^2\right)}{\left(\omega^2+\upsilon_\alpha^2\right)\left[\left(\omega_{c\alpha}^2+\upsilon_\alpha^2-\omega^2\right)+4\upsilon_\alpha^2\omega^2\right]}\right]$$

$$D_{yz\alpha R} = -\frac{(\omega_{cy\alpha}\omega_{cz\alpha}\upsilon_\alpha\left(\omega_{c\alpha}^2+\upsilon_\alpha^2-3\omega^2\right)+\omega_{cx\alpha}\left(\upsilon_\alpha^2+\omega^2\right)\left(\omega_{c\alpha}^2+\upsilon_\alpha^2-\omega^2\right)}{(\omega^2+\upsilon_\alpha^2)[(\omega_{c\alpha}^2+\upsilon_\alpha^2-\omega^2)+4\upsilon_\alpha^2\omega^2]}$$

$$D_{yz\alpha I} = \left[\frac{(-\omega_{cy\alpha}\omega_{cz\alpha}\omega\left(\omega_{c\alpha}^2+3\upsilon_\alpha^2-\omega^2\right)+2\omega_{cx\alpha}\upsilon_\alpha\omega\left(\upsilon_\alpha^2+\omega^2\right)}{\left(\omega^2+\upsilon_\alpha^2\right)\left[\left(\omega_{c\alpha}^2+\upsilon_\alpha^2-\omega^2\right)+4\upsilon_\alpha^2\omega^2\right]}\right]$$

$$D_{zy\alpha R} = -\frac{(\omega_{cy\alpha}\omega_{cz\alpha}\upsilon_\alpha\left(\omega_{c\alpha}^2+\upsilon_\alpha^2-3\omega^2\right)+\omega_{cx\alpha}\left(\upsilon_\alpha^2+\omega^2\right)\left(\omega_{c\alpha}^2+\upsilon_\alpha^2-\omega^2\right)}{(\omega^2+\upsilon_\alpha^2)[(\omega_{c\alpha}^2+\upsilon_\alpha^2-\omega^2)+4\upsilon_\alpha^2\omega^2]}$$

$$D_{zy\alpha I} = \left[\frac{(-\omega_{cy\alpha}\omega_{cz\alpha}\omega\left(\omega_{c\alpha}^2+3\upsilon_\alpha^2-\omega^2\right)+2\omega_{cx\alpha}\upsilon_\alpha\omega\left(\upsilon_\alpha^2+\omega^2\right)}{\left(\omega^2+\upsilon_\alpha^2\right)\left[\left(\omega_{c\alpha}^2+\upsilon_\alpha^2-\omega^2\right)+4\upsilon_\alpha^2\omega^2\right]}\right]$$

$$D_{zx\alpha R} = \frac{-\omega_{cx\alpha}\omega_{cz\alpha}\upsilon_\alpha\left(\omega_{c\alpha}^2+\upsilon_\alpha^2-3\omega^2\right)-\omega_{cy\alpha}\left(\upsilon_\alpha^2+\omega^2\right)\left(\omega_{c\alpha}^2+\upsilon_\alpha^2-\omega^2\right)}{(\omega^2+\upsilon_\alpha^2)[(\omega_{c\alpha}^2+\upsilon_\alpha^2-\omega^2)+4\upsilon_\alpha^2\omega^2]}$$

$$D_{zx\alpha I} = \left[\frac{-\omega_{cx\alpha}\omega_{cz\alpha}\omega\left(\omega_{c\alpha}^2+3\upsilon_\alpha^2-\omega^2\right)-2\omega_{cy\alpha}\upsilon_\alpha\omega\left(\upsilon_\alpha^2+\omega^2\right)}{\left(\omega^2+\upsilon_\alpha^2\right)\left[\left(\omega_{c\alpha}^2+\upsilon_\alpha^2-\omega^2\right)+4\upsilon_\alpha^2\omega^2\right]}\right]$$

$$D_{zy\alpha R} = -\frac{(\omega_{cy\alpha}\omega_{cz\alpha}\upsilon_\alpha\left(\omega_{c\alpha}^2+\upsilon_\alpha^2-3\omega^2\right)+\omega_{cx\alpha}\left(\upsilon_\alpha^2+\omega^2\right)\left(\omega_{c\alpha}^2+\upsilon_\alpha^2-\omega^2\right)}{(\omega^2+\upsilon_\alpha^2)[(\omega_{c\alpha}^2+\upsilon_\alpha^2-\omega^2)+4\upsilon_\alpha^2\omega^2]}$$

$$D_{zy\alpha I} = \left[\frac{(-\omega_{cy\alpha}\omega_{cz\alpha}\omega\left(\omega_{c\alpha}^2+3\upsilon_\alpha^2-\omega^2\right)+2\omega_{cx\alpha}\upsilon_\alpha\omega\left(\upsilon_\alpha^2+\omega^2\right)}{\left(\omega^2+\upsilon_\alpha^2\right)\left[\left(\omega_{c\alpha}^2+\upsilon_\alpha^2-\omega^2\right)+4\upsilon_\alpha^2\omega^2\right]}\right]$$

$$D_{zz\alpha R} = \frac{(\upsilon_\alpha^3(\upsilon_\alpha^2+\omega_{c\alpha}^2+\omega_{cz\alpha}^2+2\omega^2)+\upsilon_\alpha[\omega_{cz\alpha}^2(\omega_{c\alpha}^2-3\omega^2)+\omega^2(\omega_{c\alpha}^2+\omega^2)]}{(\omega^2+\upsilon_\alpha^2)[(\omega_{c\alpha}^2+\upsilon_\alpha^2-\omega^2)+4\upsilon_\alpha^2\omega^2]}$$

$$D_{zz\alpha I} = \left[\frac{\upsilon_\alpha^2\omega\left(\upsilon_\alpha^2-\omega_{c\alpha}^2+3\omega_{cz\alpha}^2+2\omega^2\right)+\omega\left(\omega_{c\alpha}^2-\omega^2\right)\left(\omega_{cz\alpha}^2-\omega^2\right)}{\left(\omega^2+\upsilon_\alpha^2\right)\left[\left(\omega_{c\alpha}^2+\upsilon_\alpha^2-\omega^2\right)+4\upsilon_\alpha^2\omega^2\right]}\right]$$

3. Numerical Analysis and Results

Using Eqs. (1), (2), (3) and (4) the diffusion coefficients for the heights of the F-regions were computed as seasonal latitudes for the year 1990. By the agreed criteria, the IRI model was utilized to derive the ionospheric parameters that were used in the calculation [16]. We looked at the seasonal variation of Eq. (3) for the diffusion coefficients in ionospheric plasma concerning latitude at altitudes of 390, 410, 450, 500, 550 and 600 km (these heights are altitudes at which equatorial anomaly occurs at F^2-Region). Seasonal diffusion coefficients were found for both the stable Eq. (2) and unstable Eq. (3) scenarios for the critical heights of the F-region that were previously determined [17,18]. Next, each element of the diffusion tensor was examined for equinox days in local time by averaging the elements whose orders were the same under the conditions taken into consideration. Twice a year, there are equinox days when day and night are approximately equal in duration. The times throughout the Earth's orbit around the Sun when its axis is neither tilted toward nor away from the Sun are designated by these events [19]. Every year, the equinoxes fall on or around March 20 or 21 and September 22 or 23. The Earth's axis is neither tilted away from the Sun (as in winter) nor towards it (as in summer) during the equinoxes when the Sun

is directly overhead the equator of the Earth. For most places on Earth, this means that day and night last about equal amounts of time. At the vernal equinox, Figure 2 displays the local temporal fluctuation of diffusion coefficients for the conditions ω=0 and ω≠0. As a result, diffusion coefficients increase quickly in both stable and unstable states between around 1.00 and 5.00 local time, reach a maximum at precisely 6.00 o'clock, and then rapidly fall after this period. The terms ‘‘ω=0, $D_{xy}=D_{yx}$’’ refer to trigonometric exponential increases and decreases.

In terms of magnitudes, it can be listed as $D_{yy} > D_{xy} > D_{yz} > D_{xx} > D_{xz} > D_{zz}$. All values are approximately 10^8 (m^2/sec). However, looking at the same figure, the trend of change of diffusion coefficients for the ω≠0 condition is the same as for the unstable case, but their magnitude decreases dramatically. Among the tensor elements of the real part, the diagonal elements are larger and the other elements are smaller. The smallest value is D_{xzR} with a record low of 10^{-14} (m^2 / sec). As for the imaginary part, it takes the diagonal elements with higher values than other tensor elements. As for the imaginary part, it takes the diagonal elements with higher values than other tensor elements.

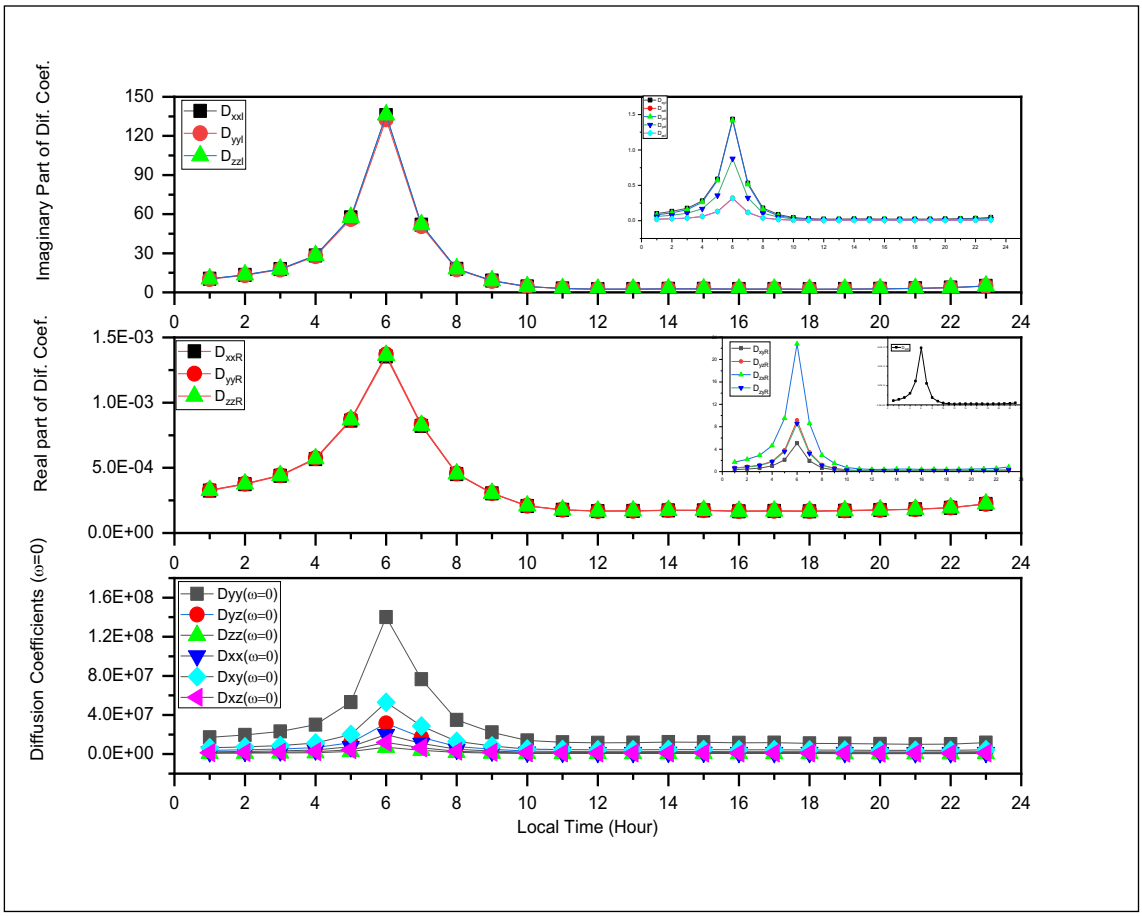

Figure 2. Variation of diffusion coefficients with local time for stable and unstable conditions at the equator (March. 21).

For the autumn equinox, the change of diffusion coefficients with local time under the considered conditions is given in Figure 3. The diagram is the same for the vernal equinox. In a steady state, the order according to the magnitude of the coefficients is $D_{xx} > D_{xy} > D_{xz} > D_{yy} > D_{yz} > D_{zx} > D_{zy} > D_{zz}$. There is no significant change in the magnitude of the diffusion coefficients during both equinoxes [20, 21]. They are almost equal to each other. In the steady state, the magnitudes of the diffusion coefficients are 10^8 m^2/sec, in the unstable state, the diagonal elements of the real part tensor of the diffusion coefficients are on the order of 10^{-4}, and other tensor elements outside the diagonal elements have values close to the magnitudes of the imaginary part tensor, except D_{xzR} [22, 23]. The diagonal elements of the imaginary part are the largest, and the other elements are 100 times smaller than their diagonal elements. Sizes vary between 0.5-150 m^2/sec.

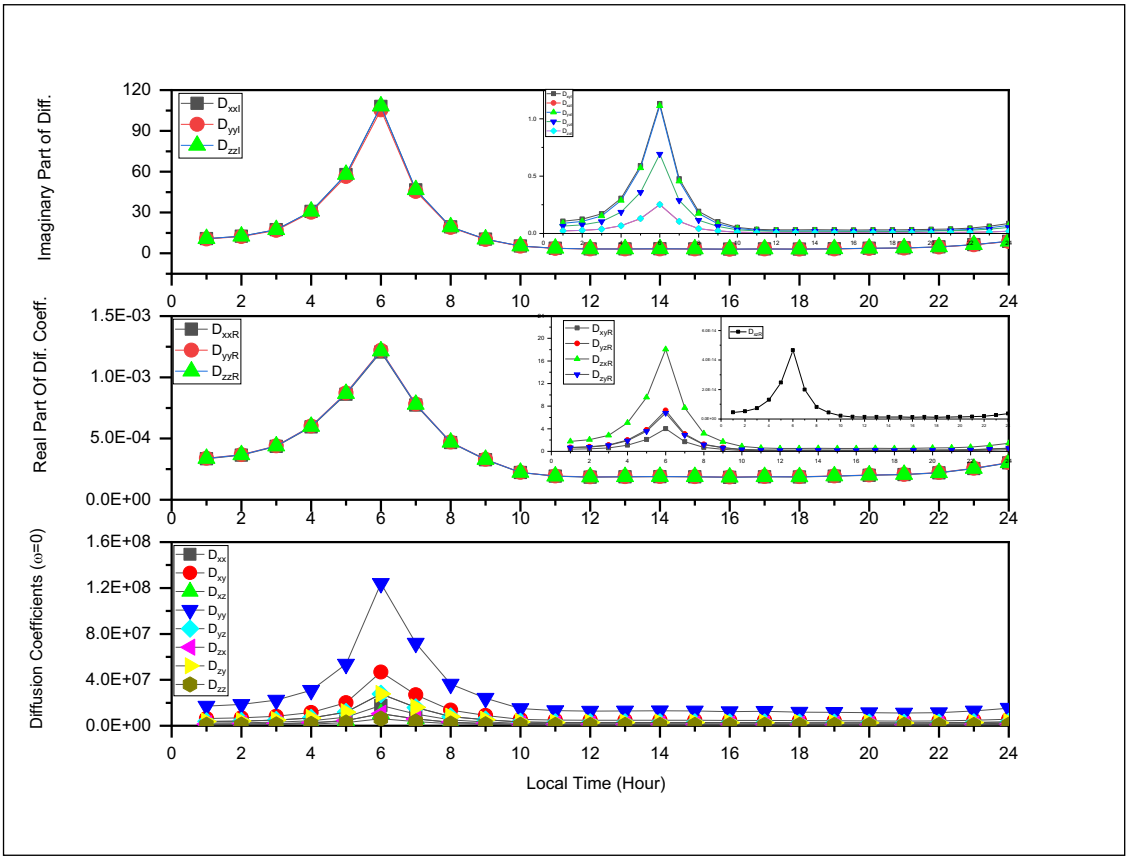

Figure 3. Variation of diffusion coefficients with local time for stable and unstable conditions at the equator (Sempt. 23).

4. Conclusion

This study aims to solve the diffusion equations, which are the most significant transport processes in the ionospheric plasma, analytically in both steady and unstable states. It does this by utilizing the northern hemisphere's actual magnetic field geometry and by applying these equations to specific conditions in the ionosphere to produce numerical results. Outcomes attained in the previously agreed circumstances

1- At six in the morning, all diffusion tensor elements, in both stable and unstable scenarios, reach their maximum.

2. Diffusion coefficients in steady state are around 10^8 (m^2/sec).

3. The real part's diagonal elements have sizes in the order of 10^{-4} (m^2/sec) in the unstable scenario.

4- The imaginary part's tensor elements in the unstable scenario range in magnitude from 0 to 150 m^2/sec.

The electron density of the ionosphere affects its properties, particularly the F region, which is crucial for radio wave reflection, propagation, and refraction. The conditions of reflection will alter if there is an anomaly in the electron density for whatever reason. The results of this study show that the electron density forms a peak and trough around the equator due to diffusion coefficients, which are responsible for phenomena like ‘‘equality of day and night,’’ ‘‘spring and autumn equinoxes,’’ and ‘‘vertical rays of the sun. ’’ The reflection height shortens on the hills and increases in the troughs as a result of these hills and troughs. Every diffusion coefficient exhibits this condition.

References

[1] Sağır S, Yeşil A. The relation between the refractive index of the equatorial ionospheric F2 region and long-term solar indices. Wirel Pers Commun 2018;102: 31-40.

[2] Yeşil A, Sağır S, Kurt K. The behavior of the classical diffusion tensor for equatorial ionospheric plasma. Journal of Science, 2016; 13: 123.

[3] Rishbeth H. Physics and chemistry of the ionosphere. Contemp Phys 1973;14(3): 229-249.

[4] Rishbeth H, Garriot OK. Introduction to Ionospheric Physics. New York, USA: Academic Press, 1969.

[5] Timoçin E, Yeşil A, Ünal İ. The effect of the geomagnetic activity to the hourly variations of ionospheric foF2 values at low latitudes. Arab J Geosci 2014; 7: 4437-4442.

[6] Kurt K. The Seasonal Behavior of the Characteristic Wave in Low Latitudes. Int J Innovative Eng Appl 2021; 5(1): 36-39.

[7] Mungufeni P, Rabiu BA, Okoh D, Jurua E. Characterisation of Total Electron Content over African region using Radio Occultation observations of COSMIC satellites. Adv Space Res 2020; 65(1): 19-29.

[8] Yesil A, Sagir S, Kurt K. The Behaviour of the Classical Diffusion Tensor for Equatorial Ionospheric Plasma. J Sci 2016; 13:123-127.

[9] Denisenko VV, Rycroft MJ, Harrison RG. A Mathematical Model of the Global Ionospheric Electric Field Generated by Thunderstorms. Bull Russ Acad Sci: Phys 2023; 87(1): 118-123.

[10] Tabassum A, Park K, Shin J, Jin HG, Baik JJ. Long-term changes in temperature, specific humidity, and precipitation in Bangladesh revealed by ERA5 data. Theor Appl Climatol 2023; 1-11.

[11] Olsen RC, Shawhan SD, Gallagher DL, Green JL, Chappell CR, Anderson RR. Plasma observations at the Earth's magnetic equator. J Geophys Res Space Phys 1987;92(A3): 2385-2407.

[12] Razzhevaikin VN. Instability of stationary nonmonotone solutions of the reaction equation with diffusion depending on density. Differ Equ 2006; 42: 567-575.

[13] Kolesnikov AF. Tirskii GA. The Stefan-Maxwell equations for diffusion fluxes of plasma in a magnetic field. Fluid Dyn 1985;19(4): 643–649.

[14] Yesil A. Sagir S. Kurt K. The Behaviour of the Classical Diffusion Tensor for Equatorial Ionospheric Plasma, J. Sci 2016; 13:123-127

[15] Timoçin E, Ünal İ, Yeşil A. The Effect of the midlatitude electron density trough on the ionospheric conductivities. Iran J Sci Technol Trans A: Sci 2019; 43: 297-307.

[16] Sağir S, Yaşar M, Atici R. The Relationship between Dst, IMF-Bz and collision parameters for $O^{+}+ N_2 \rightarrow NO^{++} N$ reactive scattering in the ionosphere. Geomagnetism and Aeronomy, 2019; 59: 1003-1008.

[17] Mendonça JT. Diffusion of magnetic field lines in a toroidal geometry. Phys Fluid Plasma Phys 1991; 3(1): 87-94.

[18] Kurt K, Yeşil MB. The Comparison of the Group and Phase Velocity of the Polarized Wave and the Equatorial Anomaly of the Ionosphere. Eur J Res Dev 2022; 2(2): 466-474.

[19] Katlamudi MR, Bulusu J. Low latitude Pi^2 pulsations at Desalpar, Gujarat, India: A statistical analysis of the influences of magnetic storms/substorms, seasons, and solar cycles. J Atmos Sol Terr Phys 2023; 252: 106145.

[20] Yeşil A, Sağır S. The New Diffusion Tensor and the Equatorial Anomaly Altitudes of F-Region. Celal Bayar Univ J. Sci 2017; 13(3): 717-723.

[21] Yasar M. The solar eclipse effect on diffusion processes of $O^{+}+ O_2 \rightarrow O_2^{+}+ O$ reaction for the upper ionosphere over Kharkov. Therm Sci, 2021; 25(1): 57-63.

[22] Ünal İ, Karatay S, Yeşil A, Hançerlioğulları A. Seasonal variations of impedance in the ionospheric plasma. 2020; J Polytech.

[23] Yasar M. The change of diffusion processes for $O^{+}+ N_2 \rightarrow NO^{+}+ N$ reaction in the ionospheric F region during the solar eclipse over Kharkov. Therm Sci 2021; 25(1): 51-56.

Turkish Journal of Science & Technology
19(2), 415-425, 2024

Research Paper
https://doi.org/10.55525/tjst.1463429

Diagnosis of Permanent Magnet Assisted Synchronous Reluctance Motor Winding Fault by Convolutional Neural Network

Ayse BAYRAK[1], Canan TASTIMUR[2*], Erhan AKIN[3]
[1,3] Department of Computer Engineering, Faculty of Engineering, Firat University, Elazig, Türkiye
[2] Department of Computer Engineering, Faculty of Engineering-Architecture, Erzincan Binali Yildirim University, Erzincan, Türkiye
[*] ctastimur@erzincan.edu.tr

(Geliş/Received: 02/04/2024; Kabul/Accepted: 27/07/2024)

Abstract: In recent years, the use of machine learning models for fault detection has become commonplace. Its goal is to identify and fix problems with permanent magnet synchronous reluctance motors. This research's primary goal is to identify and categorize errors in their early stages. We classified winding faults using machine learning approaches, such as Independent Component Analysis and Deep Learning models. We could distinguish between vibration and current signals from the engine signals by using Independent Component Analysis (ICA). We experimented on multiple architectures using the convolutional neural network (CNN) architecture we designed from scratch and the Transfer Learning technique, testing two distinct datasets we generated using the signals we got. According to experimental findings, the suggested scratch CNN model performed exceptionally well in classification, achieving 98.6% with current signals and 99.4% with vibration signals.

Key words: Circuit faults, fault detection, machine learning, permanent magnet motors.

Kalıcı Mıknatıs Destekli Senkron Relüktans Motor Sargı Arızasının Evrişimli Sinir Ağı ile Teşhisi

Öz: Son yıllarda hata tespiti için makine öğrenmesi modellerinin kullanımı yaygınlaşmıştır. Amacı, kalıcı mıknatıs destekli senkron relüktans motor ilgili sorunları tanımlamak ve düzeltmektir. Bu araştırmanın temel amacı, hataları erken aşamalarında tanımlamak ve sınıflandırmaktır. Bağımsız Bileşen Analizi ve Derin Öğrenme modelleri gibi makine öğrenimi yaklaşımlarını kullanarak motor arızalarını sınıflandırdık. Bağımsız Bileşen Analizi (ICA) kullanarak titreşim ve akım sinyallerini motor sinyallerinden elde ettik. Sıfırdan tasarladığımız evrişimsel sinir ağı (CNN) mimarisini ve Transfer Öğrenme tekniğini kullanarak birden fazla mimari üzerinde denemeler yaptık ve elde ettiğimiz sinyalleri kullanarak oluşturduğumuz iki farklı veri setini test ettik. Deneysel bulgulara göre, önerilen sıfırdan CNN modeli, sınıflandırmada son derece iyi performans göstererek akım sinyallerle %98,7 ve titreşim sinyalleriyle %99,4'e ulaşmıştır.

Anahtar kelimeler: Devre arızaları, arıza tespiti, makine öğrenmesi, kalıcı mıknatıslı motorlar.

1. Giriş

Permanent magnet synchronous reluctance motors have become popular in recent years and are widely used in various industries, including high-speed trains, electric vehicles, household appliances, and production processes [1]. These motors feature non-conductive rotors with a cavity structure and flux barrier, requiring minimal maintenance. Their brushless design, efficient material usage, low cost, and ease of production have contributed to their increased utilization. Ensuring the seamless operation of these motors in diverse industrial applications is crucial. Prompt diagnosis and intervention in case of system malfunctions while the motor is in operation directly impact its efficiency.

With the continuous development of computer technology in recent years, intelligent diagnostic methods have been preferred by researchers and have developed rapidly. Intelligent diagnostic methods for fault detection and diagnosis of complex systems have higher accuracy than traditional analysis methods such as support vector machines (SVM), expert systems, neural networks, fuzzy logic, and machine learning theory-based diagnostic methods. The intelligent diagnosis method uses artificial information technology such as expert systems, fuzzy logic reasoning, and neural networks to imitate the human mind's judgment process using accumulated fault detection and diagnosis knowledge and logical reasoning knowledge. In addition, the intelligent diagnostic method performs complex fault monitoring and diagnosis of motors in engineering applications [2].

When the literature studies were examined, it was observed that malfunctions were detected using various methods. The most common methods used in recent years are signal-based approaches. In all diagnostic methods, acquiring signal data is essential to determine the type of fault in the motor. These signals include current, voltage,

[*] Corresponding author: ctastimur@erzincan.edu.tr. ORCID Number of authors: [1] 0009-0000-4242-2330, [2] 0000-0002-3714-6826, [3] 0000-0001-6476-9255

vibration, torque, etc., which are indicative of motor faults. Signals such as noise and heating that may occur in the motor are processed using machine learning methods to analyze and address fault situations for detection and classification. The primary objective of these studies is to identify and categorize faults at an early stage [3].

Torres et al., in their study titled "Detection of Eccentricity Faults in Five-Phase Ferrite-PM Assisted Synchronous Reluctance Machines" published in 2017, stated that faults in the air gap disrupt the magnetic flux. They mentioned that various strategies are employed for detecting this fault, including spectral vibration analysis, acoustic analysis [4-5], thermal analysis [6], air gap flux analysis, and MCSA (motor current signature analysis). They also highlighted the lack of information on this topic in the literature and suggested that their study could be beneficial for developing fault diagnosis strategies after thorough analysis and interpretation [7]. In [8], eccentricity failures of 3-phase and 5-phase motor faults were analyzed using finite element analysis, irrespective of their phase numbers. The fault characteristics of the motor, such as torque fluctuations, average torque, and back-EMF harmonics, were extracted because of these analyses. Arafat and Choi [9] explored fault tolerance control and optimal phase progression for various fault conditions in 5-phase in their study. They analyzed an optimally designed five-phase permanent magnet synchronous reluctance motor under different open-phase fault conditions. Furthermore, fault endurance tests were conducted commonly used in air applications [10]. In the study, a 3-phase motor was separately isolated and divided in a manner that prevented phase overlap, and the motor's behavior was analyzed using the finite element method under various fault conditions.

In his 2017 study, Wided Zine [11] examined the machine learning method for sensor control of IPMSMs, which is structurally the closest motor type. Since fault diagnosis is crucial at an early stage for this motor type, widely used in electric vehicles, the signal injection method is chosen to cover zero and low speeds while the engine is running, while the machine learning method is utilized at high and medium speeds. In a publication from 2018 [12], motor fault diagnosis was conducted using a deep learning method. Based on Long Short-Term Memory (LSTM), one of the deep learning algorithms, the 3-phase current values from previous sampling moments are stored in memory, making the next sampling instantly predictable by the system. In another study [13], Kao et al. detected faults at various intensities across a wide speed range using a deep learning algorithm. They employed two methods for feature extraction in their research. The first method involved wavelet packet transform for classification, while the second method utilized a deep 1-D convolutional neural network with a softmax layer in a 2019 study titled "Faults and Diagnosis Methods of Permanent Magnet Synchronous Motors: A Review" [14]. This study explains fault and diagnostic methods for PMSM motors, commonly used in the industrial field. The electrical, mechanical, and magnetic faults in the motor are summarized, followed by an explanation of the diagnostic methods found in the literature. Among these methods, it is noted that the most used fault diagnosis method is artificial intelligence-based.

As a result of the literature studies, it is seen that various methods are used for fault detection in permanent magnet synchronous reluctance motors. However, it has been understood that studies based on machine learning are not used frequently. In this study, vibration and current data of a 3-phase 1 kW motor in different stator fault states are used. Vibration and current data in healthy and stator inter-coil short circuit fault operating conditions were obtained for the motor used. The motor was operated under the same torque and rotational speed. By applying the confusion matrix method, one of the machine learning methods, to the obtained data, the existing situation in the data set and the number of correct and incorrect predictions of the classified model are given in a table.

2. Fault Detectıon of Permanent Magnet Synchronous Reluctance Motors

Faults occurring can be classified as electrical, magnetic, and mechanical faults. Magnetic faults generally include magnet demagnetization and fracture. Electrical faults include short circuits between windings, connection errors in windings, stator open-circuit, phase-to-ground short circuits, and phase-to-phase short circuits. Mechanical failures consist of unstable conditions such as bent shafts or dynamic misalignment, static and dynamic air gap irregularity, and damaged bearing failures [15].

In Figure 1, the basic block diagram of the signal-based approach for fault diagnosis in a motor is provided.

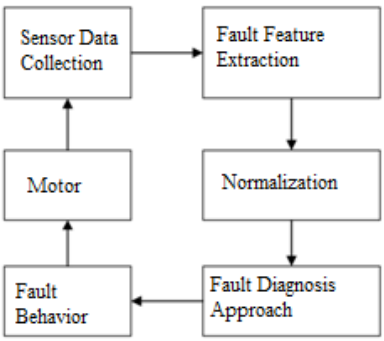

Figure 1. Signal-based diagnostic approach used in motors [16].

This study, it is aimed to diagnose faults on the motor with deep learning and ICA. A defect situation was created by making various changes to the motor. The parameter values of the motor used in the study are provided in Table 1.

Table 1. Parameters of the proposed approach.

Parameter	Value
Rated power	1 kW (kilowatt)
Input Voltage	380 V
Frequency	60 Hz (hertz)
Number of phases	3
Rated speed	3000 RPM
Rated torque	3.18 Nm (Newton meter)
Inter-coil resistance value (Rcc)	0.0409 Ohm

The data used in the study were obtained by short-circuiting the motor stator. One method to induce a fault in the motor stator is by increasing the stator resistance (open circuit fault), while another method is by reducing the stator resistance (short circuit fault). Short-circuiting the stator leads to more pronounced and severe faults in the motor, creating a direct path for the driving current. Consequently, the normal current flowing through the stator coil decreases in accordance with Kirchhoff's law, resulting in a short circuit in the stator and a torque induced in the motor's electromagnetic field [17].

Stators short-circuit faults of two different intensities were created by reducing the motor resistance value with the short-circuit fault on the motor used in this study. The healthy and stator short-circuit malfunctioning operating states of the motor were analyzed in the MATLAB Simulink environment. The simulation results of the motor used in normal operating conditions are shown in Figures 2, 3, and 4.

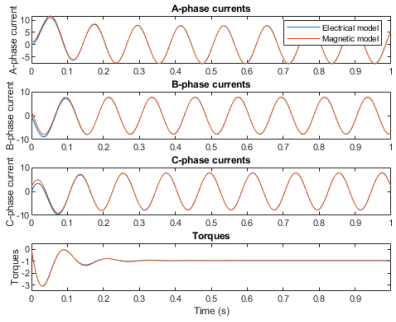

Figure 2. Current and torques waveform in healthy condition.

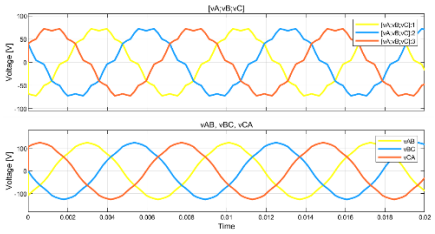

Figure 3. Phase voltages waveform in healthy condition.

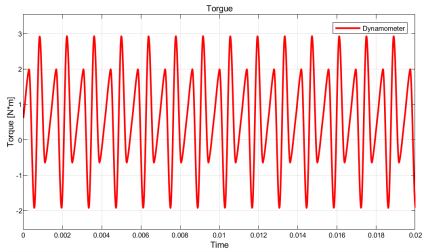

Figure 4. Torgue waveform in healthy condition.

In Figure 5, simulation results show stator inter-coil short circuit faults with intensities of 0.68% and 0.81%, healthy and defective respectively.

(a) (b)

Figure 5. (a) Healthy and (b) defective current and torques waveform inter-coil short circuit fault.

3. Material and Method

Classification of motor faults involves a two-stage approach: ICA and CNN. We transformed the current and vibration signal data acquired from a 3-phase 1 kW motor in various stator fault conditions into images using ICA. Due to the large volume of data in the signal images, approximately 1 million, we conducted signal sampling based on the sampling period for the current and vibration signals. Each set of current and vibration signal data falls into three categories (normal, fault-1, and fault-2). These data were segmented using a 10-second sampling period and converted into image format. Consequently, our image dataset is prepared for use in the proposed model. Examples of sample current and vibration signal images are depicted in Figure 6 and Figure 7. Each signal is categorized into three types: normal, fault type 1, and fault type 2. Figures 6 and 7 display two sample images of the current and voltage signals in our dataset.

The proposed CNN network model includes 5 convolution layers, 5 maxPooling layers, 2 dense layers, and SoftMax classifier layers. The hyperparameters of the model are as follows: input size 150x150, epoch 100, batch size 32, optimizer Adam, learning rate 0.001, pooling size 2x2, convolution filter size 3x3, numbers of convolution filters 32, 64, 64, 128, and 256, stride value 1, no padding, ReLU activation function, L2 regularization, pooling type MaxPooling. We presented this model in Figure 9. We also used the Transfer Learning (TL) technique to compare the network model we developed. We tested both our current and vibration datasets on DenseNet121, DenseNet169, DenseNet201, InceptionResNetV2, MobileNet, MobileNetV2, and VGG16 architectures. TL involves freezing all parameters, layers, and weights in a pre-trained network architecture and applying it to a new dataset. In our study, we only updated the number of classes by adjusting the value on the Softmax layer, which is the classifier layer.

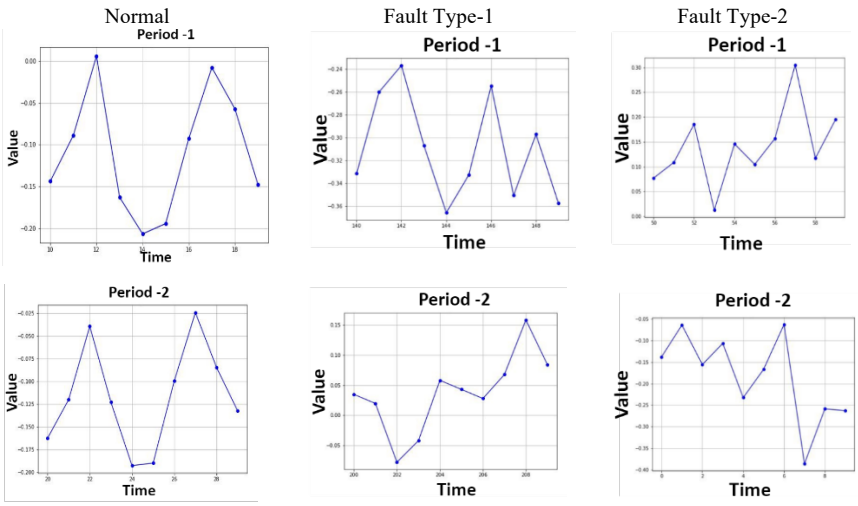

Figure 6. Samples of the current signals.

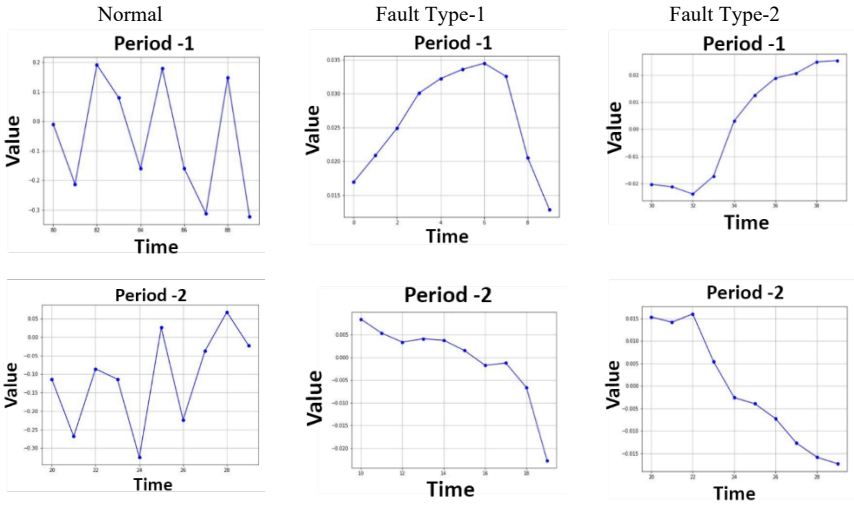

Figure 7. Samples of the vibration signals.

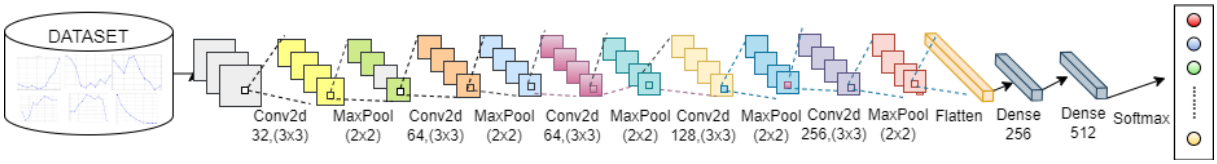

Figure 8. Proposed scratch CNN model.

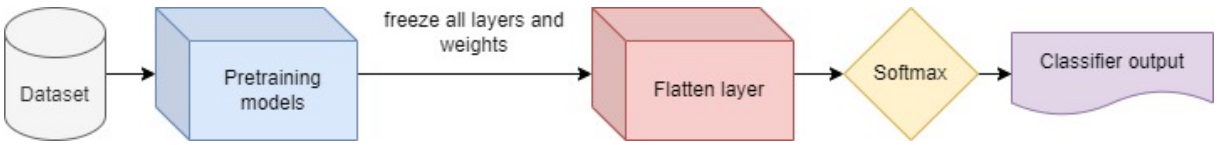

Figure 9. General scheme of TL method functioning.

4. Experimental Results

Fault diagnosis is conducted by analyzing the signal information received from the motor in an actual setup. The technical specifications of the motor used in the experiments are as follows: The motor has a nominal power of 1 kW and operates with a 380 V input voltage. It is designed to function in a three-phase system with a frequency of 60 Hz. The motor's nominal speed is 3000 RPM, and its nominal torque value is 3.18 Nm. The intermediate winding resistance (Rcc) of the motor was measured as 0.0409 Ohm.

For direct current signals, current values are determined by measuring the voltage drop across shunt resistors placed in the motor circuit. Hall effect sensors detect the magnetic field generated by the motor and calculate the current. In the case of alternating currents, high currents are safely measured using current transformers. Vibration signals are typically captured using accelerometers or piezoelectric sensors, which transform mechanical vibrations into electrical signals for transmission to data acquisition systems. The acquired data is digitally recorded at a specified sampling rate. Subsequently, the numerical data is analyzed in both time and frequency domains and converted into image data. These images are further transformed into current and voltage representations with a sampling interval of 10 seconds. This process allows for the evaluation of the motor's performance and the identification of potential malfunctions.

The results for the motor with vibration – intercoil – 1kW data are provided in this section. A total of 1,048,575 data points were entered into the system. The vibration data class obtained from normal operation was labeled as the vibration data class from the short circuit fault condition, operating with intensities of 0.68 and 0.81, was labeled as Type-1 and Type-2, respectively. This research was conducted using a desktop computer equipped with an Intel(R) Core(TM) i7 processor with Turbo Boost up to 5.0 GHz, running at 5.20GHz, 32GB of DDR5 RAM, and an NVIDIA RTX 4070 GPU.

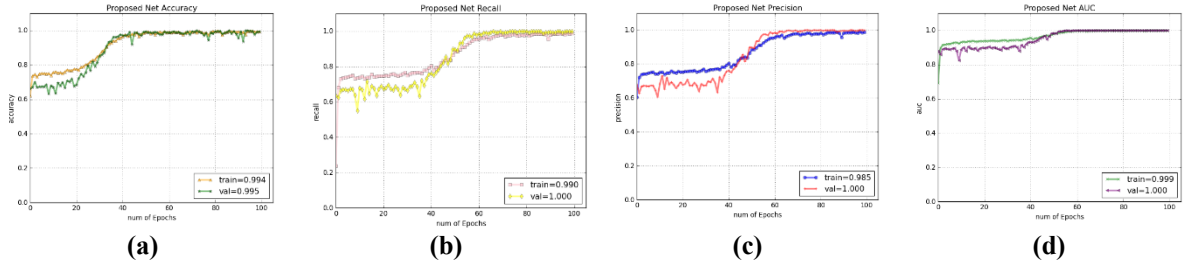

Figure 10. a) Accuracy b)Recall c)Precision and d)AUC rates of proposed CNN model on vibration signal.

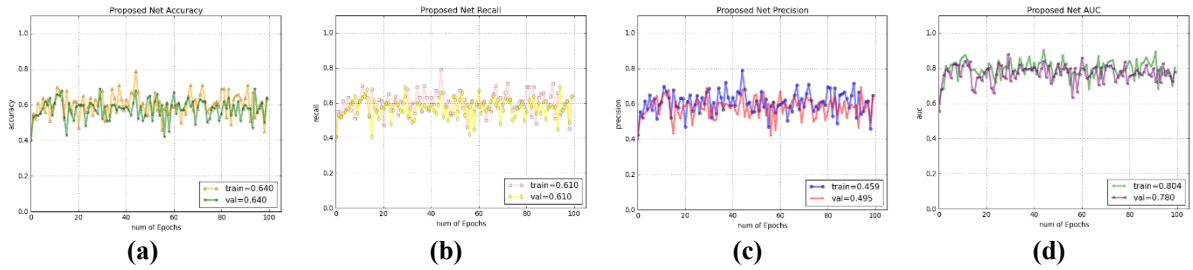

Figure 11. a) Accuracy b)Recall c)Precision and d)AUC rates of DenseNet121 on vibration signal.

Table 2. Performance of Vibration –intercoil – 1kW result.

Method	Accuracy	Recall	Precision	AUC
Proposed CNN	**0.994**	**0.990**	**0.985**	**0.999**
DenseNet121	0.640	0.610	0.459	0.804
DenseNet169	0.650	0.520	0.707	0.785
DenseNet201	0.640	0.580	0.650	0.803
InceptionResNetV2	0.520	0.550	0.694	0.718
MobileNet	0.630	0.630	0.580	0.795
MobileNetV2	0.610	0.630	0.640	0.738
VGG16	0.660	0.610	0.713	0.850

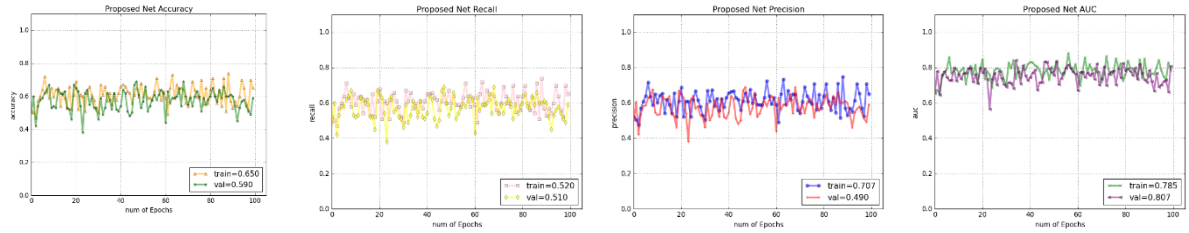

(a) **(b)** **(c)** **(d)**

Figure 12. a) Accuracy b)Recall c)Precision and d)AUC rates of DenseNet169 on vibration signal.

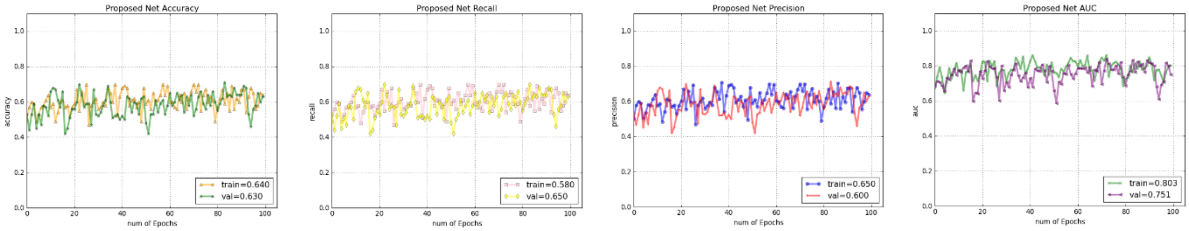

(a) **(b)** **(c)** **(d)**

Figure 13. a) Accuracy b)Recall c)Precision and d)AUC rates of DenseNet201 on vibration signal.

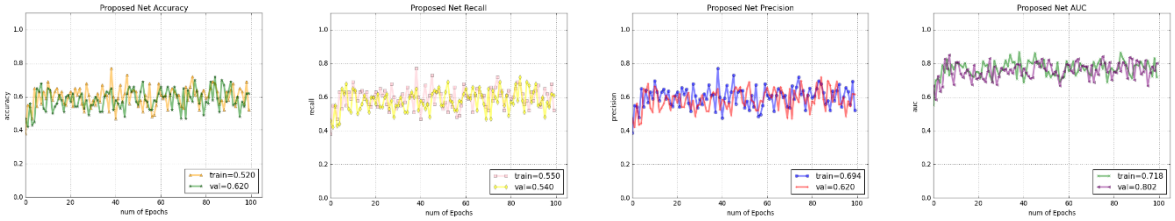

(a) **(b)** **(c)** **(d)**

Figure 14. a) Accuracy b)Recall c)Precision and d)AUC rates of InceptionResNetV2on vibration signal.

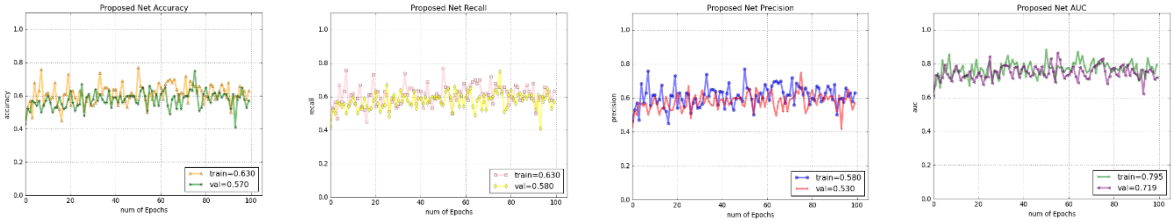

(a) **(b)** **(c)** **(d)**

Figure 15. a) Accuracy b)Recall c)Precision and d)AUC rates of MobileNet vibration signal.

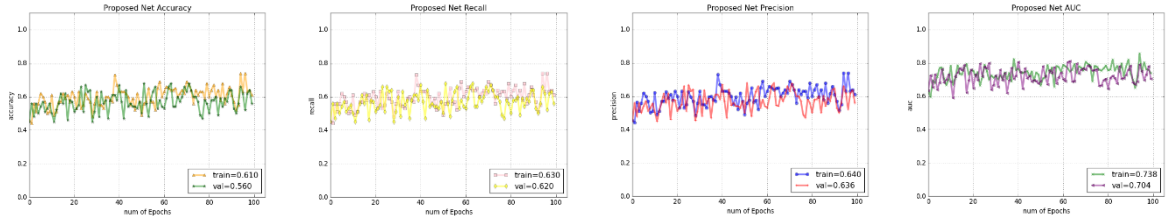

(a) **(b)** **(c)** **(d)**

Figure 16. a) Accuracy b)Recall c)Precision and d)AUC rates of MobileNetV2 vibration signal.

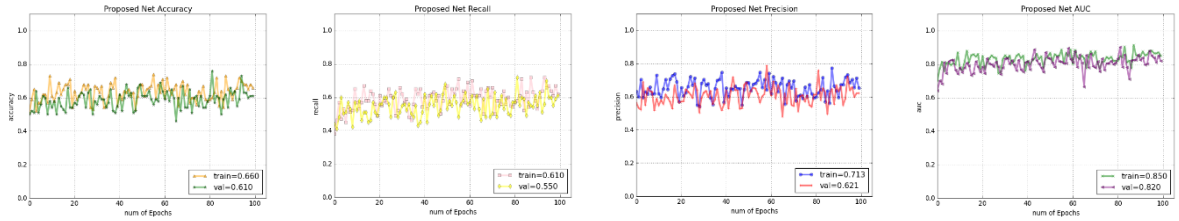

(a) **(b)** **(c)** **(d)**

Figure 17. a) Accuracy b)Recall c)Precision and d)AUC rates of VGG16 vibration signal.

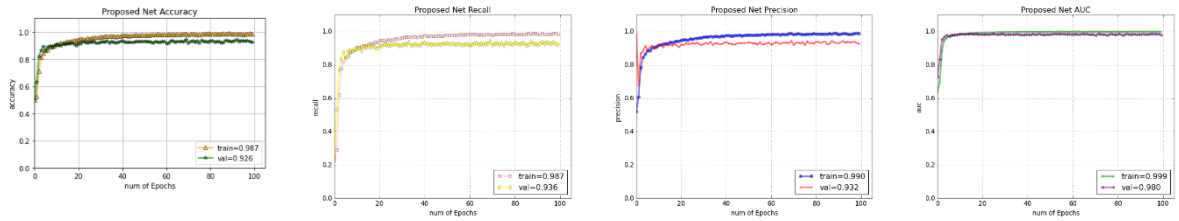

(a) **(b)** **(c)** **(d)**

Figure 18. a) Accuracy b)Recall c)Precision and d)AUC rates of proposed CNN model on current signal.

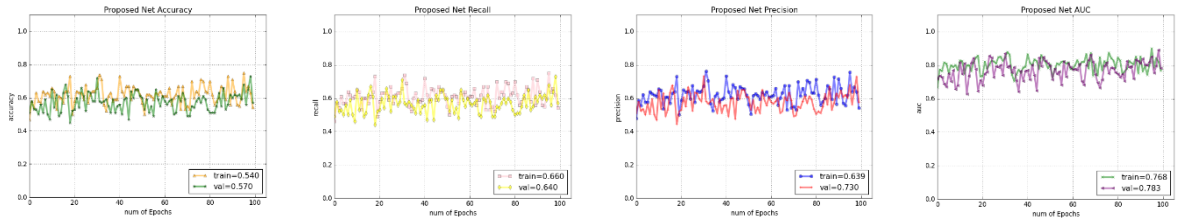

(a) **(b)** **(c)** **(d)**

Figure 19. a) Accuracy b)Recall c)Precision and d)AUC rates of DenseNet121 on current signal.

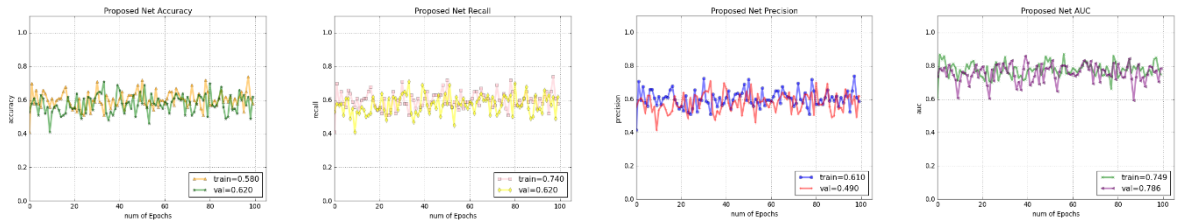

(a) **(b)** **(c)** **(d)**

Figure 20. a) Accuracy b)Recall c)Precision and d)AUC rates of DenseNet169 on current signal.

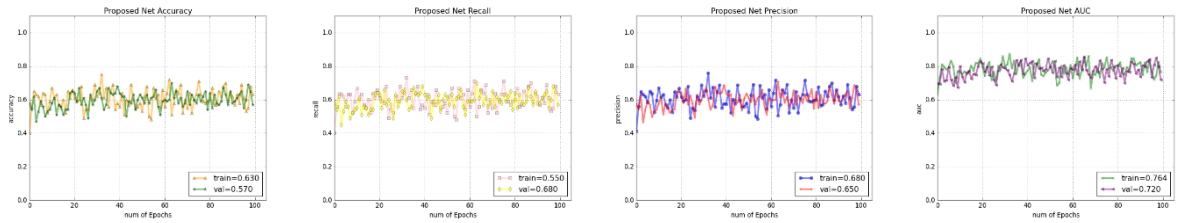

(a) **(b)** **(c)** **(d)**

Figure 21. a) Accuracy b)Recall c)Precision and d)AUC rates of DenseNet201 on current signal.

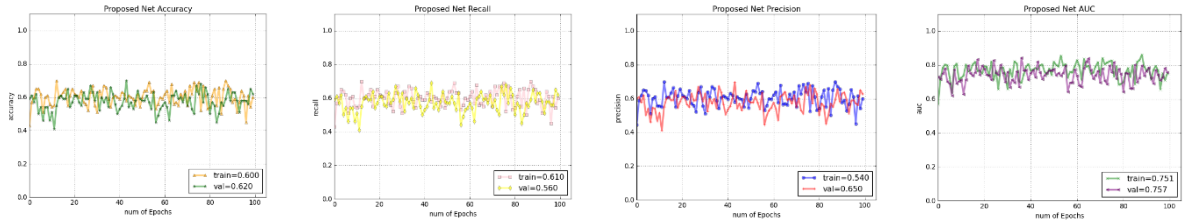

(a) **(b)** **(c)** **(d)**

Figure 22. a) Accuracy b)Recall c)Precision and d)AUC rates of InceptionResNetV2 on current signal.

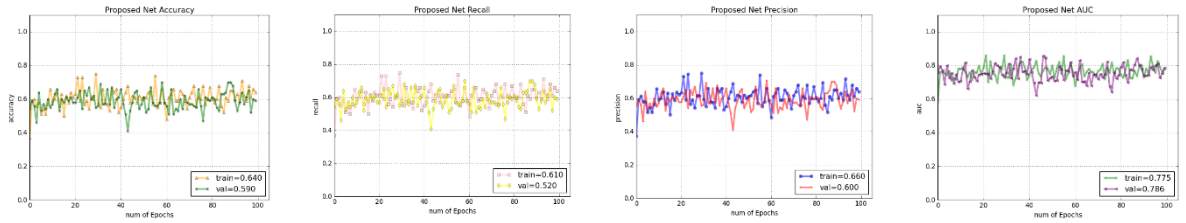

(a) **(b)** **(c)** **(d)**

Figure 23. a) Accuracy b)Recall c)Precision and d)AUC rates of MobileNet on current signal.

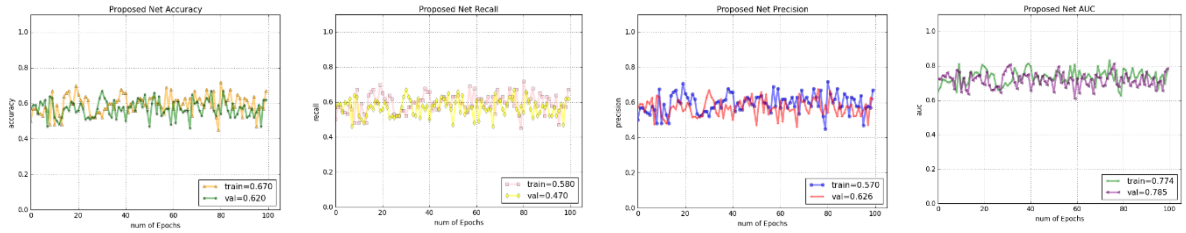

(a) **(b)** **(c)** **(d)**

Figure 24. a) Accuracy b)Recall c)Precision and d)AUC rates of MobileNetV2 on current signal.

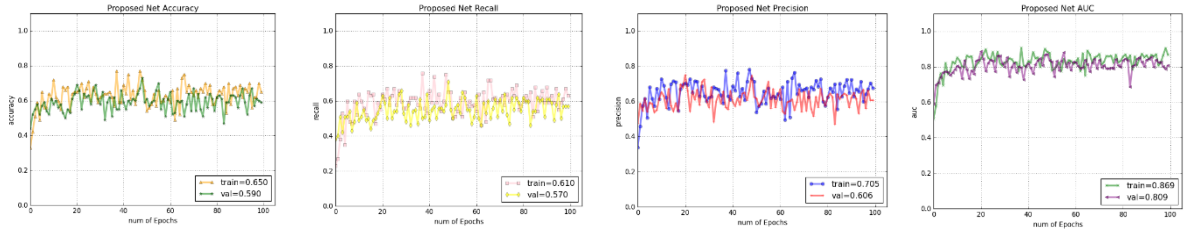

(a) **(b)** **(c)** **(d)**

Figure 25. a) Accuracy b)Recall c)Precision and d)AUC rates of VGG16 on current signal.

Table 3. Performance of Current –intercoil – 1kW result.

Method	Accuracy	Recall	Precision	AUC
Proposed CNN	**0.987**	**0.987**	**0.990**	**0.999**
DenseNet121	0.540	0.660	0.639	0.768
DenseNet169	0.580	0.740	0.610	0.749
DenseNet201	0.630	0.550	0.680	0.764
InceptionResNetV2	0.600	0.610	0.540	0.751
MobileNet	0.640	0.610	0.660	0.775
MobileNetV2	0.670	0.580	0.570	0.774
VGG16	0.650	0.610	0.705	0.869

Table 2 and Table 3 illustrate the classification performance in fault diagnosis of voltage and current signals. Upon examining the results generated by these data using various methods in the tables, it is evident that the method proposed in this study yields significantly higher results in terms of accuracy, recall, precision, and AUC factors compared to other transfer learning methods. The graphical representations in Figure 10 and Figure 25 depict the results of accuracy, recall, precision, and AUC metrics on the transfer learning of current and vibration data, as well as the proposed methods. The experimental results obtained indicate that the proposed scratch CNN architecture is highly successful in both current and vibration chemical data, achieving 98.70% and 99.40% accuracy, respectively. Furthermore, TL, a machine learning method used for comparison, has been evaluated across various architectures. Following the proposed CNN architecture, the highest success rates were achieved with VGG16 at 66.00% on vibration data and MobileNetV2 at 67.00% on current data. The results demonstrate that the proposed method outperforms transfer learning methods. This success can be attributed to the fact that transfer learning models train the network on different datasets and update the weight values accordingly. This discrepancy arises because the images in our dataset are unrelated to the datasets.

5. Conclusions

In this study, fault detection and classification of a permanent magnet synchronous reluctance motor using a confusion matrix, one of the machine learning methods, has been conducted. The synchronous reluctance motor, widely utilized in various industries, has seen increased popularity in electric vehicles and hybrid electric vehicles, particularly in recent years. Early-stage diagnostics for motor are crucial. By inducing a short circuit fault in the study, the motor's resistance value was decreased, resulting in two different stator short circuit faults with magnitudes of 0.68% and 0.81%. Initially, normal operation and faulty states' vibration and current motor data occurring in the stator were trained on the model. The motor signal data was transformed into vibration and current signals using the ICA technique. Subsequently, the datasets containing the current and vibration signals were tested on the proposed CNN model and TL. Each dataset comprised three classes: Normal, Defective Type-1 (0.68%), and Defective Type-2 (0.81%). A success rate of 99.40% was achieved on the vibration dataset, and 98.7% on the current dataset.

References

[1] Jung W, Yun SH, Lim YS, Cheong S, Park H. Vibration and current dataset of three-phase permanent magnet synchronous motors with stator faults. Data in Brief 2023; 47, 108952.
[2] Arafat AKM, Choi S. Optimal Phase Advance Under Fault-Tolerant Control of a Five-Phase Permanent Magnet Assisted Synchronous Reluctance Motor. IEEE Trans Ind Electron 2018; 65(4): 2915-2924.
[3] Soualhi A, Clerc G, Razik H, & Ondel O. Detection of induction motor faults by an improved artificial ant clustering. In: IECON 2011-37th Annual Conference of the IEEE Industrial Electronics Society; 10 November 2011; Melbourne, VIC, Australia: IEEE. pp. 3446-3451.
[4] Glowacz A, & Glowacz Z. Diagnosis of stator faults of the single-phase induction motor using acoustic signals. Appl Acoust 2017; 117: 20-27.
[5] Glowacz A. Diagnostics of rotor damages of three-phase induction motors using acoustic signals and SMOFS-20-EXPANDED. Arch Acoust 2016; 41(3): 507-515.
[6] Glowacz A, & Glowacz Z. Diagnostics of stator faults of the single-phase induction motor using thermal images, MoASoS and selected classifiers. Meas 2016; 93: 86-93.
[7] López TC, Riba JR., Garcia A, & Romeral L. Detection of eccentricity faults in five-phase ferrite-PM assisted synchronous reluctance machines. Appl Sci 2017; 7(6): 565.
[8] Pazouki E, Islam MZ, Bonthu SSR, & Choi S. Eccentricity fault detection in multiphase permanent magnet assisted synchronous reluctance motor. In: 2015 IEEE International Electric Machines & Drives Conference (IEMDC); 13 May 2015; United States: IEEE. pp. 240-246.
[9] Moradi CH, & Behroozi L. Analytical design, electromagnetic field analysis and parametric sensitivity analysis of an external rotor permanent magnet-assisted synchronous reluctance motor. Electr Eng 2020; 102(4): 1947-1957.
[10] Wang B, Wang J, Sen B, Griffo A, Sun Z, & Chong E. A fault-tolerant machine drive based on permanent magnet-assisted synchronous reluctance machine. IEEE Trans Ind Appl 2017; 54(2): 1349-1359.
[11] Zine W. HF signal injection and Machine Learning for the sensorless control of IPMSM-based EV drives. Ph. D. thesis, 2017.
[12] Luo Y, Qiu J, & Shi C. Fault detection of permanent magnet synchronous motor based on deep learning method. In: 2018 21st International Conference on Electrical Machines and Systems (ICEMS); 10 October 2018; Jeju, Korea (South): IEEE. pp. 699-703.
[13] Kao IH, Wang WJ, Lai Y. H, & Perng JW. Analysis of permanent magnet synchronous motor fault diagnosis based on learning. IEEE Trans Instrum Meas 2018; 68(2): 310-324.
[14] Chen Y, Liang S, Li W, Liang H, & Wang C. Faults and diagnosis methods of permanent magnet synchronous motors: A review. Appl Sci 2019; 9(10): 2116.

[15] Ebrahimi BM, Faiz J, & Roshtkhari MJ. Static-, dynamic-, and mixed-eccentricity fault diagnoses in permanent-magnet synchronous motors. IEEE Trans Ind Electron 2009; 56(11): 4727-4739.
[16] Xu X, Qiao X, Zhang N, Feng J, & Wang X. Review of intelligent fault diagnosis for permanent magnet synchronous motors in electric vehicles. Adv Mech Eng 2020; 12(7): 1687814020944323.
[17] Jung W, Yun S. H, Lim YS, Cheong S, & Park YH. Vibration and current dataset of three-phase permanent magnet synchronous motors with stator faults. Data in Brief 2023; 47, 108952.
[18] Copeland BJ, & Proudfoot D. Artificial intelligence: History, foundations, and philosophical issues. Philosophy of psychology and cognitive science, North-Holland: press, 2007.
[19] Verma M. Artificial intelligence and its scope in different areas with special reference to the field of education. Int J Adv Educ Res 2018; 3(1): 5-10.
[20] Mukhamediev RI, Popova Y, Kuchin Y, Zaitseva E, Kalimoldayev A, Symagulov A, & Yelis M. Review of artificial intelligence and machine learning technologies: Classification, restrictions, opportunities and challenges. Mathematics 2022; 10(15), 2552.
[21] Izonin I, Tkachenko R, Peleshko D, Rak T, & Batyuk D. Learning-based image super-resolution using weight coefficients of synaptic connections. In; 2015 Xth International Scientific and Technical Conference Computer Sciences and Information Technologies (CSIT); 17 Sept. 2015; Lviv, Ukraine: IEEE. pp. 25-29.
[22] Shen D, Wu G, & Suk HI. Deep learning in medical image analysis. Annu Rev Biomed Eng 2017; 19: 221-248.
[23] Panetto H, Iung B, Ivanov D, Weichhart G, & Wang X. Challenges for the cyber-physical manufacturing enterprises of the future. Annu Rev Control 2019; 47: 200-213.
[24] Tuncer T, Ertam F, Dogan S, Aydemir E, & Pławiak P. Ensemble residual network-based gender and activity recognition method with signals. J Supercomput 2020; 76: 2119-2138.
[25] Barakhnin VB, Duisenbayeva AN, Kozhemyakina OY, Yergaliyev Y. & Muhamedyev RI. The automatic processing of the texts in natural language. Some bibliometric indicators of the current state of this research area. Journal of physics. Conference series 2018; 1117(1).
[26] Hirschberg J, & Manning CD. Advances in natural language processing. Science 2015; 349(6245): 261-266.
[27] Abdullahi M, Baashar Y, Alhussian H, Alwadain A, Aziz N, Capretz LF. & Abdulkadir S. J. Detecting cybersecurity attacks in Internet of things using artificial intelligence methods: A systematic literature review. Electronics 2022; 11(2), 198.
[28] Lennartsson A. & Blomberg M. Fault Detection in Permanent Magnet Synchronous Motors using Machine Learning. 2021.
[29] Bohm T. How precise has fault detection to be? Answers from an economical point of view. In; Proceedings of the 26th International Congress on Condition Monitoring and Diagnostics Engineering Management; 5 July 2018; Rustenburg, South Africa; pp. 460-466.

Turkish Journal of Science & Technology
19(2), 427-442, 2024

Research Paper
https://doi.org/10.55525/tjst.1466307

Seismic Assessment of Masonry Minarets under Different Earthquakes

Şule SEKİN ERONAT[1], Erkut SAYIN[2*], Alper ÖZMEN[3]
[1,2] İnşaat Mühendisliği, Mühendislik Fakültesi, Fırat Üniversitesi, Elazığ, Türkiye
[3] İnşaat Mühendisliği, Mühendislik Fakültesi, İnönü Üniversitesi, Malatya, Türkiye
[1]sulesekin23@gmail.com, [2*]esayin@firat.edu.tr, [3]alper.ozmen@inonu.edu.tr

(Geliş/Received: 07/04/2024; Kabul/Accepted: 13/09/2024)

Abstract: Minarets are tall and slender structures and form important elements of mosques. Most historical minarets are constructed with masonry (brick or stone units), while modern minarets typically use reinforced concrete. Recent earthquakes have shown that the majority of these structures are highly susceptible to seismic excitation leading to a range of structural damage, from minor cracking to complete collapse. In this paper, the seismic response of a representative masonry minaret was investigated using acceleration records of the 1999 Kocaeli, 2003 Bingöl and 2011 Van earthquakes. All acceleration records were scaled according to the location of the minaret. For this purpose, a representative masonry minaret that is thought to have been built in the city's central part of Elazığ, Turkey was chosen. After the seismic analysis, displacement and stress values obtained on the minaret were presented. It was seen that the displacements were increased along the height of the minaret. Also, the maximum and minimum stress values were obtained between the cylindrical body and transition segment of the minaret in accordance with the damage zones in the past earthquakes.

Key words: Masonry minaret, finite element modeling, seismic response.

Farklı Depremler Altında Yığma Minarelerin Sismik Değerlendirmesi

Öz: Minareler, camilerin önemli yapı elemanları olup ince ve uzun yapılardır. Tarihi minarelerin çoğu yığma malzeme (tuğla veya taş üniteler) ile inşa edilirken, modern minarelerde genellikle betonarme kullanır. Son depremler, bu yapıların çoğunluğunun, çatlaklardan tamamen göçmeye kadar çeşitli yapısal hasarlara yol açan sismik hareketlere karşı oldukça duyarlı olduğunu göstermiştir. Bu çalışmada, temsili bir yığma minarenin sismik davranışı, 1999 Kocaeli, 2003 Bingöl ve 2011 Van depremlerinin ivme kayıtları kullanılarak incelenmiştir. Kullanılan tüm ivme kayıtları minarenin konumuna göre ölçeklendirilmiştir. Bu amaçla Elazığ şehir merkezinde inşa edildiği düşünülen temsili bir yığma minare dikkate alınmıştır. Sismik analizin ardından minare üzerinde elde edilen deplasman ve gerilme değerleri elde edilmiştir. Minare yüksekliği boyunca yer değiştirmelerin arttığı görülmüştür. Ayrıca geçmiş depremlerdeki hasar bölgelerine benzer şekilde minarenin silindirik gövdesi ile geçiş bölümü arasında maksimum ve minimum gerilme değerleri elde edilmiştir.

Anahtar kelimeler: Yığma minare, sonlu elemanlar modeli, sismik tepki.

1. Giriş

Minarets may be described as high towers. They are the characteristic architectural feature of the mosques, which are principally used for the call to prayer (adhan). Nowadays, minarets are no longer used for this function because of the use of loudspeakers, but they are still constructed as one of the indispensable architectural components of mosques [1, 2]. They are tall and slender engineering structures that are constructed separately or contiguous to the mosque structures. The first known minaret was constructed in 710 CE in Tunisia [3]. In the early periods of minarets, these structures did not have a specific form and were constructed using bricks, stones, and wood [4]. Also, it is accepted that the Seljuks built the earliest minarets in Anatolia, Turkey [5]. There are many masonry minarets in the world that have been built from past to present. Although the architectural characteristics of the minarets may vary according to the time and region they are built, most historical masonry minarets are constructed using brick or stone units. Classical Ottoman minarets are generally stone blocks or brick masonry, while most of the contemporary ones are usually reinforced concrete (RC) [6]. However, masonry minaret construction is still common in rural regions. As it is known from the past, the most important external effects that damage minarets are earthquakes. Seismicity is significantly high in Turkey where the African, Arabian and Eurasian plates converge. The westward motion of the Anatolian plate is accommodated by the East and North Anatolian faults [7]. During the last two decades, several destructive earthquakes like 1992 Erzincan, 1999 Kocaeli and Düzce, 2003 Bingöl, 2010 Elazığ-Kovancılar, 2011 Van and 2020 Elazığ-Sivrice have occurred on the North and East Anatolian faults. Several studies have focussed on assessing the performance of structures during these earthquakes [8–16]. In Turkey, there are no guidelines and regulations for slender masonry structures (minarets,

* Corresponding author: esayin@firat.edu.tr. ORCID Number of authors: [1] 0000-0003-3121-424X, [2*] 0000-0003-0266-759X, [3] 0000-0003-1335-3780

towers etc.). Due to their height, slim geometry and characteristical architecture, masonry minarets are vulnerable to seismic loading evidenced by the fact that a large majority of minarets were damaged or collapsed during the past earthquakes. 23 October 2011 (Mw=7.2) and 9 November 2011 (Mw=5.6) Van earthquakes resulted in heavily damaged or collapsed 63 masonry and RC minarets [17]. Significant earthquakes struck Elazığ and its surroundings in the past due to the seismic activity in the region (Fig. 1).

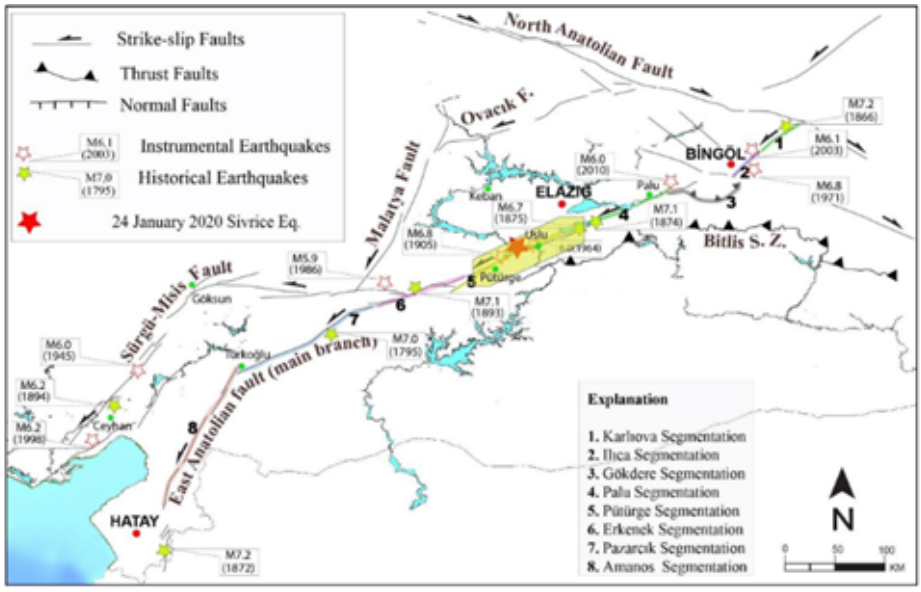

Figure 1. East Anatolian fault (historical and instrumental seismicity) [18].

Some studies have been carried out for seismic assessment of masonry and historical structures in the literature. However, the seismic behavior and performance of masonry minarets and towers are limited. Some of them can be listed as follows. Sezen et al. [19] investigated the damages and vulnerabilities of 64 reinforced concrete and masonry minarets after the 1999 Düzce and Kocaeli earthquakes. Erkek et al. [20] evaluated the seismic behavior of the historical Malatya Grand Mosque according to the Turkish Earthquake Code 2007. Oliveira et al. evaluated the seismic behavior of historical minarets which are constructed of natural block stone in Istanbul by using the finite element method and ambient vibration approach. Altunişik [21] evaluated the dynamic behavior of a masonry minaret before/after FRP (fiber-reinforced polymer) composite strengthening. For this purpose, the 1992 Erzincan earthquake was used to analyze and investigate the analytical model of the minaret. Coşgun et al. [22] studied the seismic behavior of a historical Dolmabahce mosque's minaret in Istanbul and presented a strengthening FRP procedure for the minaret. Pekgökgöz et al. [2] investigated the dynamic modulus of elasticity of the building stone of the Şanlıurfa historical Grand Mosque minaret. Measurements of the minaret were made by direct and semi-direct method. Hejazi et al. [23] assessed the structural analysis of a historical masonry minaret in Isfahan under temperature, wind, and earthquake loads. The analyses were studied for two different cases (the outer shell and the complete minaret) to investigate the effect of the central column and spiral staircase. Nohutcu et al. [24] investigated the damage and collapse mechanism in historical masonry minarets subjected to seismic loads. Hafsa Sultan minaret in the city of Manisa was selected as a numerical example Ercan et al. [25] analyzed a masonry minaret in Izmir, Turkey using linear and nonlinear time history analysis with two different acceleration records. Döven et al. [26] investigated the dynamic behavior of the Yeşil Mosque's minaret in Kütahya, Turkey in the case of closed and open balconies and compared them. For numerical analysis, ABAQUS finite element software was used. Hökelekli et al. [27] evaluated the seismic damage behaviors of stone masonry minarets with soil-structure interaction under different soil types. Türkeli [28] evaluated the historical Iskenderpaşa Mosque's masonry minaret under seismic and wind effects. For seismic effect, on 17 August 1999 Kocaeli and 12 November 1999 Düzce earthquakes were considered and top joint displacements and stress distributions were acquired. Yurdakul et al. [29] carried out a study to investigate the seismic performance of a historical minaret in Bayburt, Turkey. For this purpose, three acceleration records (1992 Erzincan, 1999 Kocaeli-Duzce, and 2011 Van-Ercis) were applied to evaluate the seismic behavior of the historical minaret.

Usta [4] studied the seismic assessment of historical masonry minarets which were placed in Antalya, Turkey. Time history analysis was performed to evaluate the earthquake performance of the minarets. Günaydın et al. [30]

presented a structural performance assessment of a historical masonry clock tower. For this purpose, a nonlinear time-history analysis was carried out and the seismic performance of the tower was evaluated. Scamardo et al. [31] evaluated the seismic behavior of a historical masonry tower located in Northern Italy. It is important to evaluate the seismic behavior of the minarets because there are no guidelines or code requirements for the design of masonry minarets in Turkey.

The aim of this study is to investigate the dynamic response of a representative masonry minaret which is thought to have been built in the city centre of Elazığ. For this purpose, three dimensional (3D) masonry minaret with typical geometry and material is modeled to study its dynamic response using ANSYS finite element software. To simulate seismic excitation, 1999 Kocaeli, 2003 Bingöl and 2011 Van earthquake acceleration records which were scaled according to the location of the minaret were considered. By performing the seismic analysis, stress values and displacement obtained on the minaret were presented.

2. Descriptions of the Representative Minaret

Minarets are interesting structures due to their vulnerability to horizontal loads and their typological characteristics. They are the main part of the mosques and are mostly constructed near or attached to the mosques. Due to their slender geometry, masonry minarets are accepted as the most vulnerable structures to earthquakes. It is believed that the square tower was abandoned for the octagonal or cylindrical minaret during the Ottoman period [5]. In the Ottoman period, slender cylindrical and polygonal shafts with conical caps constituted the specific form of Turkish minarets [32]. Although its style (shape, height and physical geometry) varies according to the region and the period it is built, the basic form of the minaret consists of a base, shaft, and gallery. In Turkish mosque architecture, minarets are frequently placed on two sides of the mosques symmetrically. Every mosque has a minimum of one minaret. The number of minarets may vary depending on the significance of the mosque. Historical masonry minarets were generally constructed using stone or brick units. In Turkey, the stone units were largely used to construct historical masonry minarets. A minaret may either have an independent foundation or the base of the minaret may be attached to the roof of the mosque [33]. Depending on the number of balconies, masonry minaret height varies generally between 25 m and 70 m [34]. There may be one or more balconies at the minaret. If the minarets have balconies or balconies, these balconies cause concentrated mass along the minaret's height and they affect the seismic structural response of the minaret. A typical minaret generally consists of eight parts or components (Fig. 2).

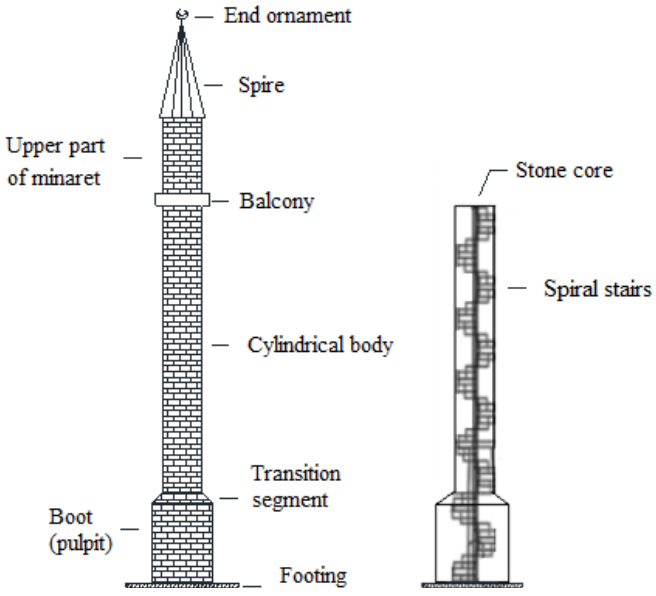

Figure 2. Typical masonry minaret.

These components are the footing (base), boot, transition segment, cylindrical or polygonal body, balcony, upper part of the minaret, spire and end ornament. Also, there is a stone core surrounded by a stone spiral stairway from the base up to the balcony level within the shaft. Stone core and stairs offer the required structural support to the shaft. The spiral stone stairways as well as the stone core end at the balcony level. The cross-section and

geometrical properties of the masonry minaret are given in Figure 3. In the middle of the minaret, there is a 0.3 m diameter stone block within the shaft. The stone block is surrounded by spiral stone stairways with 0.25 m step height from the base up to the balcony.

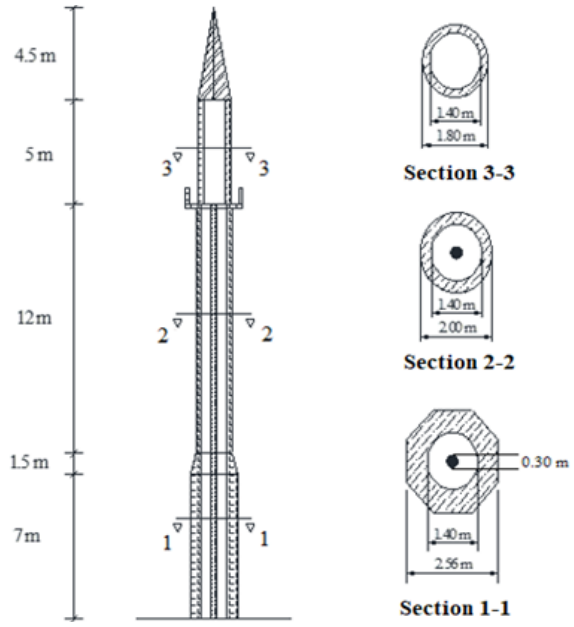

Figure 3. Cross-section and geometrical properties of the representative masonry minaret.

3. Finite Element Modeling of the Minaret

Modeling strategies of masonry structures, depending on the level of accuracy and the simplicity desired, had been divided into three groups (Figure 4). These approaches are detailed micro modeling, simplified micro modeling and macro modeling. Micro and macro models have different application fields therefore one modelling strategy cannot be preferred over the other [35, 38].

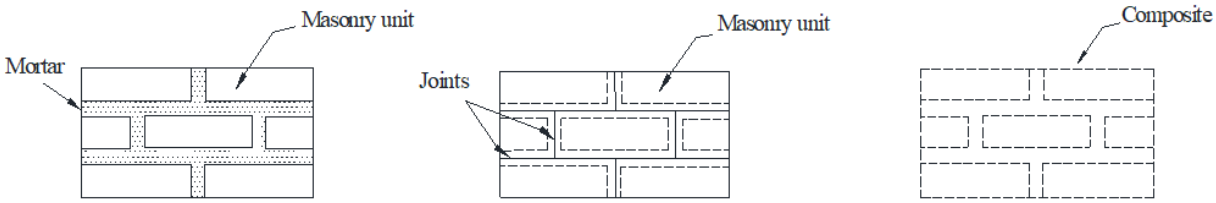

Figure 4. Modeling strategies for masonry structures [35,38].

Macro modeling is the most computationally efficient and modeling strategy, although accuracy may be sacrificed relative to micro- and simplified micro-modeling. However, given the high variability in the behavior of historical masonry constituents (stone/brick and mortar), the accuracy of micro-modeling can indeed suffer from the compounding effect of uncertainty propagation. In such cases, taking the macro-modeling approach using averaged properties can be beneficial. Moreover, given its low computational effort and sufficient validation of observational data, macro-modelling strategy is generally preferred in past studies [36–40] In this study, a representative masonry minaret with height of 30 m was developed using the macro-modelling approach in ANSYS. 3D solid finite elements (SOLID186) were considered for numerical modelling of the minaret. The element has twenty nodes and three degrees of freedom at each node, translations in the nodal x, y, and z directions. Figure 5 shows the geometry of the SOLID186 element.

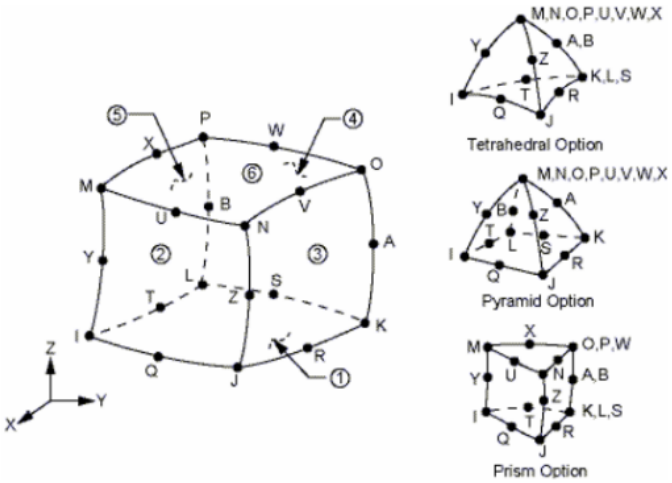

Figure 5. The geometry of the SOLID186 element [41].

The 3D finite element mesh model of the minaret and stone core with spiral stairs is given in Figure 6. The model consists of 14058 nodal points and 9673 elements. In this figure, one nodal point is selected at the top of the minaret for time history displacement graphs. It was assumed that the minaret is located on the rock soil and all degrees of freedom at the base of the minaret were selected as fixed. Linear elastic material behavior was assumed for the minaret model. Material properties used for the finite element model of the minaret were taken from the literature [34, 42]. Poisson's ratio, elasticity modulus, and unit weight of the masonry material used in the representative minaret were taken as 0.20, 10000 MPa and 2.2 t/m^3, respectively. Also, the compressive and tensile strength of the masonry material was taken as 16.9 and 0.9 MPa, respectively.

These values belong to the limestone masonry which is frequently used in the construction of the masonry minarets in Turkey and determined experimentally [43].

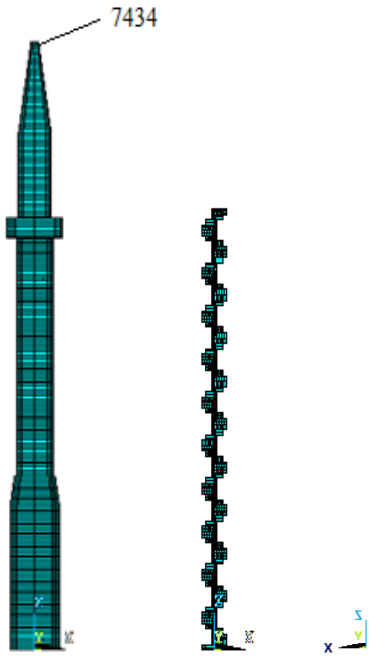

Figure 6. 3D finite element mesh model of the representative masonry minaret with stone block and spiral stairs.

4. Dynamic Analysis of the Masonry Minaret

4.1. Modal analysis

Minarets are generally slender and tall structures with low bending strength and they make large displacements under lateral loads such as earthquakes and wind. Past seismic events have shown that these tall structures are particularly vulnerable to earthquakes. They can easily collapse in the case of dynamic resonance. To define the dynamic characteristics of the masonry minaret before seismic analyses, modal analysis was performed. Mass participation ratios, mode shapes and free vibration periods of the investigated structure were obtained in the modal analysis. The damping ratio was taken into account as 5% for the Rayleigh damping coefficients in the analysis [4, 34, 44-45]. Dynamic characteristics of the minaret were calculated for the first 30 modes. The sum of the calculated effective mass participation ratios was found to be more than 90% of the total mass of the minaret for 30 modes. The first two modes of the minaret have similar frequencies because of the nearly circular symmetric shape of the minaret. The first six mode shapes and frequencies of the minaret are presented in Fig. 7.

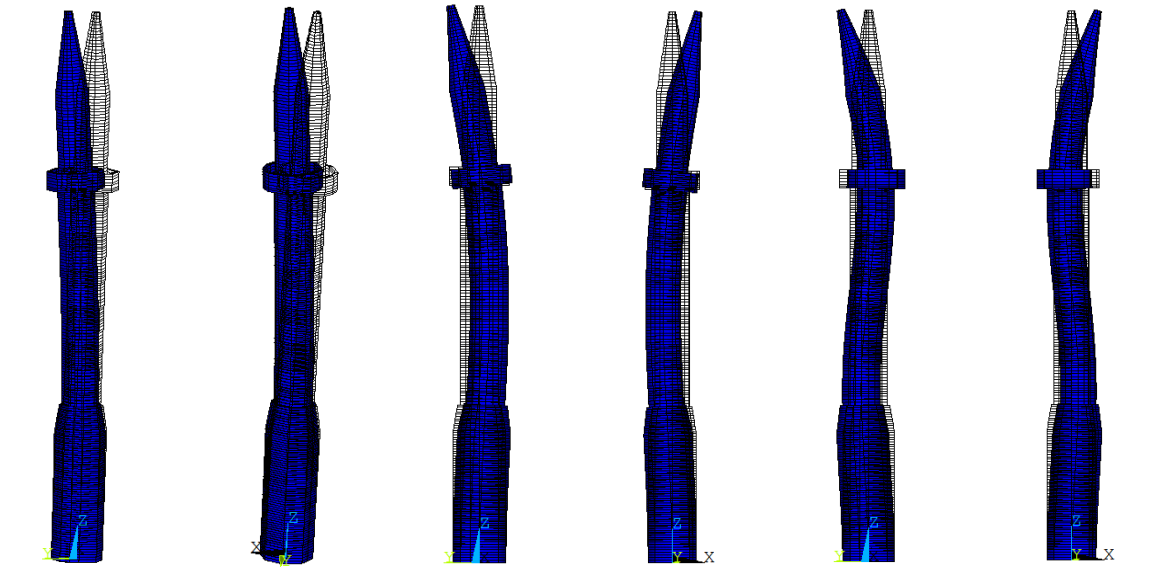

Figure 7. First six modes of the minaret.

4.2. Seismic analysis

In this study, three different strong ground motions (1999 Kocaeli, 2003 Bingöl and 2011 Van earthquakes' acceleration records) were considered to evaluate the dynamic analyses of the masonry minaret. According to the location of the minaret, these acceleration records were scaled and applied to the masonry minaret in two horizontal (x and y) directions. The earthquake records were scaled using Seismomatch software [46]. The earthquake level of the seismic ground motion was chosen as DD-2 which represents a 10% probability of exceedance in 50 years (475 years return period) [47]. East-west (E-W) and north-south (N-S) components of these records were given in Figs. 8-10. HHT-α direct integration approach was considered for the time history analysis. Acceleration records of 1999 Kocaeli, 2003 Bingöl and 2011 Van earthquakes are 52 s, 64.5 s and 83.5 s for durations, respectively. In the dynamic analysis, these records time of all earthquakes were used without shortening.

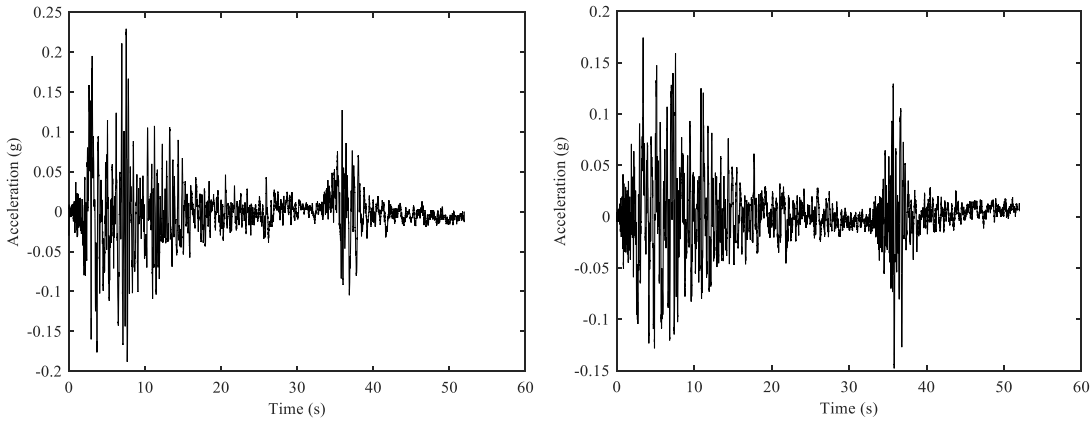

a) (E-W) component b) (N-S) component

Figure 8. Acceleration records of 1999 Kocaeli earthquake

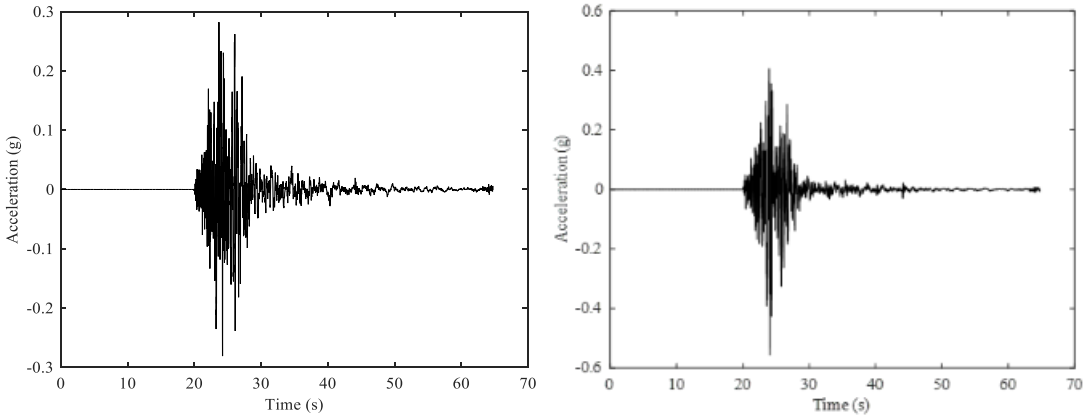

a) (E-W) component b) (N-S) component

Figure 9. Acceleration records of 2003 Bingöl earthquake

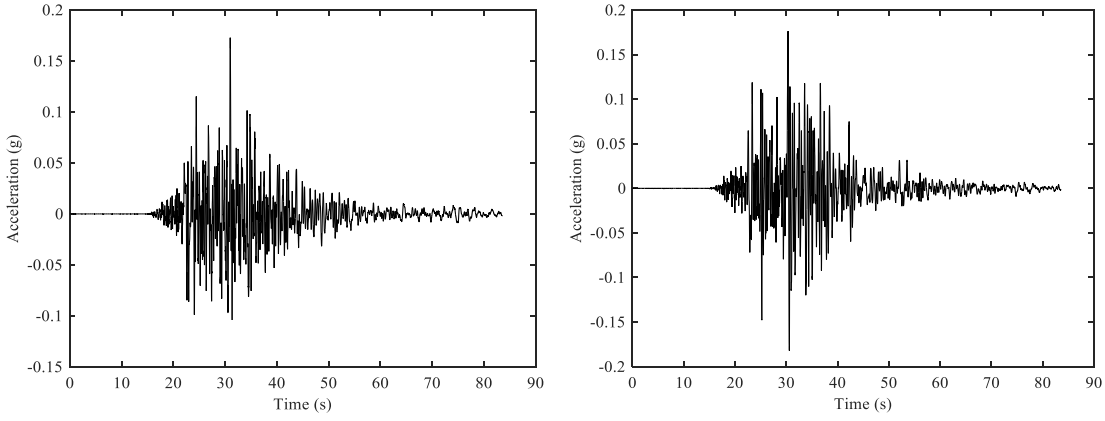

a) (E-W) component b) (N-S) component

Figure 10. Acceleration records of 2011 Van earthquake.

After the dynamic analyses, the horizontal displacements of the top of the minaret (nodal point 7434) in x and y directions were obtained for 1999 Kocaeli, 2003 Bingöl and 2011 Van earthquakes. The time histories of the displacement in x and y direction subjected to the Kocaeli, Bingöl and Van earthquakes were given in Figs.

11-13. For 1999 Kocaeli, 2003 Bingöl and 2011 Van earthquakes, absolute displacement values of the nodal point 7434 in x and y directions are 7.48 cm and 7.57 cm, 7.31 cm and 9.90 cm, 7.60 cm and 7.89 cm, respectively. When the time history graphs of displacement were examined for selected earthquake records, the maximum absolute displacement values of the minaret in the x and y directions were obtained from the 2011 Van and 2003 Bingöl earthquake acceleration records, respectively.

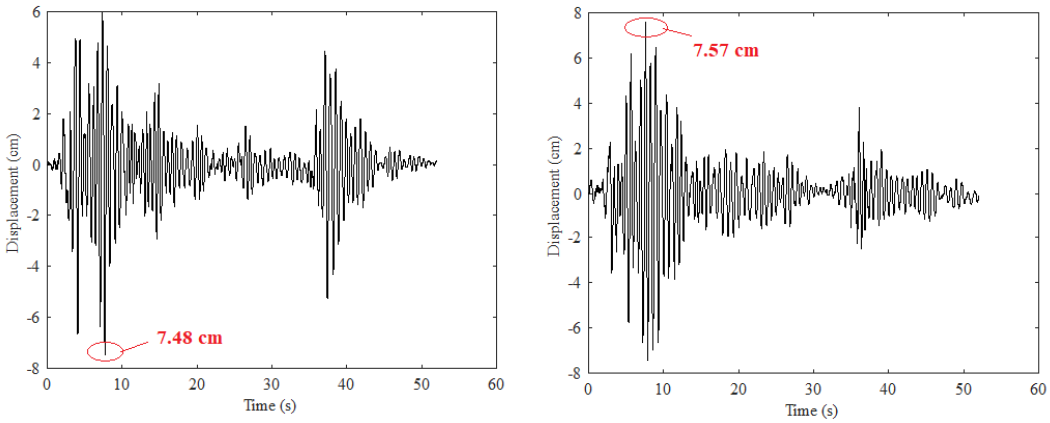

a) x direction b) y direction

Figure 11. Horizontal displacement time history graphs at the top of the minaret subjected to 1999 Kocaeli earthquake.

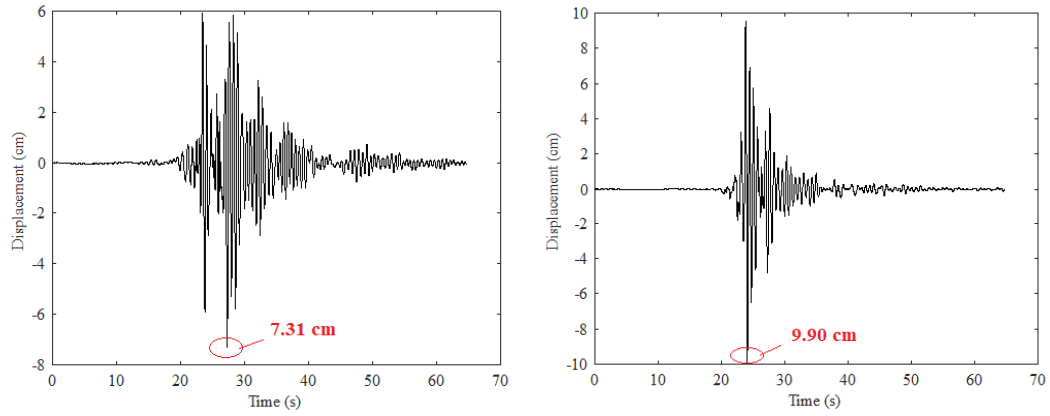

a) x direction b) y direction

Figure 12. Horizontal displacement time history graphs at the top of the minaret subjected to 2003 Bingöl earthquake.

Also, six nodal points were selected on the masonry minaret and the absolute maximum horizontal displacement of these selected points was obtained after the dynamic analyses for selected earthquakes. Tables 1-3 show the maximum horizontal displacement (in x and y directions) values of the selected nodal points over the masonry minaret. The displacements are quite small up to the relatively more rigid boot level. When the horizontal displacements were examined over the height of the minaret, the displacements started to increase above the transition segment (8 m high) for all investigated earthquakes. However, there are two inflection points (slope of the graph changes) at the transition segment and balcony level in Fig. 14. The absolute maximum horizontal displacement distribution over the height of the minaret model for investigated earthquakes is given in x and y directions in Fig. 14.

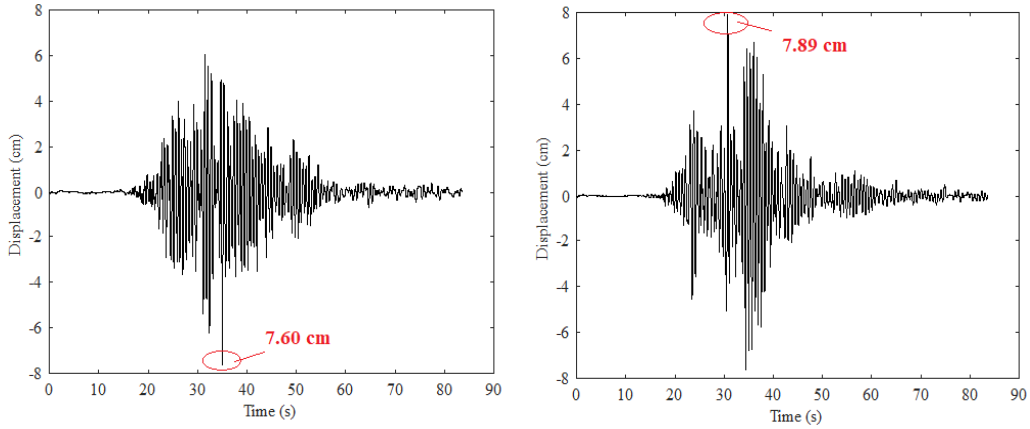

a) x direction b) y direction

Figure 13. Horizontal displacement time history graphs at the top of the minaret subjected to 2011 Van earthquake.

Table 1. Displacements for selected nodal points in x and y directions for 1999 Kocaeli earthquake.

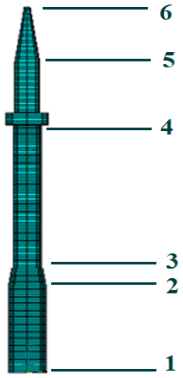

Location	Height (m)	Displacement (cm) x direction	Displacement (cm) y direction
1	0	0	0
2	7	0.31	0.38
3	8.5	0.45	0.52
4	20.5	3.39	3.41
5	25.5	5.66	5.71
6	30	7.48	7.57

Table 2. Displacements for selected nodal points in x and y directions for 2003 Bingöl earthquake.

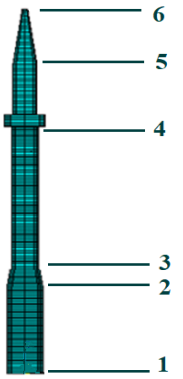

Location	Height (m)	Displacement (cm) x direction	Displacement (cm) y direction
1	0	0	0
2	7	0.38	0.46
3	8.5	0.53	0.64
4	20.5	3.24	4.33
5	25.5	5.49	7.27
6	30	7.31	9.90

Table 3. Displacements for selected nodal points in x and y directions for 2011 Van earthquake.

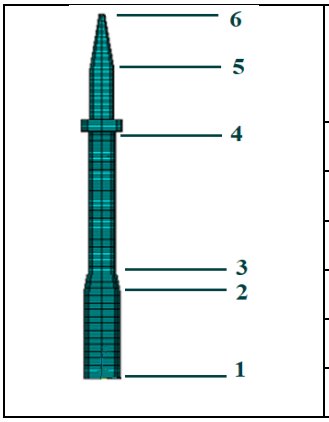

Location	Height (m)	Displacement (cm) x direction	Displacement (cm) y direction
1	0	0	0
2	7	0.34	0.37
3	8.5	0.49	0.52
4	20.5	3.43	3.40
5	25.5	5.73	5.79
6	30	7.60	7.89

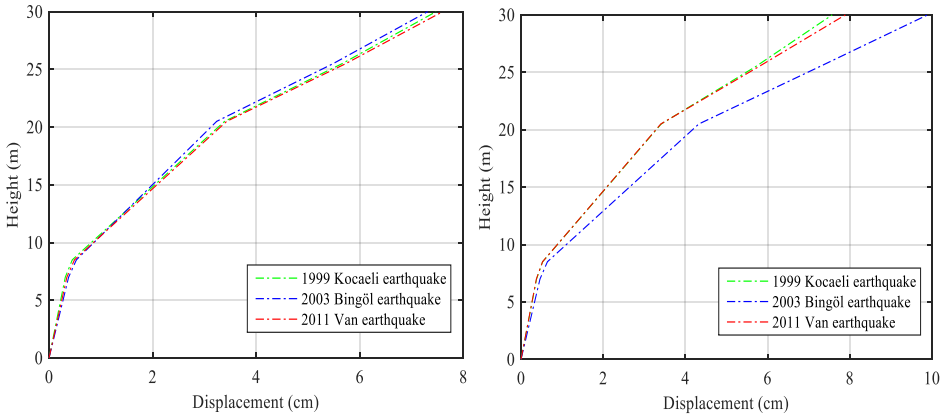

a) x direction b) y direction

Figure 14. Absolute maximum horizontal displacement distribution along the height of the minaret.

The time history graphs of the maximum and minimum principal stresses of the minaret subjected to 1999 Kocaeli, 2003 Bingöl and 2011 Van earthquakes are given in Figs. 15-17. The absolute maximum values of the maximum and minimum principal stresses for 1999 Kocaeli, 2003 Bingöl and 2011 Van earthquakes were obtained at 6.62 MPa and 6.75 MPa, 8.16 MPa and 8.30 MPa, 7.59 MPa and 7.95 MPa, respectively. Maximum and minimum stress values have occurred for 2003 Bingöl earthquake. The obtained minimum stress on the masonry minaret is below the compressive strength of the masonry material, but the maximum stress is above the tensile strength of the masonry material. For this reason, possible cracks and damages can occur in the regions where the tensile strength exceeds.

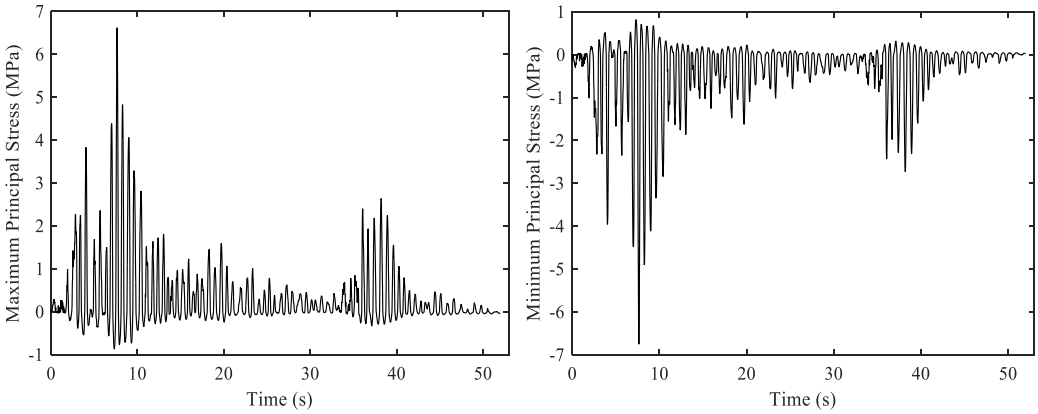

a) Maximum principal stress b) Minimum principal stress

Figure 15. Time history of the maximum and minimum principal stresses for 1999 Kocaeli earthquake.

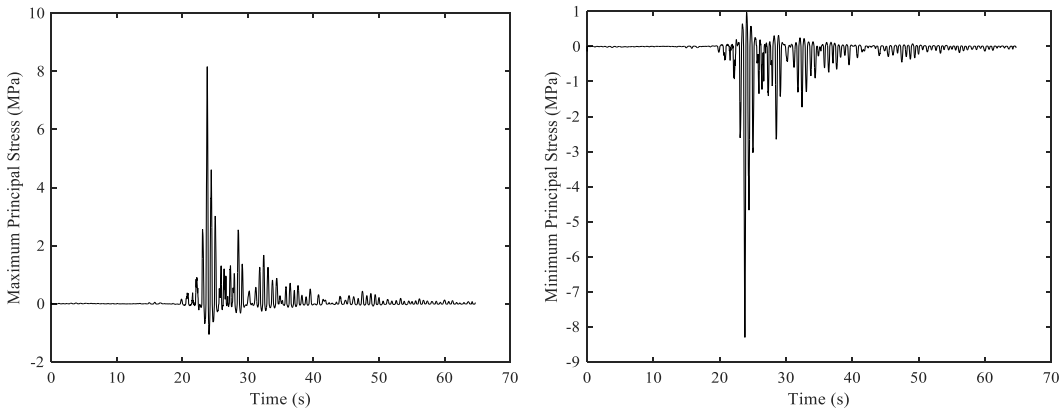

a) Maximum principal stress b) Minimum principal stress

Figure 16. Time history of the maximum and minimum principal stresses for 2003 Bingöl earthquake.

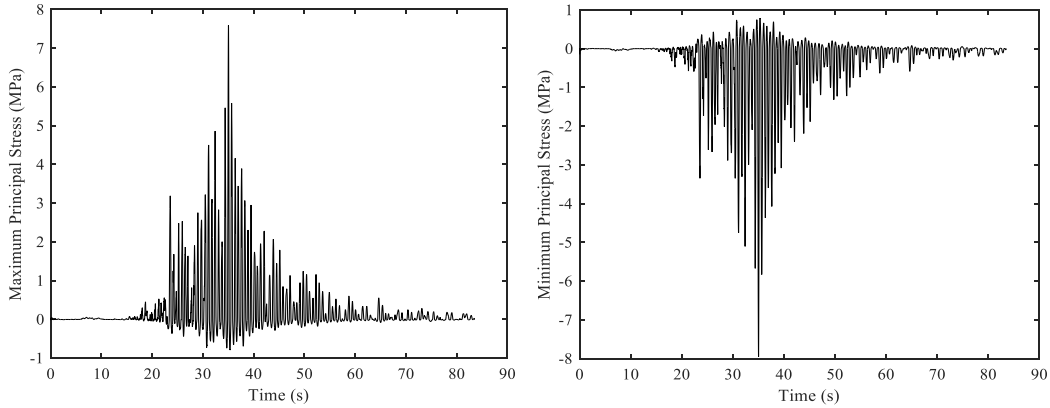

a) Maximum principal stress b) Minimum principal stress

Figure 17. Time history of the maximum and minimum principal stresses for 2011 Van earthquake.

The maximum and minimum principal stress contours of the minaret for 1999 Kocaeli, 2003 Bingöl, 2011 Van earthquakes are given in Figs. 18-20, respectively. The distribution of the stress over the minaret was described by these stress contours. After the dynamic analyses, it was seen that the maximum and minimum principal stresses occurred in the region between the cylindrical body and transition segment. Obtained potential damage zones from the analysis are compatible with the minaret failures observed during the past earthquakes. When the post-earthquake evaluations and analysis results of masonry minarets are investigated, it is seen that most of these structures failed at the bottom part of the cylindrical body, just above the transition segment [4, 21, 22]. The most vulnerable section of the minaret is above the transition segment.

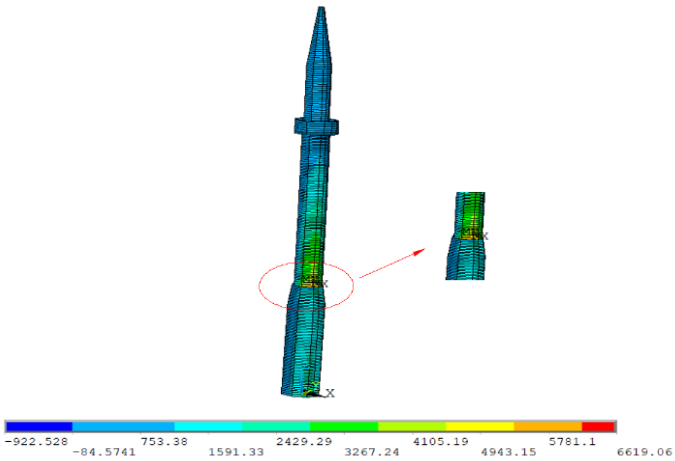

a) Maximum principal stress contours

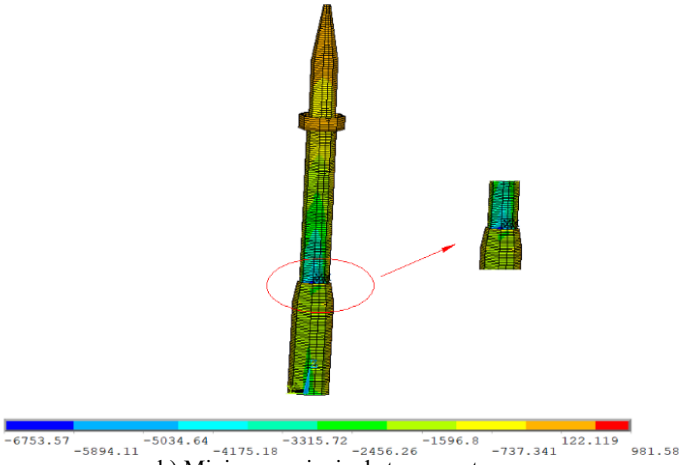

b) Minimum principal stress contours

Figure 18. Maximum and minimum principal stress contours of the minaret for 1999 Kocaeli earthquake (in kPA).

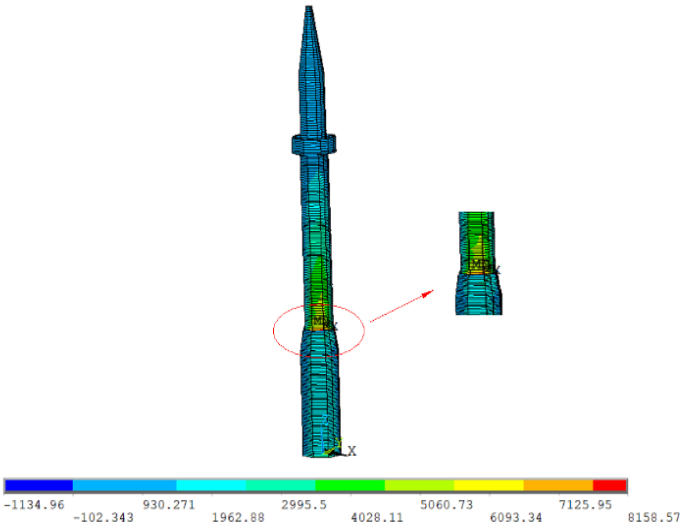

a) Maximum principal stress contours

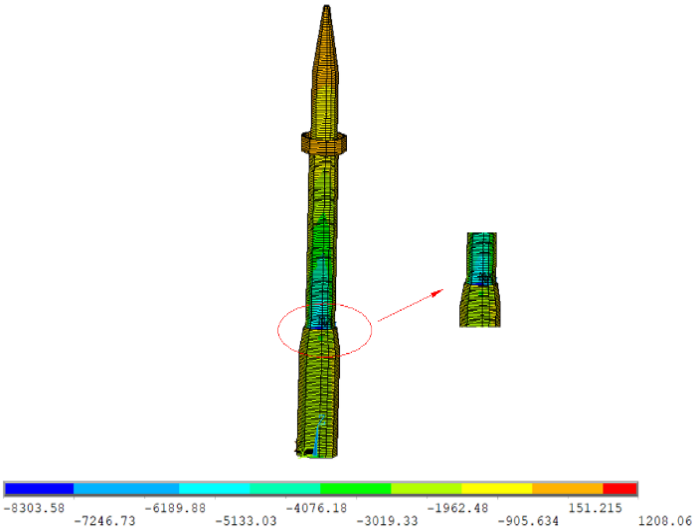

b) Minimum principal stress contours

Figure 19. Maximum and minimum principal stress contours of the minaret for 2003 Bingöl earthquake (in kPA).

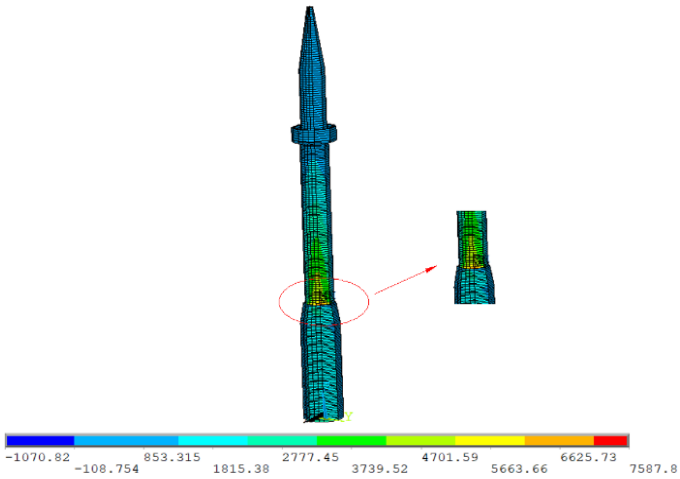

a) Maximum principal stress contours

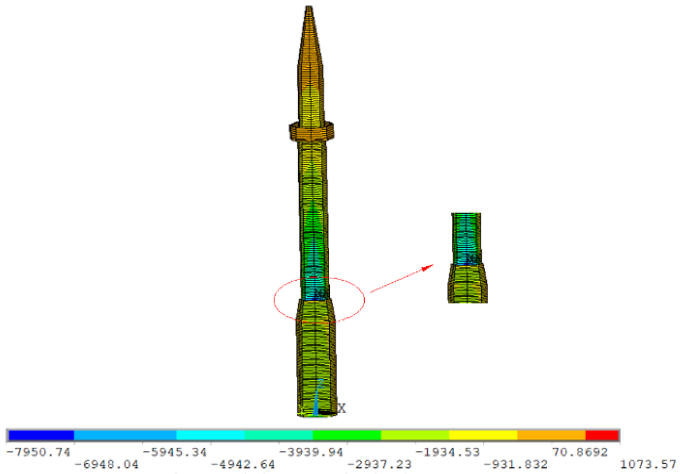

b) Minimum principal stress contours

Figure 20. Maximum and minimum principal stress contours of the minaret for 2011 Van earthquake (in kPA).

5. Conclusions

Minarets have specific role in mosque architecture despite the loss of main function. In this paper, the dynamic response of the masonry minaret presents. For this purpose, a representative masonry minaret located in Elazığ, Turkey with a height of 30 m was considered as a case study. Firstly, the structural model was constructed using solid elements with ANSYS software, and then dynamic analysis was performed using the same software. For dynamic analysis, 1999 Kocaeli, 2003 Bingöl and 2011 Van earthquakes were considered and applied to the minaret two horizontal directions. In the dynamic analyses, it can be seen that the acquired displacements increase with the height of the minaret. Also, the absolute maximum displacement occurred at the top of the minaret in x and y directions for 2011 Van and 2003 Bingöl earthquakes, respectively. Maximum and minimum principal stresses obtained from the dynamic analyses concentrated in the region between the cylindrical body and the transition segment. Therefore, it can be said that the most vulnerable part of the minaret is right above the transition segment. Also, maximum and minimum stresses values were occurred for 2003 Bingöl earthquake. For all earthquakes used in the analysis, the minimum stress on the masonry minaret is below the compressive strength of the masonry material, but the maximum stress is above the tensile strength of the masonry material. For this reason, it is likely that possible cracks and damages due to earthquakes may occur in the region between the cylindrical body and the transition segment. Finally, the obtained results in this paper comprise one representative masonry minaret but the main findings may be generally applied to other masonry minarets. In future studies,

proper and applicable retrofit methods can be investigated to increase minarets earthquake resistant by using the nonlinear material models for dynamic analyses.

References

[1] Urey O. Transformation of minarets in contemporary Mosque architecture in Turkey. Int J of Sport Cult and Sci 2013; 1(4), 95–107.
[2] Pekgökgöz RK, Gürel MA, Mammadov Z, Çili F. Dynamic analysis of vertically post-tensioned masonry minarets. J Earthq Eng 2013; 17(4), 560–589.
[3] Bayraktar A, Sevim B, Altunişik AC, Türker T. Earthquake analysis of reinorced concrete minarets using ambient vibration test results. Struct Des Tall Special Build 2010; 19(3), 257–273.
[4] Usta P. Assessment of seismic behaviour of historic masonry minarets in Antalya, Turkey. Case Stud Constr Mater 2021; 15, e00665.
[5] Creswell KAC. The evolution of the minaret, with special reference to Egypt-I. The Burlington Magazine for Connoisseurs 1926; 134–140.
[6] Saygili Ö. Investigation of The effect of slenderness ratio on the structural response of masonry minarets. Niğde Ömer Halisdemir Üniversitesi Mühendislik Bilimleri Dergisi 2020; 9(1), 366–376.
[7] McKenzie, D. Active tectonics of the Mediterranean region. Geophysical J Int 1972; 30(2), 109–185.
[8] Doğangün A. Performance of reinforced concrete buildings during the May 1, 2003 Bingöl Earthquake in Turkey. Eng Struct 2004; 26(6), 841–856.
[9] Calayır Y, Sayın E, Yön B. Performance of structures in the rural area during the March 8, 2010 Elazığ-Kovancılar earthquake. Natural Hazards 2012; 61(2), 703–717.
[10] Sayın E, Yön B, Calayır Y, Karaton M. Failures of masonry and adobe buildings during the June 23, 2011 Maden-(Elazığ) earthquake in Turkey. Eng Fail Anal 2013; 34, 779–791.
[11] Sayın E, Karaton M, Calayır Y. Nonlinear seismic analyses of historical Topuzlu Dam under different seismic loads. Građevinar 2016; 68(11.), 919–925.
[12] Valente M, Milani G. Seismic response and damage patterns of masonry churches: seven case studies in Ferrara, Italy. Eng Struct 2018; 177, 809–835.
[13] Karalar M, Yesil M. Effect of near-fault earthquakes on a historical masonry arch bridge (Konjic Bridge). Earthq Struct 2021; 21(2), 125–136.
[14] Sayın E, Yön B, Onat O, Gör M, Öncü ME, Tuğrul Tunç, E, … Calayır, Y. 24 January 2020 Sivrice-Elazığ, Turkey earthquake: geotechnical evaluation and performance of structures. Bull Earthq Eng 2021; 19(2), 657–684.
[15] Calayır Y, Yetkin M, Erkek H. Finite element model updating of masonry minarets by using operational modal analysis method. Structures 2021; 34, 3501–3507.
[16] Arslan MH, Korkmaz HH. What is to be learned from damage and failure of reinforced concrete structures during recent earthquakes in Turkey? Eng Fail Anal 2007; 14(1), 1–22.
[17] Muvafik M. Field investigation and seismic analysis of a historical brick masonry minaret damaged during the Van Earthquakes in 2011. Earthq Struct 2014; 6(5).
[18] Köküm M. 24 Ocak 2020 Sivrice depreminin (Doğu Anadolu Fayı) tetiklediği heyelan ve yanal yayılmalar. Gümüshane Üniversitesi Fen Bilimleri Enstitüsü Dergisi 2021; 11(3).
[19] Sezen H, Acar R, Dogangun A, Livaoglu R. Dynamic analysis and seismic performance of reinforced concrete minarets. Eng Struct 2008; 30(8), 2253–2264.
[20] Erkek H, Calayır Y, Sayın E. Karaton M. Seismic behaviour of historic Malatya Grand Mosque. 2. Turkey Earthq, Eng. Seismol. Conf. Earthq. Eng. Assoc. Turkey, 2013; 25–27.
[21] Altunişik AC. Dynamic response of masonry minarets strengthened with Fiber Reinforced Polymer (FRP) composites. Nat Hazards Earth Syst Sci 2011; 11(7), 2011–2019.
[22] Cosgun C, Turk, AM. Seismic behaviour and retrofit of historic masonry minaret. Građevinar 2012; 64(1), 39-45.
[23] Hejazi M, Moayedian SM, Daei M. Structural analysis of Persian historical brick masonry minarets. J Perform Constr Facil 2016; 30(2), 04015009.
[24] Nohutcu H, Hokelekli E, Ercan E, Demir A, Altintas G. Collapse mechanism estimation of a historical slender minaret. Struct Eng and Mech 2017; 64(5), 653–660.
[25] Ercan E, Arisoy B, Hökelekli E, Nuhoğlu A. Estimation of seismic damage propagation in a historical masonry minaret. Sigma J Eng Natural Sci 2017; 35(4), 647–666.
[26] Döven M, Serhatoğlu C, Kaplan O, Livaoğlu R. Dynamic behaviour change of Kütahya Yeşil Minaret with covered and open balcony architecture. Eskişehir Technical University J of Sci and Technology B-Theoretical Sciences 2018; 6.
[27] Hökelekli E, Al-Helwani, A. Effect of soil properties on the seismic damage assessment of historical masonry minaret–soil interaction systems. Struct Des Tall Special Build 2020; 29(2), e1694.
[28] Türkeli E. Dynamic seismic and wind response of masonry minarets. Period Polytech Civil Eng 2020; 64(2), 353–369.
[29] Yurdakul M, Yılmaz F, Artar M, Can Ö, Öner E, Daloğlu AT. Investigation of time-history response of a historical masonry minaret under seismic loads. In Structures 2021; 30, 265–276.
[30] Günaydin M, Ertürk E, Genç A, Okur F, Altunişik A, Tavşan C. Fe Model updating and seismic performance evaluation of a historical masonry clock tower. Earthq Struct 2022; 22(1).
[31] Scamardo M, Zucca M, Crespi P, Longarini N, Cattaneo S. Seismic vulnerability evaluation of a historical masonry tower: Comparison between different approaches. Applied Sciences 2022; 12(21), 11254.

[32] Doğangün A, Tuluk Öİ, Livaoğlu R, Acar R. (2006). Traditional Turkish minarets on the basis of architectural and engineering concepts. In Proceedings of the 1st International Conference on Restoration of Heritage Masonry Structures 2006; April, 24, p. 27.
[33] Dogangun A, Acar R, Sezen H, Livaoglu R. Investigation of dynamic response of masonry minaret structures. Bull Earthq Eng 2008; 6, 505–517.
[34] Turk AM. Seismic response analysis of masonry minaret and possible strengthening by fiber reinforced cementitious matrix (FRCM) materials. Adv Mater Sci Eng 2013; https://doi.org/10.1155/2013/952497.
[35] Lourenco P. Computational Strategy for Masonry Structures (Ph.D. Thesis,). Delft Technical University of Technology, The Netherlands, 1996.
[36] Carpinteri A, Invernizzi S, Lacidogna G. In situ damage assessment and nonlinear modelling of a historical masonry tower. Eng Struct 2005; 27(3), 387–395.
[37] Zampieri P, Zanini MA, Modena C. Simplified seismic assessment of multi-span masonry arch bridges. Bull Earthq Eng 2015; 13(9), 2629–2646.
[38] Sayin E. Nonlinear seismic response of a masonry arch bridge. Earthq Struct 2016; 10(2), 483–494.
[39] Kocaturk T, Erdogan YS. Earthquake behaviour of M1 minaret of historical sultan Ahmed Mosque (blue mosque). Struct Eng Mech, An Int'l J 2016; 59(3), 539–558.
[40] Bernardeschi K, Padovani C, Pasquinelli G. Numerical modelling of the structural behaviour of Buti's bell tower. J Cult Herit 2004; 5(4), 371–378.
[41] ANSYS. Finite Element Software. Houston, TX, USA: Swanson Analysis System. Inc., 2015.
[42] Doğangün A, Ural A, Livaoğlu R. Seismic performance of masonry buildings during recent earthquakes in Turkey. In The 14th World Conference on Earthquake Engineering October (pp. 12-17), 2008.
[43] Oguzmert M. Dynamic behaviour of masonry minarets (M.Sc.Thesis). Istanbul Technical University, İstanbul, 2002.
[44] Özmen A, Sayın E. Seismic assessment of a historical masonry arch bridge. J Struct Eng Appl Mech 2018; 1(2), 95–104.
[45] Özmen A, Sayin E. Different soil-structure interaction modelling strategies for seismic analysis of a masonry church. Int J Architect Herit, 2024; 1–22.
[46] Seismosoft Ltd. "Seismomatch (2018)" [online] Available at: https://seismosoft.com/product/seismomatch/
[47] TBEC. Turkish Building Earthquake Code 2018, Disaster and Emergency Management Agency (AFAD), 2018.

Turkish Journal of Science & Technology
19(2), 443-450, 2024

Research Paper
https://doi.org/10.55525/tjst.1511432

A New Cryptographic Key Planning Algorithm Based on Blum Blum Shub

Songül KARAKUŞ[1*], Fırat ARTUĞER[2]
[1] Computer Engineering Department, Engineering-Architecture Faculty, Bitlis Eren University, Bitlis, Turkey
[2] Computer Engineering Department, Engineering Faculty, Munzur University, Tunceli, Turkey
[*1] skarakus@beu.edu.tr, [2] firatartuger@munzur.edu.tr

(Geliş/Received: 06/07/2024; Kabul/Accepted: 28/09/2024)

Abstract: The Blum Blum Shub (BBS) algorithm is one of the known powerful pseudo random number generators. This algorithm can be used for key generation. BBS is basically based on the product of two large prime numbers and a seed value. The selection of these values is a critical issue. In this study, a new approach is proposed to overcome this problem. In the proposed approach, a prime number pool is first created. At this point, the user sets a start and end value. The primes in this range are generated and stored in an array. Then, two primes are randomly selected from this prime number pool with chaotic maps. The positions of these prime numbers in the array are recorded. The seed value is taken as the sum of the positions of these two primes. In other words, the parameters to be selected will be randomly selected in the ranges that the user will enter at that moment. In this study, two random bit sequences were obtained in this way. These sequences are 1 million bits long. NIST SP 800-22 tests were applied to these sequences and the sequences successfully completed all tests.

Key words: Blum blum shub, key generator, RNG, NIST SP 800-22 test, chaotic map.

Blum Blum Shub Tabanlı Yeni Bir Kriptografik Anahtar Planlama Algoritması

Öz: Blum Blum Shub (BBS) algoritması bilinen güçlü sözde rastgele sayı üreteçlerinden bir tanesidir. Bu algoritma anahtar üretiminde kullanılabilir. BBS temelde iki büyük asal sayının çarpımına ve bir tohum değerine dayanmaktadır. Bu değerlerin seçilmesi oldukça kritik bir konudur. Bu çalışmada bu problemin üstesinden gelmek için yeni bir yaklaşım önerilmiştir. Önerilen yaklaşımda öncelikle asal sayı havuzu oluşturulmaktadır. Bu noktada kullanıcı bir başlangıç ve bitiş değeri belirlemektedir. Belirlenen bu aralıktaki asal sayılar üretilerek bir diziye kaydedilir. Daha sonra bu asal sayı havuzundan kaotik haritalar ile rastgele iki asal sayı seçilir. Seçilen bu asal sayıların dizideki konumları kaydedilir. Tohum değeri ise bu iki asal sayının konumları toplamı olarak ele alınmıştır. Yani seçilecek olan parametreler o an kullanıcının gireceği aralıklarda rastgele bir şekilde seçilecektir. Bu çalışmada bu şekilde rastgele iki bit dizisi elde edilmiştir. Bu diziler 1 milyon bit uzunluğundadır. Elde edilen bu dizilere NIST SP 800-22 testleri uygulanmış olup diziler tüm testleri başarı ile tamamlamıştır.

Anahtar kelimeler: Blum blum shub, anahtar üreteci, RNG, NIST SP 800-22 test, kaotik harita.

1. Introduction

Today, with the rapidly developing internet technologies, the amount of data is increasing exponentially day by day. Among these data, especially personal and private ones must be protected while being transmitted or stored over networks. At this point, the concept of confidentiality emerges. The most basic technique to ensure the confidentiality of data is encryption. In other words, to ensure the confidentiality of the data, it is necessary to encrypt it with an effective encryption algorithm. Encryption approaches have been developing rapidly from the past to the present. New encryption algorithms are needed according to the increasing amount of data and various requirements in different applications. Therefore, the importance of studies on encryption approaches is increasing day by day [1]. Encryption algorithms are generally classified in two ways. The first one is the stream cipher approach. In these approaches, bits are encrypted one by one as a stream. These algorithms are highly secure but become difficult to implement as the amount of data increases. The other approach is block cipher. In block cipher, the data is divided into equal blocks and each block is encrypted separately. The encrypted blocks are then combined to obtain encrypted data. The most important advantage of these algorithms is that they work effectively, i.e. fast, no matter how large the data is. These structures are frequently used today and are of vital importance [2]. Today, the block cipher standard is the AES [3] algorithm. In both stream cipher algorithms and block cipher algorithms, all processes are known. The only unknown parameter in these algorithms is the key value. Especially in stream ciphers, since the data is passed directly through the XOR component with the key value, the key must be secure and secret [4]. How to obtain secure key values to be used in these encryption algorithms is a critical issue. Studies on this subject are increasing day by day. In other words, the complexity of the algorithms used to ensure data security is not sufficient alone. At the same time, the keys used must also be secure [5]. Random

[*] Corresponding author: skarakus@beu.edu.tr. ORCID Number of authors: [1] 0000-0003-1999-0203, [2] 0000-0002-4096-0458

number generators (RNG) are used to obtain key values securely. In other words, these keys must be obtained randomly.

RNG structures are frequently used in many fields, especially in computer science. The need for random numbers has increased in recent years. Physics, biology, simulation, and security fields are some of them. Especially in Monte Carlo simulations, random numbers are frequently used [6]. However, if random numbers are to be used in cryptological applications, they should be chosen very carefully. RNG structures are classified in two ways. The first one is true random number generators (TRNG). Here, numbers are obtained from physical sources such as mouse movements, processor run times, and radioactive disturbances. With these structures, secure numbers that are completely random can be obtained. However, these structures are often difficult to implement. The other structure is pseudo random number generators (PRNG). These are approaches in which random numbers are generated by mathematical and algorithmic processes. These techniques are easier to develop and implement. However, it is necessary to be very careful when generating these numbers. To decide that these numbers are random, various tests must be performed. Because there is an initial value called seed in PRNG structures. When this value is estimated, the same numbers can be generated again. This is an advantage for the reproduction of the sequence. However, this value should not be obtained by attackers. The capture of these values by attackers makes it easier for systems to exploit security vulnerabilities [7]. The BBS algorithm is one of the important PRNG structures. However, for this algorithm to be used in key generation, its parameters must be selected effectively. In this study, chaotic maps are used in the selection of these parameters. Chaotic maps are used in the generation of random numbers and many cryptographic applications [8]. The BBS algorithm has been used in many cryptographic studies. Some of these studies are mentioned below.

In a study by Joey [9], it was aimed to increase the random number sequence and the bits received per iteration to increase the efficiency of the BBS. To achieve this goal, it is proposed to modify the second-order generator of BBS with a matrix generator by squaring a 2x2 matrix that produces four outputs per iteration. Arroyo and Delima [10] proposed a method that combines Affine cipher and BBS algorithm. In the proposed method, the BBS algorithm is used to generate one of the secret keys by modifying the Affine cipher. To increase the unpredictability of the ciphertext, a random key sequence is generated by the BBS algorithm. According to the results obtained, it is found that the proposed method is more secure in general. Surbakti, Fauzi, and Khair [11] proposed a hybrid system using Rivest Shamir Adleman (RSA) and BBS algorithms to improve the security of database files in Binjai Regional Public Service Agency. In their proposed system, RSA algorithm is used to encode the content of the text file. Since RSA algorithm uses two different keys in encryption and decryption processes, BBS algorithm is used for key generation. As a result, the RSA and BBS hybrid system was found to work well. Rambe, Nababan, and Nasution [12] developed a method using RC5 and BBS algorithms in their research to increase message security. In this method, the key generated using BBS is integrated into the RC5 encryption algorithm to prevent key duplication and to make key generation more randomized. According to the results obtained from the tests, it is seen that the processing speed is independent of the number of characters in the plaintext and the encrypted file size with the combination of RC5 and BBS is lower than the encryption using the standard RC5 algorithm. In their study, Ndruru and Zebua [5] proposed a method based on BBS algorithm with Beaufort encryption in the process of encryption and decryption of pixels in JPG format digital images to ensure the security of digital images. BBS algorithm was used in key generation. According to the results obtained, it was seen that the keys generated by the BBS algorithm are random and do not cause repetition and make it difficult for others to recognize the original image because it increases the color weakness of the original image. Delima and Arroyo [13] used the BBS algorithm to produce a more secure ciphertext by changing the key generation process of traditional Nihilist encryption. According to the simulation results, this proposed hybrid system offers a secure encryption and decryption process. Saini and Sehrawat [14] also aimed to protect sensitive information during transmission and provide efficient and reliable decryption at the receiver side. In their proposed system, they transformed the MNIST dataset into a key generation source and combined it with the power of modern cryptographic methods. An additional layer of security is added to the cryptographic algorithm passing through the first ciphertext by using XOR and BSS. It is shown that this proposed two-layer encryption system exhibits superior performance compared to existing systems such as AES, DES, RSA, and ElGamal and can be applied for various security uses by passing NIST tests with key sizes of 128, 256, and 512 bits. In a study by Najwan [15], three types of pseudo-random number generators were used for image encryption to protect personal images from unauthorized access. These are Linear Feedback Shift Register (LFBSR), Nonlinear Feedback Shift Register (NLFBSR), and BBS. In these algorithms applied to color images, large random keys were applied. When these algorithms were compared, BBS was found to have better performance than LFBSR and NLFBSR. Laia, Zamzami, and Sutarman [16] used the DES algorithm and BBS pseudo-random number generator to generate external keys for encryption and decryption of messages. Thus, they made it difficult to guess the random number. According to the results obtained, it was determined that the combination of DES and BBS successfully encrypts and decrypts messages. In addition, the use of BBS as an external key generator in the DES algorithm did not affect the processing time. Alagaw,

Muhammed, and Geto [17] have carried out a study using a modified BBS algorithm and key flow values to improve the security of the Playfair cipher. They evaluated the performance of the application in Matlab environment in terms of avalanche effect, frequency analysis, key generation, key exchange, and resistance to brute force attack. According to the results obtained, they found that the algorithm they proposed has a good performance. Ardhianto et al. [18] investigated the effect of the Euler number applied to the BBS key generator and extended Vigenere on the utilization of information confidentiality. They used different key lengths of 32 and 64 bits using short astronomical observation speeches sent via 1 Kb telegrams. To measure the performance of the study, they calculated the entropy value of the Extended Vigenere output. According to the results obtained, there is a significant increase in information confidentiality. Sina et al. [19] proposed a method using BBS random number generator and LSB steganography together with 3DES encryption method to secure messages. In this hybrid method, they used triple DES to encrypt messages with .txt extension, BBS random number generator to determine the location of the message to be hidden in the cover image, and LSB steganography method as the hiding method. With 20 hiding operations, they hid a maximum of 150 characters and obtained an average PSNR value of 88.61 after 20 message hiding operations.

As mentioned above, the BBS algorithm has been used many times in different ways. The aim of this study is to add a new one to these methods. The proposed algorithm offers an innovative perspective on the use of the BBS algorithm in the generation of values such as keys for cryptographic applications. In this study, chaotic maps are utilized to achieve this. Chaotic maps are one of the popular topics of recent years. There are many chaotic maps in the literature. This is one of the effective aspects of the proposed work. Thanks to the diversity of these maps, any number of secure random numbers can be obtained with the proposed method. In addition, the proposed approach is simple, comprehensible and at the same time difficult to predict. It is thought that this study will be a source of inspiration for researchers in using the BBS algorithm in different ways. In the rest of this paper, in the second section, the idioms of the BBS algorithm are explained. In the third section, the proposed generator algorithm is presented with a step-by-step flow diagram. In the fourth section, the results of the analyses are given and NIST SP 800-22 tests are applied to the obtained bit sequences. In the fifth section, the results are discussed.

2. Blum Blum Shub Algorithm (BBS)

The BBS algorithm is a frequently used algorithm for generating random numbers. It was designed by Lenore Blum, Manuel Blum, and Michael Shub in 1984 for use in public key infrastructure [20]. BBS is based on the product of two prime numbers and a seed value. In this algorithm, two primes p and q, and a seed value called "seed" are determined. Then, using these values, the desired number of random numbers or bit sequences are obtained in a very simple way as given in Equation 1 and Equation 2.

$$m = p * q \tag{1}$$

$$x = seed^2 \mathrm{mod}(\mathrm{m}) \tag{2}$$

In addition, the flow diagram of the BBS algorithm is given in Table 1. As stated in Table 1, after the prime numbers and seed value are selected, any number of random numbers and ones can be generated.

Table 1. Pseudocode of the BBS algorithm.

```
begin
generate p prime number
generate q prime number
generate "seed" value
x_i = seed
m = p * q
for [0, n]:
        x_{i+1} = x_i^2 mod (m)
        print ( x_{i+1})
        x_i = x_i + 1
end for
end
```

3. Proposed Key Generator Algorithm

In this study, a new key planning algorithm is designed using the BBS algorithm. In this algorithm, the first, two large prime numbers are selected. Then these primes are multiplied to obtain a value of m. Then the numbers are generated according to the formula given in equation 2. This algorithm is quite simple. However, when the

prime numbers and seed value are chosen efficiently, unique numbers can be generated. The main problem here is how to choose the seed value and prime numbers. This point is particularly emphasized in this study. Chaotic maps are used to overcome this problem. The steps of the proposed algorithm are given below.

Step 1. The user is asked to enter a prime number range.
Step 2. A prime number pool is generated in the entered range.
Step 3. With the selected chaotic map, a prime number is randomly selected from the prime number pool (p value) and its position is recorded.
Step 4. With the other selected chaotic map, a prime number is randomly selected from the prime number pool (q value), and its position is recorded.
Step 5. The seed value is obtained by summing the location information of the calculated p and q values. (seed= location p+ location q)
Step 6. Using these values, bit sequences are generated with the BBS algorithm.
Step 7. The generated bit sequences are converted into keys of desired lengths.

As given above, in the proposed method, the user is first asked for the starting and ending values for the prime number pool. All primes between these values entered by the user are generated and stored in an array. In this way, the prime number pool will change every time the algorithm runs. This will provide an important gain, especially in security applications. Because each user will determine the prime number range randomly. This will increase the unpredictability of the algorithm. After the prime number pool is created, p and q values should be selected from this pool. These values should also be unpredictable. Therefore, in this study, it is shown that these values can be selected with chaotic maps. These values can be selected with different chaotic maps or with the same maps. In this study, different chaotic maps are used for p and q values. In this way, two primes are randomly selected from the prime number pool. After the primes are selected, the seed value needs to be determined. One of the most critical parameters of pseudo-random number generators is the seed value. This value must be chosen randomly and cannot be generated again. Because if the seed value is known, the bit sequence can be generated again. In this study, the seed value is taken as the sum of the positions of prime numbers. Since the prime number pool and the number of primes will change each time the algorithm runs, it is very difficult to estimate the seed value used here. The system model of the proposed algorithm is given in Figure 1.

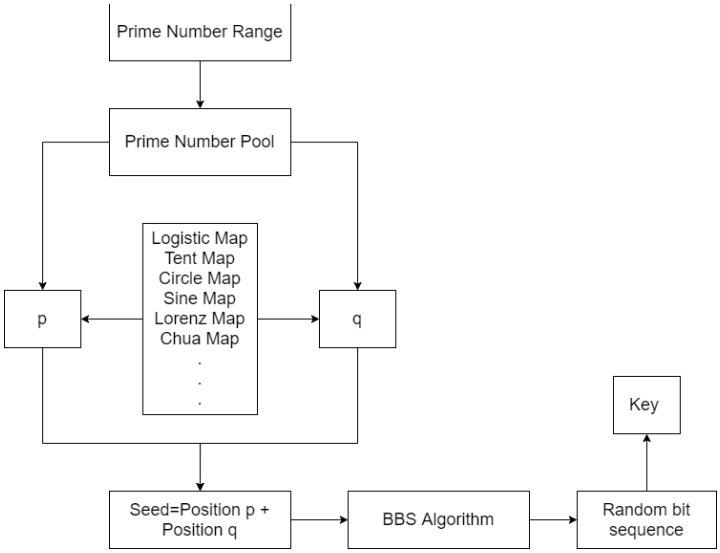

Figure 1. System model of the proposed key planning algorithm.

As seen in Figure 1, different maps can be used to select the values of p and q. Some chaotic maps are given here as examples. However, it is seen that there are more than a hundred chaotic maps in the literature. In addition, studies in which new chaotic maps are obtained are very popular today. One of the most important advantages of this study is the variety of chaotic maps. Thanks to this diversity, the unpredictability of the algorithm will increase. In addition, the seed value is completely random and is determined according to the values entered by the user at that moment. In other words, the algorithm designers and users will not be able to predict the seed value.

4. Analysis Results

The BBS algorithm is simple but effective. It should be noted that the prime numbers and the seed value are chosen randomly. In this study, the problem of selecting these values is solved with chaotic maps. There are intervals where chaotic maps in the literature show random behavior. It is known that the values produced in these intervals are random. With the algorithm proposed in this study, 2 different bit sequences are obtained by using 2 different chaotic maps. The first value, i.e. p, is obtained with the logistic map and the second value, i.e. q, is obtained with the tent map. The mathematical model of the logistic map is given in Equation 3 and the mathematical model of the tent map is given in Equation 4.

$$x_{n+1} = ax_n(1 - x_n)\,, \quad x_n \in [0,1]\,, \quad a \in [3.5, 4] \tag{3}$$

$$x_{n+1} = \begin{cases} ax_n & x_i < 0.5 \\ a(1 - x_n) & x_i \geq 0.5 \end{cases}, \quad x_n \in [0,1]\,, \quad a \in [1,2] \tag{4}$$

The fixed value intervals used in these chaotic maps are the intervals where the map shows random features. These are usually shown by bifurcation diagrams. Bifurcation diagrams of logistic and tent map are given in Figure 2.

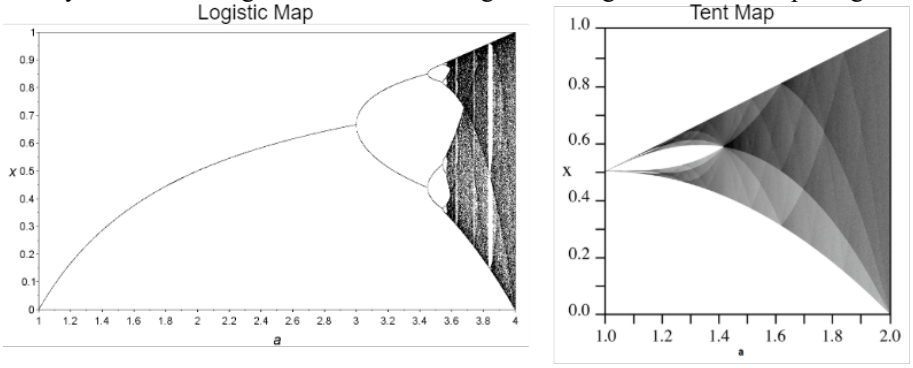

Figure 2. Bifurcation diagrams of logistic and tent maps.

To test the performance of the proposed algorithm, 2 different sequences were generated. The parameters used in the generation of these sequences are given randomly. These parameters are given in Table 2.

Table 2. Values obtained with the proposed algorithm.

Parameters	1. sequence	2. sequence
1. value entered by the user	87814024245	123416789
2. value entered by the user	87814052154	123452345
Total number of prime numbers generated	1061	1946
Number of primes "p" selected by logistic map	87814027403	123433087
Number of primes "q" selected by tent map	87814028789	123419927
Index of the 1. value	124	873
Index of the 2. value	177	181
Seed (index 1+index 2)	301	1054

Using the parameters in Table 2, two different bit sequences of length 1 million were generated. There are various methods to test whether these bit sequences are random or not. The most well-known among these methods is the NIST SP 800-22 test [21]. In this study, the NIST SP 800-22 test was applied to the bit sequences obtained. The NIST SP 800-22 test includes a total of 15 different tests. In each test, a p value is calculated. This p value is expected to be between 0 and 1. As this value approaches 1, the degree of randomness of the sequence increases. The NIST SP 800-22 tests are briefly explained below.

Test 1- Frequency Test (Monobit): The distribution of 1 and 0 values is examined. In other words, the number of 1 and 0 values in the obtained bit sequence is checked. These values are expected to be close to each other. Otherwise, the sequence is not randomly distributed.

Test 2- Frequency Test within a Block: 1 and 0 distributions are examined within various selected blocks. The numbers 1 and 0 are also expected to be close within the blocks.
Test 3- Run Test: The number of 0 and 1 blocks is examined. Here, it is determined whether the number of 0 and 1 streams is random.
Test 4- Longest Run of Ones in a Block: Here the array is first divided into blocks. Then, the number of consecutive 1s and 0s in each block is examined. It is examined whether there is a deviation between the values here and the expected values.
Test 5- Binary Matrix Rank Test: A matrix is obtained with bit blocks, each of which is expressed as a row. Then the rank of this matrix is calculated, and it is observed whether there is a dependency between the blocks.
Test 6- Discrete Fourier Transform (Spectral) Test: Discrete Fourier transform of the bit sequence is taken and its period is observed. The aim here is to detect repeating patterns.
Test 7- Non-Overlapping Template Matching Test: It examines whether a block of a certain length repeats in the sequence. If this block repeats, a new block is searched by shifting one bit from this block.
Test 8- Overlapping Template Matching Test: This test has the same logic as the previous test. The main difference here is that it repositions when a similar pattern is detected.
Test 9- Maurer's Universal Statistical Test: This test examines whether the bitstream can be compressed without data loss. If the bit sequence can be compressed properly enough without data loss, it does not show high randomness.
Test 10- Linear Complexity Test: Measures the complexity of the array by looking at its LFRS (linear feedback shift register) length. If the lengths obtained here are large enough, the array is random.
Test 11- Serial Test: The frequency of overlapping blocks in the bit array is checked. A low number of overlapping blocks is desired here.
Test 12- Approximate Entropy Test: Here the entropy of blocks of length a and a+1 is checked. Frequency is calculated as in the previous test. The frequency calculated here should not be greater than the expected value.
Test 13- Cumulative Sums (Forward) Test: The bit string is divided into blocks of the same length and the balance of 1, 0 values is checked.
Test 14- Cumulative Sums (Reverse) Test: This test is applied to the previous test with the bit string reversed.
Test 15- Random Excursions Test (State: +4): The bit string is divided into blocks of the same length and the balance of 1, 0 values is checked. The excursion is random.

The NIST SP 800-22 test results of the bit sequences generated by the proposed algorithm are given in Table 3. Looking at this table, it is seen that both bit sequences successfully completed all NIST SP 800-22 tests. The point to be considered when determining the parameters in Table 2 is to choose the prime numbers large. In the analysis results, it was seen that the bit sequences could not successfully complete the NIST SP 800-22 tests when the primes were chosen small. However, it is observed that the algorithm works effectively when the primes are at least 9 digits. With the proposed study, key values of desired lengths can be obtained. These keys can be used in existing [22] or newly developed encryption algorithms. In addition, reference [23] can be examined for analyzing the encryption speed of keys of different lengths obtained using the proposed method or different methods.

Table 3. NIST SP 800-22 test results.

PRNG		Sequence1	Sequence2
No	**Test**	**p-value**	**p-value**
1	Frequency Test (Monobit)	0.58919	0.20766
2	Frequency Test within a Block	0.32079	0.11212
3	Runs Test	0.49126	0.71168
4	Longest Run of Ones in a Block	0.43902	0.67749
5	Binary Matrix Rank Test	0.85397	0.17649
6	Discrete Fourier Transform (Spectral) Test	0.02636	0.04446
7	Non-Overlapping Template Matching Test	0.43851	0.71955
8	Overlapping Template Matching Test	0.90420	0.08871
9	Maurer's Universal Statistical test	0.22543	0.52938
10	Linear Complexity Test	0.26034	0.65046
11	Serial test	0.23690	0.32660
12	Approximate Entropy Test	0.01569	0.30734
13	Cumulative Sums (Forward) Test	0.51638	0.35201
14	Cumulative Sums (Reverse) Test	0.75238	0.35137
15	Random Excursions Test (State: +4)	0.56452	0.20341
Number of Successful Tests		15	15

5. Conclusions

In this study, a new key generator architecture is proposed for use in encryption algorithms. Random number generators are one of the most widely used methods to generate keys. This is because keys should not be guessed by attackers and should not be deterministic. BBS algorithm is one of the known effective pseudo-random number generators. In this study, it is considered that it can be used in key generation. BBS is a pseudorandom number generator based on the product of two different large prime numbers and a seed value. This algorithm is generally capable of generating high quality random numbers. However, the parameters to be used need to be chosen carefully. This paper proposes a new approach to overcome this problem.

In the proposed approach, the user is first asked to enter a range. The primes in this range are generated and saved in an array, and a prime number pool is created. Then, prime numbers are randomly selected from this prime number pool with two different chaotic maps to be used in the BBS algorithm. The positions of these selected primes are also recorded. The seed value is taken as the sum of these two positions. Thus, every time the algorithm runs, the prime number range, prime numbers, and seed value will be randomly generated. Even the user will not know the primes and the seed value. This significantly increases the randomness and privacy of these values.

To test the performance of the proposed method, two random intervals are given, and 2 different bit sequences are generated by selecting the values in these intervals. These bit sequences are 1 million long. This is because this number is generally used in the literature. NIST SP 800-22 test suite was applied to the obtained bit sequences. This test suite contains a total of 15 tests and is frequently used. It was observed that the bit sequences obtained with the proposed approach successfully completed all NIST SP 800-22 tests. It should be noted that the prime numbers should be chosen large. When primes larger than 9 digits were chosen, the bit sequences passed all the tests. However, when smaller primes were chosen, not all NIST SP 800-22 tests were passed. Thus, this study provides a roadmap for those who will use the BBS algorithm for key value.

References

[1] Liu J, Wang Y, Han Q, Gao J. A sensitive image encryption algorithm based on a higher-dimensional chaotic map and steganography. Int J Bifurcat Chaos 2022; 32(01), 2250004.

[2] Katz J, Lindell Y. Introduction to modern cryptography: principles and protocols. Chapman and hall/CRC, 2007.

[3] Daemen J, Rijmen V. The design of Rijndael. New York: Springer-verlag 2002; 2.

[4] Van Oorschot PC, Menezes AJ, Vanstone SA. Handbook of applied cryptography. New York: CRC Press, 1996.

[5] Ndruru E, Zebua T. Generate Beaufort Cipher Key Based on Blum-Blum Shub For Secure Digital Image. Instal: Jurnal Komputer 2021; 13(01).

[6] Malik K, Pulikkotil J, Sharma A. Comparison of pseudorandom number generators and their application for uncertainty estimation using Monte Carlo simulation. Mapan 2021; 36(3): 481-496.

[7] Schindler W. Random number generators for cryptographic applications, Cryptographic Engineering. In: Koç ÇK, editör. Springer, Boston, MA, 2009; 5-23.

[8] Artuğer F, Özkaynak F. A new chaotic system and its practical applications in substitution box and random number generator. Multimedia Tools Appl 2024, 1-15.

[9] Joey FL. Modification of Blum-Blum-Shub Generator (BBS) with a 2× 2 Matrix and the First Digit Property of Generated Random Numbers and Bits. AMCI 2023; 12(2): 120-129.

[10] Arroyo JCT, Delima AJP. An Improved Affine Cipher using Blum Blum Shub Algorithm. IJECS) 2020; 9(3): 3295-3298.

[11] Surbakti TB, Fauzi A, Khair H. Rivest Shamir Adleman (RSA) Hybrid Algorithm System and the deep Blum Blum Shub (BBS) Algorithm Securing E-Absence Database Files. INJECSI 2023; 1(2): 53-61.

[12] Rambe BM, Nababan EB, Nasution MK. Performance Analysis Of The Combination Of Blum Blum Shub and Rc5 Algorithm in Message Security. JITE 2024; 7(2): 409-423.

[13] Delima AJP, Arroyo JCT. An Enhanced Nihilist Cipher Using Blum Blum Shub Algorithm. IJATCSE 2020, 9(3): 3270-3174.

[14] Saini A, Sehrawat R. Enhancing Data Security through Machine Learning-based Key Generation and Encryption. ETASR 2024: 14(3): 14148-14154.

[15] Najwan AH. Color Images Encryption using Cipher System with different types of Random Number Generator. IJIRCCE 2017; 5(5).

[16] Laia O, Zamzami EM. Analysis of combination algorithm data encryption standard (DES) and Blum-Blum-Shub (BBS). In Journal of Physics: Conference Series 2021. 5th International Conference on Computing and Applied Informatics (ICCAI 2020), 1-2 December 2020; Medan, Indonesia. pp. 1-7.

[17] Muhammed AJ, Woldiegiworgies TA, Tsegaye GG. Security Enhancement of Playfair Cipher Using Modified Blum Blum Shub Algorithm and Keystream Values. Research Square 2024; 1-12.

[18] Ardhianto E, Redjeki RS, Supriyanto E, Murti H, Wahyudi EN. Adopsi Generator Kunci Euler Number dan Pembangkit Kunci Blum Blum Shub untuk Meningkatkan Confidentiality Level pada Extended Vigenere. Infotek 2024; 7(1): 1-11.

[19] Sina DR, Kiu GA, Djahi BS, Pandie ES. Aplikasi Keamanan Pesan (. Txt) Menggunakan Metode Triple DES Dan Metode Kombinasi LSB Dan BLUM-BLUM-SHUB. J-Icon 2022; 10(2): 204-209.

[20] Omorog CD, Gerardo BD, Medina RP. Enhanced pseudorandom number generator based on Blum-Blum-Shub and elliptic curves. In 2018 IEEE Symposium on Computer Applications & Industrial Electronics (ISCAIE) 28-29 April 2018, Penang, Malaysia: IEEE. pp. 269-274.
[21] Rukhin A, Soto J, Nechvatal J, Smid M, Barker E, Leigh S, Levenson M, Vangel M, et. al. A Statistical Test Suite for Random and Pseudorandom Number Generators for Cryptographic Applications. National Institute of Standarts and Technology, 2010. pp. 23-87.
[22] Etem T, Kaya T. Trivium Algoritması Kaynaklı Rastgele Permutasyon Üretimiyle Görüntü Şifreleme Uygulaması. FÜMBD 2022; 34(2): 687-697.
[23] Etem T, Kaya T. Görüntü Şifreleme için Trivium-Doğrusal Eşlenik Üreteci Tabanlı Bit Üretimi. FÜMBD 2020; 32(1): 287-294.

Turkish Journal of Science & Technology
19(2), 451-456, 2024

Research Paper
https://doi.org/10.55525/tjst.1529765

Optical Characterization of Hydrogel and Silicone Hydrogel Soft Contact Lenses

Reşit ÖZMENTEŞ[1*], Abdulkadir KORKUT
[1] Vocational School of Health Services, Bitlis Eren University, 13100 Bitlis, Türkiye
[2] Van Yüzüncü Yıl University, Faculty of Science, Department of Physics, Van, Türkiye
[*1] rozmentes@beu.edu.tr, [2] akkut@yyu.edu.tr

(Geliş/Received: 08/08/2024; Kabul/Accepted: 26/09/2024)

Abstract: Contact lenses are biomaterials that have emerged as an alternative to glasses in correcting vision defects. In this study, Nesofilcon A (Hydrogel-Hy) and Delefilcon A (Silicone Hydrogel-SiHy) daily disposable soft contact lenses were optically examined using UV-visible light spectroscopy. Optical absorption and transmittance measurements of the lenses were taken with a UV-visible spectrophotometer, and their properties of blocking the harmful part of the radiation to the eye and transmitting the harmless part were investigated. From the absorption spectrum, it was seen that the Nesofilcon A lens absorbed ultraviolet light better. From the optical absorption coefficient spectra of Nesofilcon A and Delefilcon A lenses, the absorption edges were obtained as 386 and 325 nm, and the optical band gap values were 3.34 and 3.98 eV, respectively. Additionally, the refractive index profiles of the lenses were plotted. The refractive indices of the lenses at 550 nm wavelength were calculated as 1.55 and 1.77 for Nesofilcon A and Delefilcon A, respectively. While the Delefilcon A lens transmitted visible light well, the Nesofilcon A lens blocked UV light better and its refractive index was determined to be closer to the 1.40 the value specified by the manufacturer.

Key words: Soft contact lens, UV-Visible spectroscopy, Optical properties, Silicone-Hydrogel.

Hidrojel ve Silikon Hidrojel Yumuşak Kontakt Lenslerin Optiksel Karakterizasyonu

Öz: Kontakt lensler, görme kusurlarını düzeltmede gözlük alternatifi olarak ortaya çıkan biyomalzemelerdir. Bu çalışmada, Nesofilcon A (Hidrojel-Hy) ve Delefilcon A (Silikon Hidrojel-SiHy) günlük tek kullanımlık yumuşak kontakt lensler UV-görünür ışık spektroskopisi kullanılarak optiksel olarak incelenmiştir. Lenslerin optik soğurma ve geçirgenlik ölçümleri UV-görünür ışık spektrofotometresi ile alınarak, göze gelen radyasyonun zararlı kısmını bloke etme ve zararsız kısmını geçirme özellikleri incelenmiştir. Soğurma spektrumundan, Nesofilcon A lensinin ultraviyole ışığı daha iyi emdiği görülmüştür. Nesofilcon A ve Delefilcon A lenslerinin optik soğurma katsayısı spektrumlarından soğurma kenarları 386 ve 325 nm, optik bant aralığı değerleri ise sırasıyla 3,34 ve 3,98 eV olarak elde edilmiştir. Ayrıca lenslerin kırılma indisi profilleri çizilmiştir. 550 nm dalga boyunda lenslerin kırılma indeksleri Nesofilcon A ve Delefilcon A için sırasıyla 1,55 ve 1,77 olarak hesaplandı. Delefilcon A lensi görünür ışığı iyi iletirken, Nesofilcon A lensi UV ışığını daha iyi bloke ettiği ve kırılma indeksinin üretici tarafından belirtilen 1,40 değerine daha yakın olduğu belirlendi.

Anahtar kelimeler: Yumuşak kontakt lens, UV-Görünür spektroskopi, Optik özellikler, Silikon-Hidrojel

1. Introduction

Contact lenses (CLs) are optical devices made of monomer, polymer or macromer combinations. Their structure is thin, transparent, and curved. Soft CLs are made of flexible polymers. Today's commonly used daily disposable or longer-wear CLs are made of hydrogel or silicone hydrogel materials. The first soft hydrogel contact lens was introduced in 1938 and quickly gained popularity. Hydrogel is a water-absorbent material, while silicone has good gas permeability [1-5]. Hydrogel lenses are a type of hydrophilic, water-retaining monomers (HEMA, 2-hydroxy ethyl methacrylate, NVP, N-vnyl pyrrolidone, polyvinyl alcohol). The Hy lens contains a high percent of water. This keeps the eye moisturized. They have high oxygen permeability. In this way, the eyes breathe better and they are comfortable lenses to use. It is also known to protect the eyes from harmful UV rays. Silicone hydrogel (SiHy) CLs were produced in the 2000s. They are now the most popular type of lens. These lenses, which have high oxygen permeability, also reduce the risk of infection [6-9]. SiHy lenses are an advanced version of Hy lenses. They are produced by combining Si and Hy copolimer materials. The PMMA part of the material determines its optical transparency and hardness, and the silicon part determines its oxygen permeability. Since the silicone part is hydrophobic, its wettability is low. Thanks to the Si in their structure, they provide higher oxygen permeability than Hy lenses and allow lens use for longer periods of time. It is a type of hydrophobic (water repellent) copolymer lens [10-14]. The ability of contact lenses to absorb high energy UV light of the electromagnetic spectrum is a

* Corresponding author: rozmentes@beu.edu.tr. ORCID Number of authors: [1] 0000-0002-5893-0660, [2] 0000-0003-0100-4057

very important feature for eye health. The type of material from which CL is produced has a significant impact on this characteristic. There are further studies showing that even blue light affects the eyes [15,16]. Wavelength and energy values of UV and blue light are given in Table 1.

Table 1. Wavelength and energy range values of ultraviolet (UV) and visible blue light that have harmful effects on the ocular

Radiation band type	Wavelength (nm)	Energy (eV)
UV-C	200-280	6.20 - 4.43
UV-B	280-315	4.43 – 3.93
UV-A	315-400	3.93 – 3.10
Blue	400-515	3.10 – 2.40
Desirable light	515-780	2.40 – 1.59

Almost all UV-C and UV-B light is absorbed by the ozone layer. But almost all UV-A light passes through the ozone layer and reach the earth and therefore living tissues and especially the human eye. Therefore, unless UV radiation is filtered lenses or glasses, it can reach the inner layers of the eye and cause damage. In addition, as a result of our exposure to screens, LED lamps, TVs and other electronic devices, the blue light emitted from these devices negatively affects the secretion of the melatonin hormone at night, causing sleep disorders. Exposure to high levels of blue light throughout the day can cause permanent damage to the eyes. Plasmonic contact lenses have been proposed to alleviate these negative effects of blue light [1].

There are relatively few studies in the literature on the absorption and permeability properties of soft contact lenses. Ahmet Barlık and Gonca Ateş compared the UV light absorption and visible light transmittance properties of Senofilcon A and Lotrafilcon B soft contact lenses. They concluded that although the transmittances of the lenses in the visible region are close to each other, the Senefilcon A lens absorbs, that is cut, UV light better [17]. In another study, Gonca Ateş and Selma Bilici compared the properties of CR-39 and polycarbonate (PC) organic eyeglass lenses such as absorption, transmittance, optical band gap and UV protection using UV-visible absorption spectroscopy. The authors concluded that PC organic spectacle lenses protect the eyes better from UV radiation and they calculated direct band gap values of the lenses as in the range of 3.14-4.15 eV [18]. In a similar study, Gonca Ateş measured the absorption and transmittance of mineral and organic eyeglass photochromic lenses in vertical and horizontal directions and examined the effects of the color of the lenses and the polarization of the light on the optical properties of the lenses [19]. In a parallel study, K. Jez et al. They tested the transmittance and reflection spectroscopy of organic CR-39 eyeglass lenses in the UV-Vis-NIR wavelength range. The authors noted that the eyeglass lenses exhibited a transmittance of around 90%, not the 100% stated by the manufacturer, and that only two of the six UV-coated lenses they examined performed UV protection functions [20]. In a recent study, M. Alves et al. They investigated the effect of lens care solutions on the optical properties (transmittance, reflectance, absorbance and florescence) of SiHy and Hy lens materials. The authors reported that the optical properties of contact lenses mutually change with lens care solutions [15]. J. Rex et al. examined the surface elemental composition analyzes of different types of commercial SiHy lenses using the X-ray photoelectron spectroscopy (XPS) method. Detailed XPS analysis of the lenses revealed significant differences in the chemical composition of their surfaces in terms of the content of Si [13]. In a similar study using the soft daily disposable lenses used in this study, J. Schafer et al. compared the surface refractive index values of Delefilcon A, Nesofilcon A and Etafilcon A lenses before and after 15 minutes of wearing. The study showed that the surface refractive index value of the of the Delefilcon A lens increased from 1.34 to 1.43, while there wasn't a significant change in the refractive index value of the Nesofilcon A (1.38) and Etafilcon A (1.41) [21]. In a recent study, the dehydration and rehydration processes of daily disposable (Nesofilcon A and Delefilcon A) and two-month (Comfilcon A and Lotrafilcon B) lenses and the changes in their refractive index, water content, chemical structure and thermal properties were investigated by Lira M. et al. The study showed that there was no significant change in the chemical structures of the lenses with dehydration and rehydration processes, and in the refractive index and water content with rehydration [3].

In this study, the optical properties of Nesofilcon A and Delefilcon A daily disposable lenses were investigated by spectrophotometric method. Lenses were originally characterized by reflection and refractive index dispersion curves. The aim of this study is to examine the UV-visible absorption, transmittance and reflection spectra, UV light filtering properties of contact lenses and to calculate the optical band gap and refractive index values of these materials.

2. Material and Method

The Nesofilcon A (hydrogel-Hy) and Delefilcon A (silicone hydrogel-SiHy) polymeric material contact lenses examined in this study are commercially available daily disposable lenses. The most obvious differences between these lens materials are their water content and wetting properties. While Nesofilcon A is hydrophilic and contains 78% water, Delefilcon A contains 33% water and is hydrophobic [2].

Table 2: Some physical parameters of the contact lenses examined

Parameter	CL Material	
Technical Name	Nesofilcon A	Delefilcon A
Manufacturer-Brand	Bausch+Lomb	Ciba Vision
Water Content, WC (%)	78	33
Oxygen Permeability (Dk/t)	42	156
Base Curve:	8.6 mm	8.5
Diameter:	14.2 mm	14.1 mm
Center Thıckness	0.10 mm	0.09mm
Main Monomer	Hy	SiHy
Powers	-3.00 D	+0.50 D

Daily disposable Nesofilcon A and Delefilcon A contact lenses were optically characterized using the UV-Vis spectrophotometric method. The measurements were taken with a Shimadzu UV-Vis 2450 spectrophotometer (Fig. 1a). The device measures the percentage of light that is transmitted and absorbed by the material by sending light to it at wavelengths between 200 and 900 nm. The contact lenses investigated are shown in Figure 1b.

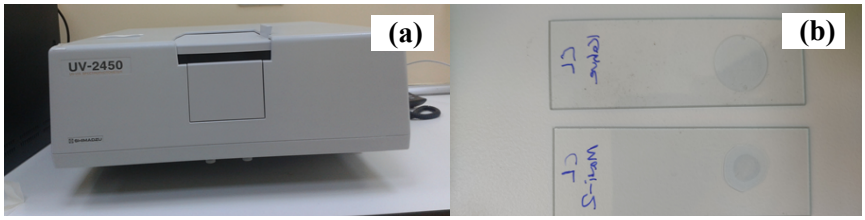

Figure 1: (a) UV-visible spectrometer used for optical absorption measurements of contact the lenses, (b) Examined lens samples

3. Results and Discussion

As can be seen from Figure 2a and b, the CLs exhibit a strong absorption in UV region (300-400 nm) and are transparent in visible region (400-700 nm). In order to determine the optical properties of the CLs; absorbance and transmission measurements were taken for determination of optical band-gap of CL materials. Optical bandgap of soft CL materials were analyzed by plotting $(\alpha h\upsilon)^2$ versus hν curve. The optical band gap of the lenses was calculated from the extrapolating of the linear portion of the curves to x-axis. Tauc plots of the CLs were obtained using Equation (1) [22,23]:

$$\alpha h\nu = A(h\nu - Eg)^n \quad (1)$$

where, α is absorption coefficient, hν is photon energy, Eg is the bandgap of the lens materials and n=1/2 for direct allowed optical band transition. After the lenses are removed from the blister package, a rapid change occurs in their physical properties depending on environmental conditions. The chemical composition, surface and mass properties of lens materials change during the dehydration process.

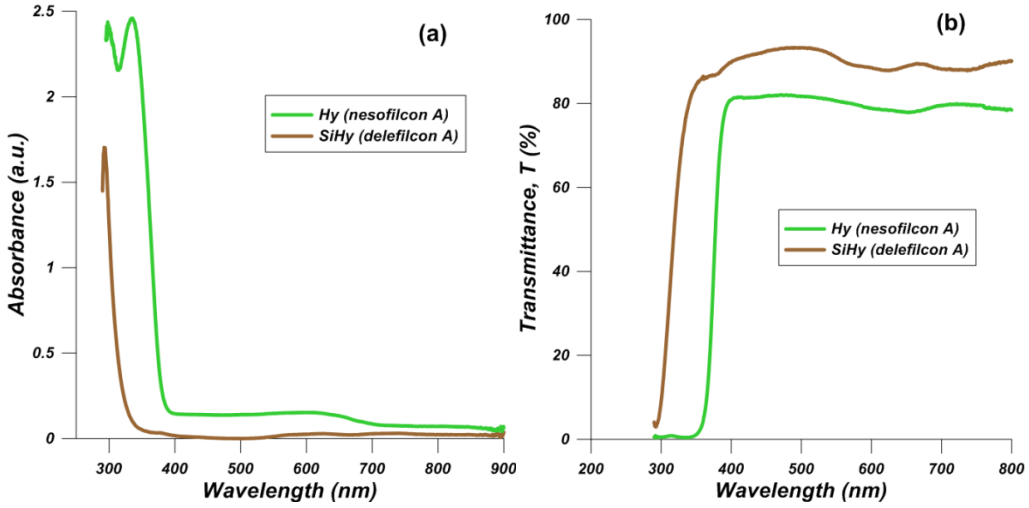

Figure 2. Absorption and transmittance variation of CLs versus wavelength (a) Absorbance - λ (nm) plots (b) Transmittance (%) - λ (nm) plots

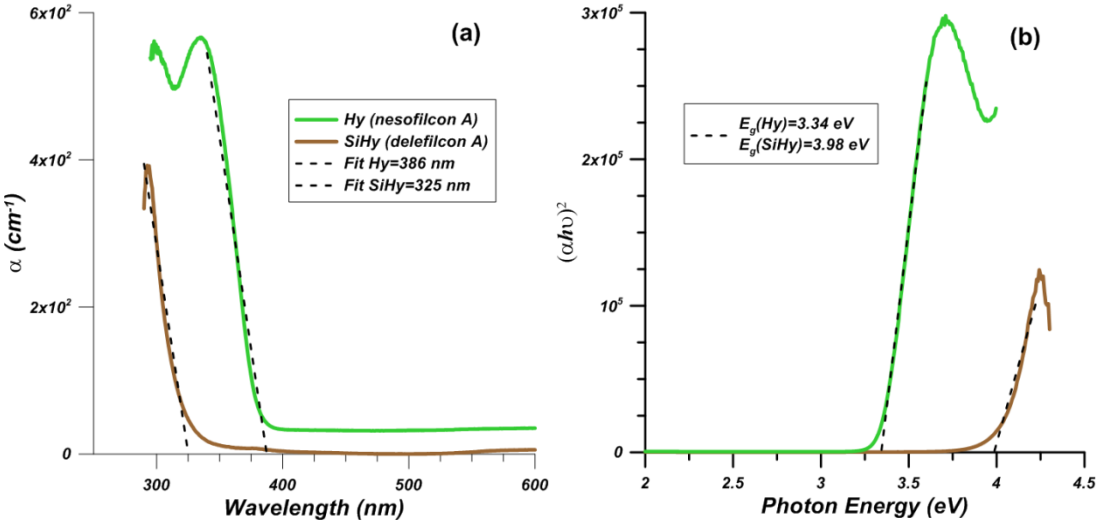

Figure 3. (a) Absorbance coefficient-wavelength plots of the CLs. (b) $\alpha(h\upsilon)^2$ versus hν curve plots of the CLs.

The two most important features of contact lenses are their water content and oxygen permeability. According to the Food and Drug Administration (FDA) classification, contact lenses typically containing less than 45% water are considered to have low water content, and lenses with a Dk value of less than 50 are considered to have low oxygen permeability. With reference to, it can be seen in Table 2 that the Nesofilcon A Hy lens (WC=78%, Dk=42) has higher water content and lower Dk oxygen permeability than the Delefilcon A (WC=33%, Dk=156) SiHy lens. CLs with Dk values below 50 were considered to have low oxygen permeability. These parameters have an impact on the optical characteristics of lenses. Since the examined lenses were produced under production conditions and methods and their chemical compositions were different, UV-Visible measurement parameters showed differences, that is, transmittance, absorption, reflection spectra, refractive index and optical band gap parameters. However, when compared with the literature, it appears that all these parameters are reasonably and compatible [1,15]. The Nesofilcon A Hy lens exhibited better UV absorption and lower transmittance and reflection characteristics in the visible region than the Delefilcon SiHy lens. Both lenses were permeable to blue light, so they could not prevent harmful UVA, UVB and blue rays from reaching the anterior and interior segments of the eye.

Table 3. Optical parameters of the examined Nesofilcon A and Delefilcon A contact lenses

CL Material	CL type	Band gap (eV)	Ref. İndex, n
Nesofilcon	Hy	3.34	1.55
Delefilcon	Si Hy	3.98	1.77

The absorption coefficient and optical band gap spectra of the lenses are given in figure 3a and b. The values of the cutting edge or absorption edge for the Nesofilcon A and Delefilcon A are 325 nm and 386 nm, respectively. These are the values at which the transmission of light begins and the optical absorption ends. Figure 2 shows that Nesofilcon A material absorbs, i.e. blocks, almost all UV light, while Delefilcon A is permeable to UV-A light. On the other hand, the band gap values were calculated by Equation (1) to be 3.34 eV for the Hy lens and 3.98 eV for the SiHy lens and are given in Table 3. If the absorption percentage of an optical material is high, the reflectance and transmittance will be low according to the A+T+R=1 rule [24]. From the reflectance spectra of the lenses in Figure 4a it can be seen that the SiHy lens has a higher reflectance characteristic. This resulted in a higher refractive index of the SiHy lens than that of the Hy lens (Fig. 4b). Equation (2) was used to calculate the refractive index of the lenses.

$$n = (1 + R^{1/2})/(1 - R^{1/2}) \quad (2)$$

Where, n is the index of refraction and R is the optical reflectance of the material. Hy and SiHy lenses reflected 4.7 % and 7.7 % of 550 nm light, respectively. The refractive index values of the lenses were calculated using formula (2) and were 1.55 and 1.77 respectively. These values are higher than the value of between 1.40 and 1.45 given by the manufacturers and in the literature [25]. A higher refractive index in contact lenses indicates that the lens is thinner and therefore may be more comfortable to wear.

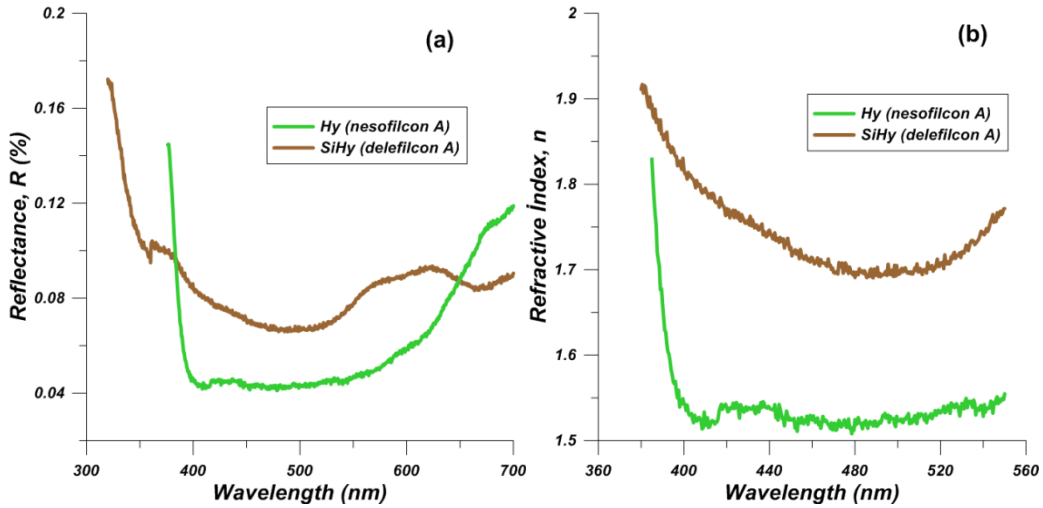

Figure 4. (a) Reflectance spectra of the contact lenses, (b) Refractive index dispersion of the contact lenses

4. Conclusion

Daily disposable soft nesofilcon A (hydrogel-Hy) and delefilcon A (silicone hydrogel-SiHy) contact lenses were optically analyzed by UV-Vis spectroscopy. The Hy and SiHy lenses showed a maximum transparency of %80 and %90 respectively in the visible region. From the optical absorption coefficient spectra of the Hy and SiHy lenses, the absorption edges were found to be 386 and 325 nm, and the optical band gap values were 3.34 and 3.98 eV, respectively. The refractive index profiles of the contact lenses were also plotted and calculated at 550 nm as 1.55 and 1.77 for Hy and SiHy, respectively. While the SiHy-Delefilcon A lens transmitted visible light well, the Hy-Nesofilcon A lens blocked UV light better and the refractive index was found to be closer to the literature values of 1.42-1.45. The nesofilcon A hydrogel contact lens was found to be relatively better at blocking UV light and its refractive index value was close to that reported in the literature.

Acknowledgment

The abstract of this article was presented at the 1st International Health Sciences Congress (1.USABK'24) on 24 May 2024.

References

[1] Elsherif M, Salih AE, Alam F, Yetisen AK, Ramadi KB, Butt H. Plasmonic contact lenses based on silver nanoparticles for blue light protection. ACS Appl Nano Mater 2024; 7: 5956−5966.
[2] Schafer J, Steffen R, Reindel W, Chinn J. Evaluation of surface water characteristics of novel daily disposable contact lens materials, using refractive index shifts after wear. Clinical Ophthalmology 2015; 1973-1979.
[3] Lira M, Lourenço C, Silva M, Botelho G. Physicochemical stability of contact lenses materials for biomedical applications. Journal of Optometry 2020; 13: 120-127.
[4] Mutlu Z, Es-haghi SS, Cakmak M. Recent Trends in Advanced Contact Lenses. Adv. Healthcare Mater 2019; 8: 1801390.
[5] Alam F, Elsherif M, AlQattan B, Ali M, Ahmed IMG, Salih A, Antonysamy DS, Yetisen AK, Park S, and Butt H. Prospects for Additive Manufacturing in Contact Lens Devices. Adv Eng Mater 2021; 23: 2000941.
[6] Guillon M. Are Silicone Hydrogel Contact Lenses More Comfortable Than Hydrogel Contact Lenses?. Eye & Contact Lens 2013; 39: 86-92.
[7] Moreddu R, Vigolo D, Yetisen AK. Contact Lens Technology: From Fundamentals to Applications. Adv Healthcare Mater 2019; 8: 1900368.
[8] Musgrave CSA, Fang F. Contact Lens Materials: A Materials Science Perspective. Materials 2019; 12, 261.
[9] Shihab AH, Eliasy A, Lopes BT, Wu R, White L, Jones S, Geraghty B, Joda A, Elsheikh A, and Abass A. Compressive behaviour of soft contact lenses and its effect on refractive power on the eye and handling off the eye. Plos One 2021; 16(2): e0247194.
[10] Zhu Y, Li S, Li J, Falcone N, Cui Q, Shah S, Hartel MC, Yu N, and et al. Lab-on-a-Contact Lens: Recent Advances and Future Opportunities in Diagnostics and Therapeutics. Adv Mater 2022; 34: 2108389.
[11] Ishihara K, Shi X, Fukazawa K, Yamaoka T, Yao G, and Wu JY. Biomimetic-Engineered Silicone Hydrogel Contact Lens Materials. ACS Appl Bio Mater 2023; 6: 3600−3616.
[12] Güngör İU, Erkan D. Kontakt Lensler: Materyallerin Fiziksel Özellikleri ve Çeşitleri. OMÜ Tıp Dergisi 2004; 21(4): 195–200.
[13] Rex J, Knowles T, Zhao X, Lemp J, Maissa C, Perry SS. Elemental Composition at Silicone Hydrogel Contact Lens Surfaces. Eye & Contact Lens 2018; 44: 221–226.
[14] Toshida H, Takahashi K, Sado K, Kanai A, Murakami A. Bifocal contact lenses: History, types, characteristics, and actual state and problems. Clinical Ophthalmology 2008; 2(4): 869-877.
[15] Alves ME, Castanheira MS, Lira M. Interactions between contact lenses and lens care solutions: Influence in optical properties. Contact Lens and Anterior Eye 2021; 44: 101414.
[16] Osuagwu UL, Ogbuehi KC. UV–vis light transmittance through tinted contact lenses and the effect of color on values. Contact Lens & Anterior Eye 2014; 37: 136–143.
[17] Barlık A, Ateş G. Measurement of Ultraviolet Light Transmittance of Different Contact Lens Types. Turkish Journal of Science & Technology 2023: 18(2): 379-385.
[18] Ateş G, Bilici S. Investigation of Spectral and Optical Properties of Some Organic Eyeglass Lenses. Journal of Inonu University Health Services Vocational School 2023, 11(1): 1042-1053.
[19] Ateş G. Investigation of Spectral and Optical Properties of Color Polarization Lenses. Journal of Physical Chemistry and Functional Materials 2023; 6(2): 15-20.
[20] Jez K, Nabıalek M, Gruszka K, Deka M, Letkıewıcz S, Jez B. Light Transmittance by Organic Eyeglass Lenses According to their Class. Materiale Plastice 2018; 55(3): 438-441.
[21] Schafer J, Steffen R, Reindel W, Chinn J. Evaluation of surface water characteristics of novel daily disposable contact lens materials, using refractive index shifts after wear. Clinical Ophthalmology 2015; 9: 1973-1979.
[22] Özmenteş R. Synthesis and Characterization of Stannic Oxide (SnO_2) Thin Film. Yuzuncu Yil University Journal of the Institute of Natural & Applied Sciences 2024; 29(1): 88-96.
[23] Jime´nez-Flores Y, Sua´rez-Quezada M, Rojas-Trigos JB, Lartundo-Rojas L, Sua´rez V, and Mantilla A. Characterization of Tb-doped hydroxyapatite for biomedical applications: optical properties and energy band gap determination. J Mater Sci 2017; 52: 9990–10000.
[24] Gomaa HM, Yahia I.S, Yousef ES, Zahren HY, Makram BMA, Saudi HAA. Novel Correction Method Toward Extraction of Reflectance and Linear Refractive Index of Some Borosilicate Glasses Doped with BaTiO3. Journal of Electronic Materials 2022; 51: 6347–6355.
[25] Childs A, Li H, Lewittes DM, Dong B, Liu W, Shu X, Sun C and Zhang HF. Fabricating customized hydrogel contact lens. Sci Rep 2016; 6: 34905.

Turkish Journal of Science & Technology
19(2), 457-473, 2024

Research Paper
https://doi.org/10.55525/tjst.1424371

The Design of Machine Learning-Based Computer-Aided System with LabVIEW For Abnormalities in Mammogram Images

Iman Hamadamın[1], Hasan Güler[2*]
[1,2] Electrical-Electronics Engineering Department, Firat university, Elazig/Turkey
[1]imanmuhammad1995@gmail.com, [2*]hasanguler@firat.edu.tr

(Geliş/Received: 23/01/2024; Kabul/Accepted: 10/05/2024)

Abstract: Mammogram is the best way of breast cancer detection nowadays, as breast cancer is the most common form of cancer in the female gender and this form of cancer usually causes death. Many scientists, doctors, and engineers are working together to deal with such serious issues in human life. This paper, it is aimed to develop a new computer-aided system with a graphical coded language to detect abnormalities in mammogram images by using machine learning technics such as ANN and SVM. The developed algorithm has a graphical user interface (GUI) and all results are shown in there. The algorithm was created using three different stages. These are image processing and mass segmentation, feature selection and extraction, and classification. To test the accuracy of the system as the sensitivity, specificity, and accuracy, mammogram images with forty benign and forty malignant masses were used. The obtained results for measuring the sensitivity, specificity, and accuracy are 95%, 97.5%, and 96.25% for ANN and 97.5%, 97.5%, and 97.5% for SVM, respectively. As can be said that the algorithm, user-friendly due to its user interface, can be preferred because it can detect many cancerous cells such as breast cancer with high accuracy.

Key words: Mammography, breast cancer detection, machine learning, graphical user interface.

Mamogram Görüntülerindeki Anormallikler İçin LabVIEW ile Makine Öğrenmesi Tabanlı Bilgisayar Destekli Sistem Tasarımı

Öz: Meme kanseri kadınlarda en sık görülen kanser türü olduğundan ve bu kanser türü genellikle ölüme neden olduğundan, günümüzde meme kanserini tespit etmenin en iyi yolu mamografidir. Birçok bilim insanı, doktor ve mühendis insan hayatındaki bu tür ciddi sorunlarla başa çıkmak için birlikte çalışmaktadır. Bu makalede, YSA ve DVM gibi makine öğrenmesi teknikleri kullanılarak mamogram görüntülerindeki anormallikleri tespit etmek için grafik kodlu bir dile sahip yeni bir bilgisayar destekli sistem geliştirilmesi amaçlanmıştır. Geliştirilen algoritma grafiksel bir kullanıcı arayüzüne (GUI) sahiptir ve tüm sonuçlar burada gösterilmektedir. Algoritma üç farklı aşama kullanılarak oluşturulmuştur. Bunlar görüntü işleme ve kütle segmentasyonu, özellik seçimi ve çıkarımı ve sınıflandırmadır. Sistemin doğruluğunu duyarlılık, özgüllük ve doğruluk olarak test etmek için kırk iyi huylu ve kırk kötü huylu kitle içeren mamogram görüntüleri kullanılmıştır. Duyarlılık, özgüllük ve doğruluk ölçümleri için elde edilen sonuçlar sırasıyla YSA için %95, %97,5 ve %96,25; DVM için %97,5, %97,5 ve %97,5'tir. Kullanıcı arayüzü sayesinde kullanıcı dostu olan algoritmanın, meme kanseri gibi birçok kanserli hücreyi yüksek doğrulukla tespit edebilmesi nedeniyle tercih edilebileceği söylenebilir.

Anahtar kelimeler: Mamografi, meme kanseri tespiti, makine öğrenmesi, grafiksel kullanıcı arayüzü.

1. Introduction

Recently, there is an increase in the rate of affected women with breast cancer. This type of cancer alone accounts for about 22% of female cancers and approximately 15% of mortality among women having cancer [1]. As a starting point toward a better understanding of breast cancer, it is important to know how cancer in general develops. Cancers occur when control of the division of normal cells is lost and they start to invade other healthy tissues which takes place when a single cell or a group of cells escapes from the usual control that regulates cellular growth when they start to multiply, spread and form a mass. When the mass is formed, it can be considered benign or malignant depending on its shape and behavior. When abnormal growth is restricted to a single and circumscribed mass of cells, it is known as benign. The term “cancer” is used to describe malignant masses which not only can invade surrounding tissues but also can spread or “metastasize” to distant areas of the body. When the breast masses reach a palpable size, this means that they are metastasized [2]. Properties such as margins and shapes help to define masses. For instance, masses with round and smooth margins indicate that they are benign while malignant masses have speculated, rough or blurry boundaries [3].

* Corresponding author: hasanguler@firat.edu.tr. ORCID Number of authors: [1] 0009-0001-2437-7262, [2] 0000-0002-9917-3619

The stages of breast cancer can be classified into three stages depending on the danger and the distance between cancer cells and the original tumor; local breast cancer, regional breast cancer, and distant breast cancer. In the first stage, breast cancer is still local. The cancer is still located inside the breast in lobules and ducts and it is not invading the neighborhood tissues. In other words, the normal tissues beyond the breast are not affected by this type of breast cancer [4]. The second stage of breast cancer is regional breast cancer. This stage occurs when the cancer cells start the invasion of neighbor tissues and try to reach the underarm lymph nodes. The lymph nodes are small organs that filter the body from foreign substances. The lymphatic system consists of lymph nodes and ducts that form a network. Its main work is to fight against the foreign substances in the body and filter them [5]. In the third stage, which is termed distant breast cancer, cancer cells are invasive and get into the lymph nodes. They also have a pathway into other parts of the body such as lungs, distant lymph nodes, skin, bones, liver, and brain [6].

The benign masses are considered to be in the first stage of breast cancer stages because they cannot metastasize and lack the invasive properties of cancer. Although benign masses can have side effects many kinds of this type of mass are not harmful to human health conditions and they are not life-threatening. The malignant masses are considered to be the second and third stages of breast cancer stages because they are not self-limited in growth. They have the capability of invading the neighboring tissues around the breast and spreading to distant regions of the body. Therefore, the term “cancer” is used for malignant masses which are usually more serious and more dangerous for human health condition.

The paper is organized into the following sections: The related work is determined in section 2, section 3 material and methods introduce the methods used in developed algorithms, in section 4, the results are given and the last section concludes the whole paper.

2. Related Works

Many scientists studying computer science, especially artificial intelligence, are working to detect cancerous cells in the early stages [7-19]. It is observed that mortality tends to decrease in line with the early detection studies that have increased in recent years [7]. Studies in which artificial intelligence methods such as machine learning are widely used determine with high accuracy in the diagnosis and prediction of various diseases such as breast cancer. The comparison of different approaches developed by many scientists in cancer detection can be seen in Table 1.

Table 1. Comparison of different approaches in cancer detection and classification.

Reference	Database	Segmentation	Classification	Results
[8]	DDSM	Texture based	Clustering	93%
[9]	MIAS	Watershed	SVM	98%
[10]	MIAS	Gabor Filter	k-means	99%
[11]	-	Entropy, mean, energy	ANN	90%
[12]	-	Statistical parameters	Triangulation	99.16%
[13]	WDBC	PCA	SVM, KNN	SVM-51.10% KNN-91.11%
[14]	WDBC	texture	SVM, NB	97.13%
[15]	WDBC	Accuracy, sensitivity	SVM	99.51%
[16]	DDSM cases	Texture descriptors	SVM	75%
[17]	WDBC	Sensitivity and specificity	MLP, NN, SVM	99.04%
[18]	MIAS	DCT and DWT	SVM	96.97%
[19]	WDBC	Wrapper method	SVM, KNN	SVM-97.18% KNN-95.12%

The authors of [8] proposed a machine-learning algorithm for extraction and clustering. While doing this, texture analysis was done for feature extractions. Another study [9] used SVM (Support Vector Machine) classifier for breast cancer detection. They reported 98% accuracy in their study. In [10], the authors presented a novel

approach to breast cancer. They used threshold parameters to differentiate pixels of cancer regions. An automated technique using ANN (Artificial Neural Network) was proposed in [11]. Inputs of ANN were selected as entropy, mean, energy correlation, texture, and standard deviation, while ANN detects whether an image is cancerous or not.

The other study [12] used different algorithms in image segmentation, triangulation, binarizations, thinning, and Euclidean distance transformation in the detection of the cancer cell. Habib Dhahri et al [13] built an automated machine-learning workflow to optimize the list of data transformations. They proposed a genetic algorithm to optimize the data and control parameters.

A comparison for performance among various machine learning algorithms such as support vector machine (SVM), decision tree, k-nearest neighbors (k-NN), and naïve bayes was given in [14-19]. The authors declared that SVM gave the highest performance when considered with accuracy.

There are some classes of abnormalities found after the mammography images are taken. Expert radiologists can determine the type of abnormality just from its appearance and then they can determine whether the mass in the mammography image is benign or malignant mass. Breast cancer screening mammograms found these types of abnormalities: calcification (i.e., macro and micro-calcifications), spiculated masses, well-defined/circumscribed masses, architectural distortion, asymmetry breast tissues, and other miscellaneous findings [3]. In mammography images, the appearance of micro-calcifications looks like large white dots distributed randomly within the breast. It is found that half of the women over 50 and 10 women under that age have macro-calcifications in their breasts. Macro-calcifications are considered noncancerous and for that reason no need to do follow-up care [6]. Although Micro-calcifications are usually not an indicator or result of breast cancer, they can become dangerous when they are clustered in a group and appear in a certain pattern, when they are grouped, they are considered a starting indicator of breast cancer.

If calcifications are detected in the breast, doctors categorize them into three types to be treated. The first category is benign calcifications which are considered harmless and no need to do treatment for them. Another is probably benign calcifications. It is found that more than 98% of this type is noncancerous. Typically, they are monitored every six months for at least one year. If there is no change found after a year of follow-up, the doctor's recommendation is to have a routine mammogram once a year [6]. A spiculated mass is considered the most dangerous class of abnormality since it is one of the primary indicators of cancer [20]. This type of mass can be anywhere inside the human body but is often found in breasts or lungs. When these spiky masses are found anywhere inside the body even in the breasts doctor's recommendation is to give a biopsy to confirm whether they are malignant or benign. If they are malignant, the treatment can range from excision to radiation.

Well-defined/circumscribed masses are another class of abnormalities found in breast cancer screening and mammography. Another term that can be used for this type of mass is circumscribed carcinoma. This term refers to ductal carcinoma that appears as circumscribed on a mammogram. Although circumscribed carcinoma is less frequently seen than typical spiculated carcinoma, it has both types of severity of abnormality benign and malignant. Circumscribed carcinoma includes medullary, invasive ductal carcinoma, and other types [21]. Architectural distortion is the last class of abnormalities discussed in this chapter. It is considered the third most common class of abnormalities according to its appearance. It is found that 6% of abnormalities have this type. The incidence of architectural distortion is small compared to calcifications and visible mass. However, when it exists in the mammography image, it is difficult to be detected and diagnosed because of its variability in presentation [22]. A scar inside the breast formed from a previous surgery that is benign can be interpreted as architectural distortion. Although the reason for architectural distortion can be a result of benign disease, it is found that almost 80% of the detected masses are a result of invasive breast cancer [22]. The appearance of architectural distortion in mammography images seems like a disruption in the structure of the breast itself. The most interesting thing in this class of abnormality is that there is no mass to indicate and name it abnormal mass but the distortion appears as a stellate shape or with radiating speculation like the masses found in speculation cases.

Nowadays, many effective methods and devices are developed for detecting breast cancer. These methods are X-ray mammography, ultrasonography, trans-illumination, thermography, Computed Tomography (CT), and Magnetic Resonance Imaging (MRI) all of which are used for breast cancer diagnosis. It has been found that X-ray mammography is the best and the most effective method used for detecting breast cancer [23]. A mass is a lesion that occupies a space in the breast and it can be seen on at least two projections or viewpoints (Carnio-caudal CC and mediolateral-oblique MLO). The view of a mammogram of Carnio-caudal CC is taken from above while the view of a mammogram of mediolateral-oblique MLO is taken as an oblique or angled view [24].

3. Material and Methods

Materials are the database and the programming language used for designing the system, Mammographic Image Analysis Society (MIAS) database images are chosen to be used in the system, 62.5% of the data set (133 images) was selected for training, 37.5% of that (80 images) is chosen and used to test in the system [25]. The developed algorithm was created using the LabVIEW platform, which is a graphic code-based software. The reason why this platform is preferred is the ease of creating a user interface and the effort to create a new algorithm by creating completely mathematical expressions by ourselves instead of using the ready-made toolbox structure of machine learning algorithms, unlike the studies done so far.

In the image processing stage, image enhancement methods are implemented to process the image to make the result more suitable than the original image as shown in Fig.1. It brings out some features in the region of interest that are invisible or difficult to notice in the original image. Image enhancement techniques include histograms, image filtering, thresholding, morphological operations, removing undesired parts, and region segmentation.

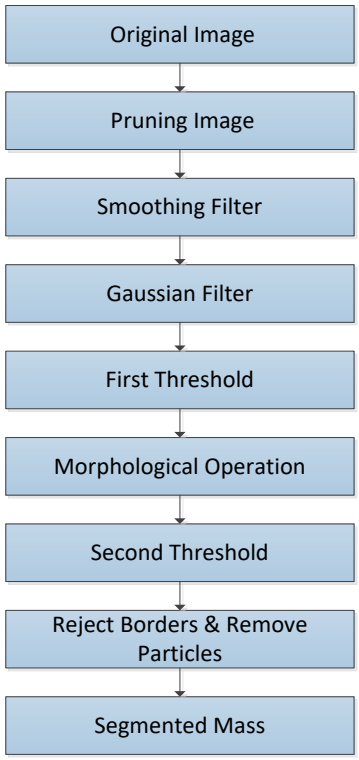

Figure 1. The steps of the Image Processing and Mass Segmentation Stage.

The histogram of a digital image in general is a discrete function that represents the number of pixels in each different gray level which is called the intensity level. It can be written as follows in Equation 1:

$$h(r_k) = n_k \tag{1}$$

Where r_k represents the k^{th} gray level and n_k is the number of pixels in an image having an intensity level r_k in equation 1. The range of intensity level for the 8-bit grayscale image will be [0, L-1]; i.e., the range will be [0 - 255] since$L = 2^k$. The histogram can be normalized and its range becomes [0 - 1] according to:

$$P(r_k) = n_k/n \tag{2}$$

Where n is the total number of pixels in the image in equation 2.

Kernel family filters contain four types of matrixes that can be used as different filters on the images which each type has some different sizes of the matrix such as (3*3, 5*5, and 7*7), the types are; Gradient, Laplacian, Smoothing, and Gaussian.

Thresholding is a simple method used for segmenting the breast in the mammography image. It is called global since it is based on the global information of the image like a histogram and a single threshold value is selected for the whole image. The global threshold value can be found easily because the intensity values of the abnormality regions are greater than the surrounding tissue [26]. It can be expressed as follows in Equation 3:

$$g(x,y) = \begin{cases} 1 & \text{if } f(x,y) \geq T \quad (ROI - Breast) \\ 0 & \text{Otherwise} \quad (Background) \end{cases} \tag{3}$$

Morphological operations are very useful in image processing for extracting, describing, and improving the shapes of regions of interest. They can be used in pre-processing and post-processing operations. Most of the time, morphological operations are used in binary images since they rely on the relative ordering of pixels and not on their numerical values [27]. Dilation and erosion are the two major morphological operations used in this work and most of the research done so far [28]. Opening and closing are two morphological operations resulting from the two basic morphological operations of dilation and erosion. They are a combination of dilation and erosion. The opening is an erosion operation followed by dilation while the closing is a dilation operation followed by erosion [29]. The expression of Dilation, Erosion, Opening and Closing respectively are as the following in Equation 4a-4d:

$$A \oplus B = \left\{ z \mid \left(\widehat{B}\right)_z \cap A \neq \emptyset \right\} \tag{4a}$$

$$A \ominus B = \{ z \mid (B)_z \subseteq A \} \tag{4b}$$

$$A \circ B = (A \ominus B) \oplus B \tag{4c}$$

$$A \bullet B = (A \oplus B) \ominus B \tag{4d}$$

In LabVIEW there are two block diagrams for rejecting borders and removing particles in the image, rejecting border can be used for rejecting the pectoral muscle and the sticker in some images, else, the removing particles are for removing all small bright particles in the image except the suspicious mass, so in this way, the mass is segmented separated from all other parts of the image and background. Image processing and mass segmentation are done, and now some features can be selected and extracted from the mass, there are seven features selected and extracted from the suspicious mass that can be used as input for the classifier. The seven features are Contrast, Standard Deviation, Mean Intensity, Skewness, Entropy, Smoothness, and Uniformity. The expressions of the features from Standard Deviation to Uniformity respectively are as the following in equation 5a, 5b, 5c, 5d, 5e and 5f.

$$\sigma = \sqrt{\mu_2(z)} = \sqrt{\sigma^2} \tag{5a}$$

$$m = \sum_{i=0}^{L-1} z_i \, p(z_i) \tag{5b}$$

$$\mu_3 = \sum_{i=0}^{L-1} (z_i - m)^3 \, p(z_i) \tag{5c}$$

$$e = \sum_{i=0}^{L-1} p(z_i) \log_2 p(z_i) \tag{5d}$$

$$R = 1 - \frac{1}{1+\sigma^2} \tag{5e}$$

$$U = \sum_{i=0}^{L-1} P^2(z_i) \tag{5f}$$

All seven features are used as an input to be fed into the classifier to classify the mass; ANN and SVM which are ones of the machine learning methods and whose competencies in scientific studies are accepted were used in the classifier part of the system.

ANN is a classifier whose construction is composed of mathematical models similar to the nervous system [26]. ANN is a classifier used to determine whether the segmented suspected mass is benign or malignant according to the extracted features. Its construction is composed of mathematical models and algorithms similar to the nervous system of humans. The construction of ANN is three main layers; the Input layer, Hidden layers, and Output layer, as shown in Fig. 2.

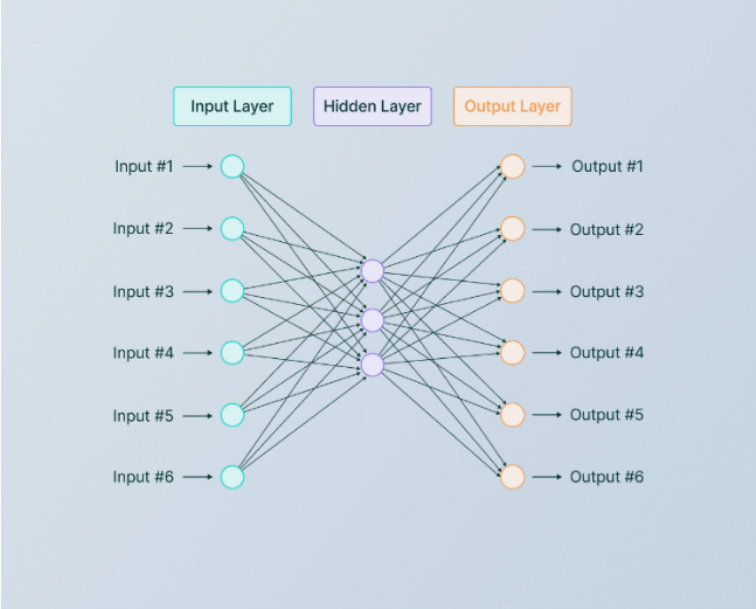

Figure 2. ANN simple Architecture.

One of the machine learning methods, SVM, also known as support vector networks, is a classification method with supervised learning algorithms that evaluate the data used for classification and regression analysis and recognize these patterns. Fig. 3 shows how SVM classifies benign and malignant masses in breast cancer [7].

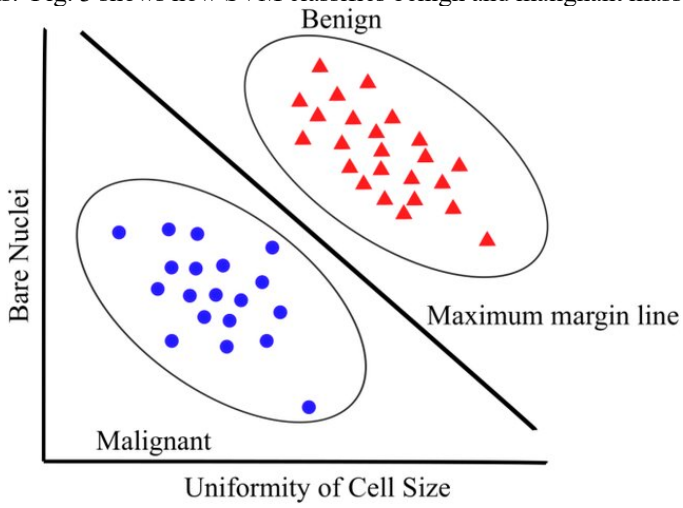

Figure 3. Demonstration of how SVM classifies benign and malignant masses in breast cancer.

The developed algorithm in the LabVIEW platform has some sub-VIs that are used to make the program work faster and easier. In the algorithm, there are five sub-VI GUIs. The GUI of the image processing and segmentation's sub-VI is given in Fig. 4.

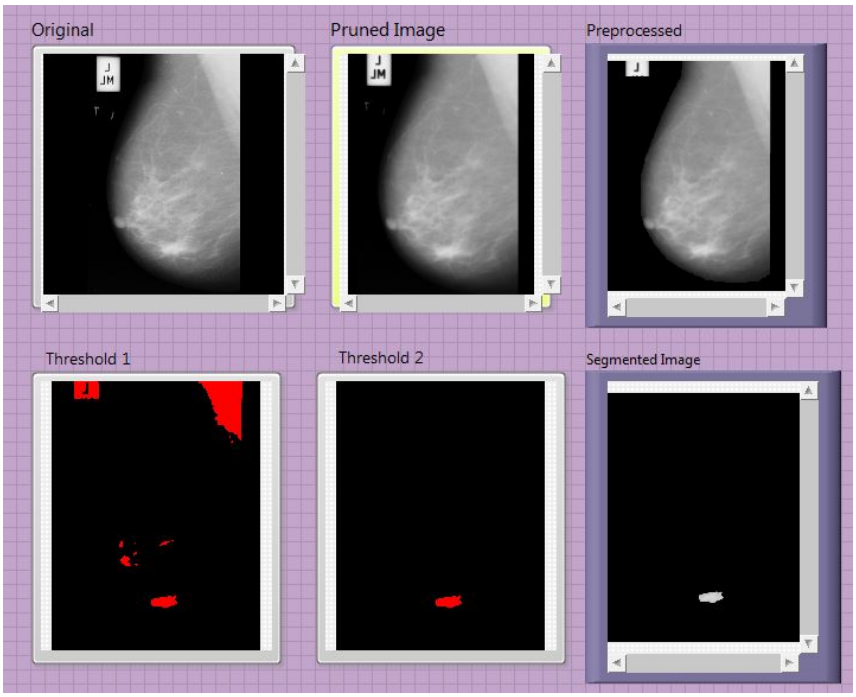

Figure 4. Image processing and Segmentation GUI.

After getting the segmented mass in the image which is the tumor of the breast, now it turns to finding its features of it for analysis and using them in the classification process. The features are Standard Deviation, Mean Intensity, Contrast, Skewness, Entropy, Smoothness, and Uniformity.

All the images in the database have to be trained to get their features, the result of every single image for all of the seven features will be like a table or like a matrix that can be safe as an excel file. For the classification stage, the ANN and SVM model can be used, and the options for input layers, hidden layers, and output layers can be chosen here for later to get the best result. The block diagrams and front panel of the last sub-VIs are shown in Fig 5-7.

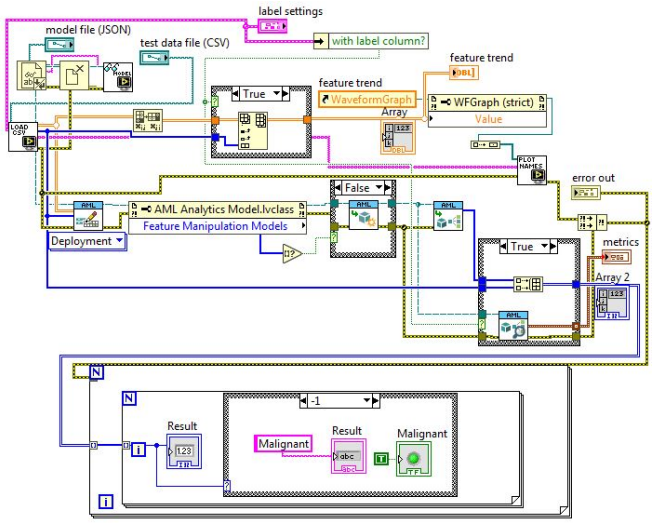

Figure 5. ANN Classification (block diagram).

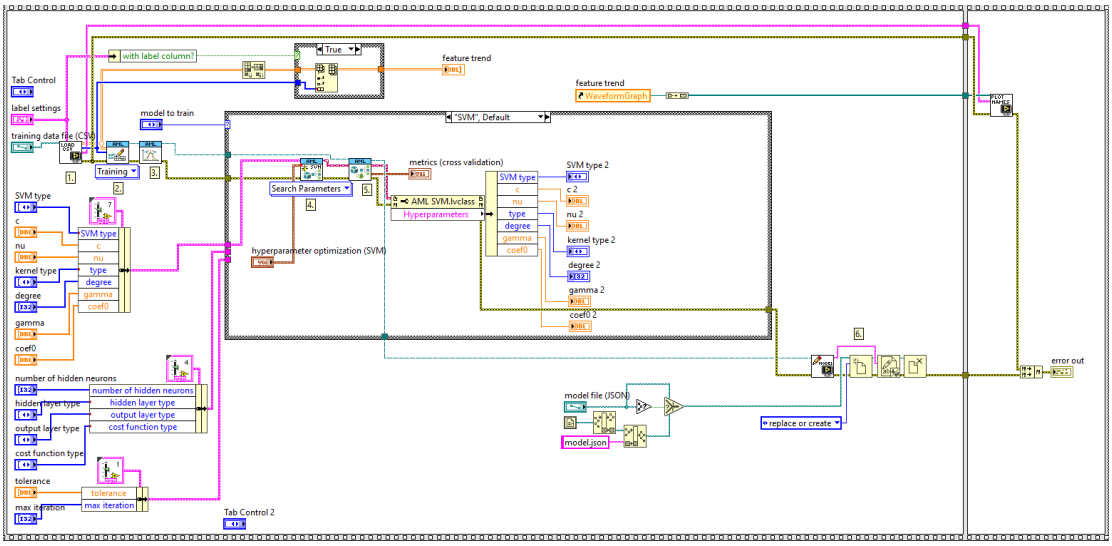

Figure 6. SVM classification (block diagram).

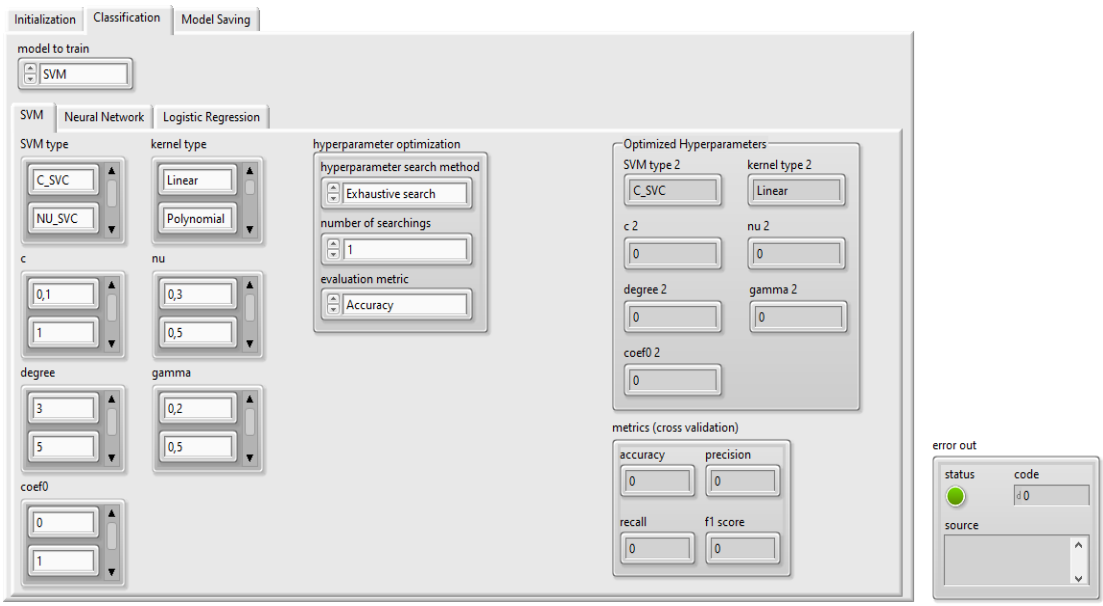

Figure 7. GUI screen for classification (front panel diagram).

With these created sub-VIs, the user will be able to determine whether the mass in the mammogram image is benign or malignant with 2 types of classification methods, which are ANN and SVM. The block diagrams given in Fig. 5 and 6 were created according to the mathematical forms of ANN and SVM algorithms.

4. Results

After applying all of the image processing algorithms one by one, a series of images are established which are shown in Fig. 8-10. The selected and extracted features from the segmented mass are shown in Table 2 and Table 3 with the result of classification with ANN and in Table 4 and Table 5 with the result of classification with SVM. The result of system classification is also compared with the provided results of the database reference, which is discussed more in the discussion section to show the efficiency of the system.

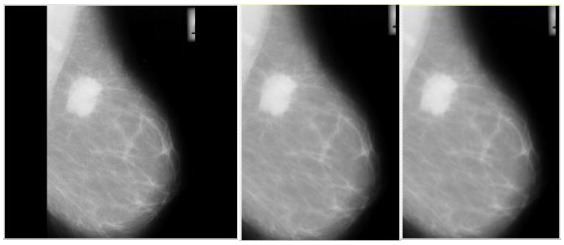

Figure 8. Original Image, Pruned Image, Applying smoothing filter on the Image.

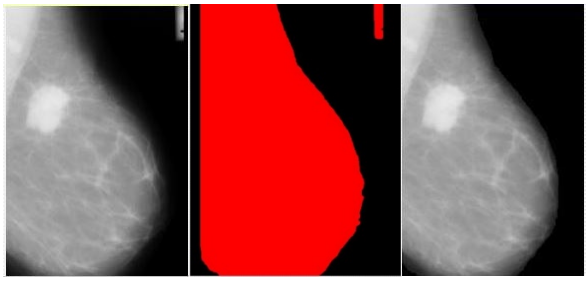

Figure 9. Applying Gaussian Filter on the Image, First Thresholding of the Image, Applying Morphological Operations on the Image.

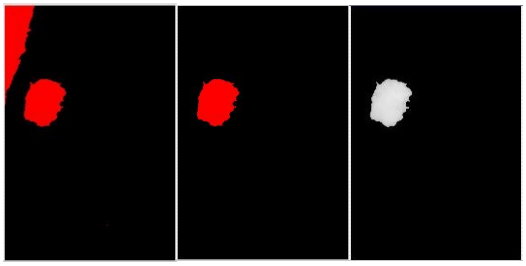

Figure 10. Second Thresholding of the Image, Removing all Undesired Parts, Segmented Mass.

The block diagram and front panel of the main program from which the 5 developed sub-VIs are run are shown in Fig. 11 and 12. In the block diagram, figure all three main stages are obvious to notice with the help of using sub-VI; Image processing and segmentation, Feature extraction, and Classification.

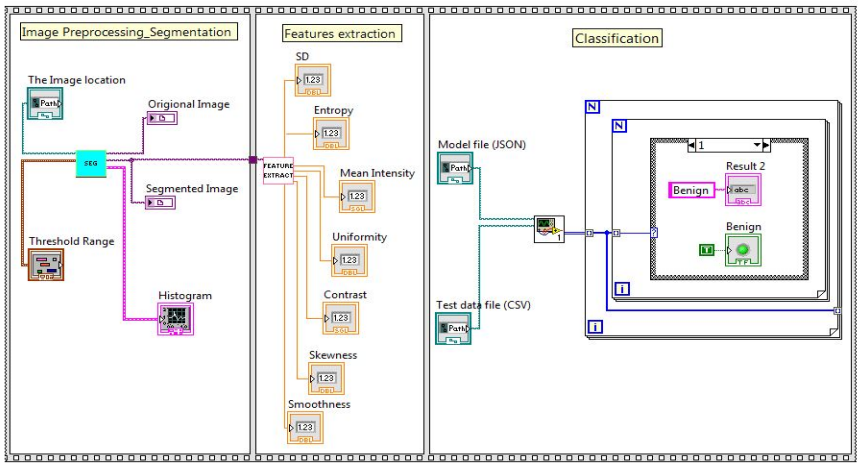

Figure 11. Main VI (block diagram).

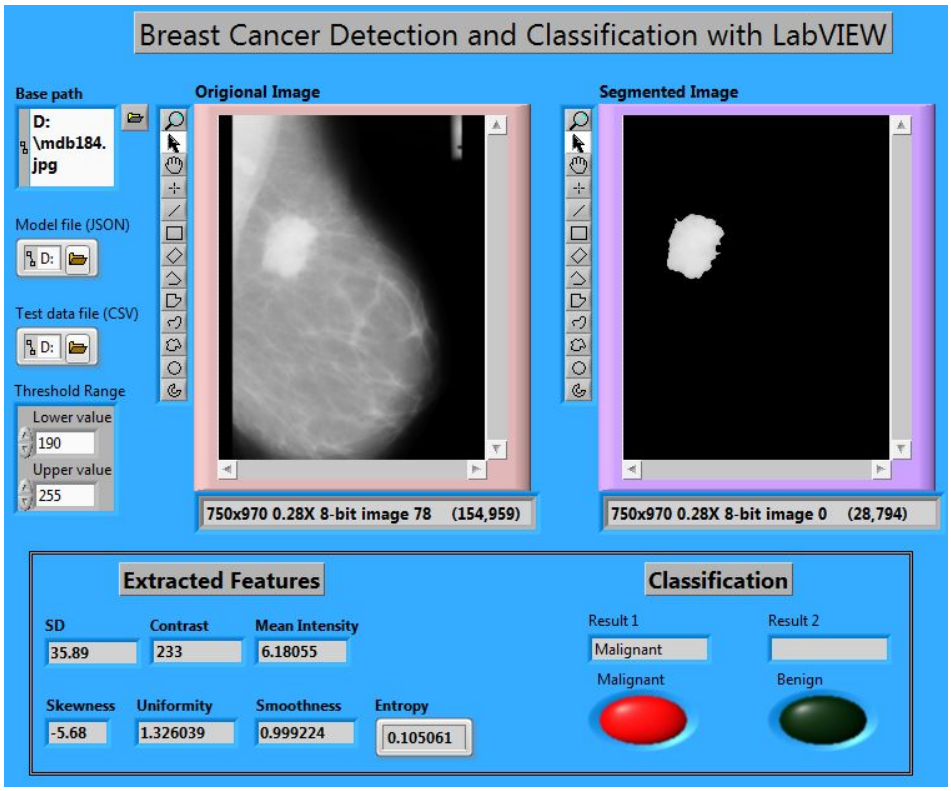

Figure 12. The developed main GUI.

From the database 62.5% of dataset images are trained into the system then the remained part of 37.5% which equals 80 images (40 benign and 40 malignant) are set to be test data. There is a matrix called the confusion matrix that shows the percentage of the correct result of any system, the matrix and the meaning of each element in the matrix is shown in Table 6 and in Equation 6.

From the database 62.5% of dataset images are trained into the system then the remained part of 37.5% which equals 80 images (40 benign and 40 malignant) are set to be test data. There is a matrix called the confusion matrix that shows the percentage of the correct result of any system, the matrix and the meaning of each element in the matrix is shown in Table 6 and in Equation 6.

$$\text{Confusion Matrix} = \begin{bmatrix} \text{TN} & \text{FN} \\ \text{FP} & \text{TP} \end{bmatrix} \tag{6}$$

Table 2. Extracted features from 40 benign images.

Image	Selected and Extracted Features							Classification with ANN	
Ref No.	Standard Deviation	Contrast	Mean Intensity	Skewness	Uniformity	Smoothness	Entropy	Original	Estimated
mdb010	27.128	4.51	199	-6.003	0.999	0.756	0.095	B	B
mdb013	45.602	11.325	221	-3.826	1	2.208	0.184	B	B
mdb015	13.488	0.95	205	-14.309	0.995	0.183	0.021	B	B
mdb017	23.049	2.849	204	-8.091	0.998	0.539	0.054	B	B
mdb021	33.892	6.583	203	-5.047	0.999	1.192	0.123	B	B
mdb025	11.156	0.661	198	-17.056	0.992	0.125	0.014	B	B
mdb080	15.194	1.467	186	-10.5	0.996	0.233	0.038	B	B
mdb081	42.052	8.923	229	-4.539	0.999	1.848	0.15	B	B
mdb083	13.041	0.861	216	-15.303	0.994	0.171	0.019	B	B
mdb091	9.262	0.513	179	-18.336	0.988	0.086	0.013	B	B
mdb099	11.778	0.739	207	-16.169	0.993	0.139	0.017	B	B
mdb104	16.755	1.429	209	-11.76	0.996	0.283	0.028	B	B
mdb121	42.736	9.521	228	-4.309	0.999	1.917	0.16	B	B
mdb126	67.676	26.88	223	-2.157	1	5.303	0.388	B	B
mdb127	9.387	0.47	205	-20.301	0.989	0.088	0.011	B	B
mdb132	10.648	0.654	198	-16.518	0.991	0.114	0.018	B	B
mdb133	12.208	0.963	177	-12.954	0.993	0.15	0.026	B	B
mdb145	35.345	6.49	221	-5.323	0.999	1.291	0.115	B	B
mdb150	21.636	2.677	201	-8.047	0.998	0.475	0.058	B	B
mdb160	13.221	0.986	199	-13.638	0.994	0.176	0.024	B	B
mdb165	26.676	3.902	202	-6.739	0.999	0.727	0.073	B	B
mdb175	16.325	1.416	211	-11.636	0.996	0.269	0.03	B	B
mdb193	39.274	7.708	225	-4.936	0.999	1.602	0.123	B	B
mdb195	10.911	0.6	210	-18.427	0.992	0.119	0.013	B	B
mdb198	20.243	2.045	216	-9.908	0.998	0.414	0.039	B	B
mdb199	20.026	2.108	210	-9.522	0.998	0.405	0.043	B	B
mdb204	16.085	1.555	186	-10.473	0.996	0.261	0.037	B	B
mdb207	33.965	6.061	218	-5.479	0.999	1.19	0.107	B	B
mdb218	**34.461**	**6.102**	**223**	**-5.529**	**0.999**	**1.225**	**0.109**	**B**	**M**
mdb219	14.084	1.119	201	-12.807	0.995	0.2	0.027	B	B
mdb222	36.359	6.666	219	-5.318	0.999	1.366	0.107	B	B
mdb227	8.847	0.427	199	-21.162	0.987	0.078	0.01	B	B
mdb236	66.086	24.124	222	-2.404	1	4.949	0.325	B	B
mdb244	57.904	17.46	229	-3.047	1	3.658	0.254	B	B
mdb248	11.496	0.748	190	-15.602	0.992	0.133	0.018	B	B
mdb252	17.052	1.85	179	-9.308	0.997	0.294	0.045	B	B
mdb290	36.166	7.098	209	-4.931	0.999	1.358	0.126	B	B
mdb312	10.629	0.58	212	-18.689	0.991	0.113	0.013	B	B
mdb314	16.506	1.633	194	-10.263	0.996	0.275	0.039	B	B
mdb315	48.575	11.686	229	-3.942	1	2.496	0.176	B	B

Table 3. Extracted features from 40 malignant images.

Image	**Selected and Extracted Features**							**Classification with ANN**	
Ref No.	Standard Deviation	Contrast	Mean Intensity	Skewness	Uniformity	Smoothness	Entropy	Original	Estimated
mdb023	21.716	2.405	217	-9.07	0.998	0.477	0.046	M	M
mdb028	**18.364**	**1.696**	**214**	**-10.82**	**0.997**	**0.34**	**0.034**	**M**	**B**
mdb058	9.163	0.453	208	-20.71	0.988	0.084	0.011	M	M
mdb072	23.955	2.789	226	-8.558	0.998	0.582	0.052	M	M
mdb075	7.099	0.348	227	-21.42	0.981	0.051	0.012	M	M
mdb092	9.541	0.539	184	-17.99	0.989	0.091	0.014	M	M
mdb095	21.397	2.451	212	-8.811	0.998	0.464	0.052	M	M
mdb102	22.438	2.5	221	-8.982	0.998	0.51	0.048	M	M
mdb105	87.503	42.187	241	-1.605	1	9.437	0.515	M	M
mdb110	25.033	3.08	222	-8.075	0.998	0.636	0.056	M	M
mdb111	31.75	4.969	224	-6.283	0.999	1.033	0.084	M	M
mdb120	21.959	2.578	211	-8.555	0.998	0.489	0.052	M	M
mdb125	49.339	13.209	219	-3.512	1	2.609	0.212	M	M
mdb130	28.315	4.045	220	-6.944	0.999	0.818	0.071	M	M
mdb134	**13.344**	**0.953**	**202**	**-14.09**	**0.994**	**0.179**	**0.022**	**M**	**B**
mdb141	25.657	3.995	187	-6.384	0.998	0.674	0.082	M	M
mdb148	56.235	19.102	221	-2.649	1	3.527	0.327	M	M
mdb171	87.781	42.626	239	-1.587	1	9.523	0.512	M	M
mdb178	33.406	6.064	220	-5.408	0.999	1.153	0.117	M	M
mdb179	29.169	3.779	240	-7.736	0.999	0.865	0.05	M	M
mdb181	34.233	7.356	202	-4.516	0.999	1.226	0.152	M	M
mdb184	35.887	6.181	233	-5.681	0.999	1.326	0.105	M	M
mdb202	42.386	10.128	214	-4.008	0.999	1.899	0.18	M	M
mdb206	30.373	5.892	189	-5.026	0.999	0.957	0.129	M	M
mdb209	38.634	8.318	212	-4.476	0.999	1.562	0.155	M	M
mdb211	49.636	14.046	222	-3.293	1	2.661	0.247	M	M
mdb213	28.255	5.216	181	-5.283	0.999	0.826	0.113	M	M
mdb216	83.16	39.91	236	-1.624	1	8.508	0.511	M	M
mdb231	19.055	2.651	161	-7.218	0.997	0.37	0.07	M	M
mdb233	35.512	7.878	202	-4.339	0.999	1.323	0.165	M	M
mdb238	34.318	7.599	188	-4.364	0.999	1.235	0.151	M	M
mdb239	75.957	31.058	233	-2.056	1	6.734	0.379	M	M
mdb241	42.164	9.494	214	-4.247	0.999	1.868	0.152	M	M
mdb245	24.639	3.617	210	-6.81	0.998	0.62	0.079	M	M
mdb249	21.092	2.301	212	-9.17	0.998	0.45	0.046	M	M
mdb253	84.173	43.274	223	-1.448	1	8.958	0.51	M	M
mdb256	53.043	16.436	221	-2.955	1	3.084	0.283	M	M
mdb270	23.252	3.103	231	-7.478	0.998	0.55	0.065	M	M
mdb271	24.133	3.298	215	-7.337	0.998	0.593	0.074	M	M
mdb274	13.378	1.238	166	-10.87	0.994	0.181	0.035	M	M

Table 4. Extracted features from 40 benign images.

Image	Selected and Extracted Features							Classification with SVM	
Ref.No.	Standard Deviation	Contrast	Mean Intensity	Skewness	Uniformity	Smoothness	Entropy	Original	Estimated
mdb010	28.352	4.245	211	-4.544	0.997	0.781	0.277	B	B
mdb013	49.446	11.416	219	-4.093	0.999	1.881	0.347	B	B
mdb015	9.541	0.539	184	-17.996	0.989	0.091	0.014	B	B
mdb017	21.397	2.451	212	-8.811	0.998	0.464	0.052	B	B
mdb021	23.955	2.789	226	-8.558	0.998	0.582	0.052	B	B
mdb025	9.541	0.539	184	-17.996	0.989	0.091	0.014	B	B
mdb080	12.525	4.219	219	-16.62	0.989	0.473	0.428	B	B
mdb081	29.316	7.521	218	-8.819	0.999	1.778	0.286	B	B
mdb083	61.764	22.34	229	-4.571	1	7.083	0.186	B	B
mdb091	28.817	4.78	245	-10.901	0.991	0.481	0.16	B	B
mdb099	19.448	8.641	228	-11.184	0.998	0.148	0.182	B	B
mdb104	21.081	3.639	217	-2.544	0.995	0.157	0.216	B	B
mdb121	31.445	16.94	229	-8.213	0.999	0.991	0.215	B	B
mdb126	31.102	18.744	214	-3.747	0.995	0.574	0.318	B	B
mdb127	11.271	7.846	199	-9.311	0.999	1.716	0.032	B	B
mdb132	19.746	11.042	219	-4.397	0.999	0.924	0.113	B	B
mdb133	14.215	9.406	217	-10.506	0.996	0.226	0.029	B	B
mdb145	**42.278**	**8.018**	**223**	**-6.436**	**0.998**	**2.101**	**0.147**	**B**	**M**
mdb150	19.181	0.614	202	-14.872	0.998	0.685	0.214	B	B
mdb160	12.345	8.051	218	-10.058	0.997	0.149	0.111	B	B
mdb165	19.824	7.203	213	-7.282	0.998	0.630	0.023	B	B
mdb175	11.113	1.335	196	-15.730	0.996	0.162	0.037	B	B
mdb193	24.605	4.064	210	-6.709	0.999	1.911	0.117	B	B
mdb195	12.515	5.029	219	-10.605	0.998	0.181	0.181	B	B
mdb198	14.134	6.411	213	-6.487	0.995	0.562	0.154	B	B
mdb199	17.536	10.022	201	-9.913	0.998	3.461	0.125	B	B
mdb204	36.515	5.216	181	-5.283	0.999	0.826	0.113	B	B
mdb207	83.16	39.91	236	-1.624	1	8.508	0.511	B	B
mdb218	19.055	2.651	161	-7.218	0.997	0.387	0.171	B	B
mdb219	35.512	5.178	212	-6.329	0.998	1.213	0.145	B	B
mdb222	34.318	7.599	188	-4.364	0.999	1.235	0.151	B	B
mdb227	43.547	30.858	231	-2.156	1	7.004	0.297	B	B
mdb236	34.614	19.412	218	-5.417	0.999	3.467	0.124	B	B
mdb244	12.319	13.110	212	-4.189	0.998	0.171	0.201	B	B
mdb248	12.982	8.051	219	-6.174	0.998	1.544	0.096	B	B
mdb252	78.713	34.714	223	-5.143	0.999	5.518	0.391	B	B
mdb290	56.043	12.136	214	-3.505	0.999	2.405	0.125	B	B
mdb312	20.512	13.033	229	-6.481	0.998	1.155	0.241	B	B
mdb314	9.312	9.418	210	-4.133	0.998	0.183	0.014	B	B
mdb315	18.748	11.481	185	-14.711	0.993	0.221	0.150	B	B

Table 5. Extracted features from 40 malignant images.

Image	**Selected and Extracted Features**							**Classification with SVM**	
Ref.No.	Standard Deviation	Contrast	Mean Intensity	Skewness	Uniformity	Smoothness	Entropy	Original	Estimated
mdb023	12.161	10.402	203	-5.283	0.999	2.241	0.152	M	M
mdb028	19.121	8.318	198	-7.624	0.996	0.896	0.121	M	M
mdb058	34.171	5.216	186	-1.218	0.997	1.011	0.177	M	M
mdb072	11.891	10.401	229	-4.339	0.998	1.805	0.366	M	M
mdb075	14.425	6.851	216	-4.364	0.999	0.412	0.118	M	M
mdb092	12.849	9.003	179	-2.056	0.998	0.458	0.365	M	M
mdb095	12.135	10.315	207	-11.121	0.998	0.099	0.145	M	M
mdb102	44.054	8.604	209	-7.419	1	0.891	0.312	M	M
mdb105	32.199	9.211	228	-4.471	0.999	0.955	0.114	M	M
mdb110	21.899	3.199	219	-14.416	0.997	0.129	0.123	M	M
mdb111	18.896	9.218	199	-8.181	0.999	1.611	0.163	M	M
mdb120	43.125	4.156	222	-5.108	0.998	1.363	0.178	M	M
mdb125	48.111	11.189	229	-5.214	0.999	5.414	0.499	M	M
mdb130	23.236	8.511	190	-1.287	0.997	2.487	0.189	M	M
mdb134	52.811	7.188	179	-9.629	0.998	2.011	0.196	M	M
mdb141	11.789	4.919	209	-6.344	0.999	0.395	0.163	M	M
mdb148	13.417	3.058	212	-5.256	1	4.489	0.275	M	M
mdb171	23.124	9.779	187	-8.017	0.999	1.955	0.201	M	M
mdb178	28.895	10.044	221	-8.849	0.998	1.718	0.255	M	M
mdb179	23.619	13.559	239	-3.316	0.999	1.611	0.102	M	M
mdb181	41.343	4.564	220	-9.156	0.999	2.428	0.132	M	M
mdb184	19.187	8.401	240	-8.851	1	3.216	0.458	M	M
mdb202	33.486	8.112	202	-7.818	0.999	4.191	0.211	M	M
mdb206	38.713	4.912	233	-6.201	0.998	1.045	0.254	M	M
mdb209	31.437	6.141	214	-2.145	0.999	2.612	0.176	M	M
mdb211	59.165	11.614	219	-11.003	1	3.866	0.321	M	M
mdb213	**18.957**	**9.916**	**212**	**-8.455**	**0.999**	**1.058**	**0.199**	**M**	**B**
mdb216	45.146	31.141	201	-5.244	0.997	6.004	0.301	M	M
mdb231	29.857	12.531	161	-5.811	0.997	1.778	0.457	M	M
mdb233	18.521	6.689	202	-4.352	0.999	3.653	0.257	M	M
mdb238	49.418	8.402	188	-4.619	0.999	2.514	0.326	M	M
mdb239	35.757	19.518	233	-3.151	1	4.437	0.233	M	M
mdb241	27.764	19.944	214	-2.141	0.999	3.618	0.304	M	M
mdb245	21.139	13.117	210	-1.991	0.998	1.121	0.039	M	M
mdb249	29.491	8.871	228	-6.571	0.998	1.415	0.099	M	M
mdb253	74.713	31.714	219	-10.844	1	4.257	0.465	M	M
mdb256	61.413	9.036	199	-7.544	0.998	5.104	0.196	M	M
mdb270	29.212	13.013	228	-4.718	0.999	1.956	0.132	M	M
mdb271	20.983	7.281	219	-6.157	0.998	4.913	0.156	M	M
mdb274	18.718	5.381	231	-9.711	0.995	3.801	0.099	M	M

Table 6. Measured and meaning of each part in the confusion matrix.

Measures	Meaning
True Negative (TN)	The mass is defined as benign by biopsy and is also classified as benign by the neural network.
False Negative (FN)	The mass is defined as malignant by a biopsy but it is classified as benign by the neural network.
False Positive (FP)	The mass is defined as benign by a biopsy but it is classified as malignant by the neural network.
True positive (TP)	The mass is defined as malignant by a biopsy and is also classified as malignant by the neural network.

After training and testing all 80 images, the results of the confusion matrix of ANN and SVM are as the following in Equation 7 and 8:

for ANN:

$$\text{Confusion Matrix} = \begin{bmatrix} 39 & 2 \\ 1 & 38 \end{bmatrix} \tag{7}$$

for SVM:

$$\text{Confusion Matrix} = \begin{bmatrix} 39 & 1 \\ 1 & 39 \end{bmatrix} \tag{8}$$

When examing Table 2 and Table 3, the missed images for ANN are the image with the reference number (mdb028 - mdb134) that are measured as a false negative, the misinterpreted image is the image with the reference number of (mdb218) that is measured as false positive. Also, while examing Table 4 and Table 5, the missed images for SVM are the image with the reference number (mdb213) that are measured as a false negative, the misinterpreted image is the image with the reference number of (mdb145) that is measured as false positive.

It is not good for the system to have a high value in FN and FP so to have an accurate diagnosis, the values of FN and FP should be small because a high value of FN means that malignant masses are missed in the handling process and high value of FP means that benign masses are misinterpreted as cancer. The obtained confusion matrix indicates some important performance measuring of the neural network classifier. These measures are sensitivity, specificity, and accuracy. They can be measured by the following expressions in equation 9a, 9b and 9c:

$$\text{Sensitivity} = \frac{\text{TP}}{\text{TP+FN}} \tag{9a}$$

$$\text{Specificity} = \frac{\text{TN}}{\text{TN+FP}} \tag{9b}$$

$$\text{Accuracy} = \frac{\text{TP+TN}}{\text{TP+TN+FP+FN}} \tag{9c}$$

After measuring the sensitivity, specificity, and accuracy the results of ANN and SVM are given in Table 7.

Table 7. The sensitivity, specificity, and accuracy of ANN and SVM classification.

Classifier	The sensitivity (%)	The specificity (%)	The accuracy (%)
ANN	95	97.5	96.25
SVM	97.5	97.5	97.5

Also, it was observed that this study gave better results in terms of sensitivity, specificity, and accuracy than studies [9], [10] and [18] that studied breast cancer using the same dataset.

5. Conclusion

Breast cancer constitutes approximately 22% of cancer types seen in women. It is known that 15% of breast cancer cases result in death. Although many scientists carry out cancer-preventive studies, an acceptable treatment protocol has not been established in the current situation. For this reason, women over the age of 40 are required to have a mammogram every 6 months. The clinician, who examines these mammogram images, decides whether the mass in the images is benign or malignant. However, a mass that is overlooked by the clinician may cause irreversible results. For this reason, many scientists use these mammogram images with various artificial intelligence methods and perform computer-assisted mass detection studies to minimize the errors that may occur due to the clinician.

In this study, a graphical user interface was designed to analyze the mammogram images with machine learning using mathematical expressions instead of using a ready-made toolbox using a graphical code-based software platform and present the masses in the images to the clinician's approval. ANN and SVM algorithms were developed to detect abnormalities in mammograms. As seen in Table 7, the results for sensitivity, specificity, and accuracy, obtained in the ANN are 95%, 97.5% 96.25%, and the same values for SVM are 97.5%, 97.5% and 97.5%, respectively. SVM algorithms gave better accuracy than ANN and also the both developed algorithms gave better results than the studies which used the same dataset and algorithms.

In future studies, it is planned to demonstrate both machine learning and deep learning algorithms on the same GUI by using different datasets and more mammogram images.

Acknowledgements

A significant part of this paper includes the Master Thesis data of the first author. The authors confirm that the data supporting the findings of this study are available within the article.

References

[1] Heber D. Nutritional oncology Elsevier.2011; 393-404.
[2] Rangayyan RM, Neuman MR, Raton EB. Breast cancer and mammography. Biomedical Image Analysis 2005, 22-27.
[3] Vanel D. The American College of Radiology (ACR) breast imaging and reporting data system (BI-RADS™): a step towards a universal radiological language?. Eur J Radiol 2007; 61(2): 183.
[4] Smith RA, Saslow D, Sawyer KA, Burke W. Costanza ME, Evans III WP, & Sener S. American Cancer Society guidelines for breast cancer screening: update 2003, CA Cancer J Clin, 53(3), 141-169.
[5] Alteri R, Barnes, C, Burke A, Gansler T, Gapstur S, Gaudet M, Xu JQ. Breast cancer facts & figures 2013-2014. Atlanta: American Cancer Society.2013,1-38,
[6] Giuliano AE, Edge SB, Hortobagyi GN. Eighth edition of the AJCC cancer staging manual: breast cancer. Ann Surg Oncol, 2018; 25(7): 1783-1785.
[7] Divyavani M, Kalpana G. An analysis on SVM & ANN using breast cancer dataset. Aegaeum J, 8,2021, 369-379.
[8] Guzman- Cabrera R, Guzman-Sepulveda JR, Torres-Cisneros M, May- Arrioja D A, Ruiz-Pinales J, Ibarra-Manzano OG Avina Cervantes C, Gonzalez Parada A. Digital Image Processing Technique for Breast Cancer Detection, Int J Thermophys 2013, Springer Science Business Media New York 2012.
[9] Monica Jenefer B, Cyrilraj V. An efcient Image Processing methods for Mammogram Breast Cancer detection, JATIT, 2014, vol,69 No.1.
[10] Kumar AS, Bhupendra GA. Novel Approch for Breast Cancer detection and segmentation in a Mammogram. Procedia Comput Sci, 2015;54:676–82.
[11] Sonal N. Early detection of Breast Cancer using ANN, IJIRCCE, 2016;4, issue ,14008-14013.
[12] Angayarkanni N, Kumar D, Arunachalam G. The Application of Image Process- ing techniques for detection and classifcation of cancerous tissue in Digital Mammograms. JPSR. 2016;8(10):1179–83.
[13] Habib D, Eslam AIM, Awais M, Wail E, Mohammed FN. Automated Breast Cancer Diagnosis based on Machine Learning Algorithms, Journal of Health Engineering, volume 2019, Article ID 425341.
[14] Akay MF. Support vector machines combined with feature selection for breast cancer diagnosis. Expert Syst Appl 2009;36:3240–7.
[15] Muhic I. Fuzzy analysis of breast cancer disease using fuzzy c-means and pattern recognition, Southeast Europe J Soft Comput, 2013;2(1).
[16] Abien FMA. On breast cancer detection: an application of machine learning algorithms on the Wisconsin Diagnostic Dataset, ICMLSC 2018.
[17] Taha M. Classifcation of mammograms for breast cancer detection using fusion of discrete cosine transform and discrete wavelet transform features. Biomed Res. 2016;27(2):322–7.

[18] Ramik R. Breast Cancer Prediction using Machine Learning, JETIR, 2020;7(5)
[19] Onega T, Hubbard R, Hill D, Lee CI, Haas JS, Carlos HA, Tosteson AN. Geographic access to breast imaging for US women. Jour of the American Coll of Radiology, 11(9), 874-882,2014.
[20] Ball JE, Bruce LM. Digital mammogram spiculated mass detection and spicule segmentation using level sets. In 2007 29th Annual International Conference of the IEEE Engineering in Medicine and Biology Society,pp. 4979-4984,2007.
[21] Ramos RL, Armán FA, García MR, Fariñas IC, Perez EC. Well-circumscribed breast carcinoma. Keys to face the challenge of malignant tumors with a benign appearance. European Congress of Radiology-ECR 2015.
[22] Ayres FJ, & Rangayvan, R M. Characterization of architectural distortion in mammograms. IEEE Eng Med Biol Mag, 24(1), 59-67, 2005.
[23] Tang J. et. Al, Computer-aided detection and diagnosis of breast cancer with mammography, recent advances. IEEE Trans Inf Technol Biomed, 2009,13(2), 236-251.
[24] Smith A. Fundamentals of breast tomosynthesis. White Paper, Hologic Inc., WP-00007, 2008,8.
[25] Suckling J, Parker J, Dance D. Mammographic Image Analysis Society (MIAS) database v1.21. [Dataset]. Apollo - University of Cambridge Repository, 2015, https://www.repository.cam.ac.uk/handle/1810/250394
[26] Cheng HD, Shi XJ, Min R, Hu LM, Cai XP, Du HN. Approaches for automated detection and classification of masses in mammograms. Pattern Recognit, 2006, 39(4), 646-668.
[27] Mencattini A, Salmeri M, Lojacono R, Frigerio M, Caselli F. Mammographic images enhancement and denoising for breast cancer detection using dyadic wavelet processing. IEEE Trans Instrum Meas 2008; 57(7): 1422-1430.
[28] Tanyıldızı E, Orhan A. An introduction to variable and feature selection. Comput Appl Eeng Educ 2009; 17(2): 187-195.
[29] Mini MG, Thomas T. A neural network method for mammogram analysis based on statistical features. In TENCON 2003. Conference on Convergent Technologies for Asia-Pacific Region, 2003, Vol. 4, pp. 1489-1492

Turkish Journal of Science & Technology
19(2), 475-483, 2024

Research Paper
https://doi.org/10.55525/tjst.1366299

A New Approach to the Solution of Facility Layout Problems with Filled Function Method

Ahmet ŞAHİNER[1], Ayşe BAŞAĞAOĞLU FINDIK[2*], Emine Rümeysa ATMACA[3], Gültekin ÖZDEMİR[4]

[1]Department of Mathematics, Faculty of Engineering and Natural Sciences, Suleyman Demirel University, Isparta, Turkey
[2,3,4]Department of Industrial Engineering, Faculty of Engineering and Natural Sciences, Suleyman Demirel University, Isparta, Turkey
[1] ahmetsahiner@sdu.edu.tr, [*2] d2040136349@ogr.sdu.edu.tr, [3] eminekocaer@sdu.edu.tr, [4] gultekinozdemir@sdu.edu.tr

(Geliş/Received: 09/10/2024; Kabul/Accepted: 26/09/2024)

Abstract: Facility layout problems are generally solved by stochastic methods in the literature. The large number of iterations used in these methods is quite costly in terms of solution time. In this study, in order to get rid of this disadvantage, the facility layout problem was solved using the filled function method, which is known to be very successful in solving global optimization problems. In order to demonstrate the effectiveness of the filled function method, the classical linear facility layout problem was handled in a non-linear manner and the problem was deliberately made more difficult. In order to use the filled function method, the facility layout problem was transformed into an unconstrained and multimodal (including more than one local minima) global optimization problem by using the hyperbolic smoothing technique and the penalty function method. Thus, in this first study in the literature where a deterministic method is combined with the solution of the facility layout problem, it is shown that the non-convex facility layout problem can be solved with the filled function method with very few iterations and short solution times.

Key words: Facility layout problem, global optimization, filled function method.

Tesis Yerleşim Probleminin Çözümüne Doldurulmuş Fonksiyon Yöntemi ile Yeni Bir Yaklaşım

Öz: Literatürdeki tesis yerleşim problemleri genellikle stokastik yöntemlerle çözülmektedir. Bu yöntemlerde kullanılan iterasyon sayısının fazlalığı çözüm süresi açısından oldukça maliyetlidir. Bu çalışmada, bu dezavantajdan kurtulmak adına tesis yerleşim problemi, global optimizasyon problemlerini çözmede oldukça başarılı olduğu bilinen doldurulmuş fonksiyon yöntemi kullanılarak çözülmüştür. Doldurulmuş fonksiyon yönteminin etkinliğini göstermek için klasik doğrusal tesis yerleşim problemi, doğrusal olmayacak şekilde ele alınmış ve problem bilinçli olarak zorlaştırılmıştır. Doldurulmuş fonksiyon yöntemini kullanabilmek adına hiperbolik yumuşatma tekniği ve ceza fonksiyonu yöntemi kullanılarak tesis yerleşim problemi kısıtsız ve multimodal (birden fazla yerel minimumun içerilmesi) bir global optimizasyon problemi haline dönüştürülmüştür. Böylece, tesis yerleşim probleminin çözümü ile deterministik bir yöntemin bir araya getirildiği literatürdeki bu ilk çalışmada, konveks olmayan tesis yerleşim problemi doldurulmuş fonksiyon yöntemi ile oldukça küçük iterasyonlar ve kısa çözüm süreleri ile çözülebileceği gösterilmiştir.

Anahtar kelimeler: Tesis yerleşim problemi, global optimizasyon, doldurulmuş fonksiyon metodu.

1. Introduction

The coordination of production tools, auxiliary facilities or workstations as a whole in terms of their physical location is called facility layout. That is, facility layout is an integration of the physical arrangement of departments, workstations, machinery, equipment, materials, common areas within an existing or proposed industry. In today's competitive global environment, optimum facility layout has become an effective tool in reducing costs by increasing efficiency. To achieve maximum capacity return, it is important that facilities have a well-organized facility layout that is optimal for all available resources. For this purpose, many techniques have been developed by scientists to achieve optimum targets Layout decision problems, which are referred to as facility layout problems or factory layout problems in the literature, are divided into four as square assignment problem, unlimited capacity facility layout, p-median and p-center [1]. Substantially, facility layout problems are based on the problem of finding the Fermat point of a triangle (Figure 1). Also, it is called the Torricelli point or Fermat-Torricelli point in the plane geometry. The problem is on "finding the point inside a triangle (not on the triangle) so that the sum of the distances from the three vertices is minimum" [2].

* Corresponding author: [1]d2040136349@ogr.sdu.edu.tr. ORCID Number of authors: [1]0000-0002-4945-2476, [2]0000-0002-1898-7718, [3]0000-0002-1822-7540, [4]0000-0001-8856-5556.

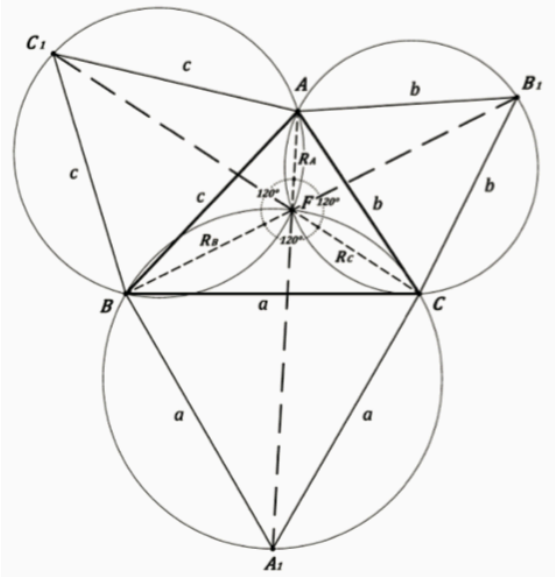

Figure 1. Torricelli construction of point of minimal sum of distances [2].

In facility layout problems, two objectives are usually tried to be optimized. The first of these purposes is to make a layout plan that will minimize the distance traveled by personnel or material between two facility locations, and the second is to make a layout plan that will maximize the predetermined proximity ratio measurements [3].

The facility layout problem deals with the efficient assignment of m facility to n location ($m \leq n$) where material handling costs and fixed costs are tried to be minimized [4]. In other words, the main motivation in mathematical models for facility layout problem is to minimize the cost of material handling. Every facility can be a candidate for every location, all combinations of facilities and locations need to be evaluated. For this reason, the solution to the facility layout problem is considered difficult. When the number of facilities is n and the number of locations is n, there are at most combinations n!. When the number of facilities is n and the number of locations is m, if these numbers are not equal, the number of combinations to be evaluated would be [m/(m − n)]! for n < m. Although this number is smaller than n!, it is still a large value [5-6]. Facility layout problems have been studied since the 1950s. With the developments in the field of operations research, the facility layout problem was first modeled as the *quadratic assignment problem* (**QAP**) by Koopmans and Beckmann [7]. Since the increase in the number of variables in the problem made the solution of the problem difficult, researchers have continued to search for new ways and develop new methods to solve the problem from the 1950s to the present.

In addition to the squareness of the QAP objective function, it has a non-convex structure. There are as many (n!) solution points and more than one local optimum solution in the QAP solution space. There is not a well disagned method that can find the optimum solution in the possible computation time for QAP with more than 20 facilities [8]. In fact, Meller and Gau argued that in some types of FLP, even for six locations, it is impossible to search for optimal solutions to this problem by applying precise methods [9-10]. The facility layout problem (FLP) is one of the NP (non-polynomial) problems because the solution time increases exponentially depending on the problem size [11]. Despite the great developments in computer technology and the abilities of researchers in recent years, large-scale facility layout problems cannot be solved by optimization methods, instead, solutions are sought with heuristics that make systematic approaches to problems and whose solution times are within polynomial limits.In the literature, Newton's method, the steepest regular method and conjugate gradient method are used generally for solving optimization problems involving only one local minimum. However, these methods are not suitable for problems with more than one local minimum. Because in optimization problems involving more than one local minimum, existing methods can get stuck in any existing local minimum and/or a local minimum worse than the existing local minimum. In this sense, it is necessary to turn to global optimization problems involving selective local minimums. The global optimization problem allows us to give clear answers to questions such as: 'How to escape the current local minimum?' and 'Is the current optimum solution global or not?'. In recent years, some effective methods have been proposed for solving global optimization problems. Among the existing methods, the filled function method (FFM) is particularly successful in detecting local minima repeatedly.

Facility layout problems are unimodal and their constraints are linear functions. In real world, it is generally encountered nonlinear situations. Recently, it has been observed that the use of humanoid robot technologies that

exhibit non-linear movements in the industry, especially in facility layout problems, has increased. Therefore, in this study, it is shown that the classical facility layout problem can be solved with FFM by removing it from its classical state and making it more difficult by transforming it into a non-linear FLP. In fact, it is made the problem so difficult that it is solved the 22-facility settlement problem instead of the 6-facility settlement problem. The reason why is chosen 22 facilities in the problem is that it is emphasized that the solution of the facility placement problem for 22 facilities cannot be done analytically in the main works it has been examined on this subject in the literature. It should be noted here that, with the method it is proposed, the analytical solution of the problem can be achieved even if there are more than 22 facilities. However, these solutions are not included so that the study is not boring for the reader. The solution of the facility layout problem with the method proposed is outlined as follows. First of all, FLP, which contains non-linear constraints, is made unrestricted using the penalty function method. Then, using the hyperbolic smoothing technique, FLP is transformed into a non-convex optimization problem in which the derivative operator can be used. As a result of all these, in order to demonstrate the effectiveness of FFM in FLP, FLP is transformed into a multi-modal, unconstrained, non-linear and non-convex global optimization problem other than the classical case. It is shown that the solution of the hardened FLP can be achieved in a short time with the deterministic-analytical method using FFM for the first time. Before giving this solution in detail, the main structure of the facility layout, (hyperbolic) smoothing technique, penalty function method and filled function method will be briefly reminded in the following subsections.

2. Methods and Literature Review

2.1. General Algorithm for Solution of the Layout Problem

Multiple facility layout algorithms are weak in the way of the representing departments. For example; Most algorithms represented partitions as squares of equal size [12] or combinations of such squares [13-14]. Some of these algorithms-imposed constraints on the models of these composite departments in order to keep the size of the problem traceable [13]. These restrictions must be decided by the user. Because the dimensions and locations where the departments can be located should appeal to the user. On the other hand, the problem in developing algorithms that allow departments of different sizes is that the final layout created may contain irregular shapes, which is not possible for a real facility.

Linear and nonlinear optimization models have been improved for modelling multiple facility layout problems. One of the first treatment of the Euclidean distance multiple facility layout problem which was presented at references [15-17] applied a linear approach for rectilinear cost distance minimization. This approach has been generalized by Morris and Verdini [18 -19], and the l_p distance measure has been minimized to solve the multi-facility location problem.

Camp et al. [20] introduced a model for an approximate the real layout problem. In this model, points had been placed in a rectangle shape. As result, it was concluded although the areas of the points are fixed, the width/length coordinates can vary.

The model generally assumes that the transportation costs between points are known. Also, the cost of the distance of each point to the outside wall is known. In this problem, the aim is to minimize the total cost of the distance between points and between the outside walls of the points.

2.2. Smoothing Technique

The smoothing technique is used to make non-differentiable functions differentiable and also continuous. This technique can be applied by adding a small, nonzero value to the corresponding non-smooth function. The advantage of smoothing method is that optimization problems with continuously differentiable functions can be solved, which have rich theory and powerful solution methods, and a local minimizer or stationary point of the original non-smooth problem can be guaranteed by updating the smoothing parameter.

If the studies on optimization theory are examined, it is seen that smoothing functions and techniques are frequently used in these studies [for more details see 31-32]. The first study about the smoothing techniques was studied by Bertsekas to detach one of the crucial optimization problems called min-max [21]. For the same problem, another important smoothing function approach is studied in the [22]. The smoothing process is beneficial for problems which include any of minimum or any operators. The smoothing technique is controlled by a parameter which gives an opportunity to obtain a precise approximation to the original non-smooth function. And also smoothing methods are not only efficient for problems with non-smooth objective functions, but also for

problems with non-smooth constraints. In this study, it is used penalty function methods and smoothing, which are well-known gradient-based optimization techniques, to solve non-uniform optimization problems. It is used the smoothing approach to locally correct the inflection points of the non-smooth function.

2.3. Penalty Function Method

With the penalty function method, the restricted programming model is made unconstrained. In this method, a penalty term is added to the objective function for each constraint and the objective function is aimed to be minimized. The added penalty is increased iteratively and continued until the minimum point for the objective function is found. In the method, the penalty added to the objective function as a result of the violation of the constraint is equal to μ times the square of the constraint function. This means to arrive at a continuous function with a continuous gradient. Considering that the constraints to be used in this study are not convex, first transforming the problem into an unconstrained problem with the penalty function method and then applying the filled function method to this unconstrained problem guarantees the finding of the local minimum point.

2.4. Use of the Filled Function Method for Solving the Facility Layout Problem

The location problem is basically an assignment problem and deals with the allocation of facilities to residential areas. If the distances and sizes between the locations of the facilities are negligible, it is not possible to place the facilities on top of each other. Facilities can be thought of as points far from each other and the problem can be addressed as a location selection problem. If the facilities are close to each other, there is a problem that the areas allocated to them overlap. It is the need to meet this constraint that makes modeling and solving the layout problem difficult. On the other hand, if the facilities to be placed are considered to be squares of equal area, the layout can be modeled as a cage structure. The layout problem, which can be thought of as a one-dimensional array in its simplest form, is too complex to be solved in a reasonable time due to its combinatorial structure. On the other hand, being stuck with the existing local minimizer and not being able to get rid of it is the main difficulty of global optimization. In this sense, many remarkable methods have been developed in global optimization theory in recent years to overcome this difficulty. Typical examples of deterministic methods are FFM [25], [26], orbital method [27], covering method [28] and tunneling method [29]. It is known that deterministic and stochastic methods have advantages and disadvantages compared to each other. Although stochastic algorithms, such as particle swarm algorithms, have the ability to search for global optimality, they may suffer from falling prematurely into local optima. Since filled function algorithms are deterministic algorithms compared to stochastic algorithms, they guarantee finding global optimization. The FFM-based algorithm finds the same result in every run and provides the exact solution. Additionally, many studies in the literature have emphasized that finding the optimal solution of FLP by applying deterministic methods is quite costly when the number of facilities is twenty or more. Meller and Gau even suggested that in some types of FLP, it is impossible to find an optimal solution to this problem by applying exact methods even for six locations [9–10].

Based on these claims, there are two main motivations for conducting this study. The first is to show that FLP can be solved in a reasonable time by a deterministic method even if the number of facilities is more than 6. The second motivation is to avoid the problem of finding random results in heuristic (or metaheuristic) algorithms, since the solution of FLP in terms of FFM is based on mathematical calculation. Thus, more successful results can be obtained by using the filled function method, which is one of the most effective deterministic methods in global optimization problems.

Using the filled function method, which is the most frequently mentioned in the literature, the above-mentioned problems were tried to be solved, based on the intended motivations, and this problem was solved in a very short time with a single iteration. Originality was achieved by proposing a new approach, the first in the literature, to solve the facility layout problem with the filled function method.

2.5. Filled Function Method

To summarize FFM in a general context, it can be explained as follows. First, a random starting point is chosen in the solution space. With the local optimization method, the local minimizer of the objective function is obtained. In the local minimizer of this objective function, a filled function with the analytic properties of the objective function is constructed. A random point that is very close to this minimizer of the objective function is then chosen as the starting point. The local minimizer of the function filled according to this point is found by the local optimization method. By taking the minimization of the resulting filled function as a starting point, a better

minimum of the objective function is found. Existing minimizers are minimized until a more general minimizer (global minimum) is found (for more details see [25-26], [30]).

Remark 1. Since most of the local optimization algorithms used in FFM require gradient information, in this study combining FFM and FLP solution, the hyperbolic smoothing method is used to differentiate the objective function.

Although the definition of the filled function was first given by [25]; there are various variations of this definition in the literature by making minor changes suitable for the purpose. However, the version of this definition that is frequently used in the literature is as follows (see for more details [30].

Definition 2.5.1. (Definition 1 in [30], page 513) A continuously differentiable function $FF(x, x_1^*)$ is said to be a filled function of $f(x)$ at x_1^* (the current local minimizer of $f(x)$) if it satisfies the following properties and Equation 1:

i) x_1^* is a strict local maximizer of $FF(x, x_1^*)$ on Ω ($FF: \Omega \subseteq \mathbb{R}^n \to \mathbb{R}$),

ii) $FF(x, x_1^*)$ has no stationary point in the set
$S_1 = \{x: f(x) \geq f(x_1^*), x \epsilon \Omega \setminus \{x_1^*\}\}$ (1)

iii) If $x_1^*$is not a global minimizer of f (x), then there exists a point x′ such that it is a local minimizer of $FF(x, x_1^*)$ on S_2 = { $x \in$ intΩ: $f(x) < f(x_1^*)$}.

The first filled function example given by Ge Ren-Pu in 1987 in accordance with the above definition is as shownn in Equation 2.

$$P(x, r, p) = \frac{1}{r + f(x)} exp\left(\frac{\|x - x_1^*\|^2}{p^2}\right) \quad (2)$$

However, the fact that this function contains an exponential expression and two parameters that are difficult to adjust has brought along computational difficulties. Therefore, in order to overcome these difficulties, researchers have defined new filled functions. In the literature, several studies were done with different filled function methods. In this study, filled function method was used as below.

An unconstrained global minimization problem can be briefly represented as Equations 3 and 4:

$$\min f(x) \quad (3)$$

$$\text{s.t. } x \in \mathbb{R}^n \quad (4)$$

where $f: \mathbb{R}^n \to \mathbb{R}$ is a continuously differentiable function. Suppose that $f(x)$ is global convex, that is $f(x) \to +\infty$, when $\|x\| \to +\infty$, therefore, there is a closed and bounded region $\Omega \subset \mathbb{R}^n$ containing all the minimizers of $f(x)$. Otherwise, unbounded global optimization problem over an unbounded region would not be solved. Thus, the Equation 3 can be written as Equations 5 and 6:

$$\min f(x) \quad (5)$$

$$\text{s.t. } x \in \Omega \quad (6)$$

The filled function method in this study, which was introduced by Lin, Gao ve Wang in 2014, was applied. Below is the algorithm of this filled function method:

Step 0: Choose an upper bound U bp of P (e.g., 10^6) and a constant $\rho > 0$ (e.g., $\rho = 10$); give the initial value of P, and some directions d_i, i =1, 2, · · · , $2n$, where d_i = (0, · · · , 1, · · · , 0)^T, 1 is at the i -th element of d_i , i = 1, 2, . . ., n and $d_i = -d_{i-n}$, $i = n + 1, \cdots, 2n$, where n is the dimension of the problem. Set k= 1. Choose any $x_1 \in \Omega$.

Step 1: Minimize $f(x)$ with the initial point $x_k \in \Omega$ so that a minimizer x_k^* of $f(x)$ is obtained.

Step 2: Construct

$$FF(x, x_1^*, P) = \frac{P}{1+\|x-x_1^*\|^2} h_{\frac{1}{p}}\big(f(x) - f(x_1^*)\big) \quad (7)$$

set i =1 and where h is one variable function such that c is a constant, and is defined by

$$h_c(t) = \begin{cases} c, & t \geq 0 \\ t^3 + c, & t < 0 \end{cases}$$

Step 3: If $i \leq 2n$, then set $x = x_k^* + \delta d_i$ and go to Step 4; Otherwise, go to Step 5.

Step 4: Use x as the initial point to minimize $FF(x, x_k^*, P)$ and denote the sequence point generated by a local optimization algorithm as x_j, j = 1, 2, · · · if $\exists j_0 \in \{1, 2, \cdots\}$ such that $x_{j_0} \notin \Omega$, set $i = i + 1$ and go to Step 3; Otherwise, find a minimizer $x' \in \Omega$ of $FF(x, x_k^*, P)$ and set $x_{k+1} = x'$, $k = k + 1$, go to Step 1.

Step 5: If P <U bp, then increase P by P = ρ × P and go to Step 2; Otherwise, the algorithm stops and x_k^* is taken as a global minimizer of $f(x)$.

3. Numerical Experiment

In this study, classical linear constraints were considered as a nonlinear constraint for FLP. The reason for contructing this is to take FLP out of its usual classical situation and make FLP a more difficult problem by randomly selecting 22 points. First of all, FLP, which contains non-linear constraints, is made unrestricted using the penalty function method. Then, using the hyperbolic smoothing technique, FLP is transformed into a non-convex optimization problem in which the derivative operator can be used. As a result of all these, in order to demonstrate the effectiveness of FFM in FLP, FLP is transformed into a multi-modal, unconstrained, non-linear and non-convex global optimization problem other than the classical case. It is shown that the solution of the hardened FLP can be achieved in a short time with the deterministic-analytical method using FFM for the first time. There are two main purposes in doing this. The first is to show that the facility layout problem can be solved in a reasonable time with a deterministic method, even if there are more than 6 facilities. The second aim is to solve this problem by using the filled function method, which is one of the most effective deterministic methods in global optimization problems. This problem was solved by using the filled function method, which is the most frequently mentioned in the literature.

In order to make the functioning of the model more understandable, it is aimed to reach the answer with very few iteration. Below, the step-by-step method to reach the global minimum will be explained. The data was constructed by us to better visualize local minima.

Problem Definiton: It was aimed to find the locations with minimum distance in a rectangular region according to the coordinates given in Table 1. Rectangular region constraints are given in Equation 9 and Equation 10. In this case, the mathematical model with objective function, such as Equation 8, is given below.

$$\underset{(x,y) \in \mathbb{R}^2}{Min} f(x,y) = \sum_{i=1}^{k} d\big((x,y),(x_i, y_i)\big) \quad (8)$$

where $d\big((x,y),(x_i, y_i)\big) = \sqrt{(x-x_i)^2 + (y-y_i)^2}$ for $i = 1,\ldots, k$ such that for $k = 22$.

Subject to

$$y - x^2 \leq 0 \quad (9)$$

$$\frac{(x-4)^2}{36} + \frac{(y-4)^2}{36} - 1 \leq 0 \quad (10)$$

Table 1. Coordinates of Departments

i	x_i	y_i	i	x_i	y_i
1	3	7	**12**	3	6
2	3	-7	**13**	1	5
3	-2	5	**14**	-1	4
4	-2	-5	**15**	-3	8
5	0	6	**16**	-3	7
6	0	-6	**17**	2	6
7	4	5	**18**	-2	7
8	4	6	**19**	-4	9
9	3	8	**20**	3	5
10	5	8	**21**	-3	5
11	5	9	**22**	3	-5

The steps of making the problem unconstrained and finding its global optimum are explained below.

Step 1. Based on the technique it is mentioned above, the smooth state of the objective function would be as in Equation 11.

$$g(x,y) = \sum_{i=1}^{k} \sqrt{(x-x_i)^2 + (y-y_i)^2 + \mathcal{E}} \quad (11)$$

$\mathcal{E}$ is a positive real number very close to zero and $f(x,y)$ for $k = 22$.

Step 2. With the Penalty function method, the model is made unconstrained.

$$\underset{(x,y) \in \mathbb{R}^2}{Min} \left(g(x,y) + m\left(\frac{(x-4)^2}{36} + \frac{(y-4)^2}{36} - 1\right)^2 + m(max(0, x-y^2))^2 \right) \quad (12)$$

Step 3. In this step, the global minimum point of the function given in Equation 12 was obtained using Matlab R2019b.

Step 4. The filled function x_1^* given in Equation 7 is set to the local minimum point. Minimizing this filled function with a local method it is obtained the minimizer $x_f^* = [2.9570 \quad 5.7636]$ of filled function which is certainly in a basin $B(x_2^*)$ lower than $B(x_1^*)$.

The correctness of solution with two different methods (fminsearch and fminunc) in Matlab was proved. It has been proved the accuracy of these points once again by putting them in equation 12 whether they are on an ellipse or not.

Step 5. After finding the best m value in the algorithm, x_1^* local minimum value is found. The difference between x_1^* and x_2^* is calculated after finding the x_2^* value, which is the lower basin of the x_1^* value. If the difference is less than the $\mathcal{E}$ value, the algorithm ends. The numerical results of the filled function algorithmare presented for $\mathcal{E} = 10^{-4}$ and m =200.

By these algorithm's, the global minimum point was found by reaching the answer with a single iteration.

The all results from Matlab R2019b are given in table 2. The meanings of the symbols used in these tables are as follows:

- k : the number of facilities

- *iterm* : the number of iterations in obtaining the global minimizer
- *fbest* : the best function value in 10 runs
- *fmean* : the mean of the best function value
- *feval* : the total number of the functions evaluations

Table 2. The results on the problem.

Method	k	iterm	fbest	fmean	feval	fevalm	Global Minimizer
FF	**22**	1	107.46	107.46	1033	1049.6	[2.9570 5.7636]

4. Conclusions and Future Works

Since facility layout problems have NP-Hard structure, the larger the problem size, the more difficult finding the optimal solution, and it also requires a lot of time to reach reliable results. Such problems cannot be solved in computation time limited by the polynomial function of the problem size. For this reason, heuristic methods that do not guarantee finding the optimum, but whose solution time remains within polynomial limits, are used in solving such problems. Most heuristics have problem-specific properties and a heuristic used for one problem cannot be used for another problem. However, interest in techniques (Anneal Simulation, Tabu Search, Artificial Neural Networks, Genetic Algorithms) that are flexible and more general in terms of their application to problems has increased in recent years. These techniques have been applied to a large number of facility layout problems and have been found to be quite powerful. However, the number of iterations in solving these FLPs is quite high and the solution time takes a very long time. Therefore, in this study, a method is proposed to reach the global optimum in a very short time with very few iterations.

Additionally, the objective function or constraints of most optimization problems encountered in the real world are nonlinear and involve more than one local minima. The facility layout problem is one of them. For problems involving a local endpoint, many local optimization methods are well known in the literature, such as the steepest descent method, Newton's method, and the conjugate gradient method. However, these methods are insufficient to find the global minimum in problems involving more than one local minimizer. Being stuck with the current local minimizer and not being able to get rid of it is the main difficulty of such problems. One of the best-known methods in the literature that can get rid of these basic difficulties is the filled function method proposed in this study.

In this study, considering FLP as a nonlinear constraint with a nonlinear objective function made the problem even more difficult. It has been made more difficult and FLP, which contains non-linear constraints, is made unrestricted using the penalty function method. Then, using the hyperbolic smoothing technique, FLP is transformed into a non-convex optimization problem in which the derivative operator can be used. Thus, FLP was constructed, which turned into a non-convex optimization problem in which the objective derivative operator could be used. As a result of all these, FLP has been transformed into a multimodal, unconstrained, non-linear and non-convex global optimization problem other than the classical case. Later, the filled function method was used due to its ability to successfully find the global reducer in multimodal global optimization problems. Thus, although there are many alternative methods to FLP, a solution was achieved in a short time with the deterministic-analytical method for the first time. Therefore, in this study, it is shown that the classical facility layout problem can be solved by FFM by removing it from its classical form and making it more difficult by converting it into a non-linear FLP.

In addition, since the solution of FLP in terms of FFM is based on mathematical calculation, the problem of finding random results in heuristic (or metaheuristic) algorithms is avoided. The FFM-based algorithm finds the same result in every run and offers an exact solution.In the following studies, it is aimed to find new filled function methods, to apply these new filled function methods to more complex facility layout problems, and to present new studies by comparing the obtained results with the previous solution methods of facility layout problems that are scientifically accepted in the literature, thus bringing a new, different and effective perspective to the solution of more advanced facility layout problems.

References

[1] Yigit V, Türkbey O. Tesis Yerleşim Problemlerine Sezgisel Metotlarla Yaklaşım. Gazi Üniversitesi Mühendislik Mimarlık Fakültesi Dergisi 2003; 18:45-56.
[2] Banjac B, Nenezic M, Petrovic M, Malesevic B, Obradovic R. moNGeometrija, 4th international scientific conference. Trifocal curves in matlab and java 2014; 346.
[3] Rosenblatt, MJ. The Facilities Layout Problem: A Multi-goal Approach. International Journal of Production Research 1986; 17:323-332.
[4] Tavakkoli- Moghaddin R, Shayan E. Unequal Area Facility Layout Using Genetic Search. IIE Transactions 1994.
[5] Sule DR. Manufacturing Facilities Location, Planning and Design. International Thomson Publishing 1994.
[6] Ulutas BH. Dinamik yerleşim probleminin çözümü için bir klonal seçim algoritması ve uygulamaları. Eskisehir Osmangazi University. Ph D Thesis 2008.
[7] Koopmans TC, Beckmann M. Assignment problems and the location of economic activities. Econometrica 1957; 25(1), 53–76.
[8] Sha DY, Chen C-W. A New Approach to The Multiple Objective Facility layout Problem. Integrated Manufacturing Systems 2001; 12(1):59-66.
[9] Kim M, Chae J. A monarch butterfly optimization for an unequal area facility layout problem. Soft Computing 2021; 25:14933–14953.
[10] Meller RD, Gau KY. The Facility Layout Problem: Recent and Emerging Trends and Perspectives. Journal of Manufacturing Systems 1996; 15(5):351-366.
[11] Mirchandani PB, Francis RL. Discrete Location Theory. John Wiley & Sons, New York, 1990.
[12] Hillier FS. Quantitative tools for plant layout analysis. Journal of lndustrial Engineering 1963; 14/1, 33-40.
[13] Bazaraa MS. Computerized layout design: A branch and bound approach. AIIE Transactions 1975; 7/4, 432-438.
[14] Hassan MMD, Hogg GL, Smith DR. SHAPE: A construction algorithm for area placement evaluation. International Journal 1986; 24/5, 1283-1295.
[15] Miele W. Link-length minimization in networks. Operations Research 1958; 6, 232-243.
[16] Wersan SJ, Quon JE, Charnes A. Systems analysis of refuse collection and disposable practices. 14: Yearbook, American Public Works Association 1962; 195-211.
[17] Wesolowsky GO, Love RF. The optimal location of new facilities using rectangular distances. Operations Research 1971; 19, 124-130.
[18] Morris JG. Convergence of the Weiszfeld algorithm for Weber problems using a generalized ‘distance’ function. Operations Research 1981; 29, 37-48.
[19] Morris JG, Verdini WA. A simple iterative scheme for solving minimum facility location problems involving lp distances. Operations Research 1979; 27, 1180-1188.
[20] Camp D, Carter M, Vannelli A. A nonlinear optimization approach for solving facility layout problems. European Journal of Operational Research 1992; 57, 174-189.
[21] Bertsekas D. Nondifferentiable optimization via approximation, Math Program Stud 1975; 3, 1–25.
[22] Zang I. A smoothing out technique for min-max optimization. Math Program 1980; 19, 61–77.
[23] Love RF, Morris JG, Wesolowsky GO. Facilities Location: Models and Methods. North-Holland, New York 1988.
[24] Bazaraa MS, Shetty CM. Nonlinear Programming: Theory and Algorithms. Wiley, New York 1979; 340-343.
[25] Ge RP. A filled function method for finding a global minimizer of a function of several variables. Math Program 1990; 46:191–204.
[26] Ge RP, Qin YF. A class of filled functions for finding global minimizers of a function of several variables. J Optim Theory Appl 1987; 54:241–252.
[27] Branin F. Widely convergent methods for finding multiple solutions of simultaneous nonlinear equations. IBM J Res Dev 1972; 16:504–522.
[28] Basso P. Iterative methods for the localization of the global maximum. SIAM J Numer Anal 1982; 19:781–792.
[29] Levy AV, Montalvo A. The tunneling algorithm for the global minimization of functions. Siam J Sci Stat Comput 1985; 6:15–29.
[30] Lin H, Gao Y, Wan Y. A continuously differentiable filled function method for global optimization. Numerical Algorithms 2014; 66:511–523.
[31] Sahiner A, Yilmaz N, Ibrahem SA. Smoothing Approximations to Non-smooth Functions. Journal of Multidisciplinary Modeling and Optimization 2019; 1(2):69-74.
[32] Sahiner A, Yilmaz N, Kapusuz G. A novel modeling and smoothing technique in global optimization. Journal of Industrial and Management Optimization 2019; 15(1):113–130.

Turkish Journal of Science & Technology
19(2), 485-495, 2024

Research Paper
https://doi.org/10.55525/tjst.1404899

A Deep Learning-based U-Net 3+ Technique for Segmentation Blood Cell

Hasan ULUTAŞ[1*]
[1]Department of Computer Engineering, Yozgat Bozok University, Yozgat
[*1] hasan.ulutas@bozok.edu.tr

(Geliş/Received: 14/12/2023; Kabul/Accepted: 15/07/2024)

Abstract: Segmentation and classification of blood cells are crucial for various medical applications, including disease diagnosis, treatment monitoring, and research purposes. This process allows for accurate identification and quantification of different cell types, aiding in the detection and understanding of various blood-related disorders. The proposed U-Net 3+ architecture incorporates structural modifications, including strengthened connections between convolutional layers, increased filter numbers, and integration of Bayesian optimization for hyperparameter tuning. The model's generalization capability is optimized through the dynamic adjustment of dropout rates and learning rates. Bayesian optimization facilitates the exploration of optimal hyperparameter combinations, allowing the model to adapt effectively to diverse datasets. Advanced training strategies, such as adaptive learning rate adjustment and early stopping, are employed to mitigate overfitting and enhance training efficiency. The proposed model exhibits exceptional performance across multiple folds, achieving low training and validation losses, high accuracy metrics, and robust segmentation indices. Evaluation metrics, including mean IoU (Jaccard Index), dice score, pixel accuracy, and precision, confirm the model's proficiency in accurately delineating blood cell boundaries. The study demonstrates the effectiveness of custom architectures and optimization techniques, achieving an average IoU (Jaccard Index) of 0.9324 and a dice score of 0.9667. The proposed U-Net 3+ model stands as a promising solution for accurate and reliable blood cell segmentation, demonstrating adaptability and robust performance across various datasets. This work sets the stage for future research in the domain of medical image segmentation, emphasizing the potential for continued advancements in precise and efficient segmentation methodologies.

Key words: blood cell, segmentation, U-Net3+, pre-processing, cross validation.

Kan Hücresinin Segmentasyonu için Derin Öğrenmeye Dayalı U-Net 3+ Tekniği

Öz: Kan hücrelerinin segmentasyonu ve sınıflandırılması, hastalık teşhisi, tedavi izleme ve araştırma amaçları dahil olmak üzere çeşitli tıbbi uygulamalar için çok önemlidir. Bu süreç, farklı hücre türlerinin doğru bir şekilde tanımlanmasına ve miktarının belirlenmesine olanak tanıyarak kanla ilgili çeşitli bozuklukların tespit edilmesine ve anlaşılmasına yardımcı olur. Önerilen U-Net 3+ mimarisi, konvolüsyonel katmanlar arasındaki bağlantıları güçlendiren, filtre sayılarını artıran ve hiperparametre ayarlaması için Bayesian optimizasyonu entegre eden yapısal değişiklikler bulunmaktadır. Modelin genelleme yeteneği, dropout oranları ve öğrenme oranlarının dinamik ayarlanması ile optimize edilmiştir. Bayesian optimizasyon, optimal hiperparametre kombinasyonlarını keşfetmeyi sağlayarak modelin çeşitli veri kümelerine etkili bir şekilde uyum sağlamasına imkan tanır. Ayrıca, aşırı uydurmayı azaltmak ve eğitim verimliliğini artırmak için adaptif öğrenme oranı ayarı ve erken durdurma gibi gelişmiş eğitim stratejileri kullanılmıştır. Önerilen model, çoklu katmanlarda düşük eğitim ve doğrulama kayıpları, yüksek doğruluk metrikleri ve güçlü segmentasyon endeksleri elde ederek olağanüstü performans sergilemektedir. Değerlendirme metrikleri, ortalama IoU (Jaccard İndeksi), dice skoru, piksel doğruluğu ve hassasiyet gibi, modelin kan hücre sınırlarını doğru bir şekilde belirleme konusundaki yetkinliğini doğrular. Çalışma, özel mimarilerin ve optimizasyon tekniklerinin etkinliğini 0,9324 ortalama IoU (Jaccard İndeksi) ve 0,9667 dice skoru ile ispatlamaktadır. Önerilen U-Net 3+ modeli, çeşitli veri kümelerinde adaptasyon yeteneği ve güçlü performansıyla umut vadeden bir çözüm olarak ön plana çıkmaktadır. Bu çalışma, medikal görüntü segmentasyonu alanında gelecekteki araştırmalara zemin oluşturarak, hassas ve etkili segmentasyon metodolojilerinde devam eden ilerlemelerin potansiyelini vurgulamaktadır.

Anahtar kelimeler: kan hücresi, segmentasyon, UNet3+, ön işleme, çapraz doğrulama.

1. Introduction

Blood cells traverse the body through the circulatory system, and in mammalian species, they can be categorized into three main types [1]. Firstly, red blood cells specialize in the vital task of transporting oxygen to various tissues and organs. Secondly, leukocytes, which are essential components of the immune system, respond to bacterial infections by concentrating at the infection site, encircling the invading bacteria, and engulfing these bacteria as part of the body's defense mechanism. Lastly, platelets play a pivotal role in hemostasis, contributing to the blood clotting process and preventing excessive bleeding in response to injuries. Together, these three types of blood cells work in harmony to ensure the proper functioning and health of the circulatory system. The shape, number, and type of these cellular components have always been a topic of interest among researchers [2].

* Corresponding author: hasan.ulutas@bozok.edu.tr. ORCID Number of author: 0000-0003-3922-934X

Especially in the field of medicine, the impact of blood components is crucial, addressing conditions ranging from easily treatable ones like anemia to more challenging diseases such as leukemia. Microscopes are used to examine the anatomical and morphological structures of these components. However, manual processes performed on images obtained through microscopes can be tedious and time-consuming due to their reliance on human expertise. To minimize human errors, achieve time efficiency, and facilitate work on a larger number of samples, the use of computer-aided systems in medical studies is increasingly on the rise [3]–[6].

The accurate classification and segmentation of blood cells are crucial for enhancing the accuracy of medical diagnoses and optimizing treatment processes. In this context, automatic or semi-automatic computer-aided methods provide valuable tools for researchers and healthcare professionals. In the literature, a variety of studies focused on the classification and segmentation of blood cells [7]–[10]. Macawile et al. employed pre-trained neural networks, including AlexNet, GoogLeNet, and ResNet-101, to discern and enumerate white blood cells [10]. Comparative analysis of the outcomes from these three networks revealed that AlexNet demonstrated superior performance. The study reported a comprehensive accuracy rate of 96.63%. Yıldırım and Çinar performed the classification of white blood cells for disease diagnosis using established deep learning models such as AlexNet, ResNet-50, DenseNet-201, and GoogLeNet, utilizing a pre-existing dataset [11]. The initial phase involved the classification of the original data with these four networks, followed by the computation of accuracy metrics. The most favorable outcome, featuring an accuracy rate of 83.44%, was noted when employing DenseNet-201 in tandem with Gaussian filtering. In a study conducted by Lu et al., a network named WBC-Net, based on UNet++ and ResNet, was employed for the segmentation of white blood cells [12]. The segmentation was tested and compared both with and without skip connections, yielding precision values of 98.48%, 98.90%, 96.20%, and 94.03% for four respective datasets. In the investigation conducted by Roy et al., the localization and identification of leukocytes in peripheral blood were accomplished through the application of deep learning methodologies. The segmentation of leukocytes utilized the DeepLabv3+ architecture. During the segmentation testing phase, the average accuracy achieved was 98.22%. Subsequently, the overall average accuracy during the validation process was computed as 98.87% ± 1 [13]. Toptas and Hanbay conducted a study on the automatic detection, classification, and segmentation of blood cells [2]. In this research, microscopic blood cell images were segmented using deep learning architectures such as DeepLabv3+, U-Net, and FCN. The highest accuracy, with a value of 95.75%, was achieved with the DeepLabv3+ architecture. These experimental results provide support for the effectiveness of the proposed method. Bozkurt proposed a study on the classification of blood cells using a Dense Convolutional Network [14]. This research was conducted on an open-access BCCD dataset consisting of 12,507 white blood cell images. Experiments demonstrate that the proposed DenseNet121 model achieved an accuracy of 94%. This high accuracy value can expedite diagnosis by automating cell classification, enabling doctors to examine more data. The study presented by Nahzat et al. aims to develop a CNN-based model for the classification of white blood cells and evaluate its performance [15]. Using white blood cell images obtained from Kaggle, the study demonstrates that the RMSprop optimizer yields the best results. Additionally, the proposed model is compared with four pre-trained models including MobileNetV2, DenseNet121, InceptionV3, and ResNet50. The results indicate that despite having the lowest number of trainable parameters and training time, the proposed model exhibits exceptional performance. Khouani et al. proposed an automated method for identifying white blood cells (WBCs) in cytological images, crucial for cancer diagnosis [16]. It introduces a deep learning-based approach to streamline tasks for hematologists. The method involves preprocessing images, applying a deep neural network for localization and segmentation, and refining outputs with combined predictions and corrections. Additionally, a novel algorithm leveraging spatial information enhances segmentation quality. Implemented using Python, TensorFlow, and Keras, the method shows promising results on datasets from Tlemcen Hospital, Algeria, achieving 95.73% accuracy with predictions in less than 1 second, outperforming existing methods. Zhang et al. present a semantic segmentation approach based on deep learning, targeting the complexities arising from variations in cell characteristics and image quality [17]. They introduce the deformable U-Net (dU-Net), which incorporates deformable convolution layers into the U-Net structure to address these challenges. The dU-Net demonstrates precise localization and resilience to diverse cell shapes and image conditions. Experiments on microscopic RBC images from SCD patients show that the dU-Net achieves superior accuracy in both binary and multi-class segmentation tasks compared to unsupervised and state-of-the-art supervised methods.

This study aims to introduce an artificial intelligence model developed to facilitate accurate segmentation of blood cells in medical imaging. The developed model features a novel architecture named U-Net 3+, which incorporates specific features not seen in previous studies. The U-Net 3+ model stands out by enhancing the existing UNet architecture with structural modifications such as reinforced connections between deeper layers, increased filter numbers, and integration of Bayesian optimization for hyperparameter tuning. The primary contribution of this study lies in presenting a new approach to accurately segmenting blood cells in medical imaging. The developed U-Net 3+ model has demonstrated higher accuracy and segmentation performance

compared to other existing methods. This study provides a significant contribution to the development of artificial intelligence-based segmentation techniques in medical imaging.

The article's remaining chapters are organized as follows: Chapter 2 provides information of dataset, image preprocessing, a summary of the deep learning methods such as U-Net, proposed U-Net3+ and evaluation metrics. The findings from U-Net3+ segmentation methods are presented in Chapter 3. The results are discussed in Chapter 4, and conclusions and explanations are provided in Chapter 5.

2. Material and Methods

2.1. Dataset

In this study, a dataset comprising publicly available blood cell images is utilized, totaling 1,328 images [18], [19]. The dataset used originally contains bounding box coordinates for each cell, and the original references of the cells were used to identify individual cells, and detailed information about the dataset is available in [19]. The dataset includes 1328 original blood cell images and an equal number of corresponding real background images. The images vary in size, with some measuring 1600x1200x3 pixels and others 1944x1383x3 pixels. All images in the dataset are in the RGB colour space. Sample images from the dataset are illustrated in Figure 1.

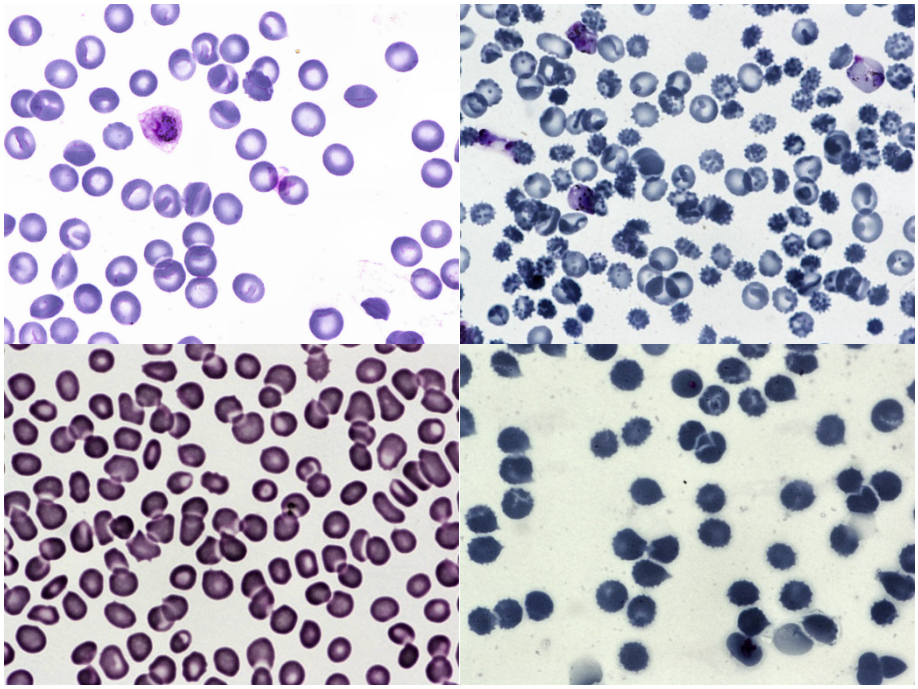

Figure 1. Original blood smear images from the used dataset

2.2. Image Pre-processing

Image pre-processing is a fundamental step in machine learning and image processing applications because these steps prepare the necessary data to obtain more accurate results. Pre-processing also includes operations such as reducing noise, increasing contrast, and adjusting image size, resulting in more reliable and consistent results. The basis of this study is to subject the images in the data set to certain image pre-processing steps before the analysis process.

Image Loading and Resizing: Each image and mask is loaded and resized to a specific target_size (256x256x3). This process standardizes the images to a fixed size, ensuring a consistent input size during the model training.

$$[R'(x,y) = R\left(\frac{x \cdot W_{original}}{W_{target}}, \frac{y \cdot H_{original}}{H_{target}}\right)] \quad (1)$$

In Equation (1), (R) represents the original image, (R') represents the resized image, ($W_{original}$) ve ($H_{original}$) represent the original width and height of the image, and (W_{target}) ve (H_{target}) represent the target width and height dimensions.

Normalization: Image and mask values are scaled from the [0, 255] range to the [0, 1] range. This enables the model to train faster and more stably because smaller input values provide less variance in weight updates and better gradient flow within the network.

$$[R''(i,j) = \frac{R'(i,j)}{255}] \quad (2)$$

In Equation (2), (R'')represents the image after normalization, (R') represents the resized image, and (i) and (j) represent pixel positions.

Grayscale Masking: Masks are loaded in grayscale, meaning they have only one channel without color information. This is because segmentation masks typically need to contain binary values (0 or 1) indicating the presence or absence of an object, and color information is not necessary for this purpose.

2.2.1. U-Net3+ and proposed model

The U-net, proposed by Ronneberger et al. in 2015 [20], is primarily a convolutional neural network architecture designed for image segmentation. The U-Net architecture is a developed image segmentation algorithm, primarily designed for tasks involving segmentation, classification, and image operations [21]. The training duration of U-Net is relatively short, featuring a simple design and fewer parameters. It requires less training data compared to other networks. U-net is symmetric, incorporating skip connections between the downsampling and upsampling paths.

The integration of features across various scales is a pivotal aspect of achieving precise segmentation. U-Net++, a modified iteration of U-Net distinguished by its embedded and densely connected skip connections, has been devised to address this need [22]. However, despite its advancements, this model still lacks in capturing adequate information, signalling a considerable scope for further refinement. In response to this, the proposed U-Net3+ architecture assumes heightened significance, strategically incorporating full-scale skip connections and introducing deep supervisions. These full-scale skip connections adeptly merge low-level details from feature maps across different scales with high-level semantic information. Concurrently, the deep supervisions effectively learn hierarchical representations from fully aggregated feature maps. Beyond the notable improvements in accuracy, U-Net 3+ also exhibits promising potential in enhancing computational efficiency by judiciously reducing network parameters, marking a comprehensive advancement in the field of image segmentation. Details of the architecture is given in Table 1. Figure 2 provides simplified summaries of U-Net, U-Net++, and U-Net 3+.

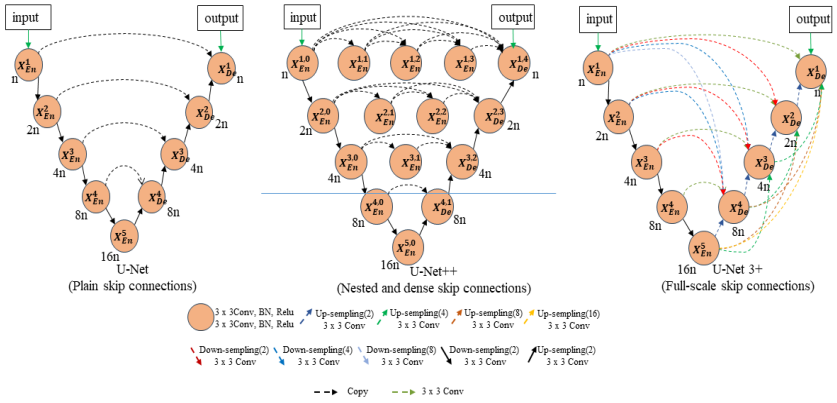

Figure 2. U-Net, U-Net++, and U-Net 3+ architecture [23].

Table 1. Details of the architecture

Layer	Layer Type	Details
Input Layer	Input	The input layer accepts input of size (256, 256, 3), indicating images with a resolution of 256 pixels in width, 256 pixels in height, and 3 color channels (RGB).
Conv Block 1	Conv2D + Activation (ReLU) + (Optional) Dropout	The first convolutional block utilizes a 3x3 kernel with 128 filters. It includes batch normalization, ReLU activation, and dropout.
MaxPooling	MaxPooling2D	A 2x2 MaxPooling operation is applied after the first convolutional block.
Conv Block 2	Conv2D + Activation (ReLU) + (Optional) Dropout	The second convolutional block employs a 3x3 kernel with 256 filters. It includes batch normalization, ReLU activation, and dropout to enhance the model's learning and generalization capabilities.
MaxPooling	MaxPooling2D	A 2x2 MaxPooling operation is applied
Conv Block 3	Conv2D + Activation (ReLU) + (Optional) Dropout	The third convolutional block uses a 3x3 kernel with 512 filters. It incorporates batch normalization, ReLU activation, and dropout to enhance the model's capacity to learn complex patterns and improve its generalization abilities.
MaxPooling	MaxPooling2D	A 2x2 MaxPooling operation is applied
Conv Block 4	Conv2D + Activation (ReLU) + (Optional) Dropout	The fourth convolutional block employs a 3x3 kernel with 1024 filters. It includes batch normalization, ReLU activation, and dropout to capture intricate features and further enhance the model's ability to generalize.
MaxPooling	MaxPooling2D	A 2x2 MaxPooling operation is applied
Bridge	Conv2D + Activation (ReLU)	The bridge layer, or skip connection, uses a 3x3 kernel with 2048 filters and includes ReLU activation. Skip connections are often used to facilitate the flow of information between the encoder and decoder parts of the U-Net architecture, aiding in the preservation of spatial information.
Upsample Block 1	UpSampling2D + Concatenate + Conv Block	An upsampling and concatenation operation is performed, followed by the application of a convolutional block. Upsampling is typically used to increase the spatial resolution of the feature maps.
Upsample Block 2	UpSampling2D + Concatenate + Conv Block	An upsampling and concatenation operation is performed, followed by the application of a convolutional block.
Upsample Block 3	UpSampling2D + Concatenate + Conv Block	An upsampling and concatenation operation is performed, followed by the application of a convolutional block.
Upsample Block 4	UpSampling2D + Concatenate + Conv Block	An upsampling and concatenation operation is performed, followed by the application of a convolutional block.
Output Layer	Conv2D + Activation (Sigmoid/Softmax)	The final layer uses a 1x1 kernel based on the number of classes. It includes either sigmoid or softmax activation, depending on the nature of the task
Total params: 125,547,521, Trainable params: 125,523,969, Non-trainable params: 23,552		

2.3. Evaluation metrics

Rigorous assessment of the U-Net 3+ architecture for blood cell segmentation involves the application of a comprehensive suite of evaluation metrics, addressing considerations of accuracy. The Equations (3)- (6) [24]:

- TP represents the number of pixels that truly belong to class P and are correctly classified as P by the model.
- TN denotes the count of pixels that truly belong to class N and are accurately classified as N by the model.
- FN signifies the number of pixels that actually belong to class P but are misclassified as N by the model.
- FP indicates the count of pixels that truly belong to class N but are misclassified as P by the model.

$$Accuracy = \frac{T_N+T_p}{T_N+T_p+F_N+F_p} \quad (3)$$

$$Precision = \frac{T_p}{T_p+F_p} \quad (4)$$

$$Recall = \frac{T_p}{T_p+F_N} \quad (5)$$

$$F1 - Score = \frac{2xPxR}{P+R} \quad (6)$$

The Jaccard Index, also known as the Intersection over Union (IoU) value, provides the percentage of overlap between predicted masks and ground truth masks. It is a metric that quantifies the similarity of two sets by measuring the intersection divided by the union and given in Equation (7) [25].

$$Jaccard\ (JAC) = \frac{TP}{TP+FN+FP} \quad (7)$$

The Dice Index is a metric that measures the similarity between predicted and underlying ground truth images, as expressed in Equation (8) [25].

$$Dice = \frac{2TP}{2TP+FN+FP} \quad (8)$$

The critical metric "Pixel Accuracy" is employed to evaluate the performance of segmentation models. This metric measures how well the model's predictions align with the ground truth data. Pixel Accuracy is calculated by dividing the number of pixels correctly classified by the model by the total number of pixels [26]. In other words, it quantifies the concordance between the predicted mask generated by the model and the actual mask and given in Equation (9).

$$Pixel\ Accuracy = \frac{pixels\ correctly\ classified}{the\ total\ number\ of\ pixels} \quad (9)$$

3. Experimental Results

In customizing the U-Net3+ architecture, various modifications are implemented to enhance segmentation accuracy and create a structure resistant to overfitting while preserving the fundamental principles of the U-Net3+ architecture. Among the changes made are strengthening the connections between convolutional layers, increasing the number of filters, and integrating hyperparameter optimization mechanisms. Specifically, dropout and learning-rate ratios were adjusted using Bayesian optimization to increase the model's generalization ability. This method provides flexibility in determining the optimal network structure and parameters during the model's adaptation to different datasets and noise profiles. Furthermore, advanced training strategies such as adaptive learning rate adjustment and early stopping are adopted to improve the efficiency of the training process. These strategies serve as mechanisms supporting the model's rapid convergence and protection against overfitting, contributing to more robust and reliable segmentation results. The flowchart of the system is given below:

1. *Data Loading and Pre-processing*
    - Images and masks are loaded.
    - Each image and mask are resized to a specified dimension.
    - Pixel values are normalized to a range between 0 and 1.
2. *Data Splitting*
    - Images and masks are split into training and testing sets.
3. *Model Creation (U-Net 3+)*
    - U-Net 3+ model is constructed.
    - The model is configured with a specific number of layers and filters.
4. *Hyperparameter Optimization (Bayesian Optimization)*
    - Optimal values for certain hyperparameters (e.g., dropout rate and learning rate) are searched.
5. *Model Training*

- The model is trained on different subsets of data using the k-Fold Cross-Validation method.
- Callbacks such as ModelCheckpoint, ReduceLROnPlateau, and EarlyStopping are utilized during training.

6. *Model Evaluation*
   - The trained model is evaluated on the test dataset.
   - Performance metrics (e.g., accuracy, precision, IoU, Dice Score) are computed.
7. *Analysis and Visualization of Results*
   - Training and validation losses, accuracies, and other metrics are visualized on graphs.
   - Model predictions on the test set are compared with actual labels for visual analysis.

Bayesian Optimization is a statistical method used to adjust the hyperparameters of our model, in this case, dropout_rate and learning_rate, to maximize the performance of our deep learning model. The goal of this method is to maximize the accuracy of our model on the validation dataset.
Firstly, the range of values to be explored for the model's hyperparameters is being defined. For example, a range can be set between 0 and 0.5 for the dropout rate, and for the learning rate (10^{-5}) and (10^{-2}). Next, the Bayes theorem is used to predict how the model will perform with these hyperparameter values. This theorem allows us to calculate the probability of the model's performance given certain hyperparameter values. Mathematically, this is expressed using the Bayes theorem as given in Equation (10):

$$[P(performance|hyperparameters) = \frac{P(hyperparameters|performance)\times P(performance)}{P(hyperparameters)} \quad (10)$$

In this formula, each term represents, respectively, the probability of the model's performance given the hyperparameters, the probability of hyperparameters given the model's performance, and the marginal distributions of these two probabilities. Finally, using this probability distribution, the most suitable hyperparameter combinations are determined for our model. This process ensures the adjustment of hyperparameters in a way that maximizes the performance of our model on the validation set. In summary, Bayesian Optimization provides us with the opportunity to fully harness the potential of our model. With this method, we can effectively manage the complex structure of our deep learning model and optimize its performance. Parameters obtained with Bayesian optimization are listed in Table 2.

Table 2. Obtained parameters with Bayesian optimization

	Dropout	**Learning Rate**
Initial Value	0.1	0.00001
Value after optimization	0.184389873055315	0.004261879524120684

ReduceLROnPlateau and EarlyStopping are callback methods utilized to optimize the training process of the U-Net 3+ model in our paper, with the goal of preventing issues like overfitting.

ReduceLROnPlateau (Reducing Learning Rate): ReduceLROnPlateau is employed to dynamically adjust the model's learning rate during training. Throughout the training process, if there is no improvement in a specified metric (e.g., validation loss) for a certain number of epochs, it reduces the learning rate. This method aids the model in making finer adjustments and prevents it from getting stuck in local minima.

The proposed U-Net 3+ model demonstrates excellent performance across multiple folds, as evidenced by the results presented in Table 3. Throughout the training process, the model consistently achieves low training and validation losses, indicative of its ability to minimize errors and generalize well to unseen data. The high values for accuracy, precision, recall, and area under the curve (AUC) further underscore the model's proficiency in accurately segmenting blood cells. Notably, the model maintains a high level of precision and recall, striking a balance between minimizing false positives and false negatives. The consistency of these results across different folds highlights the robustness and reliability of the proposed model. Results of the segmentation are shown in Figure 3.

Table 3. Results of the proposed model

fold	train_loss	val_loss	train_ accuracy	val_ accuracy	train_ precision	val_ precision	train_ recall	val_ recall	train_ auc	val_ auc
1	0.0334	0.0338	0.9798	0.9792	0.96047	0.9623	0.9720	0.9699	0.9814	0.9807
2	0.0331	0.0344	0.9797	0.9802	0.96041	0.9624	0.9732	0.9670	0.9812	0.9799
3	0.0333	0.0342	0.9798	0.9788	0.96005	0.9566	0.9725	0.9748	0.9820	0.9820
4	0.0328	0.0341	0.9799	0.9794	0.96117	0.9607	0.9723	0.9700	0.9817	0.9808
5	0.0321	0.0361	0.9805	0.9779	0.96089	0.9636	0.9740	0.9650	0.9817	0.9776

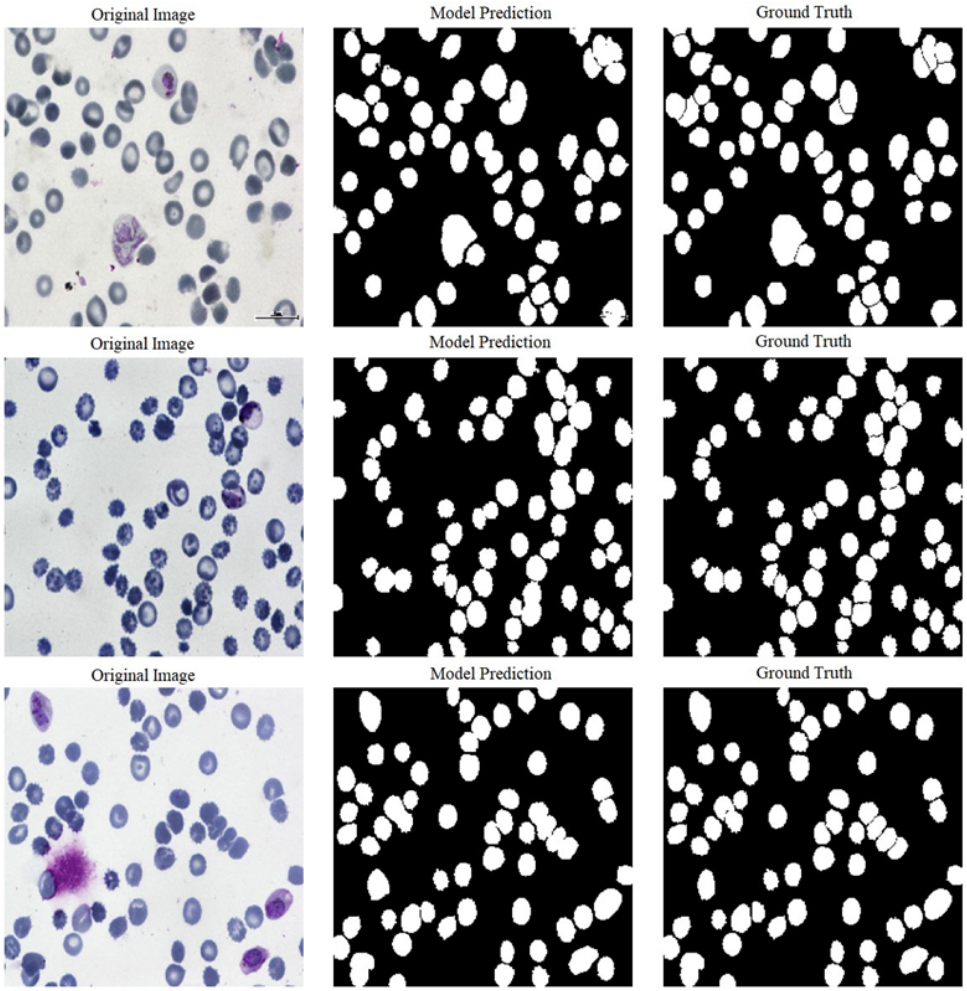

Figure 3. Results of the segmentation

In Table 4, the test results reinforce the model's effectiveness in segmentation tasks. The Mean IoU (Jaccard Index) of 0.9324 indicates a substantial overlap between the predicted and ground truth masks, emphasizing the model's ability to delineate cell boundaries accurately. The Dice score of 0.9667 further corroborates the model's segmentation accuracy. The Pixel Accuracy of 0.9796 signifies a high proportion of correctly classified pixels, attesting to the model's precision at the pixel level. Additionally, the exceptionally high precision value of 0.9968 underscores the model's capability to minimize false positives, crucial in medical image segmentation where accuracy is paramount. These results suggest that the proposed U-Net 3+ model excels in blood cell segmentation, providing accurate and reliable predictions across various evaluation metrics. The combination of low losses, high accuracy, and robust segmentation metrics positions the model as a promising solution for medical image segmentation tasks. In conclusion, the achieved performance metrics, particularly the high accuracy, precision, and spatial overlap metrics, demonstrate the effectiveness of the U-Net 3+ model for blood cell segmentation. The model exhibits robust generalization across different folds, showcasing its potential for accurate and reliable

segmentation of blood cell images. Loss and accuracy graphs for average training and validation are given in Figure 4.

Table 4. Test results of the proposed system

Metrics	Value
Mean IoU (jaccard index)	0.9324
Dice score	0.9667
Pixel accuracy	0.9796
Precision	0.9968

Figure 4. Loss and accuracy graphs for average training and validation

Table 5. Assessment of segmentation performance across various algorithms on the same dataset

Method	Dice-coefficient (%)	Jaccard Index (%)	Reference
Otsu's method	92.60	86.50	[19]
BHT	52.50	49.48	
Watershed	78.21	68.21	
U-Net	93.09	87.16	
U-Net++	88.80	81.44	
TernausNet	93.38	87.65	
R2U-Net	86.76	77.77	
Attention U-Net	91.00	83.73	
Attention R2U-Net	78.52	65.28	
FCN	85.41	75.29	
U-Net 3+	96.67	93.24	Prosed Model

Our model exhibits a significant advantage over other methods in terms of segmentation performance. For instance, in terms of both Dice coefficient and Jaccard index, our U-Net 3+ model outperforms all other methods. Specifically, while our U-Net 3+ model achieves a Dice coefficient of 96.67% and a Jaccard index of 93.24%, its closest competitor, TernausNet, achieves values of 93.38% and 87.65% respectively. Other methods in the comparison include Otsu's method, BHT, Watershed, U-Net++, R2U-Net, Attention U-Net, Attention R2U-Net, and FCN. Each of these methods employs different approaches to fulfill specific segmentation tasks. Additionally, it is crucial to understand why our model outperforms others by evaluating the performance of other methods in comparative analysis. Factors such as an enhanced architecture, more effective feature extraction, or optimized

hyperparameters could contribute to the success of our model. This way, the contribution of the study and the value of our model can be better understood.

4. Discussion

This chapter delves into the findings, providing an in-depth analysis of the performance of the enhanced U-Net 3+ model for blood cell segmentation. The model, which incorporates advancements such as strengthened connections and an increased number of filters, has demonstrated notable improvements in accuracy and precision across multiple folds and the test dataset. These structural enhancements are critical in enabling the model to minimize errors and exhibit robust generalization to novel data. In particular, the bolstered connections facilitate more effective information flow within the network, while the augmented filter numbers enable finer feature extraction, which are both essential for precision in segmenting intricate blood cell structures. The use of Bayesian optimization for hyperparameter tuning is a key aspect of refining the model. This optimization strategy, by systematically adjusting parameters such as dropout and learning rates, has significantly contributed to the adaptability and accuracy of the model. The emphasis on Bayesian methods underscores our commitment to leveraging advanced statistical techniques to fine-tune the model's performance, ensuring optimal generalization across diverse datasets. The achieved mean IoU (Jaccard Index) of 0.9324 and Dice score of 0.9667 serve as testaments to the model's efficacy in accurately predicting cell masks, thereby highlighting its potential in medical image analysis. These metrics reflect not only the model's precision in delineating cell boundaries but also its capability to achieve consistency in segmentation tasks. The exceptional Pixel Accuracy of 0.9796 and high precision value of 0.9968 further highlight the model's adeptness at minimizing false positives, a critical aspect in the realm of medical image segmentation, where accuracy is of paramount importance. This study positions the proposed U-Net 3+ model as a state-of-the-art solution for blood cell segmentation, representing a considerable advancement in the field of deep-learning-based medical image segmentation. The model's ability to accurately and reliably segment images is a significant step forward, and its performance aligns with and extends existing literature, demonstrating the profound impact of advanced architectures and optimization techniques in achieving superior results. However, it is essential to recognize the limitations of this study to gain a comprehensive understanding. The model's performance may be influenced by the specific characteristics of the dataset, highlighting the need for further validation across diverse datasets. Variations in image quality and potential biases within the dataset can impact the model's generalization capabilities. Future research directions should explore transfer-learning approaches to enhance the model's adaptability to different imaging modalities and investigate its applicability in various medical imaging scenarios.

5. Conclusions

This study introduces a novel and customized U-Net 3+ model for blood cell segmentation, integrating substantial structural improvements and advanced optimization techniques. The model has demonstrated exceptional performance, as evidenced by consistently low training and validation losses, high accuracy metrics, and robust segmentation indices. The use of Bayesian optimization for hyperparameter tuning has been instrumental in enhancing the generalization capabilities of the model. The achieved Mean Intersection over Union (IoU) of 0.9324 and Dice score of 0.9667 highlight the model's proficiency in accurately predicting cell masks, emphasizing its potential utility in medical image analysis. The pixel accuracy of 0.9796 and the precision of 0.9968 further illustrate the model's precision at both the pixel and class levels, which is crucial in medical scenarios where accuracy is paramount.

The discussion provides a nuanced analysis, recognizing the model's strengths while acknowledging potential limitations and suggesting directions for future research. This study contributes significantly to the field of deep learning-based medical image segmentation, demonstrating the effectiveness of customized architectures and optimization strategies. In conclusion, the U-Net 3+ model, with its high accuracy and reliability for segmenting blood cells, has emerged as an innovative and effective solution in this domain, setting a benchmark for future advancements.

References

[1] Zhu Z, et al. RETRACTED: BCNet: A Novel Network for Blood Cell Classification. Front Cell Dev Biol. 2002; (9): 813996.

[2] Toptaş M and Hanbay D. Mikroskobik Kan Hücre Görüntülerinin Güncel Derin Öğrenme Mimarileri ile Bölütlemesi. Mühendislik Bilimleri ve Araştırmaları Dergisi, 2023; 5(1): 135-141.

[3] Habibzadeh M, Jannesari M, Rezaei Z, Baharvand H, Totonchi M. Automatic white blood cell classification using pre-trained deep learning models: Resnet and inception. InTenth international conference on machine vision (ICMV 2017) 13 April 2018: SPIE. Vol. 10696, pp. 274-281.

[4] Sahin ME. Image processing and machine learning-based bone fracture detection and classification using X-ray images. Int J Imaging Syst Technol. May 2023; 33(3): 853-65.

[5] Şahin ME. A Deep Learning-Based Technique for Diagnosing Retinal Disease by Using Optical Coherence Tomography (OCT) Images. Turkish Journal of Science and Technology. 1 July 2022; 17(2): 417-26.

[6] Ulutas H, Sahin ME, Karakus MO. Application of a novel deep learning technique using CT images for COVID-19 diagnosis on embedded systems. Alexandria Eng J. 1 July 2023; 74: 345-58.

[7] Alam MM, Islam MT. Machine learning approach of automatic identification and counting of blood cells. Healthcare Technol Lett. August 2019; 6(4): 103-8.

[8] Shahin AI, Guo Y, Amin KM, Sharawi AA. White blood cells identification system based on convolutional deep neural learning networks. Comput Methods Programs Biomed. 1 January 2019; 168: 69-80.

[9] Banik PP, Saha R, Kim KD. An automatic nucleus segmentation and CNN model based classification method of white blood cell. Expert Syst. Appl. 1 July 2020; 149: 113211.

[10] Macawile MJ, Quiñones VV, Ballado A, Cruz JD, Caya MV. White blood cell classification and counting using convolutional neural network. In2018 3rd International conference on control and robotics engineering (ICCRE) 20 April 2018: IEEE. pp. 259-263.

[11] Yildirim M, Çinar A. Classification of white blood cells by deep learning methods for diagnosing disease. Rev d'Intelligence Artif. November 2019; 33(5): 335-40.

[12] Lu Y, Qin X, Fan H, Lai T, Li Z. WBC-Net: A white blood cell segmentation network based on UNet++ and ResNet. Applied Soft Computing. 1 March 2021; 101: 107006.

[13] Reena MR, Ameer PM. Localization and recognition of leukocytes in peripheral blood: A deep learning approach. Comput. Biol. Med. 1 November 2020; 126: 104034.

[14] Bozkurt F. Classification of blood cells from blood cell images using dense convolutional network. Journal of Science, Technology and Engineering Research. November 2021; 2(2): 81-8.

[15] Nahzat S, Bozkurt F, Yağanoğlu M. White blood cell classification using convolutional neural network. Journal of Science, Technology and Engineering Research. 2022; 3(1): 32-41.

[16] Khouani A, El Habib Daho M, Mahmoudi SA, Chikh MA, Benzineb B. Automated recognition of white blood cells using deep learning. Biomed Eng Lett. August 2020; 10: 359-67.

[17] Zhang M, Li X, Xu M, Li Q. Automated semantic segmentation of red blood cells for sickle cell disease. IEEE J Biomed Health Inf. 22 June 2020; 24(11): 3095-102.

[18] Dataset, https://github.com/Deponker/Blood-cell-segmentation-dataset.

[19] Depto DS, Rahman S, Hosen MM, Akter MS, Reme TR, Rahman A, Zunair H, Rahman MS, Mahdy MR. Automatic segmentation of blood cells from microscopic slides: a comparative analysis. Tissue and Cell. 1 December 2021; 73: 101653.

[20] Ronneberger O, Fischer P, Brox T. U-net: Convolutional networks for biomedical image segmentation. InMedical image computing and computer-assisted intervention–MICCAI 2015: 18th international conference, 5-9 October 2015; Munich, Germany: proceedings, part III, Springer International Publishing. pp. 234-241.

[21] Yan X, Tang H, Sun S, Ma H, Kong D, Xie X. After-unet: Axial fusion transformer unet for medical image segmentation. InProceedings of the IEEE/CVF winter conference on applications of computer vision 2022 pp. 3971-3981.

[22] Huang H, Lin L, Tong R, Hu H, Zhang Q, Iwamoto Y, Han X, Chen YW, Wu J. Unet 3+: A full-scale connected unet for medical image segmentation. InICASSP 2020-2020 IEEE international conference on acoustics, speech and signal processing (ICASSP) 4 May 2020: IEEE. pp. 1055-1059.

[23] Deng Y, Hou Y, Yan J, Zeng D. ELU-net: An efficient and lightweight U-net for medical image segmentation. IEEE Access. 31 March 2022; 10: 35932-41.

[24] Sahin ME. Deep learning-based approach for detecting COVID-19 in chest X-rays. Biomed Signal Process Control. 1 September 2022; 78: 103977.

[25] Vasconcelos FF, Medeiros AG, Peixoto SA, Reboucas Filho PP. Automatic skin lesions segmentation based on a new morphological approach via geodesic active contour. Cognit Syst Res. 1 June 2019; 55: 44-59.

[26] Liu J, Yildirim O, Akin O, Tian Y. AI-driven robust kidney and renal mass segmentation and classification on 3D CT images. Bioengineering. 13 January 2023; 10(1): 116.

Turkish Journal of Science & Technology
19(2), 497-508, 2024

Research Paper
https://doi.org/10.55525/tjst.1445681

Automatic Classification of Defective Photovoltaic Module Cells Based on a Novel CNN-PCA-SVM Deep Hybrid Model in Electroluminescence Images

Andaç İMAK[1*],
[1] Department of Electrical and Electronic Engineering, Faculty of Engineering, Munzur University, Tunceli, Turkey
[*1] andacimak@munzur.edu.tr

(Geliş/Received: 01/03/2024; Kabul/Accepted: 28/09/2024)

Abstract: In today's world, the rapid development of photovoltaic (PV) power plants has facilitated sustainable energy production. Maintenance and defect detection play crucial roles in ensuring the continuity of energy production. The manual inspection of electroluminescence (EL) images of PV modules requires significant human power and time investment. This study presents a method for the automatic fault detection of PV cells in EL images using hybrid deep features optimized with a principal component analysis (PCA) feature selection algorithm. A lightweight and high-performance model that combines the strengths of convolutional neural network (CNN) architectures was proposed. First, data augmentation techniques were employed owing to the imbalance between the defective and functional classes in the dataset containing EL images. In experimental studies conducted by integrating the PCA algorithm into MobileNetV2, DenseNet201, and InceptionV3 CNN models, accuracy, precision, recall, and F1-score values of 92.19%, 92%, 90%, and 91%, respectively, were achieved. When the results were analyzed, it was observed that the proposed method was effective in detecting faults in PV panel cells.

Key words: Deep learning, photovoltaic cells, defect detection, feature selection.

Yeni Bir CNN-PCA-SVM Derin Hibrit Modeline Dayalı Arızalı Fotovoltaik Modül Hücrelerinin Otomatik Sınıflandırılması

Öz: Günümüzde sürdürülebilir enerji üretimi için fotovoltaik (PV) enerji santrallerinin hızlı gelişimine olanak sağlamıştır. Enerji üretiminin sürekliliğinin sağlanması için bakım ve arıza tespiti önemli bir rol oynamaktadır. PV modüllerinin elektrolüminesans (EL) görüntülerinin manuel olarak incelenmesi, büyük bir insan gücü ve zaman yatırımını gerektirir. Bu çalışmada, EL görüntülerde PV hücrelerinin otomatik arıza tespiti için hibrit derin özniteliklerin, temel bileşenler analizi (PCA) öznitelik seçme algoritması ile optimize edilen bir yöntem sunmaktadır. Evrişimsel sinir ağı (CNN) mimarilerinin güçlü yönlerini birleştiren, hafif ve yüksek performanslı bir model önerilmektedir. İlk olarak EL görüntülerini içeren veri setindeki arızalı ve işlevsel sınıflarına ait veri dengesizliğinden dolayı veri arttırma teknikleri kullanılmıştır. MobileNetV2, DenseNet201 ve InceptionV3 CNN modellerine entegre edilen PCA algoritması ile hibrit kullanılarak gerçekleştirilen deneysel çalışmalarda doğruluk, kesinlik, duyarlılık ve F1-skoru değerleri sırasıyla %92.19, %92, %90 ve %91 olarak elde edilmiştir. Sonuçlar analiz edildiğinde, önerilen yöntemin PV panel hücrelerindeki arızaların tespitinde etkili bir performansa sahip olduğu gözlemlenmiştir.

Anahtar kelimeler: Derin öğrenme, fotovoltaik hücreler, kusur tespiti, özellik seçimi.

1. Introduction

The extensive utilization of fossil fuels has led to severe environmental pollution issues, resulting from an increase in carbon dioxide and other greenhouse gases in the atmosphere. This situation has triggered challenging global issues such as climate change, air pollution, and excessive use of natural resources. Therefore, the increasing energy consumption and demand for environmental protection underscore an urgent need for sustainable and clean energy sources. In recent years, there has been growing interest in renewable energy sources such as geothermal, hydroelectric, solar, and wind power. Renewable resources have emerged solutions capable of meeting energy needs while reducing environmental impacts [1], [2]. This transition plays a significant role in supporting environmental sustainability and contributes to a cleaner and more efficient future in the energy sector. Compared with wind energy systems, there has been a rapid increase in the interest and capacity of solar energy systems worldwide. Solar energy is one of the most attractive renewable energy sources because of its abundance, easy accessibility, and free usage [2], [3]. This situation is supported by the development of Photovoltaic (PV) technology for solar energy conversion and cost reduction.

PV modules, designed to last 25 years or longer, can experience various failure modes owing to environmental factors such as mechanical stress, humidity, high temperatures, and exposure to ultraviolet radiation. Consequently, these factors can degrade the solar cell performance even within the 25-year manufacturer warranty period [4], [5]. PV panels are typically installed outdoors with the assistance of aluminum frames and glass

[*] Corresponding author: andacimak@munzur.edu.tr. ORCID Number of authors: 0000-0002-3654-040X

lamination to protect them from environmental conditions. However, harsh climatic conditions and mechanical impacts during installation can lead to various failure modes, such as panel breakage, cracking, falling tree branches, snow accumulation, insect traces, burn marks, shading, and color changes. Additionally, manufacturing defects can also cause damage to PV panels, impeding the flow of current in PV systems and reducing the production capacity and efficiency. Therefore, effectively addressing the issues in solar energy technologies is crucial for ensuring sustainable and efficient energy production [6], [7], [8], [9].

Generally, the majority of solar power plants consist of thousands of modules with multi-megawatt (MW) capacity spread over large areas. However, monitoring this large number of modules individually is laborious and expensive. Studies reveal that long-term outdoor use of PV modules may be subject to premature failure due to a variety of factors, including lack of maintenance, enclosure issues, thermal cycling, grounding issues, and corrosive environments [10], [11], [12]. Efforts to identify power attenuation caused by microcracks in PV modules are going beyond traditional methods and are being strengthened by deep learning techniques. According to previous studies, microcracks can lead to a strength loss between 0.9% and 42.8% and cause hotspot effects [13], [14]. An advanced approach to detect such defects involves infrared thermal (IRT) imaging technology alongside I-V curve analysis [15]. However, the low resolution of these methods may limit the detection of microcracks that do not affect power efficiency.

High-resolution electroluminescence (EL) imaging systems have become an effective technology for defect detection in PV modules [16]. EL imaging offers a nondestructive approach capable of identifying microcracks and other defects with high resolution [17]. Defects in EL images typically manifest as dark grey lines and areas. However, the use of traditional methods to manually identify these defects is time consuming and may offer limited performance. In this context, deep learning techniques accelerate the processes of automatic defect detection and analysis, offering the potential to effectively identify microcracks in PV modules.

Owing to the powerful feature extraction capabilities of convolutional neural networks (CNNs), particularly in deep learning techniques, they have become increasingly popular for the detection of defects in EL images. Artificial intelligence models enable rapid detection of defects in EL images obtained over large areas, thereby streamlining the process. In the industrial field, there is a growing demand for deep architectural models that can satisfy the requirements of lightweight and effective detection networks in terms of both higher accuracy and speed in defect detection.

Research on the detection of surface defects in PV cells show an increasing trend. Tsanakas et al. in their study proposed the use of image histogram and Canny edge detector to detect defective cells through thermal images and separate these cells into specific regions. By applying the proposed method to two PV arrays mounted on a roof, they successfully detected 40 of the 43 defective cells [18]. Pratt et al. investigated the use of a U-Net-based semantic segmentation model of EL images to detect defects in solar PV modules. Their experimental results suggested that the trained U-net model can be used to quantify damage and determine the electrical performance during accelerated stress tests of PV modules [19]. Oliveira et al. conducted a study to detect defective PV modules in IRT images using a two-stage method comprising Laplacian-based edge detection and a CNN algorithm to segment defective solar panels. They classified defect detection using the developed neural network model into three categories [20]. Deitsch et al. used a CNN neural network model to detect defects on the surface of PV modules with EL images. They compared the results of the traditional machine learning method and the deep learning architecture, observing a 6% higher performance than the traditional machine learning method, with an accuracy score of 88.36% [21]. Tang et al. proposed a model using data augmentation and CNN architectures for automatic classification of defects in an EL image. To obtain a large number of high-resolution EL images, the generative adversarial network (GAN) image augmentation technique was utilized. An experimental study was subsequently conducted using the VGG16, ResNet50, Inception V3, and MobileNet architectures [22]. Hong et al. proposed a model containing YOLOv5 and the ResNet algorithm for defect detection in a PV module containing visible and infrared images. They observed that the proposed method significantly increased defect detection accuracy by up to 95% [23]. Zhao et al. proposed a CNN-based system for defect detection in PV modules that contains 19 types of defect classes to meet the inspection requirements of the production line. A dataset consisting of 5983 EL images was created, and using the labeled images, 19 different classes of defects were identified [24]. Sizkouhi et al. presented an autonomous fault-detection method that was developed to automatically detect common faults and defects that can be visually noticed in their work. The proposed network is based on a VGG16 model in an encoder-decoder architecture. Experimental studies have shown that the proposed network can precisely predict PV modules at the pixel level with an average accuracy of 98% and 93%, respectively [25]. There are studies examining the effectiveness of the YOLO algorithm for hotspot detection in PV modules and defect detection in solar power plants. There are studies examining the effectiveness of the YOLO algorithm for hotspot detection in PV modules and defect detection in solar power plants [26], [27], [28]. In this study, Açıkgöz and Korkmaz employed a transfer learning approach using SqueezeNet to create skip connections from the firing modules. They achieved a performance of 91.29% using the proposed method [29]. Demirci et al. compared the

performances of these models using Alexnet, GoogleNet, MobilenetV2 and SqueezeNet transfer learning methods. Although the training load decreased with the transfer learning method, accuracy rates remained relatively low, between 76% and 79% [30]. In later years, Demirci et al. proposed an architecture in which 4 different deep learning architectures were used as a hybrid. In the PV dataset, they allocated 80% for training and 20% for testing for two classes. 5120 features were obtained with the deep network model, and 2000 sub-features were obtained with the minimum redundancy maximum relation (mRMR) algorithm. As a result of classification with machine learning methods such as support vector machine (SVM), k-nearest neighbour (KNN), decision tree (DT), random forest (RF) and naive bayes (NB), high accuracy rates of 94.52% were obtained for 2 classes (defective/functional) with the best performance SVM. In addition, a lightweight CNN architecture (L-CNN) they proposed in this study was trained from scratch without initial weights and achieved an accuracy rate of 89.33% [31].

Despite the utilization of advanced image processing and deep learning techniques in the literature, there are still many shortcomings in defect detection in PV modules. Therefore, efforts are being made to develop new methods to improve the reliability and efficiency of energy systems.

In this study, a deep learning-based classification method was proposed to detect faults in PV panel cells from EL images. The proposed method consists of a two-stage system that, includes deep learning architectures and a feature selection algorithm. The model provides a fast and simple fault detection method that utilizes effective deep learning architectures such as MobileNet V2, DenseNet201, and InceptionV3. Although MobileNetV2 stands out for its lightweight structure and high performance, DenseNet201 and InceptionV3 are deep network architectures capable of successfully handling large and complex feature spaces. In addition to the designed hybrid transfer learning approach, the integration of the principal component analysis (PCA) feature selection algorithm allows the model to focus on more effective and informative subset features, thus enhancing the usefulness of the method. The experimental studies resulted in an accuracy score of 92.19% with the proposed method. This hybrid model, reinforced with transfer learning approaches, provides a practical solution for classifying faults in PV panel cells with a fast implementation and more effective feature selection.

The remainder of this paper is organized as follows. In the first section, some information about the PV panel cells is presented. In the materials and methods section, detailed information is provided regarding the dataset used, deep models, feature selection algorithm, and architectural structure of the proposed model. The third section presents the experimental results. The final section presents the conclusions and potential future research directions.

2. Material and Methods

2.1. Dataset description and data augmentation

In this study, a dataset obtained from high-resolution EL images of both monocrystalline and polycrystalline PV panels was utilized [21], [32]. This publicly available dataset comprises 2624 EL images with a resolution of 300×300 pixels. It included 44 different PV panels, consisting of 18 monocrystalline and 26 polycrystalline panels. Among a total of 2624 images, 715 images are categorized as label 1 (defective), 295 images as label 0.66 (having surface defects), 106 images as label 0.33 (having minor defects without full faults), and 1508 images as label 0 (functional) without any detectable defects. Only the EL images with defective and functional labels were used in this study. The input images were resized to 224×224 pixels. Downsizing the input size helps optimize resource usage by reducing the computational workload. Figure 1 illustrates a few EL sample images belonging to defective and functional classes in the dataset used in the study.

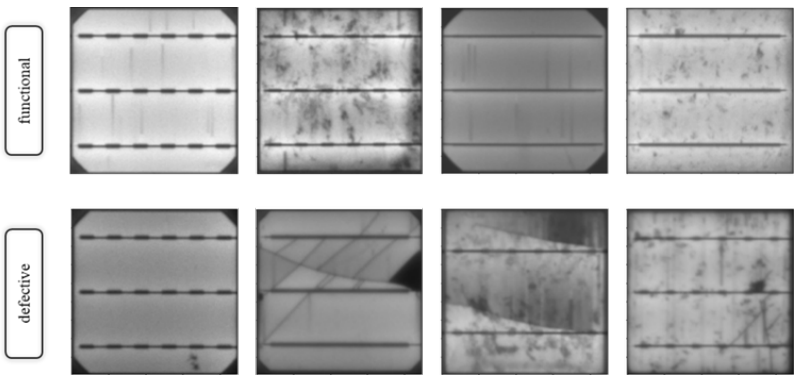

Figure1. Sample EL images of functional and defective classes

Data augmentation is a highly efficient technique for growing datasets with a small number of images. Effective data augmentation strategies can lead to a significant improvement in the system performance in image classification [33], [34]. The PV dataset edited in this study contained 2,223 EL images belonging to defective and functional classes. However, it is noteworthy that there are only 715 images for the defective class, which is less than half of the functional class. Because this unbalanced distribution may particularly affect the training performance of the proposed network, the number of samples needs to be increased. A system containing data augmentation techniques was used under Albumentation heading within Python libraries. The augmented synthetic images shown in Figure 2 were obtained by using horizontal flip, random rotation 90°, and vertical flip in the specified library for the images of the defective class in the training set.

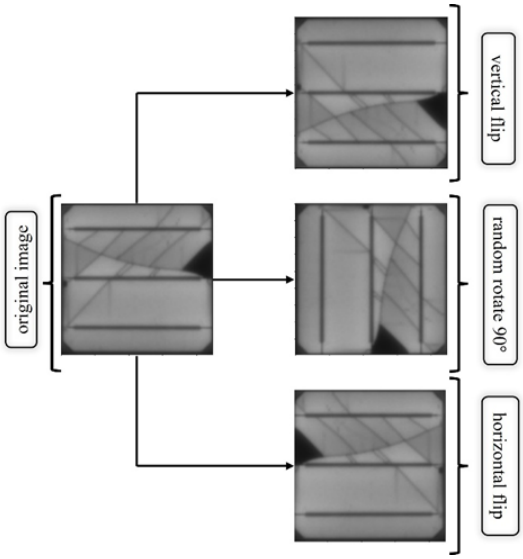

Figure 2. Synthetic images obtained with data augmentation techniques

2.2. Deep models and PCA

Deep learning architectures, such as InceptionV3, DenseNet201, and MobileNetV2, have proven their performance worldwide and have gained great popularity in recent years. These three architectures are known for their impressive success with large datasets. In particular, the InceptionV3 architecture is an improved and optimized version of the previous versions, InceptionV1 and InceptionV2. This architecture builds on previous models, such as GoogleNet by Szegedy et al. It provides versatile architecture that can successfully handle complex feature spaces [35]. The Dense201 model stands out because it optimizes the information transfer at the maximum level using dense connections. Dense connectivity is a structure in which the features obtained from each layer are connected to all the layers in the previous layer. This contributes to a more effective transfer of knowledge and to increases the learning capabilities of deeper networks [36], [37]. MobileNetV2 has a lightweight structure and effective performance in the field of CNN. This model is specifically designed for situations with resource constraints or application requirements. The proposed technique was based on the concept of MobileNetV2, an evolved version of MobileNet. MobileNetV2 offers a more effective and powerful convolutional neural network model by improving the features of the original MobileNetV1 [38].

Feature selection is the process of determining a subset that best represents the data and reduces the dimensionality while minimizing information loss. In this study, the principal component analysis (PCA) algorithm was used to find the most effective transformation that can express deep features with fewer variables. This method, proposed by Karl Pearson, minimizes information loss by determining the directions of the principal components while preserving the maximum variance without considering the class label. In this way, the representation of the data is strengthened, and the deep features analyzed are found in a more meaningful manner [39], [40].

2.3. Classification Method

Support Vector Machines (SVM) are a machine learning algorithm that generally separates data into different classes with a defined hyperplane. The primary objective of SVM is to identify the optimal hyperplane for data separation in classification tasks (as illustrated in Figure 3). The SVM algorithm, known for its success in classification and regression, aims to reduce generalization error when applied to unknown data [41].

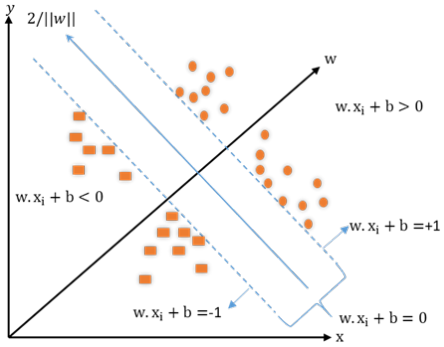

Figure 3. General illustration of SVM structure

The basic working principle of SVM is to keep the distance between the closest data points belonging to two classes at the maximum level. The higher the distance between the classes, the higher the classification performance. Suppose a d-dimensional dataset x(i) and an n-dimensional training set with binary class labels (-1,1). The SVM algorithm tries to obtain the hyperplane wx + b = 0 where the maximum level of the closest distance between the data points belonging to two classes is obtained [42].

The margin is defined as shown in Equation (1):

$$\text{Margin} = \frac{2}{||\text{w}||} \tag{1}$$

Here, w is the weight vector, ||·|| is the Euclidean norm of w. To maximize the hyperplane distance between classes, it is equivalent to minimizing ||w|| in accordance with the conditions outlined in Equation (2):

$$\begin{aligned} &\min \frac{1}{2}||\text{w}||^2 \\ &\text{y}_\text{i}(w.\text{x}_\text{i} + \text{b}) \geq 1 \end{aligned} \tag{2}$$

The optimization problem can be solved by converting it into binary form using the Lagrange multipliers in Equation (3):

$$L(w,b,a) = \frac{1}{2} * \left|\left|\text{w}\right|\right|^2 - \sum a(i) * [y((i) * (w \cdot x(i) + b) - 1] \tag{3}$$

Here, a(i) represents the Lagrange multiplier. The most appropriate w (weight) and b(bias) values can be found by maximizing L(w,b,α), subject to the constraints α(i) ≥ 0 and ∑α(i) * y(i) = 0. SVM tries to define the hibernation plane separating positive and negative examples in linearly separable data. Also, in some classification problems, if the training data is not linearly separable, a kernel function is used to transform it to a higher dimensional space. Therefore, the non-linearly separable examples are transferred from the current space to various spaces with kernel functions such as radial basis function (RBF) and Gaussian [43], [44].

2.4. Proposed Method

In the proposed method, image augmentation techniques were first applied to the original dataset to ensure the optimal learning of CNN models. In the second step, the increased data were used as input to the proposed hybrid transfer learning methods consisting of MobileNetV2, DenseNet201, and InceptionV3 deep architectures. In addition, a global average pooling layer has been added to the last section to increase the representation ability of the features obtained from the transfer learning methods used. The PCA feature selection algorithm was applied

separately to the various features obtained from the three different transfer learning models. The purpose of this step was to improve the representation of the feature set obtained from the model and to take advantage of the dimensionality reduction. As the second step in obtaining features from the model, the separated features were combined to obtain a more comprehensive perspective. These concatenated features were subjected to PCA. At this stage, feature selection was observed to play a critical role; therefore, a comprehensive analysis was conducted to determine the most appropriate feature subset. This analysis includes accuracy assessments performed with support vector machine (SVM) [41] applied to a series of values, starting from 50 and increasing the number of components by 25 to 500. This rigorous evaluation process was carried out to determine the best optimized values for the number of components of the PCA, regularization parameter (C) of the SVM, and coefficient (γ) of the RBF kernel. These optimum parameter values were used to obtain the ideal performance for the classifier model and ensure the accurate detection of faults in PV panel cells. Consequently, these new features were classified using the SVM algorithm, and a high-performance model was created to detect faults in PV panel cells. The block diagram of the proposed method is shown in Figure 4.

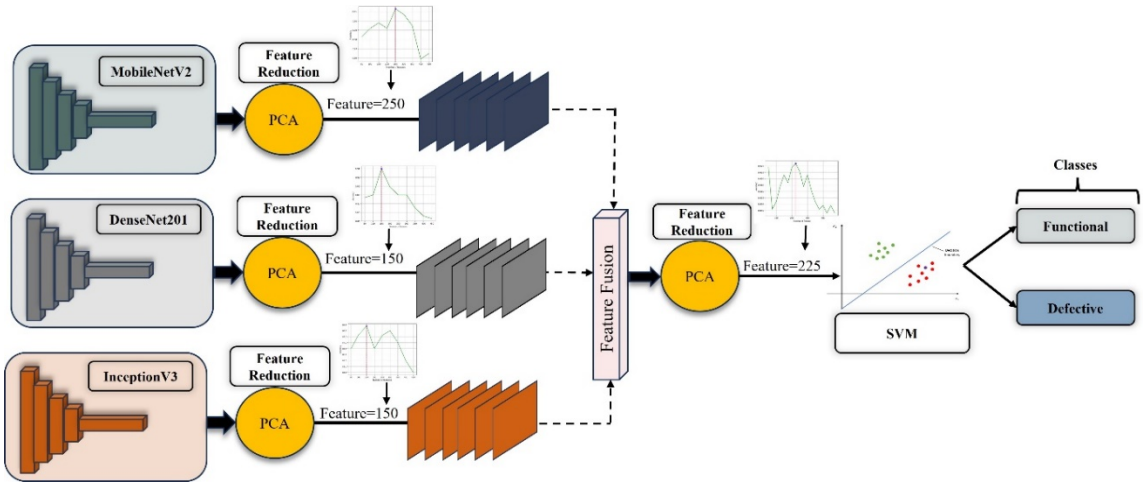

Figure 4. Block diagram of the proposed hybrid method

3. Experimental Results

In experimental studies, as a first step, 70% of the images in the data set are divided into training, 15% for testing, and 15% for validation. In a second step, data augmentation techniques were applied to the defective class section due to the irregularity between the defective and functional classes in the images allocated for training [45], [46], [47].

Performance metrics such as accuracy, precision, recall and F1-score were used to analyze the results obtained in the deep learning method proposed for PV cell defective detection. Performance metrics can be defined by the following mathematical Equations (4 to 7)

$$\text{Accuracy} = (\text{TP} + \text{TN})/(\text{TP} + \text{FN} + \text{TN} + \text{FP}) \quad (4)$$

$$\text{Precision} = \text{TP}/(\text{TP} + \text{FP}) \quad (5)$$

$$\text{Recall} = \text{TP}/(\text{TP} + \text{FN}) \quad (6)$$

$$\text{F1-score} = 2\,\text{TP}/(2\text{TP} + \text{FP} + \text{FN}) \quad (7)$$

It consists of 4 basic parameters obtained from the confusion matrices: true positive (TP), true negative (TN), false positive (FP) and false negative (FN).

Experimental studies on fault diagnosis in PV panel cells were carried out meticulously using state-of-the-art software such as Python 3.7.13, Tensorflow 2.8.0 and Keras 2.8.0. In addition, it was compiled using hardware technologies such as Intel(R) Xeon(R) CPU @ 2.30GHz, 27.6 GB RAM, Tesla T4- 16. During the training process, the epoch size was determined as 100 and the batch size was 16. The 'Adam' optimization method was used with a learning rate of 0.0001. The initial learning rate was set to 0.0001, and when the validation loss did not decrease

after 10 epochs, the learning rate was reduced to 0.00001 using ReducLROnPlateau. Binary crossentropy loss function was used in these models. These adjustments were carefully selected to achieve optimal training results for PV panel cell defective classification. The hyperparameters used in the MobileNetV2, DenseNet 201 and InceptinV3 CNN models are given in Table 1.

Table 1. Hyper-parameter values used in hybrid-CNN models

CNN models	Image Size	Optimization Methods	Momentum	Epoch	Mini Batch	Learning Rate
MobileNetV2	224×224	Stochastic Gradient Descent	0.9	50	16	1e-4
DenseNet 201						
InceptionV3						

As shown in the block diagram given in Figure 4, the proposed approach consists of three main stages: extraction of deep features, feature selection, and classification. The study analyzes how the hybrid use of transfer learning methods and the inclusion of feature selection algorithms contribute to the overall success. In the task of feature extraction, these CNN models utilize a global average pooling layer for their outputs, aiming to maintain the learning levels of the CNN model optimally. The curves of the proposed MobileNetV2, DenseNet201, and InceptionV3 transfer learning methods are shown in Figure 5. Figure 5 illustrates the training (in red) and validation accuracy curves (in green). It also includes loss and accuracy curves for both the training and validation sets.

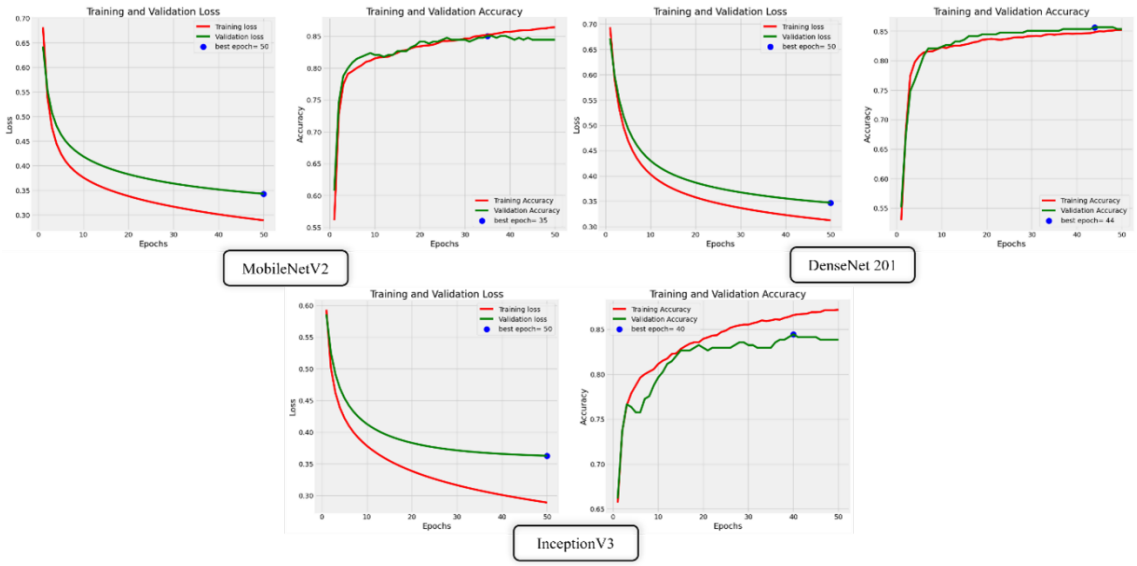

Figure 5. Loss and accuracy graphs obtained with the proposed deep architectures

As seen in Figure 5, training accuracies increased by over 80% in the first few steps, and similarly training loss values regularly dropped below 0.5. In the first stage, the features obtained from the last layer (global average pooling) of three different transfer learning methods, namely MobileNetV2, DenseNet 201 and InceptinV3, without including the PCA feature selection algorithm, and the results of classifying these features with the SVM classification algorithm are shown in Table 2.

Table 2. Results of the proposed methods (a system where PCA is not used)

CNN models+SVM	Accuracy	Precision	Recall	F1-score
MobileNetV2	0.84	0.82	0.84	0.83
DenseNet 201	0.84	0.82	0.83	0.83
InceptionV3	0.85	0.83	0.85	0.84

When referring to Table 2, it becomes evident that in the three transfer learning methods, MobileNetV2 and DenseNet 201 achieved similar performance results with 84% accuracy, 82% precision, approximately 84% recall, and 83% F1-score. On the other hand, the InceptionV3 CNN model outperformed the other two methods with 85% accuracy, 83% precision, 85% recall, and 84% F1-score values, showing a 1% higher performance. These results are important to understand the effectiveness between the models.

In the second stage, PCA feature selection algorithm was employed to obtain the best feature subset from the features obtained from three different transfer learning methods: MobileNetV2, DenseNet 201 and InceptinV3. To optimally select the number of components, which is a determining parameter of PCA, the number of components was determined to be 50, and the feature and accuracy values were observed to obtain the highest level of performance with a technique that increased by 25 to 500. At the end of this meticulous process, the most effective number of components was determined to be 250, 150, and 150 for MobileNetV2, DenseNet201, and InceptionV3, respectively, as illustrated in Figure 6. Maximum performance results according to the features in the system where the PCA feature selection algorithm and the SVM classifier are integrated are given in Table 3.

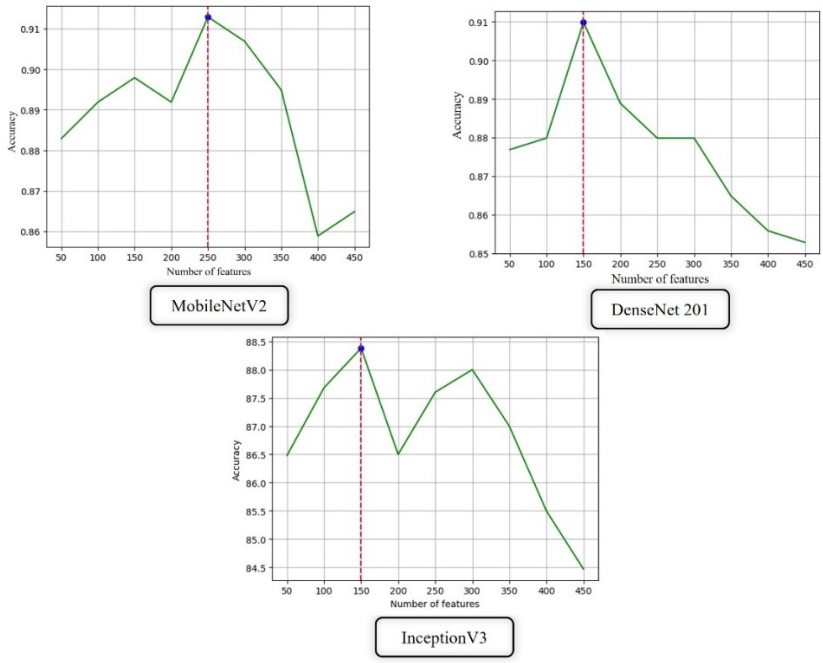

Figure 6. Accuracy graphs according to the number of features of 3 different CNN models

Table 3. Results of the proposed methods (a system integrated with PCA)

Models	Number of features	Classification	Accuracy
MobileNetV2	250	SVM	0.9129
DenseNet201	150		0.9099
InceptionV3	150		0.8838

The obtained features were classified using an SVM classifier, and the confusion matrices resulting from SVM classification are presented in Figure 7. According to the results in Table 3, applying the PCA feature selection algorithm to CNN models yielded accuracy results of 91.29% for MobileNetV2, 90.99% for DenseNet201, and 88.28% for InceptionV3. Upon observation of the results, it is evident that the features selected by PCA optimize the representation capabilities, allowing for the differentiation of defective and functional PV cell samples. The SVM algorithm effectively distinguishes between defective and functional cells by classifying these features. Comparing these results with Table 2, MobileNetV2 exhibited 7.29%, DenseNet201 showed 6.99%, and InceptionV3 displayed 3.28% higher accuracy performance. Detailed confusion matrices resulting from the PCA feature selection algorithm integrated into three separate CNN models are detailed in Figure 7.

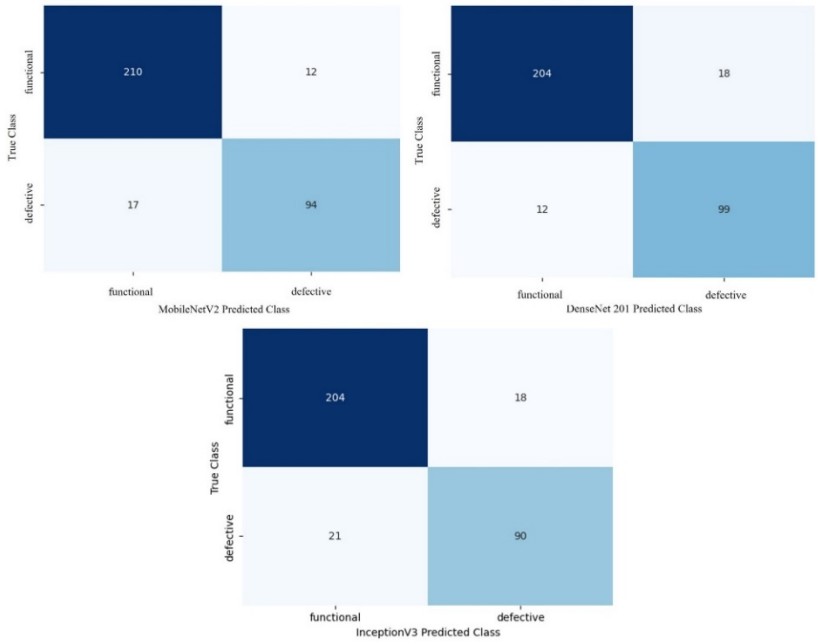

Figure 7. Confusion matrices obtained with feature subset

The performance metrics obtained at each stage of the proposed model shed light on the strengths and weaknesses of the transfer learning methods integrated for defect detection in EL images. These experimental results aim to help researchers choose the most appropriate transfer learning approach for similar tasks.

In the final stage of the experimental study, features detailed from the MobileNetV2, DenseNet201, and InceptionV3 CNN models, as elaborated in Figure 6, were combined to create 550 new feature subsets for each image. To focus on a more effective and informative subset of features, the PCA algorithm was applied again. In Figure 8, a graph of accuracy is presented based on the number of components detailed in the previous step, aiming to determine the best subset component count from the merged features. In addition, Figure 8 shows in detail the confusion matrices obtained from the classification of the best features by the SVM algorithm.

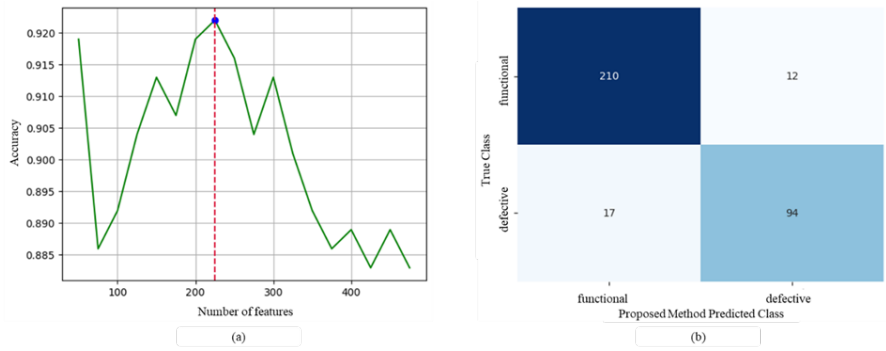

Figure 8. The proposed model; (a) accuracy plot according to the number of features, (b) confusion matrices

The performance metrics calculated with confusion matrices obtained from experimental studies using the proposed combination of fusion, PCA, and SVM are presented in Table 4. Upon evaluating the performance results obtained, the proposed method demonstrated superior performance compared to other results. Additionally, it is compared with the two-class (functional/defective) study conducted by Açıkgöz and Korkmaz [29] using the same dataset, as shown in Table 5. Both studies utilized the same training, testing, and validation rates for the two-class dataset. When the performances were compared for 70% training, 15% testing, and 15% validation, the proposed method exhibited approximately 1% higher performance using 225 features. This literature comparison highlights the importance and effectiveness of the proposed method. Furthermore, Demirci et al. [31], who employed the same dataset in their study, divided the dataset into 80% for training and 20% for testing. They achieved accuracies

of 89.33% and 94.52%, respectively, with the L-CNN and deep feature-based SVM (DFB-SVM) methods proposed in their study. Upon observing the performance results of 2000 features produced using the DFB-SVM approach described by Demirci et al. [31], performance results close to these were obtained with 225 features generated using the proposed method. However, it is not appropriate to compare the performance of the proposed model with previous studies where separated datasets for training and testing were used in different proportions. Dataset sections used in different proportions may affect the model's performance and may not be suitable for an accurate comparison.

Table 4. The results of the proposed Hybrid CNN-PCA method

CNN models	Accuracy	Precision	Recall	F1-score
Proposed method	0.9219	0.92	0.90	0.91

Table 5. The comparison of the proposed method with the method using the same dataset

CNN models	Accuracy	Precision	Recall	F1-score
Açıkgöz and Korkmaz [29]	0.9129	0.8421	0.8972	0.8688
Proposed method	**0.9219**	**0.92**	**0.90**	**0.91**

4. Conclusion

In this study, an improved transfer learning method is presented for effective detection of faults in PV panel cells. PCA algorithm was integrated separately using widely preferred deep learning models such as MobileNetV2, DenseNet201 and InceptionV3. In the next stage, the resulting feature subsets were combined and processed again with the PCA algorithm. This approach aims to benefit from information at different scales while preserving the unique attributes of each model. The obtained features were processed with the SVM algorithm and the defects in PV panel cells were classified. As a result of the experimental studies, an accuracy rate of 92.19% was achieved. The proposed method performed approximately 1% better than the study conducted using the same dataset in the literature.

In future studies, it is aimed to optimize this method for defective detection in the cells of PV panels and to enable it to work in real time on embedded systems. Additionally, it is planned to contribute to the literature by creating a more comprehensive PV panel dataset.

Reference

[1] Pillai DS, and Rajasekar N. A comprehensive review on protection challenges and fault diagnosis in PV systems. Renewable and Sustainable Energy Reviews, 2018; 91:18–40.
[2] Eltamaly AM. A novel benchmark shading pattern for PV maximum power point trackers evaluation. Sol Energy, 2023; 263:111897.
[3] Demir A, Dinçer AE, and Yılmaz K. A novel method for the site selection of large-scale PV farms by using AHP and GIS: A case study in İzmir, Türkiye. Sol Energy, 2023;259:235–245.
[4] Omazic A et al. Relation between degradation of polymeric components in crystalline silicon PV module and climatic conditions: A literature review. Sol Energy Mater Sol Cells, 2019;192:123–133.
[5] Vázquez M, and Rey-Stolle I. Photovoltaic module reliability model based on field degradation studies. Prog Photovoltaics Res Appl, 2008;16(5):419–433.
[6] Silvestre S, Kichou S, Chouder A, Nofuentes G, and Karatepe E. Analysis of current and voltage indicators in grid connected PV (photovoltaic) systems working in faulty and partial shading conditions. Energy, 2015;86:42–50.
[7] Dhoke A, Sharma R, and Saha TK. PV module degradation analysis and impact on settings of overcurrent protection devices. Sol Energy, 2018;160:360–367.
[8] Wang H, Zhao J, Sun Q, and Zhu H. Probability modeling for PV array output interval and its application in fault diagnosis. Energy, 2019;189:116248.
[9] Gong B, An A, Shi Y, and Zhang X. Fast fault detection method for photovoltaic arrays with adaptive deep multiscale feature enhancement. Appl Energy, 2024;353:122071.
[10] Munoz MA, Alonso-García MC, Vela N and Chenlo F. Early degradation of silicon PV modules and guaranty conditions. Sol Energy, 2011;85(9):264–2274.
[11] Djordjevic S, Parlevliet D, and Jennings P. Detectable faults on recently installed solar modules in Western Australia. Renew Energy,2014; 67:215–221
[12] Dhoke A, Sharma R, and Saha TK. PV module degradation analysis and impact on settings of overcurrent protection devices. Sol. Energy, 2018;160:60–367.

[13] Dhimish M. Micro cracks distribution and power degradation of polycrystalline solar cells wafer: Observations constructed from the analysis of 4000 samples. Renew Energy, 2020;145:466–477.
[14] Abdelhamid M, Singh R, and Omar M. Review of microcrack detection techniques for silicon solar cells. IEEE J Photovolt, 2014;4(1):514–524.
[15] Tsanakas JA, Ha L, and Buerhop C. Faults and infrared thermographic diagnosis in operating c-Si photovoltaic modules: A review of research and future challenges. Renewable Sustainable Energy Rev., 2016;62:695–709.
[16] Fuyuki T, and Kitiyanan A. Photographic diagnosis of crystalline silicon solar cells utilizing electroluminescence. Appl Phys A Mater Sci Process,2009;96(1):189–196.
[17] Breitenstein O et al. Can luminescence imaging replace lock-in thermography on solar cells. IEEE J Photovolt, 2011;1(2):159–167.
[18] Tsanakas JA, Chrysostomou D, Botsaris PN, and Gasteratos A. Fault diagnosis of photovoltaic modules through image processing and Canny edge detection on field thermographic measurements. Int J Sustainable Energy, 2013;34(6):351–372.
[19] Pratt L, Govender D, and Klein R. Defect detection and quantification in electroluminescence images of solar PV modules using U-net semantic segmentation. Renew Energy, 2021;178:1211–1222.
[20] Vidal De Oliveira AK, Rüther R, and Aghaei M. Automatic Fault Detection of Photovoltaic Arrays by Convolutional Neural Networks During Aerial Infrared Thermography. In Proceedings of the 36th European Photovoltaic Solar Energy Conference and Exhibition,2019;9-13.
[21] Deitsch S et al. Automatic classification of defective photovoltaic module cells in electroluminescence images. Sol Energy, 2019;185:455–468.
[22] Tang W, Yang Q, Xiong K, and Yan W. Deep learning based automatic defect identification of photovoltaic module using electroluminescence images. Sol Energy, 2020;201:453–460.
[23] Hong F, Song J, Meng H, Rui W, Fang F, and Guangming Z. A novel framework on intelligent detection for module defects of PV plant combining the visible and infrared images. Sol Energy, 2022;236:406–416.
[24] Zhao Y, Zhan K, Wang Z, and Shen W. Deep learning-based automatic detection of multitype defects in photovoltaic modules and application in real production line. Prog Photovoltaics Res Appl., 2021;29(4):471–484.
[25] Moradi Sizkouhi A, Aghaei M, and Esmailifar SM. A deep convolutional encoder-decoder architecture for autonomous fault detection of PV plants using multi-copters. Sol Energy, 2021;223:217–228.
[26] Sun T, Xing H, Cao S, Zhang Y, Fan S, and Liu P. A novel detection method for hot spots of photovoltaic (PV) panels using improved anchors and prediction heads of YOLOv5 network. Energy Reports, 2022;8:1219-1229.
[27] Yanilmaz S, Türkoğlu M, and Aslan M. Güneş enerjisi santrallerinde YOLO algoritmaları ile hotspot kusurlarının tespiti. Fırat University Journal of Engineering Science, 2024;36(1):121-132.
[28] Cao Y, et al. Improved YOLOv8-GD deep learning model for defect detection in electroluminescence images of solar photovoltaic modules, Eng Appl Artif Intell, 2024;131:107866.
[29] Açikgöz H, and Korkmaz D. Elektrolüminesans görüntülerde arızalı fotovoltaik panel hücrelerin evrişimli sinir ağı ile otomatik sınıflandırılması. Fırat University Journal of Engineering Science, 2022;34(2):589–600.
[30] Demirci MY, Beşli N, and Gümüşçü A. Defective PV cell detection using deep transfer learning and EL imaging. In International Conference on Data Science, Machine Learning and Statistics 2019 (DMS-2019), 2019;311–314.
[31] Demirci MY, Beşli N, and Gümüşçü A. Efficient deep feature extraction and classification for identifying defective photovoltaic module cells in Electroluminescence images, Expert Syst Appl, 2021;175:114810.
[32] Deitsch S et al. Segmentation of photovoltaic module cells in uncalibrated electroluminescence images. Mach Vis Appl, 2021;32(4):1–23.
[33] Imak A, Celebi A, Siddique K, Turkoglu M, Sengur A, and Salam I. Dental caries detection using score-based multi-input deep convolutional neural network. IEEE Access, 2022;10:18320–18329.
[34] Turkoglu M. COVIDetectioNet: COVID-19 diagnosis system based on X-ray images using features selected from pre-learned deep features ensemble. Appl Intell, 2021;51(3)1213–1226.
[35] Szegedy C, Vanhoucke V, Ioffe S, Shlens J, and Wojna Z. Rethinking the inception architecture for computer vision. In Proceedings of the IEEE conference on computer vision and pattern recognition, 2016;2818–2826.
[36] Wang SH, and Zhang YD. DenseNet-201-based deep neural network with composite learning factor and precomputation for multiple sclerosis classification. ACM Transactions on Multimedia Computing, Communications, and Applications (TOMM), 2020;16(2).
[37] Turkoglu M, Hanbay D, and Sengur A. Multi-model LSTM-based convolutional neural networks for detection of apple diseases and pests. J Ambient Intell Humaniz Comput, 2022;13(7):3335–3345.
[38] Sandler M, Howard A, Zhu M, Zhmoginov A, and Chen LC. MobileNetV2: Inverted residuals and linear bottlenecks, 2018;4510–4520.
[39] Pearson K. LIII. On lines and planes of closest fit to systems of points in space. The London, Edinburgh, and Dublin Philosophical Magazine and Journal of Science, 1901; 2(11):559–572.
[40] İmak A, Doğan G, Şengür A, and Ergen B. Asma Yaprağı türünün sınıflandırılması için doğal ve sentetik verilerden derin öznitelikler çıkarma, birleştirme ve seçmeye dayalı yeni bir yöntem. International Journal of Pure and Applied Sciences, 2023;9(1):46–55.
[41] Cortes C, and Vapnik V. Support-vector networks. Mach Learn, 1995;20(3):273–297.
[42] Serin J, Vidhya KT, Deepa IMI, Ebenezer V, and Jenefa A. Gender classification from fingerprint using hybrid CNN-SVM. Journal of Artificial Intelligence and Technology, (2024);4(1):82-87.

[43] Demir F. DeepBreastNet: A novel and robust approach for automated breast cancer detection from histopathological images. Biocybernetics and biomedical engineering, (2021);41(3):1123-1139.
[44] Polat H, Türkoğlu M, Polat O, and Şengür A. A novel approach for accurate detection of the DDoS attacks in SDN-based SCADA systems based on deep recurrent neural networks. Expert Systems with Applications, (2022);197:116748.
[45] Doğan G, and Ergen B. A new mobile convolutional neural network-based approach for pixel-wise road surface crack detection. Measurement, 2022;195:111119.
[46] Doğan G, and Ergen B. Karayollarındaki asfalt çatlaklarının tespiti için yeni bir konvolüsyonel sinir ağı tabanlı yöntem. Fırat University Journal of Engineering Science, 2022;34(2):485–494.
[47] Imak A, Çelebi A, Polat O, Türkoğlu M, and Şengür A. ResMIBCU-Net: an encoder–decoder network with residual blocks, modified inverted residual block, and bi-directional ConvLSTM for impacted tooth segmentation in panoramic X-ray images. Oral Radiol., 2023;1:1–15.

C O P Y R I G H T R E L E A S E F O R M

TURKISH JOURNAL OF SCIENCE AND TECHNOLOGY (TJST)
Published by Firat University

Firat University, Fen Bilimleri Enstitüsü Müdürlüğü
Turkish Journal of Science & Technology Editörlüğü
Elazığ-TURKEY,
Manuscript title: .....
.....
.....
Full names of all authors (in order to appear on manuscript): .....
.....
Name, address etc. of corresponding author: .....
.....
.....
ID Number: ..... Telephone: .....
E-mail: ..... Mobile phone: .....

The author(s) warrant(s) that:
a) the manuscript submitted is his/her/their own original work;
b) all authors participated in the work in a substantive way and are prepared to take public responsibility for the work;
c) all authors have seen and approved the manuscript as submitted;
d) the manuscript has not been published and is not being submitted or considered for publication elsewhere;
e) the text, illustrations, and any other materials included in the manuscript do not infringe upon any existing copyright or other rights of anyone. Notwithstanding the above, the Contributor(s) or, if applicable the Contributor's Employer, retain(s) all proprietary rights other than copyright, such as
a) patent rights;
b) to use, free of charge, all parts of this article for the author's future works in books, lectures, classroom teaching or oral presentations;
c) the right to reproduce the article for their own purposes provided the copies are not offered for sale.
However, reproduction, posting, transmission or other distribution or use of the article or any material contained therein, in any medium as permitted hereunder, requires a citation to the Journal and appropriate credit to Firat University as publisher, suitable in form and content as follows:
Title of article, author(s), journal title and volume/issue, Copyright© year.
All materials related to manuscripts, accepted or rejected, including photographs, original figures etc., will be kept by Turkish Journal of Science and Technology editority for one year following the editor's decision. These materials will then be destroyed.
I/We indemnify Firat University and the Editors of the Journals, and hold them harmless from any loss, expense or damage occasioned by a claim or suit by a third party for copyright infringement, or any suit arising out of any breach of the foregoing warranties as a result of publication of my/our article. I/We also warrant that the article contains no libelous or unlawful statements and does not contain material or instructions that might cause harm or injury.
This copyright form must be signed by all authors. Separate copies of the form (completed in full) may be submitted by authors located at different institutions; however, all signatures must be original.

ID number: ..... ID number: .....
Full name (block letters) ..... Full name (block letters) .....
Signature ..... Date ..... Signature ..... Date .....
ID number: ..... ID number: .....
Full name (block letters) ..... Full name (block letters) .....
Signature ..... Date ..... Signature ..... Date .....
ID number: ..... ID number: .....

Turkish authors must supply their ID card number; foreign authors must supply their passport number (if possible)